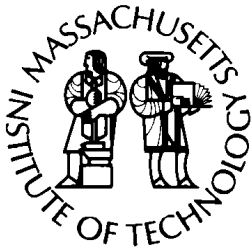Massachusetts Institute of Technology
Woods Hole Oceanographic Institution

**Joint Program
in Oceanography/
Applied Ocean Science
and Engineering**

DOCTORAL DISSERTATION

Slope/shelf Circulation and Cross-slope/shelf Transport
Out of a Bay Driven by Eddies from the Open Ocean

by

Yu Zhang

September 2009

MIT/WHOI

2009-18

Slope/shelf Circulation and Cross-slope/shelf Transport Out of a Bay Driven by Eddies from the Open Ocean

by

Yu Zhang

Massachusetts Institute of Technology
Cambridge, Massachusetts 02139

and

Woods Hole Oceanographic Institution
Woods Hole, Massachusetts 02543

September 2009

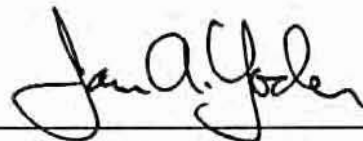**DOCTORAL DISSERTATION**

Approved for Distribution:

_____
Robert A. Weller, Chair
Department of Physical Oceanography

_____
Ed Boyle
MIT Interim Director of Joint Program

_____
James A. Yoder
WHOI Dean of Graduate Studies

Slope/shelf Circulation and Cross-slope/shelf Transport out of a Bay driven by Eddies from the Open Ocean

By

Yu Zhang

B.A. in Oceanography, Ocean University of China, 2001

Submitted in partial fulfillment of the requirements for the degree of

Doctor of Philosophy

at the

MASSACHUSETTS INSTITUTE OF TECHNOLOGY

and the

WOODS HOLE OCEANOGRAPHIC INSTITUTION
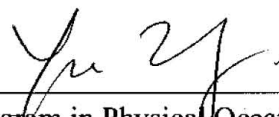
September, 2009

©2009 Yu Zhang
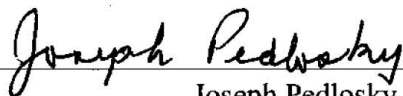
Signature of Author

_____

Joint Program in Physical Oceanography
Massachusetts Institute of Technology and Woods Hole Oceanographic Institution
August 27, 2009

Certified by

Joseph Pedlosky
Senior Scientist
Thesis Co-Supervisor

Glenn Flierl
Professor
Thesis Co-Supervisor

Accepted by

_____

Raffaele Ferrari
Chair, Joint Committee for Physical Oceanography

Slope/shelf Circulation and Cross-slope/shelf Transport

out of a Bay driven by Eddies from the Open Ocean

by

Yu Zhang

Abstract

Interaction between the Antarctic Circumpolar Current and the continental slope/shelf in the Marguerite Bay and west Antarctic Peninsula is examined as interaction between a wind-driven channel flow and a zonally uniform slope with a bay-shaped shelf to the south.

Two control mechanisms, eddy advection and propagation of topographic waves, are identified in barotropic vortex-escarpment interactions. The two mechanisms advect the potential vorticity (PV) perturbations in opposite directions in anticyclone-induced interactions but in the same direction in cyclone-induced interactions, resulting in dramatic differences in the two kinds of interactions. The topographic waves become more nonlinear near the western(eastern if in the Northern Hemisphere) boundary of the bay, where strong cross-escarpment motion occurs. In the interaction between a surface anticyclone and a slope penetrating into the upper layer in a two-layer isopycnal model, the eddy advection decays on length scales on the order of the internal deformation radius, so shoreward over a slope that is wider than the deformation radius, the wave mechanism becomes noticeably significant. It acts to spread the cross-isobath transport in a much wider range while the transport directly driven by the anticyclone is concentrated in space.

A two-layer wind-driven channel flow is constructed to the north of the slope in the Southern Hemisphere, spontaneously generating eddies through baroclinic instability. A PV front forms in the first layer shoreward of the base of the topography due to the lower-layer eddy-slope interactions. Perturbed by the jet in the center of the channel, the front interacts with the slope/shelf persistently yet episodically, driving a clockwise mean circulation within the bay as well as cross-isobath transport. Both the transports across the slope edge and out of the bay are comparable with the maximum Ekman transport in the channel, indicative of the significance of the examined mechanism. The wave-boundary interaction identified in the barotropic model is found essential for the out-of-bay transport and responsible for the heterogeneity of the transport within the bay. Much more water is transported out of the bay from the west than from the east, and the southeastern area is the most isolated region. These results suggest that strong out-of-bay transport may be found near the western boundary of the Marguerite Bay while the southeastern region is a retention area where high population of Antarctic krill may be found.

3

Acknowledgments

My sincere gratitude goes to many people who have given me support, care, and encouragement throughout the process of writing the thesis.

Above all, I owe my deepest gratitude to my supervisor, Prof. Joe Pedlosky, who has been supportive and attentive to me in many aspects. He gave me helpful suggestions when I had problems about the science, offered me wise advice when I could not determine the direction of the thesis. His encouragement helped me through some hard times when I was low in spirit, and his friendship will be a great treasure of my lifetime.

I am also deeply indebted to my secondary supervisor, Prof. Glenn Flierl, who gave me the interesting yet challenging topic in the first place and helped me find answers to many physical and numerical problems. He is full of ideas and solutions, and conversations with him were always enlightening, informative and enjoyable.

Other members of my thesis committee, Prof. Carl Wunsch, Prof. Glen Gawarkiewicz, and Prof. Raf Ferrari provided me with very helpful suggestions that greatly improved the thesis. Their great enthusiasm toward the science always inspired me throughout the dissertation process.

I would like to thank Dr. Robert Hallberg at GFDL, who developed the Hallberg Isopycnal Model that is used in Chapter 3 and 4 in the thesis, and dedicated a lot of time answering my questions about the model. At MIT, Constantinos Evangelinos, Patrick Heimbach and Jean-Michel Campin all helped me set up the model.

As a student of the MIT-WHOI Joint Program, I am surrounded by not only talented scientists mentioned above, but also helpful and friendly administrators like Ronni and Marsha, and great fellow students like Stephanie, Hristina, and Tatiana, who have made my life more joyful.

I am also grateful to Dr. Ruixin Huang at WHOI, who is an old friend of mine and also my first mentor in pursuing Physical Oceanography as profession. Without him, I probably would not have been here at MIT.

My husband, Shaoyu, has been supporting me all these years. He shared with me happiness and

pains, comforted me when I was upset. Because of him, I never felt lonely in a place thousands of kilometers away from home. Lastly, I would like to thank my parents, who know nothing about Physical Oceanography but their unconditional love always has been and always will be the source of my courage.

Contents

Chapter 1

Introduction

Water exchange between the deep ocean and the coastal sea and the related heat, salt, and nutrient fluxes are often essential for the regional physics, chemistry, and biology. In some regions, the cross-shelf-break transport is even important for the global system such as the shelf region off the west coast of Antarctic Peninsula.

The west Antarctic Peninsula (WAP) shelf region extends some 1500km northeastward and about 200km from the coast to the shelf-break (Fig.1.1). It is deep compared with most of the other shelf regions, and much of the shelf is deeper than 500m. The WAP shelf region is a distinctive area in Southern Ocean because of the absence of the Antarctic Slope Front, a density front that is usually found over the outer shelf break and the slope around Antarctic. It may act as a dynamical barrier of interaction between the deep ocean and the shelf region. The WAP shelf region is special also because of the proximity of the Antarctic Circumpolar Current (ACC) and associated water masses. As the only current that goes around the globe, ACC consists of several thermal fronts that are related to deep-reaching, intense oceanic jet streams. The three major, persistent, circumpolar fronts in the ACC are, from north to south, the Subantarctic Front, the Polar Front, and the Southern ACC Front. The Southern ACC Front is right along the outer WAP shelf break (Orsi et al., 1995) as displayed in Fig.1.2 and the Circumpolar Deep Water (CDW), the greatest volume water mass transported in the ACC, is present at the outer edge of the shelf at depths of 200-600m (Hofmann and Klinck, 1998). Thus, this shelf region is directly affected by the open ocean current and a
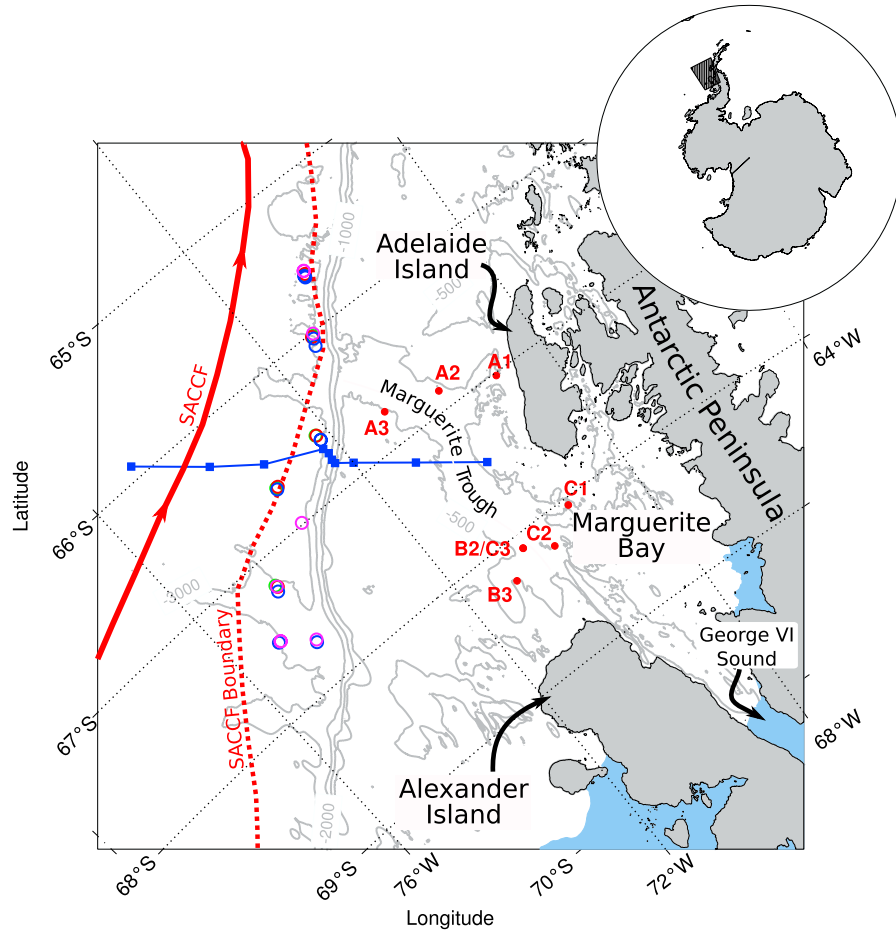
Figure 1.1: The west Antarctic Peninsula shelf region which is also the study region of the Southern Ocean Global Ecosystem Dynamics (SO GLOBEC). The red lines indicate the location of the Southern Antarctic Circumpolar Current Front (SACCF) (solid line) and its southern boundary (dashed line) from historical data (Orsi et al., 1995). From Moffat (2007).

slightly colder and fresher version of CDW is found widely exist over the shelf below the permanent pycnocline at about 150-200m. Above the modified CDW is the cold and fresh Antarctic Surface Water, which is replaced by the colder Winter Water during the austral fall and winter. Moreover, there is no formation of the cold, salty, and dense Antarctic Bottom Water in the WAP shelf region as found in the Weddell and Ross Seas.

The onshore transport of the relatively warm and salty CDW supplies a consistent deep source of heat and salt for the WAP shelf region. Model results show that the heat and salt transported across the shelf break are essential for the heat and salt budget in this area, and much of this onshore

heat and salt transport is balanced by the exchanges with atmosphere and offshore transport of near-surface waters (Dinniman and Klinck, 2004). The presence of the warm oceanic water over the shelf also acts to reduce the winter ice formation and so reduce the brine rejection (Smith et al., 1999). This may contribute to the absence of formation of cold, dense, bottom water in this area.

Antarctic krill is a key species of Southern Ocean ecosystem, offering an essential food supply for many large, top predators such as penguins, seals, and whales. The distribution of Antarctic krill is circumpolar in the Southern Ocean, but is not symmetric (Marr, 1962). The WAP region is one of the areas around the continent with large populations of Antarctic krill. This region is also thought a source area of Antarctic krill for regions to the north and east (Hofmann and Murphy, 2004). Marguerite Bay and surrounding area are characterized by several factors that are thought important for the Antarctic krill: the relative warm environment supported by the onshore intrusion of CDW is favorable to the reproductive cycle of krill; nutrients brought onshore with CDW offer krill food sources; in addition, the clockwise circulation gyre (Beardsley et al., 2004) promotes retention of Antarctic krill. Therefore, Marguerite Bay was chosen to be one focus of the Southern Ocean Global Ocean Ecosystems Dynamics Program (SO GLOBEC) (Hofmann et al., 2002).

At least two mechanisms have been suggested to form the CDW intrusion onto the WAP shelf. One is associated with the along-shore wind. For example, along shore upwelling-favorable winds drive surface Ekman transport offshore and upwelling of deep water along the coast. The climatological winds over the WAP shelf region are from the northeast (Beardsley et al., 2004) driving downwelling along the coast, so can not induce the subsurface CDW transport onshelf. However, the wind is highly variable (Beardsley et al., 2004), so it is still possible that the wind-driven upwelling contributes to the onshore transport of CDW.

Another mechanism was provided by Potter and Paren (1985). They suggested that the buoyancy produced from the ice melt drives a surface flow offshore while the CDW intrudes onshore below the ice and supplies heat to melt ice. However, the WAP shelf region is completely ice-free during the austral summer (Stammerjohn and Smith, 1996), and the observed CDW intrusions don't show any seasonal variations (Moffat, 2007). Therefore, other mechanisms may still contribute to the cross-shelf transport.
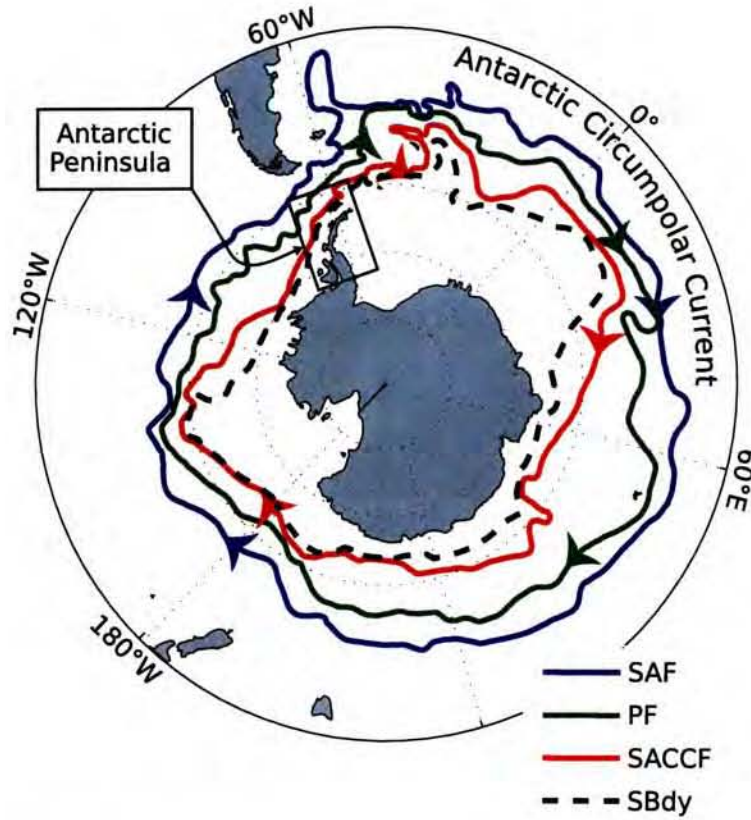
Figure 1.2: Location of the Subantarctic (SAF), Polar (PF), Southern ACC (SACCF) fronts and the Southern Boundary of the ACC (SBdy). Data from Orsi et al. (1995). From Moffat (2007).

Using hydrographic and current velocity observations, Moffat (2007) studied the characteristics of the CDW intrusions onto the WAP shelf and Marguerite Bay. He found that the intrusion of CDW is a frequent phenomenon, occurring roughly four times a month. Warm eddy-like structures were observed during intrusions. Drifter measurements of surface currents in this region during austral summer and fall in 2001 and 2002 also demonstrate mesoscale eddy variability with horizontal scales well in excess of the local Rossby deformation radius, which is about $10\sim15km$ during austral summer and fall (Beardsley et. al., 2004). Based on these facts and the aforementioned proximity of the ACC as well as the absence of the Antarctic Slope Front, we propose that the forcing from the ACC is important in driving the cross-shelf transport and the actual mechanism is the interaction between the continental slope/shelf and eddies from the ACC.

The WAP shelf region is a relatively simple physical system because of the absence of the

Antarctic Slope Front and the formation of the Antarctic Bottom Water. Nevertheless, the problem is still quite complicated if all of the factors such as the ACC, atmospheric forcing, stratification over the shelf, and bottom topography are considered. Actually, understanding the ACC dynamics itself is a huge challenge, let alone the interactions among those factors. The problem is simplified by neglecting one or more elements mentioned above. The ACC is thought crucial for the WAP shelf region because it is close to the shelf-break and is turbulent, spontaneously generating eddies or meanders to force the shelf. This phenomenon has been reasonably represented by eddy-resolving quasi-geostrophic (QG) models of a wind-driven, adiabatic flow in a zonally reentrant channel (McWilliams et al., 1978; Wolff et al., 1991). In their models, the ocean starts from rest and is forced by a steady, zonal wind stress that is symmetric around the central latitude. Zonal flows develop in all layers, and the total potential energy increases nearly linearly with time. After the flow becomes baroclinically unstable, a small perturbation in the center of the channel induces the instability from which a vigorous eddy field develops. Mean potential energy is converted to eddy potential energy and at the same time, eddies feed kinetic energy back into the mean. In the quasi-steady state, the wind energy input is mostly balanced by bottom dissipation. The flow in the channel is turbulent characterized by strong eddy variability. One limitation of the QG models is that the layer thickness variation as well as the height of the bottom topography is assumed small compared with the layer thickness itself. The application of this assumption becomes questionable in the problem of eddy interaction with the continental slope extending from the ocean bottom at the depth of several thousand meters to a few hundred meters and intersecting isopycnals. However, large variations of layer thickness are allowed in primitive equation (PE) models and PE models in density coordinate can represent adiabatic processes very accurately. Hence, the ACC is simulated in the thesis as a wind-driven channel flow using a two-layer Hallberg Isopycnal Model (HIM). When the wind stress applied in HIM has the same symmetric profile in the QG models, the resulting flow shows an asymmetric structure about the central latitude because of the big layer thickness variations, and this structure is completely absent in QG results.

The Marguerite Bay/WAP shelf region is simulated as a bay-shaped shelf next to the southern boundary of the channel. The two regions, the model ACC region and the model shelf region, are connected by a zonally uniform slope. The length scales of the channel as well as the bay-shaped

15

shelf are set to resemble the geometry of the WAP shelf region described earlier. Some simplifications are also made about stratification, atmospheric forcing and bottom topography over the shelf. Due to the absence of the Antarctic Bottom Water formation and the relatively uniform stratification beneath the surface, we think the stratification within this region is less important than the forcing by the ACC and so neglect stratification over the shelf. Since there is no evidence showing the seasonal variations of the subsurface intrusion of CDW, we don't think the strong seasonal variation induced by the atmospheric heating/cooling is essential for the cross-shelf exchange. The shelf region features rough bathymetry. For example, a deep trough called the Marguerite Trough, starts near the shelf-break running southeastward across the shelf with the maximum depth about 1600m. There are observations of the CDW intrusions onto the WAP shelf region suggesting that the intrusion tends to occur at specific locations such as the Marguerite Trough (Moffat et al., 2009). In the present work, for simplicity, the bottom of the shelf region will be assumed to be flat. Naturally, it is then impossible to study the influence of the topography within the bay on the nature of the intrusion into the bay. This would be a good problem for future work.

Sea ice is a very important component of the Antarctic ecosystem. The presence of sea-ice cover strongly affects fluxes of heat, salt, and momentum between atmosphere and ocean surface. Biologically, the sea-ice cover provides a complex habitat for marine species like Antarctic krill and top predators. Variations of the sea-ice cover are closely related to climate change. The WAP shelf region is ice-free during the austral summer (Stammerjohn and Smith, 1996), and ice-covered in the austral winter. There is a trend for decrease of the winter sea-ice duration observed in the WAP shelf region, which is also undergoing a rapid increase in the winter air temperature (Stammerjohn et al., 2008). The seasonal cycle of the sea-ice cover and its variability will definitely influence the wind-driven transport in the Ekman layer. The onshore intrusion of the CDW is however well below the surface. The offshore forcing that will be examined in the thesis is the ACC, which reaches deep in the water column with strong flow. Based on these two reasons, we don't think the sea-ice cover in this region exerts strong influence on the ACC-driven cross-shelf transport of the CDW although it plays an important role in the entire ecosystem.

Compared with prior theoretical studies on eddy-topography interactions, this thesis has two new features. First, it is the first to examine the eddy-topography interaction problem in the presence

of a strong offshore current that spontaneously generates eddies or meanders to force the shelf and slope region. Second, the shelf geometry is chosen to resemble that of Marguerite Bay with isobaths intersecting the coastline. The significance of the two new features and the possible applicability of the model to regions other than Marguerite Bay/WAP will be demonstrated through a brief review of observational and theoretical work.

1.1   Review of Observations

Eddy-slope interactions have been widely observed around the world oceans. The best documented examples are those of rings, robust eddies forming directly from strong ocean currents (Olson, 1991) through instability process. As these big eddies approach the continents and interact with topography, they radiate topographic Rossby waves (Louis and Smith, 1982), drive cross-isobath motions (Evans et al., 1985; Churchill et al., 1986; Joyce et al., 1992), and form a cyclonic eddy from the topography (Kennelly et al., 1985; Evans et al., 1985). Meanwhile, the eddy motion, shape (Evans et al., 1985), and dissipation rate (Cheney and Richardson, 1976) are changed as the result of the interaction.

The Gulf Stream warm-core rings have been frequently observed to drive cross-shelf water exchange by streamers. A streamer is a strong advective feature with the along-feature dimension greatly exceeding the across-feature dimension. The entrainment by streamers is episodic depending on the streamer occurrence, but is also persistent. Seven years of imagery collected by satellite showed that the shelf water entrainment onto the slope by streamers associated with warm-core rings is a frequent phenomenon (Garfield and Evans, 1987): 49 warm-core rings were identified to pass south of the Georges Bank region between 1979 and 1985 with an average of seven rings per year. Streamer entrainment occurred approximately 70% of the time with a large annual variability depending on the passage of warm-core rings.

Similar phenomena have also been found in other coastal regions. Off the coast of southwestern Africa, rings from the Agulhas retroflection occasionally draw large volumes of coastal water off shore (Duncombe Rae, 1991). In the Gulf of Alaska, anticyclonic eddies are important agents in

17

driving the shelf water into the deep ocean (Okkonen et al., 2003).

1.2 Review of Theoretical Work

Earlier theoretical investigations of the eddy-topography interactions focused on the motion of an isolated eddy on a sloping bottom. Nof (1983) found that a cold eddy over a uniformly sloping bottom will translate along the slope and the propagation speed depends on the stratification, the Coriolis parameter and the bottom slope. In a two-layer system, Swaters and Flierl (1990) studied the propagation and structure of cold-core eddies on a sloping bottom, considering the dynamical and thermodynamical interaction of eddies with the warmer surrounding water. However, the non-linear effects are absent by assuming the bottom slope as well as the ratio of eddy thickness to the mean upper layer thickness is very small.

A relevant study of the nonlinear eddy-topography interaction was done by Smith and O Brien (1983) using a two-layer numerical model. They showed that when an eddy moves over a slope that is entirely in the lower layer, the topographic and the planetary beta effects will induce dispersion which gives the eddy an asymmetric structure. This asymmetry allows for the nonlinear propagation tendencies that are different for anticyclones and cyclones. As a result, cyclones are more likely to propagate onto the slope than anticyclones of equal strengths.

Theoretical work has also been carried out to study the response on slope and shelf due to the offshore eddy forcing. Louis and Smith (1982) studied the topographic Rossby waves generated by a vorticity source on the slope in a homogeneous and linear model. Shaw and Divakar (1991) studied the generation mechanism of topographic waves by nonlinear advection of the rings density over a sloping bottom using linear momentum equations and nonlinear density equation. According to their results, the strength of the ring can affect waves amplitudes, but not the generation and propagation of waves. Chapman and Brink (1987) examined shelf and slope responses to the offshore forcing in a linear model with continuous vertical stratification and arbitrary cross-shelf bottom topography. When the forcing is periodic in the along-shore direction and in time, responses vary with the forcing frequency. When the forcing is an anticyclonic eddy translating steadily in the

along-shore direction, it drives a shelf circulation.

In above investigations, the offshore forcing is specified beforehand as an initial or boundary condition. The possible evolution of the eddies as a result of interaction with topography is not allowed, so the effect of eddy evolution on the slope response can not be studied.

Wang (1992) was first to study the problem that actively involves both the process on shelf and evolution of the eddy field. He examined several important aspects of the eddy-topography interactions within a one-layer ocean including the motion of the forcing eddy, the formation of the topographic cyclone, the excitement of topography-trapped waves, and the cross-topography transport.

White and McDonald (2004) studied the interaction between point vortices in a two-layer fluid and a large-amplitude step-like topography. Although the topography is higher than the interface, the depth variation over the topography in the upper layer is small compared with the total layer thickness. The model results showed that cyclones propagate toward and even cross the step, whereas anticyclones propagate away from the step due to dipole formation.

Frolov et al. (2004) examined the interaction of a LCE(Loop Current Eddy)-type anticyclone with a realistic western boundary topography that is high enough to intersect the layer interface in a two-layer ocean model. They showed that the anticyclone generates a surface cyclone from the slope and then moves together with it. Lower eddy structures are induced by the motion of the surface eddies and in turn affect their evolution. In the situation of a narrow shelf, the boundary's effect in advecting the surface eddies along the boundary due to the image theory becomes obvious.

In all theoretical work reviewed above, the eddy-topography interaction is examined between a "designed" eddy or offshore forcing, whose size, strength and location are prescribed as parameters, and a slope. Only phenomena related to this single event are investigated. The exploration of the persistence and the intermittency, the two important features of the cross-shelf exchange observed in shelf regions such as the Mid-Atlantic Bight is impossible, neither is the exploration of the steady response over the slope and shelf. Therefore, examining the interaction between the WAP shelf and the ACC can also help us understand the regional circulation and cross-shelf exchange in other shelf areas such as the Mid-Atlantic shelf.

Prescribing the shelf geometry either as an unbounded region or a region bounded by a straight coastline parallel with the continental slope is common to prior theoretical studies, and the effect of the coastline on the eddy-topography interaction is usually neglected. The bay-shaped shelf in the thesis represents the shelf geometry in a more realistic way and offers the opportunity to study the resultant circulation within this semi-closed area.

1.3 Outline of the Thesis

The interaction between eddies and a continental slope with a bay-shaped shelf is studied with three numerical models from simple to more complicated. In the first two models and also the first two chapters, the interaction is between a single eddy and a slope plus a bay. Although the effect of the shelf geometry on the eddy-topography interaction is an important focus, the basic mechanisms as well as dependence of the eddy-topography interactions on variable parameters will also be thoroughly examined. Results of these two chapters therefore have universal applications, i.e. are not limited to a specific geographical region.

In Chapter 2, the eddy-topography interaction is simplified as the interaction between a point vortex and a step-like topography in a one-layer contour dynamics model. The basic mechanisms of this simplified system and the boundary's effects on the mechanisms are main questions to be answered. It will be shown that there are two control mechanisms, eddy advection and propagation of topographic waves, governing the vortex-escarpment interactions. The topographic waves propagate only in one direction, which is westward in the Southern Hemisphere with shallow water to the south (eastward if in the Northern Hemisphere). In the presence of a curved coastline, the waves' properties are affected and their interaction with the boundary is strong near the western boundary of the bay (eastern if in the Northern Hemisphere) where the cross-escarpment motion is intensified. This phenomenon is pivotal for the transport out of the bay that is under the persistent forcing of an strong, open ocean current in Chapter 4.

The simplifications of the stratification and topography in Chapter 2 lead naturally to Chapter 3, a study of eddy-topography interaction in a two-layer Hallberg Isopycnal Model. The model do-

main is a zonally reentrant channel with a bay in the south and a zonally-orientated slope against the northern edge of the bay intersecting the interface. The eddy interacting with the slope is still prescribed at the beginning as in Chapter 2. New features associated with the basic mechanisms found in Chapter 2 and characteristics of the basic mechanisms in driving the cross-slope/shelf transport are explored. The transport across the bay opening is found strengthened near the western boundary (eastern if in the Northern Hemisphere) of the bay due to the interaction between topographic waves and the curved coastline.

The shape of the domain in Chapter 4 is the same as that in Chapter 3, and is in the Southern Hemisphere. A strong wind-driven current is simulated in the region north of the bay which, in its turbulent state, forces the slope as well as the shelf. A complicated dynamical system will be resolved from the model demonstrating rich phenomena such as eddy/meander formation from instability of the jet, interaction between eddy/meander and slope, forced mean circulation and variability over the slope and within the shelf, and volume transport across the slope and out of the bay. Characteristics of the two basic mechanisms and the boundary's influence in this system will be examined. The path along which waters are transported out of the bay is of special interest since it answers the question of whether the exchange is homogeneous along the shelf-break if the water depth is constant over the shelf. Simulations of flow within a zonal channel that has a flat bottom or a sloping bottom with a zonally uniform slope near the southern boundary and entirely submerged in the lower layer are also examined. The former case is used to understand the dynamics of the wind-driven channel flow in Hallberg Isopycnal Model and its difference between the QG model results. The purpose of the second case is to examine the effects of a zonally-orientated slope on the dynamics of the wind-driven channel flow.

It will be demonstrated in Chapter 4 that the interaction between eddies and the zonally uniform slope in the lower layer would induce the formation of a strong PV front in the upper layer near the base of the topography. This topographically generated PV front is associated with a local maximum of the zonal flow, suggesting a possibility of the formation mechanism of those circumpolar fronts in the ACC such as the Southern ACC Front. This "new" PV front interacts with the jet in the center of the channel and meanwhile forces the slope and the bay to its south episodically. Because the wind stress is assumed zero within the bay, the transport out of the bay is solely driven by

the variability associated with this offshore PV front. The amplitude of the out-of-bay transport is found comparable with the Ekman transport in the center of the channel indicative of the potential significance of the proposed mechanism in driving the cross-shelf exchange. Under the persistent forcing of the model ACC and the new PV front offshore, strong wave motions are continuously excited over the slope. The interaction between waves and the western boundary of the bay is essential for the transport out of the bay. Consequently, much more bay water is transported out of the bay from the west, along the western boundary; and the water well inside the bay tends to be transported westward. The southeastern region of the bay is the most isolated area, and tracers originating from that area are expected to be hardly transported out of the bay even after a very long time. This result implies that the southeastern area may serve as an important retention location for species like Antarctic krill, while strong cross-shelf exchange occurs in the north and west. There are observations suggesting that krill are not associated with regions where intrusions of CDW onto the shelf are present, but with regions of low current magnitude and horizontal current gradient (Lawson et al., 2007). In addition, the offshore persistent forcing from the model ACC generates a clockwise mean circulation around the model Marguerite Bay and the surrounding area, consistent with the observed circulation in the WAP shelf region.

As mentioned, the two new features of the thesis are the presence of a strong offshore current and a bay-shaped shelf. Although originally intended for Marguerite Bay/WAP shelf region, they are potentially applicable to regions other than the Southern Ocean. In many coastal regions such as the Gulf of Maine, Gulf of Mexico, and Gulf of Alaska, the coastline bends relative to isobaths in such a way that a bay-shaped shelf forms in between. The model results that are consequences of the curved coastline, such as interaction between topographic waves and the boundary and the associated character of the out-of-bay transport, can be applied in these regions. The model results reflecting the basic mechanism of the interaction between the strong offshore current and the slope are also enlightening to similar processes in regions such as the Mid-Atlantic Bight shelf, where the strong western boundary current, Gulf Stream, flows by from its south. However, since the current and the topography configurations in the thesis are made similar to that of the ACC and the Antarctic continental slope, in applying the model results to other regions, it should be kept in mind that different relative location of the jet and the slope may result in different dynamical balance. As

22

a result, the effects of the eddies may be different from that in the thesis and the actual process of jet interacting with topography would be different.

Chapter 2

Barotropic Interaction between a Vortex and a Small Escarpment with a Bay-shaped Shallow Area

2.1 Introduction

The problem of circulation within a bay area as well as cross-slope/shelf transport driven by eddies spontaneously generated from a strong open ocean current is rather complex as it involves not only eddy-topography interaction, but also dynamics of the current as well as the effect of an indented coastline. At first, we only examine the effect of the boundary on eddy-topography interaction without considering the eddy generation mechanism. In this chapter, we further simplify the problem as interactions between a point vortex and a step-like topography in a homogeneous fluid in Northern Hemisphere by ignoring factors like the external forcing, stratification, and irregular bottom topography.

The water depth difference across the escarpment produces a potential vorticity (PV hereafter) front that is along the topography when the fluid is at rest. When the front is perturbed, there are water columns crossing the topography and being stretched or squeezed. To conserve PV, these water columns generate relative vorticity which in turn forces the front as well as the vortex. Vortex-

25

escarpment interaction is therefore dynamically equivalent to interaction between a vortex and a PV front. It is also analogous to the interaction of a vortex with a shear flow which has been investigated by a number of researchers (Bell 1990, Stern 1991 and Bell and Pratt 1991). The work most close to this chapter is that of Wang (1992) which treated the barotropic eddy-topography interaction in an infinite domain. Using a contour dynamics model, Wang examined several important aspects of the vortex-escarpment interaction including topographic eddy formation, vortex propagation and topography-trapped waves. In interactions between an anticyclonic vortex and the escarpment, a cyclonic eddy containing the shallow water forms from the topography and moves with the vortex away from the escarpment, but similar phenomenon was not found for cyclone-escarpment interactions. One important result was that the vortex interaction with a large escarpment is qualitatively similar to the quasi-geostrophic case in which the escarpment is small compared with the water depth itself. This result indicates that the quasi-geostrophic assumption will not affect the basic mechanisms of vortex-escarpment interaction and so is applied through our study in this chapter.

The problem in this chapter is basically about interactions among three factors, the vortex, the escarpment, and the curved boundary. Using two limiting cases in which either the vortex or the depth difference across the topography is absent, we find the vortex-escarpment interaction is controlled by two basic mechanisms: one is vortex advection and the other is propagation of topographic waves. The waves propagate along the topography, eastward in Northern Hemisphere with shallow area in the south. Both mechanisms are influenced by the curved coastline. The interaction between the topography-trapped waves and the boundary differs dramatically from the west and east due to the waves' single propagation direction. The two mechanisms also exist and signify in the eddy-slope interaction in a two-layer isopycnal model in Chapter 3. The wave-boundary interaction is essential for the transport out of the bay under the persistent and episodic forcing of a strong open ocean current in Chapter 4.

2.2 Model Set-up

The model domain contains two sub-regions as shown in Fig.2.1: northward of the dash-dot line, there is a zonally periodic channel representing the flat-bottomed deep ocean; southward of the dash-
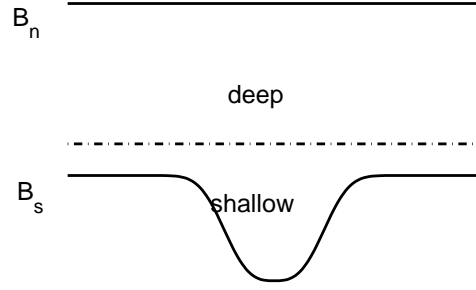
Figure 2.1: A schematic displaying the model domain bounded by a northern boundary B_n and a southern boundary B_s. The dash-dot line denotes the southern boundary of the flat-bottomed deep area.
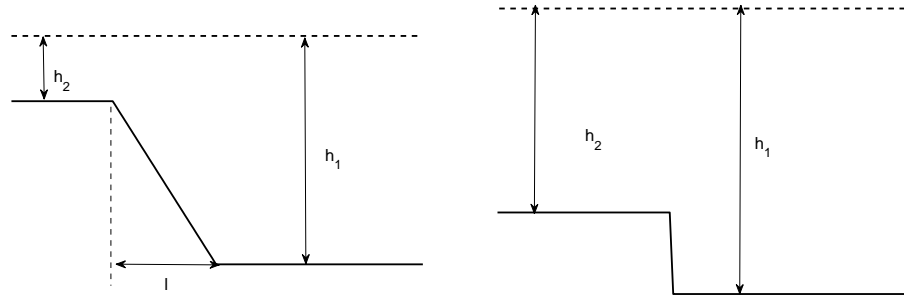
Figure 2.2: Left panel: a schematic of the cross-channel depth profile. h_1 is the water depth in the deep ocean and h_2 is the water depth in the flat-bottomed bay area. l denotes the cross-channel length scale of the slope. Right panel: a schematic of the escarpment.

dot line, the water depth first decreases across a zonally uniform slope (Fig.2.2) and then remains constant within a bay area like Marguerite Bay on the Antarctic continent. Under the assumption that the meridional scale l of the sloping bottom is much smaller than L, the scale of the motion that is of interest, the sloping topography is approximated as an infinitely long and straight escarpment at $y = 0$. Across the escarpment, the water depth changes abruptly from h_1 in the channel to h_2 in the bay($h_2 < h_1$). PV is piece-wise constant within the domain and discontinuous at $y = 0$, i.e., it is $\dfrac{f}{h_1}$ in the channel and $\dfrac{f}{h_2}$ in the bay. Without friction and any other external forces, PV is conserved following water particles. In the Northern Hemisphere and with the present configuration, water columns crossing the topography from south generate positive relative vorticity while water columns crossing the topography from north generate negative relative vorticity. The associated velocity field further deforms the PV front and generates new relative vorticity. This is how the system evolves in time.

2.3   Equations, Matching Conditions, and Boundary Conditions.

If motions occur near and above the bottom slope have length scales L much greater than the water depth H and the length scale of the slope is also greater than H, we could use the shallow water system to study the evolution described above. The length scale L is further assumed much smaller than the external deformation radius, so the rigid-lid approximation is valid:

$$\frac{\partial u}{\partial t} + u\frac{\partial u}{\partial x} + v\frac{\partial u}{\partial y} - fv = -\frac{\partial p}{\partial x}, \tag{2.1}$$

$$\frac{\partial v}{\partial t} + u\frac{\partial v}{\partial x} + v\frac{\partial v}{\partial y} + fu = -\frac{\partial p}{\partial y}, \tag{2.2}$$

$$\frac{\partial}{\partial x}(hu) + \frac{\partial}{\partial y}(hv) = 0. \tag{2.3}$$

In above equations, x-axis directs to the east, y-axis to the north and water depth h has a jump at $y = 0$:

$$h = \begin{cases} h_1 & \text{if } y > 0 \\ h_2 & \text{if } y < 0. \end{cases}$$

28

The stream function ψ is defined in flat-bottom regions satisfying relations $u = -\dfrac{\partial \psi}{\partial y}$ and $v = \dfrac{\partial \psi}{\partial x}$.
The conservation of PV can be written in the following form:

$$\frac{d}{dt} \frac{\nabla^2 \psi + f}{h} = 0, \tag{2.4}$$

where $\dfrac{d}{dt} = \dfrac{\partial}{\partial t} + \mathbf{u} \cdot \nabla$ is the material derivative. Along solid boundaries, ψ is constant in order to satisfy no normal flow conditions. Allowing no zonal transport through the channel, we can simply set the constant to zero on each wall.

The discontinuity of PV at $y = 0$ requires matching solutions of $y > 0$ and $y < 0$. A natural way to find matching conditions, as addressed by Thompson (1991), is to consider the flow field induced when a uniform flow impinges on topography which changes from one value to another linearly over a finite distance. By taking the limit of the distance going to zero, it is found that the cross-topography transport and the along-topography velocity are continuous. The pressure, which can be written as $p = F(\Psi) - \dfrac{u^2 + v^2}{2}$ in the steady state, where Ψ is the transport stream function and F is an arbitrary function of it, is discontinuous as the distance of variation goes to zero. Though the shallow water equations are not valid anymore when the distance is small enough to be comparable with the typical vertical scale, it has been proved through a similar derivation allowing the aspect ratio to be order one (Grimshaw and Yi, 1991), that the same matching conditions can still be obtained.

Multiplying Eq.2.1 with h and Eq.2.3 with u and adding the resultant equations together lead to

$$h \frac{\partial u}{\partial t} + \frac{\partial h u^2}{\partial x} + \frac{\partial h u v}{\partial y} - f v h = -h \frac{\partial p}{\partial x}. \tag{2.5}$$

If we integrate Eq.2.2, Eq.2.3 and Eq.2.5 with respect to y from $-\epsilon$ to ϵ ($\epsilon > 0$), in the limit of $\epsilon \to 0$, integrations that do not contain y-derivatives of the integrands are 0 and we are left with following relations:

$$[hv] = 0, \tag{2.6}$$

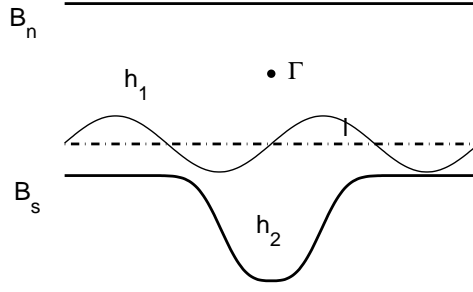$$[huv] = 0 \Rightarrow [u] = 0, \tag{2.7}$$

Figure 2.3: A schematic of the model domain bounded by a northern boundary B_n and a southern boundary B_s. The dash-dot line denotes the escarpment at $y = 0$. The vortex is represented by the black dot in the deep ocean and the PV interface is denoted by the thin solid line l.

$$\left[\frac{v^2}{2} + p\right] = 0, \tag{2.8}$$

where the square bracket denotes the jump of the value inside across $y = 0$. The velocity normal to the escarpment is discontinuous from Eq.2.6, so the pressure is also discontinuous from Eq.2.8.

Under the quasi-geostrophic assumption which requires the ratio of the depth difference Δh across $y = 0$ to the total depth h is on the order of Rossby number, matching conditions are $[v] = 0$ and $[p] = 0$ with discontinuities across the step occurring on the order of Rossby number. Since $[v] = 0$ is essentially the same as $[p] = 0$ according to the geostrophy, another condition $[u] = 0$ needs to be applied.

2.4   Solution Methodology

The shallow water system is solved by first finding the proper velocity field corresponding to relative vorticity induced by deformations of the PV front as well as the point vortex and then integrating Eq.2.4 forward to get relative vorticity at the next time step.

For interactions between the topography and a point vortex within a domain displayed in Fig.2.3, the stream function is the solution of the following equation:

$$\nabla^2 \psi^* = q^* + \Gamma^* \delta(x^* - X^*, y^* - Y^*), \tag{2.9}$$

where "∗" denotes dimensional variables, q^* is the relative vorticity of water columns that have crossed the topography from either side of the escarpment, and Γ^* is the circulation of the vortex located at (X^*, Y^*). In the Northern Hemisphere where f is positive, water columns gain positive relative vorticity $q^{*+} = \dfrac{h_1^* - h_2^*}{h_1^* h_2^*} f h_2^*$ by crossing the escarpment from the south and get negative relative vorticity $q^{*-} = -\dfrac{h_1^* - h_2^*}{h_1^* h_2^*} f h_1^*$ by crossing the escarpment from the north. In the quasi-geostrophic regime, the ratio between the depth difference and the depth itself is of order $O(R)(R \ll 1)$, so to the lowest order, $\dfrac{h_1^* - h_2^*}{h_1^* h_2^*} f h_1^* = \dfrac{h_1^* - h_2^*}{H} f$, where $h_1^* \approx h_2^* \approx H$ and the relative vorticities gained by crossing $y = 0$ from either side of the escarpment are equal and opposite to each other as $q^{*+} \approx -q^{*-} \approx \dfrac{h_1^* - h_2^*}{H} f = \Delta q^*$.

Two important scales are used to dimensionalize Eq.2.9. One is the length scale $L = \sqrt{S}$, where S is the area of the bay; the other one is Γ_0, the scale of the circulation Γ^*. The dimension of Γ^* is $UL = \dfrac{L^2}{T}$. According to this relation, the scale for time is $T_0 = \dfrac{L^2}{\Gamma_0}$ and the scale of velocity is $U = \dfrac{\Gamma_0}{L}$. The relative vorticity Δq^* is nondimensionalized as $\Delta q = \dfrac{\Delta q^*}{\Delta q_0} = \Delta q^* \dfrac{L^2}{\Gamma_0}$, where Δq_0 is the scale of Δq^*.

So the problem that is going to be solved consists of the nondimensional form of Eq.2.9:

$$\nabla^2 \psi = q + \Gamma \delta(x - X, y - Y) \tag{2.10}$$

with boundary conditions

$$\psi = 0 \text{ on } B_1, B_2, \tag{2.11}$$

$$\psi(x + a, y) = \psi(x, y), \tag{2.12}$$

and the continuity condition at $y = 0$. a is the length of the channel.

31

2.4.1 The Poisson Equation

We split ψ into a special solution ψ_p and a homogeneous solution ψ_h, which satisfy the following equations and boundary conditions:

$$\nabla^2 \psi_p = q + \Gamma \delta(x - X, y - Y), \tag{2.13}$$

$$\psi_p(x + a, y) = \psi_p(x, y), \tag{2.14}$$

$$\nabla^2 \psi_h = 0, \tag{2.15}$$

$$\psi_h(x + a, y) = \psi_h(x, y). \tag{2.16}$$

$$\psi_h = -\psi_p = 0 \ \text{on} \ B_1, B_2, \tag{2.17}$$

For a distributed source as $q(x, y)$, the Poisson equation can be solved via the Greens function method, i.e., finding the Greens function $G(x, y, \xi, \eta)$ that satisfies the following equations:

$$\nabla^2 G = \delta(x - \xi, y - \eta), \tag{2.18}$$

$$G = 0 \ \text{on} \ B_1, B_2, \tag{2.19}$$

$$G(x + a, y, \xi, \eta) = G(x, y, \xi, \eta), \tag{2.20}$$

and then integrating G over the whole source area A:

$$\psi_{pF} = \iint_A q(\xi, \eta) G(x, y, \xi, \eta) d\xi d\eta, \tag{2.21}$$

where the subscript "F" reminds us that this is only part of the special solution induced by the front deformations. The part induced by the point vortex is simply $\psi_{pV} = \Gamma G(x, y, X, Y)$.

To find the Green's function that is induced by a monopole at $(\xi, \eta)(0 < \xi < a)$ and is periodic in x, we consider a domain extending from $-\infty$ to ∞ in x. Within the domain, an infinite number of monopoles, each of which has the same strength as well as the meridional location as the original

one, are lined up and spaced in such a way that their zonal locations are $\xi, \xi \pm a, \xi \pm 2a$ .... In the complex plane $z = x + iy$, the complex potential of a single monopole at $z_0 = \xi + i\eta$ is $W = -\dfrac{i}{2\pi} \ln(z - z_0)$, and the velocity is $\dfrac{dW}{dz} = u - iv = -\dfrac{i}{2\pi(z - z_0)}$. Therefore, the velocity field from the string of monopoles is the sum of infinite number of analytic functions each of which has a simple pole located at $z_0 + na, n = 0, \pm 1, \pm 2, ...$:

$$u - iv = \sum_{n=-\infty}^{n=\infty} -\frac{i}{2\pi(z - (z_0 + na))}. \tag{2.22}$$

Equivalently, Eq.2.22 can be written as a cot function, which, when $a = 2m\pi$ (m is any positive integer), is

$$u - iv = -\frac{i}{4m\pi} \cot\left(\frac{z - z_0}{2m}\right), \tag{2.23}$$

and the stream function is

$$G(x, y, \xi, \eta) = \mathrm{Im}\left(\frac{i}{2\pi} \ln\left(\sin\frac{z - z_0}{2m}\right)\right). \tag{2.24}$$

Integrating G around source area and applying derivatives lead to:

$$\begin{aligned}
u_{pF} &= -\frac{\partial}{\partial y} \iint_A q(\xi, \eta) G(x, y, \xi, \eta) d\xi d\eta \\
&= -\iint_A q(\xi, \eta) \frac{\partial}{\partial y} G(x, y, \xi, \eta) d\xi d\eta,
\end{aligned} \tag{2.25}$$

$$\begin{aligned}
v_{pF} &= \frac{\partial}{\partial x} \iint_A q(\xi, \eta) G(x, y, \xi, \eta) d\xi d\eta \\
&= \iint_A q(\xi, \eta) \frac{\partial}{\partial x} G(x, y, \xi, \eta) d\xi d\eta.
\end{aligned} \tag{2.26}$$

$q(\xi, \eta)$ only has two different values within the domain, either Δq or $-\Delta q$, so we can split the entire source area A into two groups of area patches A^+ and A^-. A^+ includes all patches that have positive relative vorticity q^+ and A^- includes all that have q^-, where $q^+ = \Delta q$ and $q^- = -\Delta q$. We use L^+ and L^- to represent the patch boundaries. Being constant within each patch, q can be taken out of the integrals in Eq.2.25 and 2.26. According to Eq.2.24, derivatives of Greens function with respect to x and y can be related to those to ξ and η: $\dfrac{\partial G}{\partial y} = -\dfrac{\partial G}{\partial \eta}, \dfrac{\partial G}{\partial x} = -\dfrac{\partial G}{\partial \xi}$. Applying

33

these two relations to Eqs.2.25 and 2.26 leads to

$$
\begin{aligned}
u_{pF} &= q^+ \iint_{A+} \frac{\partial}{\partial \eta} G d\xi d\eta + q^- \iint_{A-} \frac{\partial}{\partial \eta} G d\xi d\eta \\
&= q^+ \oint_{L^+} G d\xi + q^- \oint_{L^-} G d\xi
\end{aligned}
\tag{2.27}
$$

$$
\begin{aligned}
v_{pF} &= -q^+ \iint_{A+} \frac{\partial}{\partial \xi} G d\xi d\eta - q^- \iint_{A-} \frac{\partial}{\partial \xi} G d\xi d\eta \\
&= -q^+ \oint_{L^+} G d\eta - q^- \oint_{L^-} G d\eta.
\end{aligned}
\tag{2.28}
$$

Thus integrals across the entire source area A has been changed into integrals across different area patches and finally into line integrals along the boundaries of all patches. In Fig.2.4, the front is in the deep ocean in the east part of and in the shallow area in the west. Bounded by the front and the escarpment and separated by three intersection points, C_1 in the west, C_2 in the middle and C_3 in the east, two patches have relative vorticities: the one to the north of the shelf-break has positive relative vorticity and the one to the south of the shelf-break has negative relative vorticity. In calculating u_{pF} and v_{pF}, we need to integrate the Greens function along two contours: one starts from the middle intersection point C_2 goes along the x-axis to the east intersection point C_3 and then goes westward along the PV front back to the middle intersection point; the other contour starts from the middle intersection point, goes westward along x-axis to the west intersection point C_1 then goes eastward along the front back to the middle intersection point. This is a case when the contour consists of not only the PV front but also the shelf-break. If a blob of shelf water is isolated in the deep sea, then the line integral only involves the PV front.

In the quasi-geostrophic regime, $q^+ = \Delta q = -q^-$, so integrals along boundaries of all patches can be simplified as integrals along the PV front l and the x axis:

$$
\begin{aligned}
u_{pF} &= q^+ \iint_{A+} \frac{\partial}{\partial \eta} G d\xi d\eta + q^- \iint_{A-} \frac{\partial}{\partial \eta} G d\xi d\eta \\
&= \Delta q \left(\oint_{L^+} G d\xi - \oint_{L^-} G d\xi \right) \\
&= \Delta q \left(\oint_{y=0} G d\xi - \oint_l G d\xi \right)
\end{aligned}
\tag{2.29}
$$

$$v_{pF} = -q^+ \iint_{A^+} \frac{\partial}{\partial \xi} G d\xi d\eta - q^- \iint_{A^-} \frac{\partial}{\partial \xi} G d\xi d\eta$$

$$= -\Delta q \left(\oint_{L^+} G d\eta - \oint_{L^-} G d\eta \right) \tag{2.30}$$

$$= -\Delta q \oint_{l} G d\eta$$

The velocity induced by the point vortex is

$$u_{pV} - i v_{pV} = -\frac{i\Gamma}{4m\pi} \cos \left(\frac{z - z_0}{2m} \right). \tag{2.31}$$

In seeking the homogeneous solution, we put two sets of monopoles outside the model domain. One set is lined up next to the northern boundary B_n; the other set is next to the southern boundary B_s. Since they are located outside the domain, these monopoles satisfy the homogeneous equation Eq.2.15 within the domain. Suppose N monopoles are applied outside the domain denoted as black dots in Fig.2.5. Among them, $N1$ monopoles are along the boundary B_n and $N2$ along the boundary B_s. Meanwhile, we pick up N locations on these two boundaries that are not coincident with locations of those monopoles ($N1$ on B_n, and $N2$ on B_s) and calculate the normal velocities at these locations forced by the PV front deformations as well as vortices within the domain. The results are written as an N by 1 column vector denoted as V_0. If every monopole outside the domain has unit strength, we can also calculate the normal velocities from each of the N monopoles at each of the N locations denoted as circles in Fig.2.5and the results form an N by N matrix M. The N elements in each row of M are the normal velocities induced by N monopoles at one single location. The N elements in each column of M are normal velocities at N different locations induced by one single monopole. Of course, to counter the normal velocity on boundaries that are induced by all monopoles inside the domain, strengths of monopoles outside the domain can not be uniformly one. Defining an N by 1 unknown column vector P representing the real strengths of those monopoles should have leads to the relation

$$MP = -V_0, \tag{2.32}$$

and the vector P is found via inverting the matrix M:
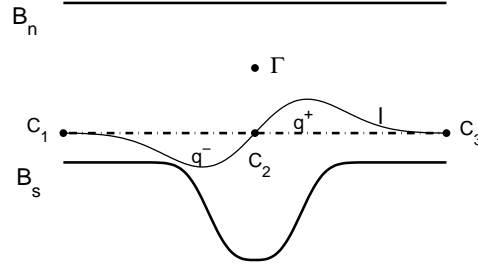
$$P = -M^{-1}V_0. \tag{2.33}$$

35

Figure 2.4: A schematic of the model domain bounded by a northern boundary B_n and a southern boundary B_s. The dash-dot line denotes the escarpment at $y = 0$. The PV interface is denoted by the thin solid line l. The line l insects with the line of $y = 0$ at three locations denoted as C_1, C_2 and C_3.
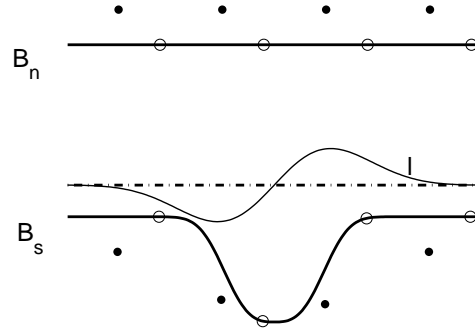

Figure 2.5: A schematic of the model domain bounded by a northern boundary B_n and a southern boundary B_s. The dash-dot line denotes the escarpment at $y = 0$. Black dots denote monopoles located outside the model domain. Black circles denote locations on boundaries where the velocities normal to the boundaries are set to be zero in calculating strengths of those monopoles.

The velocity field $\mathbf{u_h}$ forced by these monopoles can now be calculated. Both $\mathbf{u_p}$ and $\mathbf{u_h}$ are continuous across the topography, so the complete solution of Poisson's equation is obtained by simply adding them together.

There are several things need to be noticed about this part of calculation. First, different from the way finding the velocity $\mathbf{u_p}$, the way of seeking $\mathbf{u_h}$ is numerical. An assumption we need to make is that the no normal flow condition is satisfied everywhere on boundaries if it is satisfied at the finite number of locations denoted as circles in Fig.2.5. Second, the locations of the N monopoles outside the domain are fixed in time, and so is the matrix M, but at each time step, as $\mathbf{u_p}$ changes, the N monopoles adjust their strengths accordingly to satisfy the boundary condition.

2.4.2   Time Integrations

In solving the special solutions, we have made it clear that the locations of the PV front and the point vortex are required, both of which are functions of time. In solving the homogeneous solution, we calculate velocities only at fixed locations on boundaries. Only the PV contour and the point vortex need to be updated with time. The meridional location of the front l evolves in time according to the equation:

$$\frac{\partial l}{\partial t} + u_l \frac{\partial l}{\partial x} = v_l, \tag{2.34}$$

where u_l and v_l are the zonal and meridional velocities on the front. Eq.2.34 shows explicitly the nonlinearity and time dependency of the system. As to the vortex, its location (X, Y) changes according to the following equations:

$$\frac{dX}{dt} = U, \tag{2.35}$$

$$\frac{dY}{dt} = V, \tag{2.36}$$

where (U, V) are the fluid velocities at the vortex.

The process of solving the entire problem in the quasi-geostrophic regime can be summarized as follows. First, given locations of the two zonal boundaries of the domain, pick up N locations on the boundaries and calculate the matrix M using Eq.2.32. Second, given the initial velocity, location, and the strength of the front and the point vortex, using Eqs.2.29, 2.30 and 2.31 find velocities of the front and the point vortex, and the normal velocity vector V_0 at those N boundary locations. Third, calculate the strength vector using Eq.2.33. Fourth, using Eq.2.23 and P to calculate the velocity on the front and the point vortex produced by each monopole outside the domain and sum them up. The last step, add velocities obtained from the fourth step to those from the second step to get u_l, v_l, U, V and use Eqs.2.34, 2.35 and 2.36 to get the locations of the front and the vortex at the next time step.
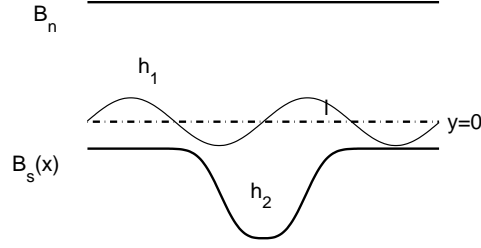
Figure 2.6: A schematic of the model domain bounded by a northern boundary whose meridional location is B_n and a southern boundary whose meridional location is B_s. The dash-dot line denotes the escarpment at $y = 0$. The meridional location of the PV interface is l.

2.5 Linear Analysis of the Free Problem

The topography at the shelf-break supports topography-trapped waves which, like the planetary Rossby waves, owe their existence to the PV variation, however our simplification of the continental slope into a step topography makes the waves possible only along the escarpment. The character of the free escarpment waves is examined in this section through linear analysis of the free problem.

In the absence of the point vortex, the only source of the relative vorticity is generated by deformations of the PV front. Using the Heaviside function, the governing equation for the system is

$$\nabla^2 \psi = \Delta q \left[H(y) - H(y - l) \right]. \tag{2.37}$$

With the assumption that the amplitude of the front deformations are small compared with their length scales, we expand $H(y - l)$ in Taylor series and keep only the first two terms:

$$\nabla^2 \psi = \Delta q \left[H(y) - H(y) + l(y) \right] = \Delta q l(y). \tag{2.38}$$

Everywhere except at $y = 0$, ψ also satisfies Laplace equation:

$$\nabla^2 \psi = 0. \tag{2.39}$$

Linearizing the evolution equation of the front Eq.2.34 gives

$$\frac{\partial l}{\partial t} = v_l, \tag{2.40}$$

38

where v_l is evaluated at $y = 0$ rather than at the front. In the quasi-geostrophic regime, Eq.2.40 indicates the continuity of the meridional velocity as well as the stream function at the escarpment. Integrating Eq.2.38 across a very small range $(-\epsilon, \epsilon)$ in y leads to:

$$\int_{-\epsilon}^{\epsilon} \frac{\partial^2 \psi}{\partial x^2} dy + [\frac{\partial \psi}{\partial y}]_{-\epsilon}^{\epsilon} = \int_{-\epsilon}^{\epsilon} \Delta q l(y) dy. \tag{2.41}$$

In the limit of $\epsilon \to 0$, the first term vanishes as the stream function is continuous at $y = 0$, so the zonal velocity experiences a jump across the escarpment:

$$[\frac{\partial \psi}{\partial y}]_{-\epsilon}^{\epsilon} = \Delta q l. \tag{2.42}$$

The linear system is therefore governed by Eqs.2.39, 2.40, and 2.42. In the situation where y locations of the two boundaries B_n and B_s vary with x, the solution of ψ can not be in pure sinusoidal form. With the assumption that the length scales of the front deformations are small compared with the length scales of variations of the boundaries' y locations, we can use the WKB method and expect the solution to be in a wave-like form: $l = l_0(x) \exp(ic(x) - i\omega t)$. Both the wave amplitude and wave number vary in x, though much slower than the phase, so to the lowest order, A and $\frac{\partial c}{\partial x}$ are constants. Accordingly, the stream function $\psi = A \exp(ic(x) - i\omega t)\phi(y)$. Substituting ψ into Eq.2.39 leads to:

$$[\frac{\partial^2 A}{\partial x^2} + i(2k\frac{\partial A}{\partial x} + A\frac{\partial k}{\partial x}) - k^2 A]\phi + A\frac{\partial^2 \phi}{\partial y^2} = 0, \tag{2.43}$$

where $k = \frac{\partial c}{\partial x}$.

Looking only at the real part of Eq.2.43 and ignoring the x derivative of wave amplitude, we obtain an equation for ϕ:

$$-k^2 \phi + \frac{\partial^2 \phi}{\partial y^2} = 0. \tag{2.44}$$

If the northern boundary B_n is zonal and very far away from the escarpment, ϕ is expected to decay northward like $A_N e^{-ky}$ in the region of $y > 0$. Southward of $y = 0$, ϕ is in the form of $A_S \sinh k(y - B_s)$ in order to satisfy the zero boundary condition at B_s. Both solutions decay away from the escarpment, so waves are trapped at the topography. Conditions at the escarpment include
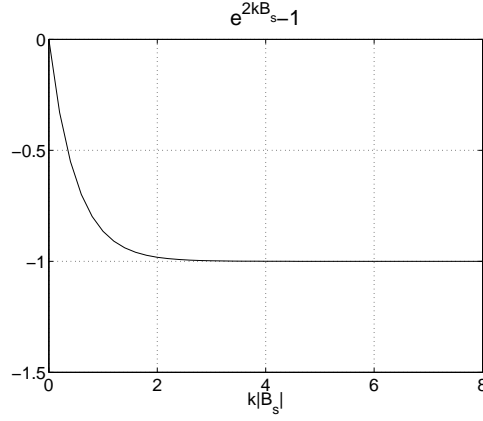
Figure 2.7: The x-dependent part of the frequency versus the product of the wave number k and the shelf's width $|B_s|$.

both the continuity of the stream function as well as the discontinuity of the zonal velocity:

$$\psi_N = \psi_S, and \tag{2.45}$$

$$[\frac{\partial \psi_N}{\partial y}]_{y=0} - [\frac{\partial \psi_S}{\partial y}]_{y=0} = \Delta q l_0, \tag{2.46}$$

from which coefficients A_N and A_S are solved as $A_N = \frac{\Delta q l_0}{k} \frac{e^{2kB_s} - 1}{2}$ and $A_S = -\frac{\Delta q l_0}{k} e^{kB_s}$. Substituting solutions of l and v_l in Eq.2.40, we get the frequency $\omega = -\frac{\Delta q}{2}(e^{2kB_s} - 1)$. Note that the PV difference across the escarpment Δq is positive, the position of the southern boundary B_s is negative, so the sign of the frequency is the same as that of the wave number k, which means the topography-trapped waves are propagating towards the east with higher PV on its right hand side, in the same fashion as Rossby waves. In Southern Hemisphere, if the water depth is still shallower south of the escarpment, the PV value is greater (small and negative) north of the escarpment, so the topography-trapped waves will propagate westward. The group speed $c_g = -\Delta q B_s e^{2kB_s} > 0$, indicating that the energy is transported along the topography in the same direction as wave phase.

The dispersion relation is explicitly dependent on x, so the wave keeps its frequency constant but changes its wave number as $\frac{1}{|B_s|}$ during propagation. The wave length is elongated in area with wider shelf and shortened where the shelf is narrow. As illustrated in Fig.2.7, the boundary's effect on wave properties diminish for short waves. When the wave length is much smaller than half of the

shelf width, waves have the same properties as those propagating without boundaries: waves with different length scales propagate with uniform frequency $\frac{\Delta}{2}$ dependent only on the depth difference across the topography and no energy is transported.

The variation of the wave amplitude in x is obtained from the imaginary part of Eq.2.43:

$$\frac{\partial}{\partial x}(Ak^{1/2}) = 0. \tag{2.47}$$

With k changing with $\frac{1}{|B_s|}$, A varies as $\sqrt{|B_s|}$ and kA varies as $\frac{1}{\sqrt{|B_s|}}$. Although the amplitude is amplified as the wave propagates into the region with wider shelf, the growth is slower than that of the wave length. The ratio between the wave amplitude and the wave length increases with decreasing shelf width, which means waves become steeper and more inclined to break in narrow shelf regions. This effect of the boundary is found to be very important for shelf/slope circulation as well as cross-shelf/slope transport in Chapter 4.

2.6   Interaction of A Vortex with a Small Escarpment

2.6.1   Numerical Scheme

The vortex and the front are stepped forward to new positions using a second order Runge-Kutta scheme. Contour Surgery is performed whenever necessary and we give a brief description of its implementation here. There is a wide range of application of this technique. For more details on its geophysical fluid application and implementation, readers are referred to Dritschel (1988). During evolution of the front, if some points on the front get very dense in one area while sparse in other regions, spacing adjustment is used to rearrange points according to weighted distance, which is the physical distance times the local curvature. If two successive elements of a contour are so close that they are almost coincident with each other, which looks like a tail, the snipping adjustment can cut the tail off the front and connect the two parts where the tail starts. If two different parts of a contour are close to each other, the pinch adjustment can connect them at the closest point.
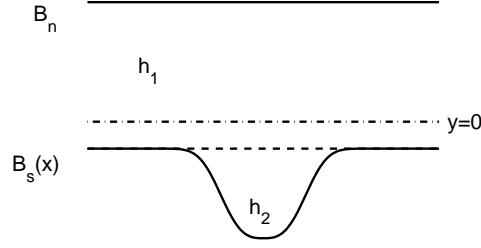
Figure 2.8: A schematic of the model domain. Thick solid lines represent the two boundaries of the domain B_n and B_s. The dash-dot line denotes the escarpment at $y = 0$. The dashed line denotes the northern edge of the bay.

2.6.2 Solutions and Discussion

Quasi-geostrophic vortex-escarpment interactions are studied in this section. The vortex can be either a cyclone (counter-clockwise circulation in the Northern Hemisphere with $\Gamma > 0$) or an anticyclone (with $\Gamma < 0$). The domain, as described in previous sections, contains a channel extending zonally from $x = 0$ to $x = a$ with a northern boundary at $y = B_n$ and a southern boundary at $y = B_s$, which together with the escarpment along $y = 0$ partially encloses the shallow area into a bay. The length of the channel, a is set to 16π, as is explained in APPENDIX A. The southern boundary's y location B_s varies in x as a Gaussian function:

$$B_s = -d_1 - d_2 \exp(-w(x - 0.5a)^2),$$ (2.48)

where d_1 denotes the meridional distance from the escarpment to the northern edge of the bay as denoted by the dash line in Fig.2.8, d_2 denotes the distance from the southern tip of the bay to its northern edge, and w is a parameter determining the zonal length scale of the bay. In almost all experiments except mentioned otherwise, $d_1 = 0.01$, $d_2 = 0.5$, and $w = 1$. The position of the northern boundary B_n is set to be much greater than that of the bay's meridional width d_2 so the wall has little effect on motions near the escarpment.

Since we have scaled the length and time variables using the area of the bay and the strength of the vortex circulation, the remaining independent parameters are the initial location of the vortex and the strength of the relative vorticity Δq or the depth difference across the escarpment. It is impossible to cover the whole parameter space, so only responses within parameter ranges consid-

ered to be closer to the oceanic conditions and our quasi-geostrophic assumptions are discussed. Nevertheless, the evolution of the front in the nonlinear regime is still very complicated as results of interactions among several physical elements including the vortex, the boundary and the PV front. We therefore begin with cases illustrating the control mechanisms of the system.

Control Mechanisms

The control mechanisms are found via two limiting cases, in which the physics is simplified as one physical element is absent. In the first limiting case, the effect of the topography is totally removed by setting $\Delta q = 0$, while in the second limiting case, the point vortex has zero circulation.

1. The case without the topography: eddy advection

With $\Delta q = 0$, the original problem only involves interactions between a point vortex and the curved southern boundary. Vortex-wall interactions are often studied using the image theory. In the simplest case, for a vortex northward of a straight wall, the effects of the boundary are equivalent to those of a vortex which has equal but opposite strength and is at the symmetric location about the wall to the original vortex. The resulting velocity field is the sum of that generated by the two vortices. If the vortex is an anticyclone, the flow near the wall is directed westward; forced by its image vortex, a cyclone on the other side of the wall, the anticyclone goes westward along the wall. If the vortex is a cyclone, the flow field next to the wall as well as the movement of the vortex is opposite to that in the case of an anticyclone.

Without the PV difference across the topography, there is no longer a PV front. We examine the time evolution of the interface initially at $y = 0$ which, as shown in Fig.2.9 is anti-symmetric in the anticyclone-induced and cyclone-induced cases. An anticyclonic vortex located northward of the bay generates a clockwise velocity field, opposite to that produced by a cyclonic vortex as shown in panels of $t = 0.0$ in Fig.2.9. Correspondingly, a crest (trough) and a trough (crest) of the interface form on the western and the eastern side of the anticyclone (cyclone) and are advected westward (eastward) at the same time. As the crest grows northward as forced by the vortex, the trough is deepened southward and starts to touch the boundary first in narrow shelf region. By time $t = 16.0$, the troughs in both cases have been attached to the boundary almost everywhere within the bay

43

indicating almost all the bay water has been taken off the topography. Meanwhile, the anticyclone (cyclone) is advected westward (eastward) by the boundary pushing the crest further westward (eastward) along the wall. At time $t = 40.0$, the crests have become long and thin filaments circling around the anticyclone (cyclone) clockwise (anti-clockwise).

The vortices in both cases propagate along the curved boundary though their trajectories are anti-symmetric to each other as in Fig.2.10. The zonal scale of the vortex translations within 40.0 time units is roughly equal to the distance the bay water is advected along the boundary. Therefore, the zonal translation of the streamer along the coastline is caused by the propagation of the vortex. Without the boundary, the vortex is expected to remain fixed at its initial location while the streamer circles around the vortex.

In the limit of no topography, the evolution of the interface is determined by the vortex advection. The boundary affects the evolution of the front by inducing propagation of the vortex. When the vortex is located closer to the coastline, this effect is expected to be stronger and the bay water, which is in from of a long and thin streamer circling around the vortex, can be advected further along the coast. Before the vortex is started, the only interface where the shelf water meets the deep ocean is the bay's opening, while in the shape of a streamer, the bay water is surrounded by the deep-ocean water through a much greater area, which can greatly enhance the mixing of any properties that have different values between the shallow and the deep region.

It is very important to note that both the PV front evolution and the vortex translation that are forced solely by the eddy advection mechanism are antisymmetric in the anticyclone- and cyclone-induced interactions.

2. The case without vortices: propagation of topographic waves.

The second limiting case is the free problem with the existence of the topography and is essentially the nonlinear evolution of topography-trapped waves.

The front is initially perturbed southward in the west and northward in the east as shown in the panel of $t = 0.0$ of Fig.2.11, so positive relative vorticity is generated between the crest and the escarpment and negative relative vorticity is generated between the trough and the escarpment denoted
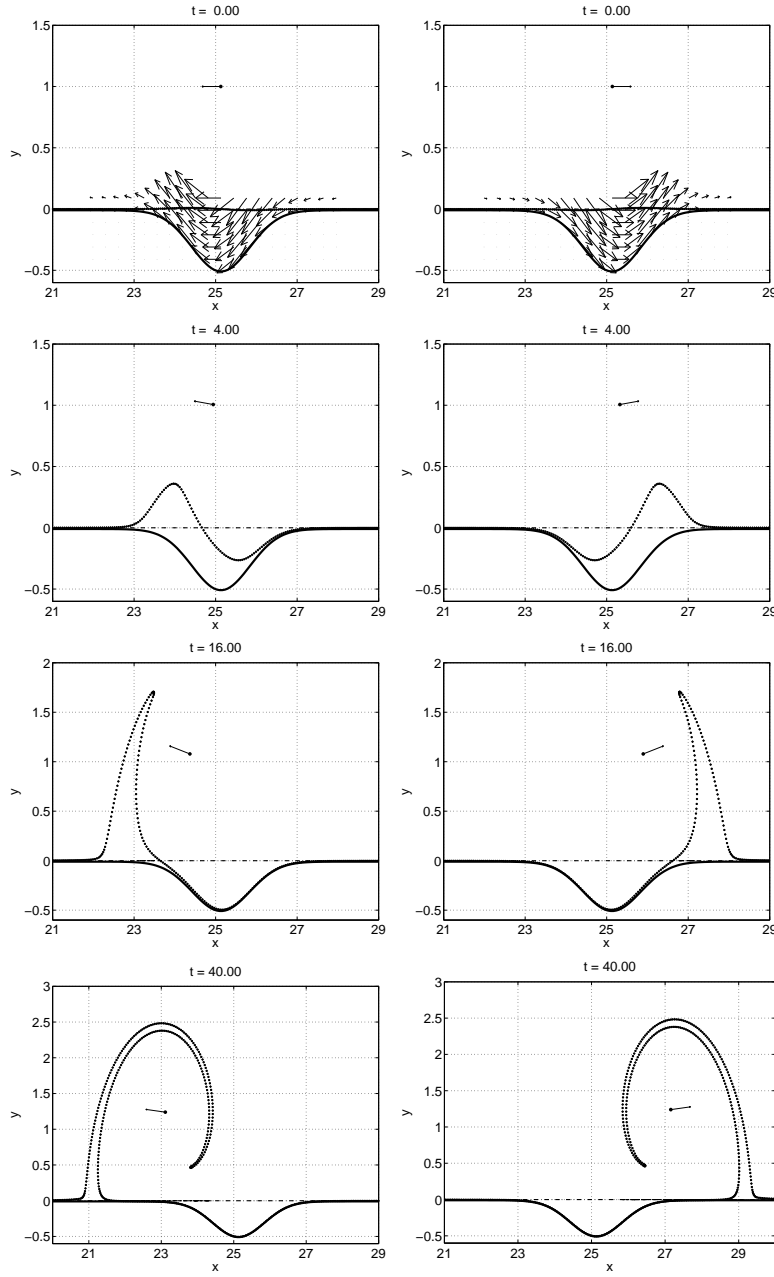
44

Figure 2.9: Limiting case 1: no topography $\Delta q = 0$. The time evolution of the interface which is along $y = 0$ initially. The left column of panels is for the case with an anticyclone; the right column of panels is for a cyclone. In both cases, $|\Gamma| = 1$, $\Delta q = 0.0$, $X_0 = 8\pi$, $Y_0 = 1$. The thick solid line denotes the southern boundary of the domain. The dash-dot line denotes the position of the escarpment. The dotted line denotes the PV front. The velocity vector of the vortex is illustrated by an arrow starting from a dot representing the location of the vortex. In panels of $t = 0.0$, velocity vectors within the bay are also plotted.
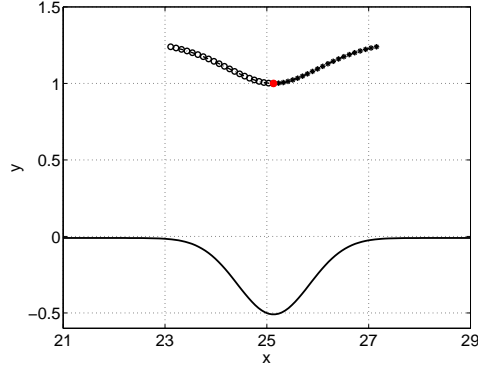
Figure 2.10: Limiting case 1: no topography $\Delta q = 0$. The thick solid line represents the southern boundary. The dash-dot-circle line denotes the trajectory of the anticyclonic vortex, the dash-dot-star line denotes the trajectory of the cyclonic vortex. The red dot indicates the initial position of the vortex.

as "+" and "-". These relative vorticities advect water particles near the escarpment meridionally to form new wave patterns following the initial one, and move the whole structure eastward as in the panel of $t = 4.0$. The the small distance between the southern boundary and the escarpment near the eastern edge of the bay prevents southward motions of water particles, so the trough is blocked by the boundary. The initial crest, however, can be advected over the eastern edge of the bay into the deep ocean as in the panel of $t = 16.0$. Wave patterns following the initial trough continue to propagate eastward squeezing the trough against the eastern side boundary of the bay. The length scale of waves are therefore shortened towards the eastern boundary as in the panel of $t = 26.0$, consistent with the results of the linear analysis. The effect of the nonlinear advection grows: the clockwise velocity field of the initial trough extends itself southward along the eastern boundary and the anti-clockwise velocity field of the crest following the trough amplifies its amplitude northward. The squeezing of the initial trough by the following crest continues till the crest is pushed over the bay's eastern edge as shown in the last panel of Fig.2.11. It is a persistent feature that as wave patterns are continuously generated and propagated eastward, the troughs are blocked by the eastern boundary of the bay and extend themselves along the boundary southward while crests are pushed over the eastern edge of the bay and then continue to move eastward along the zonal wall. Some of the bay water is transported by these crests into the deep ocean. This interesting phenomenon occurs only near one side of the bay's boundary since topographic waves propagate in only one direction. By blocking the eastward propagation of the waves, the eastern boundary
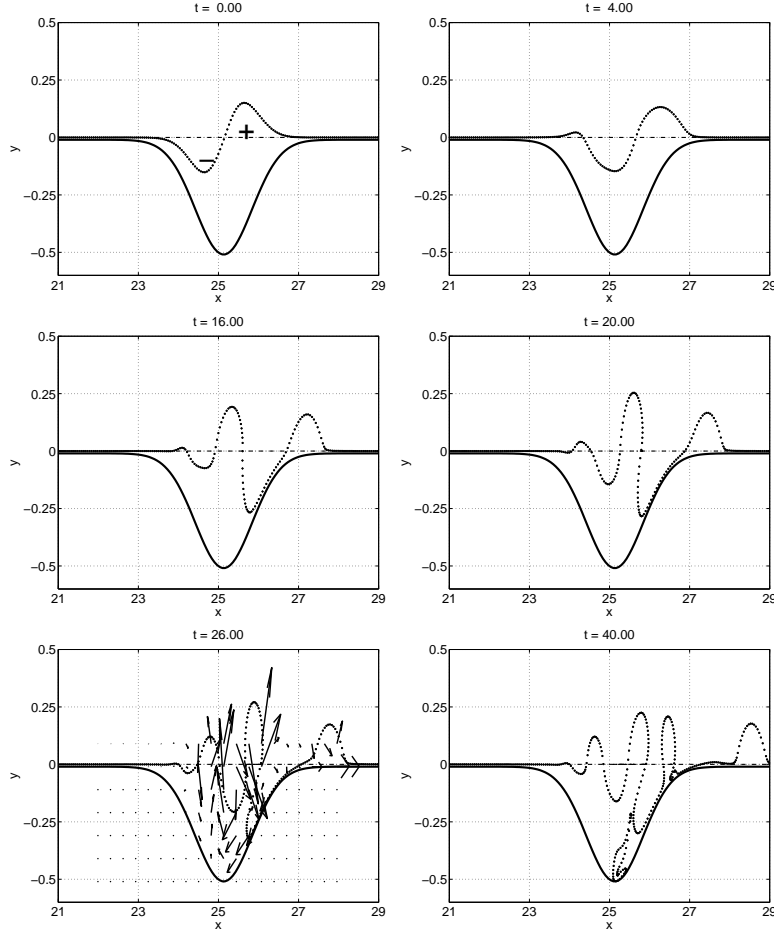
46

Figure 2.11: Limiting case 2: no vortex and $\Delta q = 1$. The time evolution of the PV front. The "-" in the panel of $t = 0.0$ denotes the negative relative vorticity of water columns contained within the trough and the "+" denotes the positive relative vorticity of water columns contained within the crest. The thick solid line denotes the southern boundary of the domain. The dash-dot line denotes the position of the escarpment. The dotted line denotes the PV front. The velocity field is also plotted in the panel of $t = 26.0$.
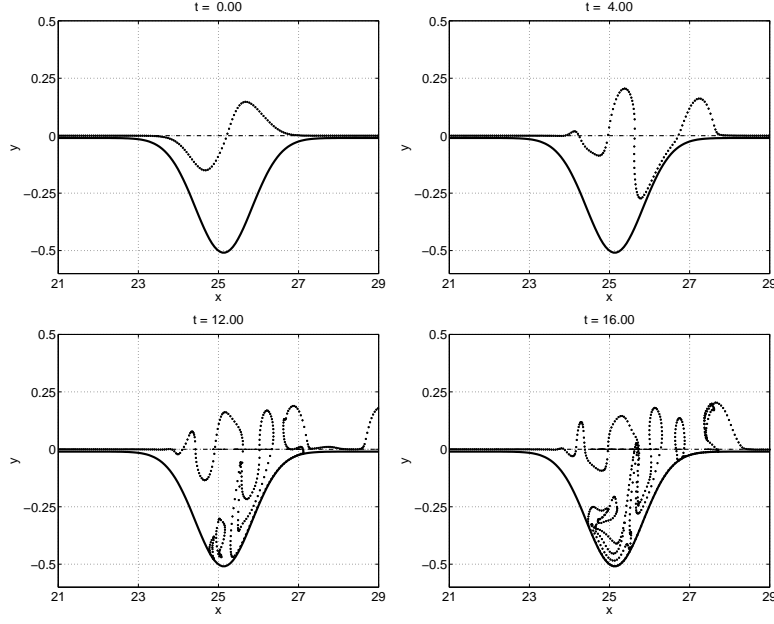
Figure 2.12: Limiting case 1: no vortex and $\Delta q = 4$. The time evolution of the PV front. The thick solid line denotes the southern boundary of the domain. The dash-dot line denotes the position of the escarpment. The dotted line denotes the PV front.

enhances the nonlinear effect which amplifies both the northward extension of crests into the deep ocean and the southward intrusion of troughs into the bay. Also due to the blocking of the eastern boundary, water is taken away from the eastern edge of the bay by crests. In contrast, the region near the western boundary is very quiet. The PV front is nearly aligned with the escarpment with only very small perturbations indicating that the cross-topography transport is weak. As shown in the panel of $t = 26.0$ in Fig.2.11, the flow velocity within the bay is much stronger near the eastern boundary and there is an eastward jet right along the coastline associated with the eastward-moving crest.

According to the linear analysis of the topography-trapped waves, the wave phase speed is linearly proportional to Δq; with the water depth difference 4 times bigger than the case displayed in Fig.2.11, the PV front evolves much faster. For example, by time $t = 12.0$, the second crest of the PV front is about to be pushed over the eastern edge of the bay as in the third panel of Fig.2.12 while in the case with $\Delta q = 1$ as in Fig2.11, the same situation occurs around $t = 40.0$.

If the coastline is further south of the escarpment, i.e., the parameter d_1 in the profile of B_s is set
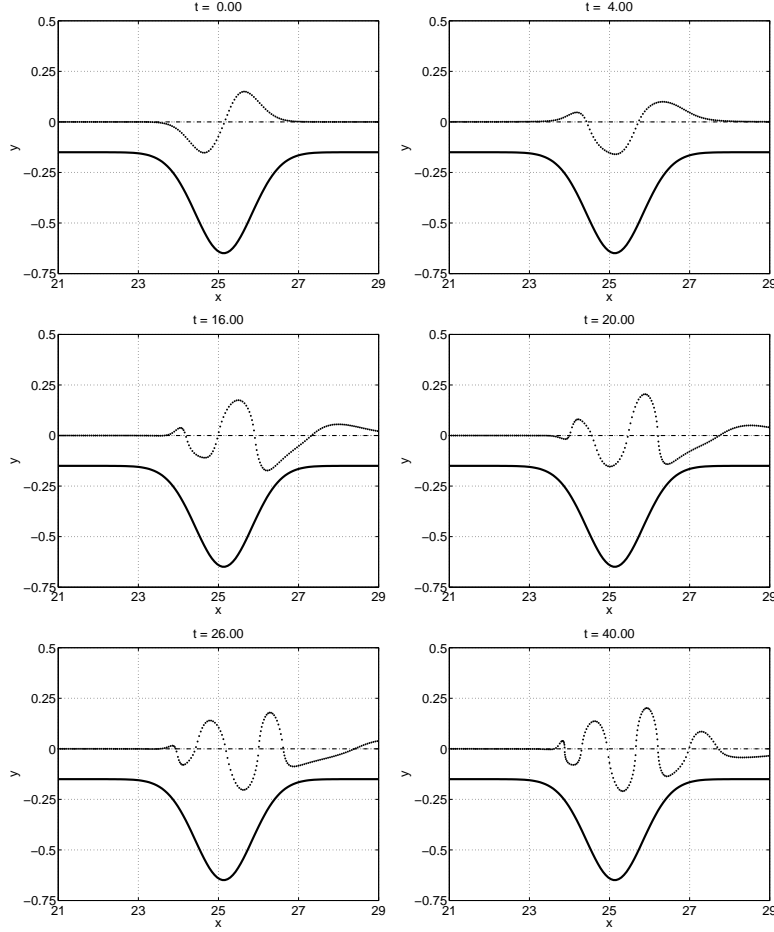
48

Figure 2.13: The case with $\Delta q = 1$ and $\Gamma = 0$ in which the distance between the northern edge of the bay and the escarpment is 0.15. The thick solid line denotes the southern boundary of the domain. The dash-dot line denotes the position of the escarpment. The dotted line denotes the PV front.

to 0.15 instead of 0.01, blocking of escarpment waves by the boundary will be weakened and so is the strengthening of the nonlinear advection towards the eastern boundary. The time evolution of the PV front with such a coastline is shown in Fig.2.13. Both the value of Δq and the initial perturbation of the front are the same as those in Fig.2.11. Clearly, waves can successfully propagate through the narrowest shelf region with no troughs trapped within the bay although there is still a trend of increase for wave amplitude in wide shelf region.

Through the two limiting cases, two basic mechanisms are found in the vortex-escarpment interactions. One is the vortex advection mechanism by which the PV front is merely advected by the vortex; the other is the propagation mechanism by which the frontal structure propagates only

49

towards the east (west if in Southern Hemisphere) as water particles move meridionally back and forth. Although the two mechanisms do not act independently, i.e., with relative vorticities due to the nonzero Δq, crests or troughs of the front can affect the motions of the vortex and hence influence the advection of the front, considering the effects of the two mechanisms separately is still very helpful to understanding the front evolution in cases including both the topography and the vortex.

Both mechanisms are influenced by the boundary. The image effect of the boundary makes the vortex translate along the coastline and indirectly influences the evolution of the front. The wave mechanism is strongly affected by the boundary especially when the boundary is not too far away from the escarpment. Troughs are blocked by the eastern boundary(western if in the Southern Hemisphere) while crests containing bay water move over the bay's eastern edge into the deep ocean. Corresponding to the squeezed troughs and amplified crests to the east, there is strong cross-escarpment transport near the eastern boundary. Near the western boundary however, the front deformation is much smaller. Differences of the PV front evolution near the western and the eastern boundary are due to the single propagation direction of topography-trapped waves. This difference is responsible for the inhomogeneous cross-shelf transport within the bay in the much more complicated model where the shelf/slope is continuously forced by an open ocean current.

The relation between the two mechanisms depends on the sign of the vortex. In cyclone-induced interactions, both the vortex advection and the wave propagation tend to move the frontal structure eastward; in anticyclone-induced interactions, the frontal structure tends to be advected in opposite directions by the two mechanisms. This asymmetry is also caused by the single propagation direction of the topographic waves, and is found to be the reason for the differences between anticyclone- and cyclone-induced front evolutions which will be demonstrated in the following cases.

The Standard Case

In the standard case, both the anticyclone and the cyclone are initially located at $X_0 = 8\pi$, $Y_0 = 1.0$ and the circulation strength of the vortex, $|\Gamma|$, is set to 1, equal to Δq. In nondimensionalizing the problem, we used the square root of the area of the bay, $\sqrt{S^*}$, to scale the length, $l = l^* \sqrt{S^*}$. If the nondimensional area S is equal to 1 and all the water within the bay is driven off the topography

as a big cyclone, the strength of this cyclone would be the same as that of the vortex and the total relative vorticity of the deep-ocean water within the bay.

Initially after the vortex is switched on, the front deforms as in the first limiting case. In the experiment with an anticyclone, a crest appears in the west of the bay and a trough appears in the east as shown in the panel of $t = 2.0$ in Fig.2.14. Both the crest and the trough amplify in time as forced continuously by the anticyclone. There is a tendency for the front that is between the crest and the trough to extend northward reflecting the effect of the wave mechanism which advects the frontal structure eastward. This is quite different from the limiting case of no topography where the crest is advected by the anticyclone westward out of the bay. The crest in Fig.2.14 is limited to the western edge of the bay. The trough is blocked by the eastern boundary and extends southwestward along the boundary. This is due to velocity fields generated by its own field of negative relative vorticity and the anticyclonic vortex. Near the western edge of the bay, the flow is eastward as forced by the positive relative vorticity field of the crest, so the western foot of the crest approaches the eastern foot or the tip of the trough. The crest thus turns into a big head with an narrowing opening on the bay's boundary. At time $t = 14.0$, almost all the bay water has been squeezed into the big head. Meanwhile, the big head is advected northward by the anticyclone, so its connection to the boundary is elongated into a narrow neck. When the neck becomes narrower than some prescribed threshold, one procedure of the contour surgery cuts the big head off and turns it into an isolated cyclone as in the panel of $t = 20.0$ in Fig.2.15. This cyclone forms a dipole with the vortex moving northward in the deep ocean. The flow field around the bay is now entirely induced by the negative relative vorticity field of the deep-ocean water and so is clockwise. At time $t = 30.0$, the dipole has been very far north and its distance to the escarpment is more than 7 times greater than the meridional depth of the bay. This northward motion of the dipole is expected to continue for some time before turning back towards the bay.

For the cyclone-induced interaction, the initial deformation of the front is nearly symmetric to its anticyclonic counterpart as shown by panels of $t = 2.0$ in Fig.2.14. As deformation's amplitude becomes finite, the cyclone- and anticyclone-induced interactions start to show differences. Since both the propagation mechanism and the advection mechanism act to move the frontal structure in the same direction, the front deformation is moving faster eastward in the cyclone-induced
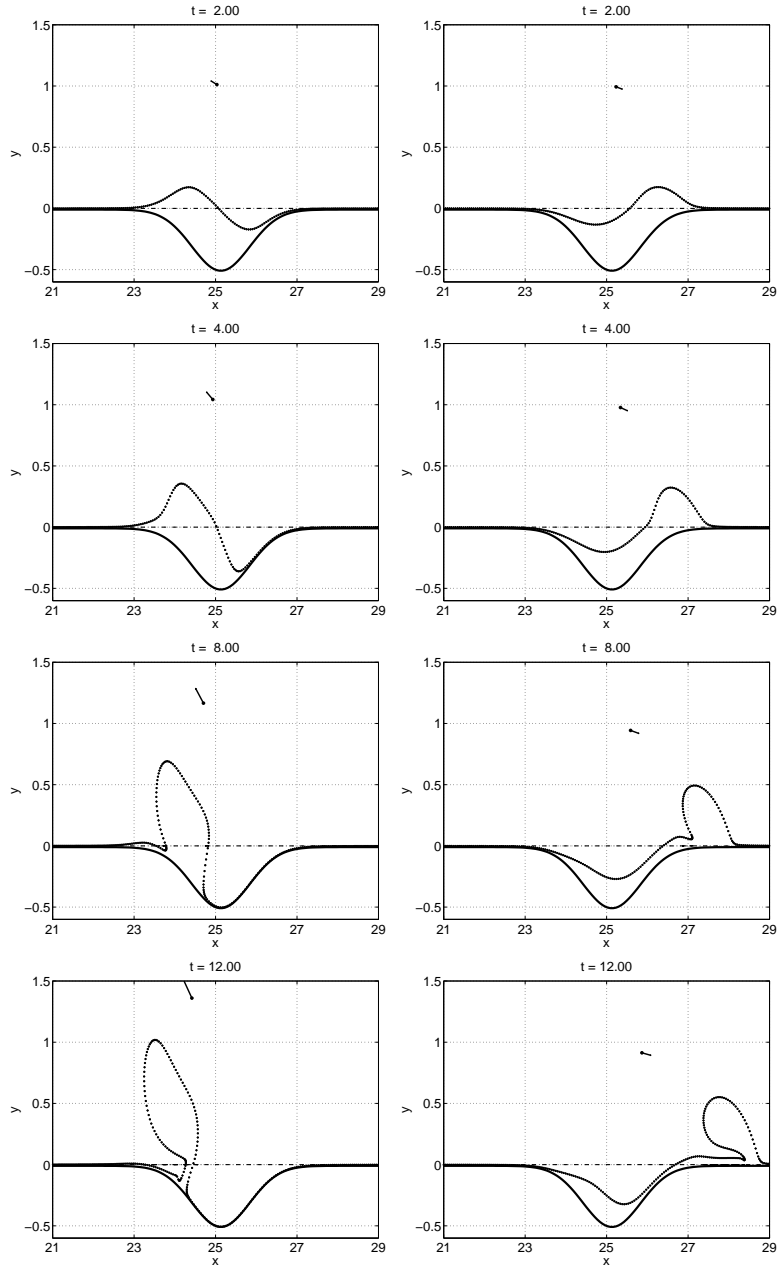
51

Figure 2.14: The standard case. The time evolution of the PV front for the anticyclone-induced (left column) and the cyclone-induced (right column) interactions. In both interactions, $|\Gamma| = 1$, $\Delta q = 1$, $X_0 = 8\pi$, $Y_0 = 1$. The thick solid line denotes the southern boundary of the domain. The dash-dot line denotes the position of the escarpment. The dotted line denotes the PV front. The velocity vector of the vortex is illustrated by an arrow starting from a dot representing the location of the vortex.
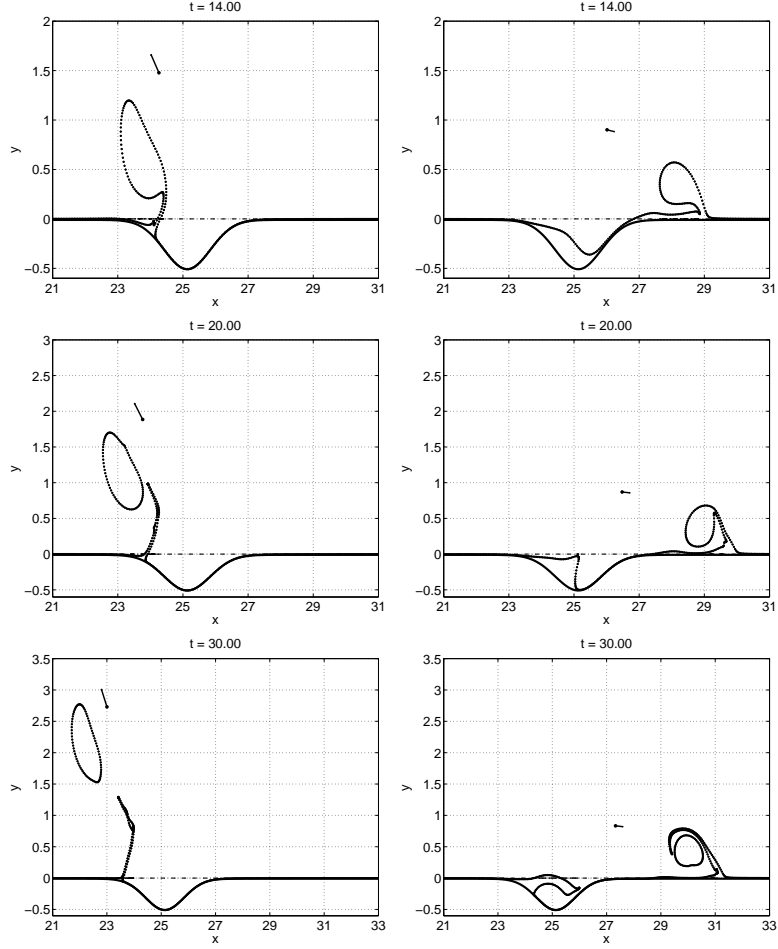
Figure 2.15: The standard case. The time evolution of the PV front for the anticyclone-induced (left column) and the cyclone-induced (right column) interactions. In both interactions, $|\Gamma| = 1$, $\Delta q = 1$, $X_0 = 8\pi$, $Y_0 = 1$. The thick solid line denotes the southern boundary of the domain. The dash-dot line denotes the position of the escarpment. The dotted line denotes the PV front. The velocity vector of the vortex is illustrated by an arrow starting from a dot representing the location of the vortex.
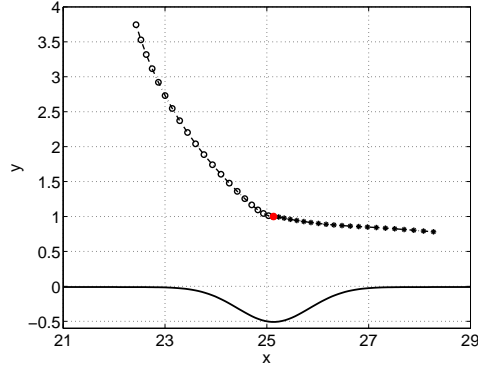
Figure 2.16: The standard case. The thick solid line represents the southern boundary. The dash-dot-circle line indicates the trajectory of the anticyclonic vortex, the dash-dot-star line denotes the trajectory of the cyclonic vortex. The red dot indicates the initial position of the vortex.

interaction. At $t = 4.0$, the trough in the cyclone-induced interaction is flatter than that in the anticyclone-induced interaction. The crest has been advected partially over the eastern edge of the bay while in the anticyclone-induced interaction, it is limited to the region of the bay opening. In spite of advecting the frontal structure eastward, the cyclonic vortex also generates southward flow within the bay, but the southward deepening of the trough is overwhelmed by its eastward motion. Consequently, before the trough reaches to the southernmost point of the bay, its eastern side has attached to the bay's eastern boundary as in the panel of $t = 14.0$ in Fig.2.15. Therefore, part of the bay water is isolated between the bay's boundary and the trough. By $t = 14.0$, the crest has been entirely advected out of the bay into the deep ocean and continues to move eastward along the zonal coast. Forced by the cyclonic vortex to its northwest and the positive relative vorticity inside itself, the southern portion of the crest moves eastward faster than its northern portion. As time goes on, it turns into a head with a narrowing part connected to the boundary and finally detaches from the coast as an isolated cyclone as shown in the panel of $t = 30.0$ in Fig.2.15. The bay water that remains within the bay is advected by the clockwise velocity field of the negative relative vorticity contained in the trough. By time $t = 30.0$, it has deformed into a streamer extending clockwise.

The asymmetry between the two experiments are also clearly demonstrated by the trajectories of the two vortices in Fig.2.16. In the anticyclone-induced interaction, both relative vorticities contained in the crest and the trough tend to advect the vortex northward initially after the vortex is switched on. As the crest quickly grows northward approaching the vortex, the vortex is more af-

54

fected by the crest and moves quickly northwestward. After all the bay water leaves the escarpment as a cyclonic eddy, the vortex and the eddy form a dipole moving along an arc path extending northward. In the cyclone-induced interaction, during initial period, both the crest and the trough pulls the vortex towards the escarpment. As the vortex gets closer to the bay, it is more affected by the trough as well as the boundary and moves eastward towards the crest. Meanwhile, it continues to move towards the coast as forced by the crest to its east.

In order to have a better understanding of the boundary's role in the above process, we carry out two more experiments in which the boundary's effect is negligible. For this purpose, the two boundaries B_n and B_s are aligned with x-axis and located very far away from the escarpment, so the evolution of the PV front in such configuration is close to that in an unbounded domain. In the two experiments, the vortex has the same but opposite circulation $|\Gamma| = 1$and is located at $(X_0 = 8\pi, Y_0 = 1.0)$; the depth difference is the same as that in the standard case $\Delta q = 1$. The time evolutions of the PV front for both cases as displayed in Fig.2.17 are found very similar to those in Wang (1992). The effect of the boundary is found through comparison of Figs.2.14, 2.15 and 2.17.

Removing the boundary's effect doesn't change the fact that a cyclonic eddy forms in the anticyclone-induced interactions but not in the cyclone-induced interactions. Therefore, it is the relative relation between the two control mechanisms that determines the differences between the two kinds of interactions. The balance between the two mechanisms can only be achieved in anticyclone-induced interactions as they advect the frontal structure in opposite directions.

Although the boundary is not the reason for the qualitative differences between the anticyclone- and the cyclone-induced interactions, its effect on the PV front is obvious by comparing the bounded and the unbounded case. Initially after the anticyclonic vortex is switched on, a crest and a trough with similar amplitudes appear in the case with the boundary as shown in the panel of $t = 2.0$ in Fig.2.14. Water columns between the trough and the escarpment have negative relative vorticity generating clockwise velocity field in the east of the bay. Due to the image theory, the boundary works to amplify the trough shoreward till the front attaches to the wall. Meanwhile, the crest grows seaward till a cyclonic eddy forms and detaches from the front. In Fig.2.17 however, the amplitude
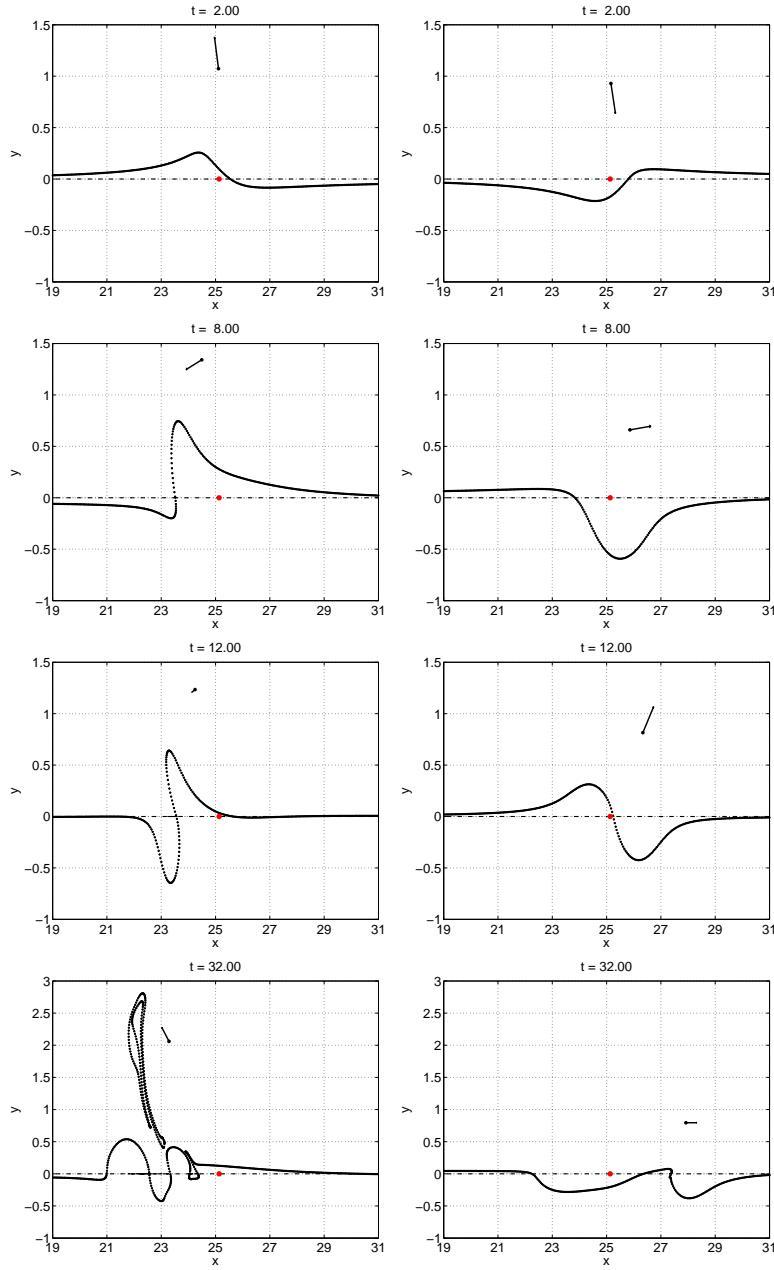
55

Figure 2.17: The case in which the boundary's effect is negligible. The time evolution of the PV front for the anticyclone-induced (left column) and the cyclone-induced (right column) interactions. In both interactions, $|\Gamma| = 1$, $\Delta q = 1$, $X_0 = 8\pi$, $Y_0 = 1.0$. The dash-dot line denotes the position of the escarpment. The dotted line denotes the PV front. The velocity vector of the vortex is illustrated by an arrow starting from a dot representing the location of the vortex. The red dot denotes the position of $(x = 8\pi, y = 0)$

of the initial trough at $t = 2.0$ is much smaller than that of the crest and is also smaller than that of the trough in the bounded case. Furthermore, the intersection point between the front and the line of $y = 0$ at $t = 2.0$ is at the center of the bay opening in Fig.2.14 but is more to the east in Fig.2.17. These two differences indicate that the bay's boundary tends to slow down the propagation of topography-trapped waves. The southward extension of the trough due to the vortex advection in the unbounded case is quickly reversed by the wave propagation, so the trough's amplitude is small. According to our results of the linear analysis of topography-trapped waves, in the unbounded case, all escarpment waves propagate at the same frequency $\dfrac{\Delta}{2}$. When the shallow region is bounded by a shoreward indented coastline, the wave frequency which is also a function of wave length is smaller than $\dfrac{\Delta}{2}$. Therefore, waves that have the same wave length propagate faster in the unbounded domain. Another difference is that in the case without the boundary, wave patterns are successively generated to the west of the initial crest while in the bounded domain, deformations other than the initial crest and the trough are blocked by the wall.

Moreover, the volume of the cyclonic eddy formed in the bounded domain is much greater than that in the infinite domain suggesting that the strengthening of the wave mechanism(increase of the wave frequency) may act to prevent the cross-escarpment exchange. This is consistent with results of experiments that have variable values of Δq.

As displayed by the right column of panels in Fig.2.17, the eastward propagation tendency of the frontal structure is obvious in the cyclone-induced interaction as the vortex advects the front eastward. The initial trough is quickly amplified shoreward and advected eastward, so the amplitude of the initial crest is very small as that of the initial trough in the anticyclone-induced interaction.

The balance of the two control mechanisms is found obtainable only in anticyclone-induced interactions, so the formation of a cyclonic eddy occurs only when the forcing vortex is anticyclonic. This result is independent of the boundary in the shallow region.

Generally speaking, the boundary's effect on the PV front evolution is to weaken the wave mechanism by slowing down the propagation of topography-trapped waves. For anticyclone-induced interaction in an unbounded domain, the PV front deformations are small to the east of the anticyclonic vortex (west if the topography-trapped waves propagate westward) but large to the west.

57

It is quite remarkable that in the bounded case, all the bay water is transported off the topography in form of a cyclonic eddy, so it is interesting to know what will happen if the strengths of the two mechanisms are variable. The question can be answered by more parameter studies. As mentioned above, two parameters can be changed independently in the nondimensional problem: one is Δq, the PV difference across the topography, the other one is (X_0, Y_0), the initial location of the vortex. The phase speed of escarpment waves is proportional to the depth difference, so with varying Δq the frontal structure tends to be advected eastward at variable speeds. In addition, water columns that have crossed the escarpment have variable relative vorticity strengths. With varying initial positions of the vortex, the vortex advection is different.

Effects of the Wave Mechanism

While studying the parameter Δq, we fix the vortex initial location and strength as $(X_0 = 8/pi, Y_0 = 1.0)$ and $|\Gamma| = 1$. We first set Δq to be 2, twice of that in the standard case. In the anticyclone-induced interaction, differences of the time evolution of the PV front in the case with $\Delta q = 2$ (Fig.2.18) and in the standard case (Fig.2.15) exist in two aspects. First, the topography-trapped waves propagate faster with larger Δq. By time $t = 4.0$, the crest of the front in Fig.2.18 is more to the east compared with that in Fig.2.15. Second, the velocity fields generated by the relative vorticity contained within the front deformations become stronger as the water depth difference is doubled. The interactions among the point vortex, the cyclonic eddy consisting of the bay water, and the anticyclonic eddy consisting of the deep-ocean water are changed. As more and more bay water is replaced by the deep-ocean water, the strengths of the cyclonic and anticyclonic eddies become greater than that of the point vortex. Forced by both the point vortex and the anticyclonic eddy, the cyclonic eddy is stretched in the middle as in the panel of $t = 14.0$ in Fig.2.18. The western portion is more influenced by the vortex so extends northwestward, while the eastern portion is more affected by the anticyclone within the bay and moves clockwise. Finally, the cyclonic eddy splits into two smaller eddies: one pairs away with the vortex and the other moves around the bay.

For the cyclone-induced interaction, the time evolution of the PV front in the case with $\Delta q = 2$ (Fig.2.19) and the case with $\Delta q = 1$ look similar to each other. As in the anticyclone-induced
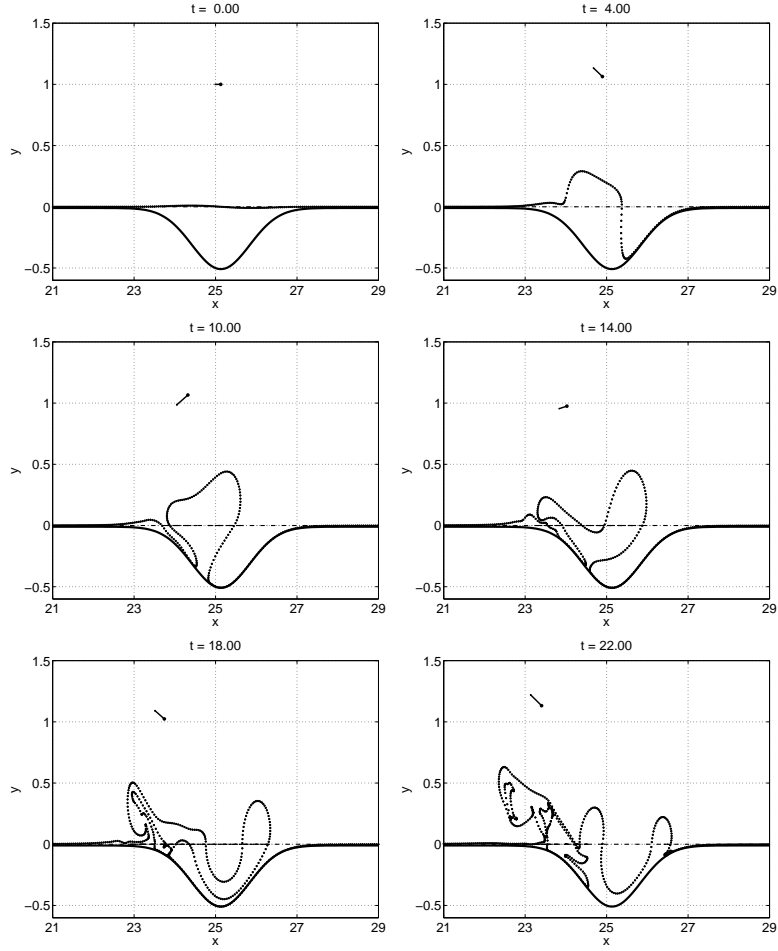
Figure 2.18: The case with $\Delta q = 2$ and $\Gamma = -1$. The time evolution of the PV front for the anticyclone-induced interaction. The initial location of the vortex is $(X_0 = 8\pi, Y_0 = 1)$. The thick solid line denotes the southern boundary of the domain. The dash-dot line denotes the position of the escarpment. The dotted line denotes the PV front. The velocity vector of the vortex is illustrated by an arrow starting from a dot representing the location of the vortex.
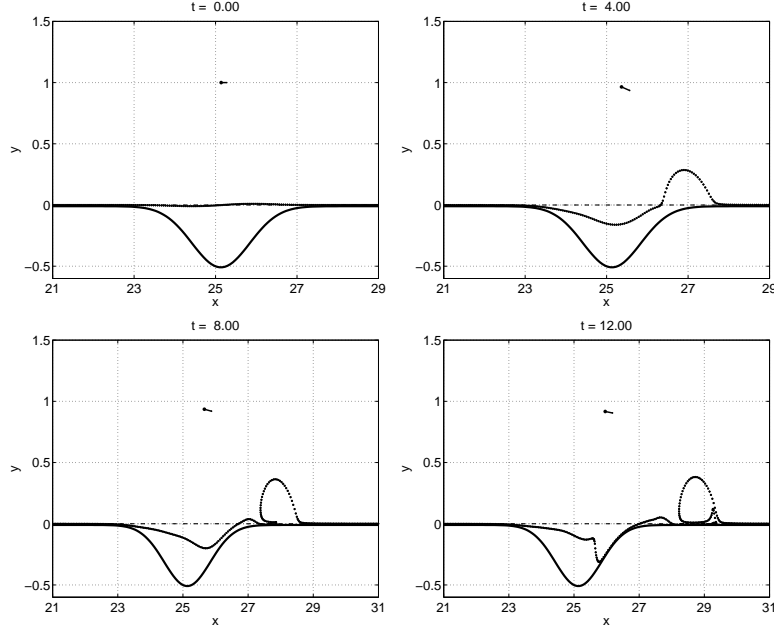
Figure 2.19: The case with $\Delta q = 2$ and $\Gamma = 1$. The time evolution of the PV front for the cyclone-induced interaction. The initial location of the vortex is $X_0 = 8\pi$, $Y_0 = 1$. The thick solid line denotes the southern boundary of the domain. The dash-dot line denotes the position of the escarpment. The dotted line denotes the PV front. The velocity vector of the vortex is illustrated by an arrow starting from a dot representing the location of the vortex.

interaction, there are two main differences. The frontal structure moves much faster eastward, so by time $t = 8.0$, the eastern part of the trough in Fig.2.19 has almost attached to the eastern boundary of the bay, while in the standard case, the same situation won't happen until $t = 12.0$. With less time to grow, amplitudes of both the trough and the crest are smaller in the case with $\Delta q = 2$. Compared with the standard case, less bay water is taken away from the eastern edge of the bay by the crest.

When the value of Δq is decreased, i.e., $\Delta q = 0.5$, both the time evolution of the PV front in the anticyclone- and cyclone-induced interactions are similar to those in standard cases as shown in Figs.2.20 and 2.21. Since the strength of the point vortex is greater than the strength of the topography, the advection mechanism becomes more important than the wave mechanism. Judged by the meridional scale, the crests are more stretched meridionally by the vortices than those in the standard cases. In the anticyclone-induced interaction, before the crest separates from the coast as an cyclonic eddy, its meridional axis is much longer than its zonal axis. In the cyclone-induced
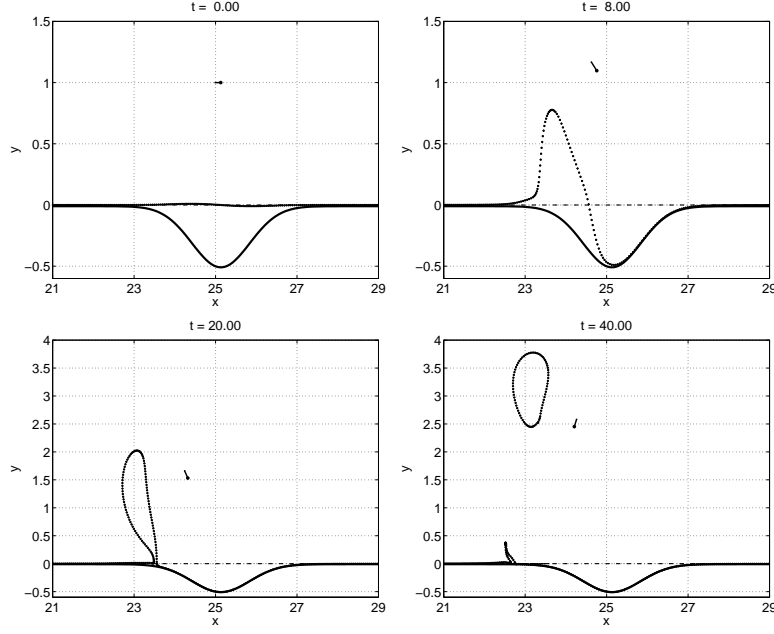
60

Figure 2.20: The case with $\Delta q = 0.5$ and $\Gamma = -1$. The time evolution of the PV front for the cyclone-induced interaction. The initial location of the vortex is $X_0 = 8\pi$, $Y_0 = 1$. The thick solid line denotes the southern boundary of the domain. The dash-dot line denotes the position of the escarpment. The dotted line denotes the PV front. The velocity vector of the vortex is illustrated by an arrow starting from a dot representing the location of the vortex.

interaction, the crest moving eastward along the coast extends very far northward into a long, thin streamer. In addition, more water is wrapped into the crest and moved out of the bay.

The anticyclone-induced interactions show a strong dependence on Δq, the parameter determining the strength of the propagation mechanism. With small Δq, the vortex advection wins against the propagation mechanism, so the front tends to be elongated and moved westward along the coast. When the value of Δq is roughly the same as that of the vortex strength, a topographic eddy containing all the bay water forms from the bay. When Δq is greater, the evolution of the front becomes complicated as interactions between the cyclonic eddy consisting of the bay water and the anticyclonic eddy consisting of the deep-ocean water gets stronger. Furthermore, only part of the bay water can be finally taken away by the vortex into the open ocean, so the big depth difference across the escarpment acts as a barrier blocking the volume transport. The total volume taken away by the vortex decreases with Δq and increases with the strength of the vortex.

The cyclone-induced interactions are not very sensitive to Δq, at least within the parameter
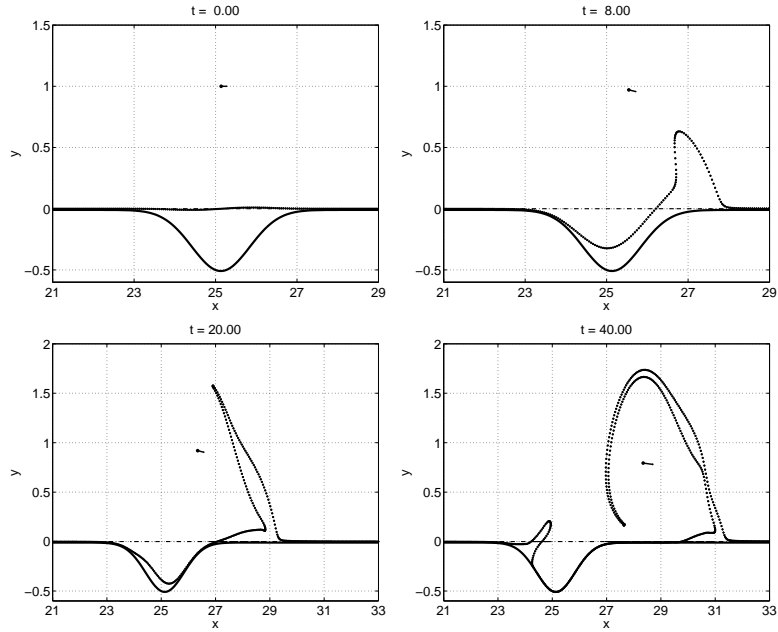
Figure 2.21: The case with $\Delta q = 0.5$ and $\Gamma = 1$. The time evolution of the PV front for the cyclone-induced interaction. The initial location of the vortex is $X_0 = 8\pi$, $Y_0 = 1$. The thick solid line denotes the southern boundary of the domain. The dash-dot line denotes the position of the escarpment. The dotted line denotes the PV front. The velocity vector of the vortex is illustrated by an arrow starting from a dot representing the location of the vortex.

range that is explored. In all cases, the initial crest is moved eastward out of the bay from the bay's eastern edge and then continuously advected eastward along the zonal coast. The bay water that is originally in the southernmost area of the bay tends to be trapped there. One similarity found between the anticyclone- and cyclone-induced interactions is that the cross-escarpment volume decreases as Δq is increased.

Effects of the Vortex Advection Mechanism

With the vortex strength fixed, we study the effects of the advection mechanism by changing the initial location of the vortex. We first look at experiments in which the meridional location of the vortex is $Y_0 = 0.5$. Due to the short distance between the vortex and the escarpment, the crest of the front first extends northward and then is stretched clockwise around the vortex after its northern end is beyond the meridional location of the vortex as shown in Fig.2.22. Around $t = 12.0$, almost all the bay water has been squeezed into the crest, which is about to separate from the coast as an independent cyclonic eddy. Compared with the panel of $t = 8.0$ in Fig.2.14 for the standard case, more bay water has been driven off the topography in the panel of $t = 8.0$ in Fig.2.22, therefore, the cross-escarpment transport is enhanced when the vortex is closer to the escarpment. After separation, motions of the isolated cyclonic eddy are mostly determined by the vortex as in the standard case. Splitting into two or more smaller eddies is possible as the northern part of the eddy is continuously stretched into a long and thin streamer by the vortex as shown by the panel of $t = 20.0$ in Fig.2.22. In the cyclone-induced interaction (Fig.2.23), the crest extends counterclockwise around the vortex as it is advected eastward along the coast. By time $t = 12.0$, its northern part has arrived at the escarpment after finishing one rotation around the point vortex.

When the distance between the vortex and the escarpment is doubled from that in the standard case as shown in Fig.2.24 and Fig.2.25. The cross-escarpment transport is greatly slowed down in the anticyclone-induced interaction: around $t = 20.0$, a big cyclonic eddy containing almost all shelf water forms on the coast while in the standard case, that happens around $t = 12.0$. The vortex advection is westward and weak around the topography, opposite to the velocity field of the anticyclonic eddy consisting of water from the deep ocean. Therefore, the cyclonic eddy doesn't
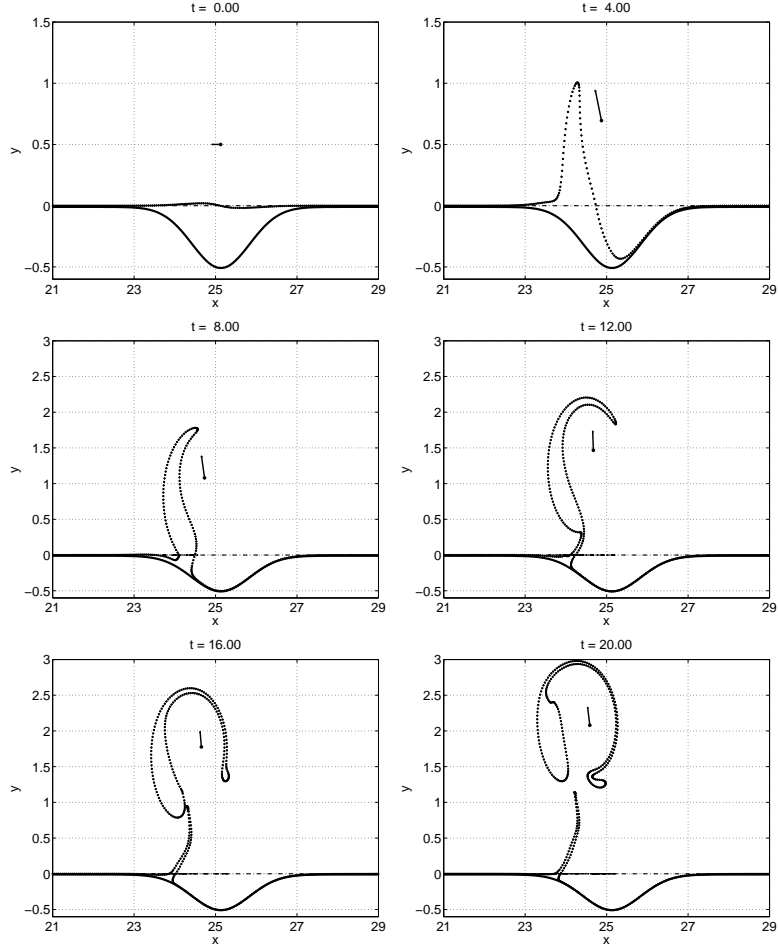
Figure 2.22: The case with $X_0 = 8\pi$, $Y_0 = 0.5$, $\Delta q = 1$ and $\Gamma = -1$. The time evolution of the PV front for the anticyclone-induced interaction. The thick solid line denotes the southern boundary of the domain. The dash-dot line denotes the position of the escarpment. The dotted line denotes the PV front. The velocity vector of the vortex is illustrated by an arrow starting from a dot representing the location of the vortex.

Figure 2.23: The case with $X_0 = 8\pi$, $Y_0 = 0.5$, $\Delta q = 1$ and $\Gamma = 1$. The time evolution of the PV front for the cyclone-induced interaction. The thick solid line denotes the southern boundary of the domain. The dash-dot line denotes the position of the escarpment. The dotted line denotes the PV front. The velocity vector of the vortex is illustrated by an arrow starting from a dot representing the location of the vortex.
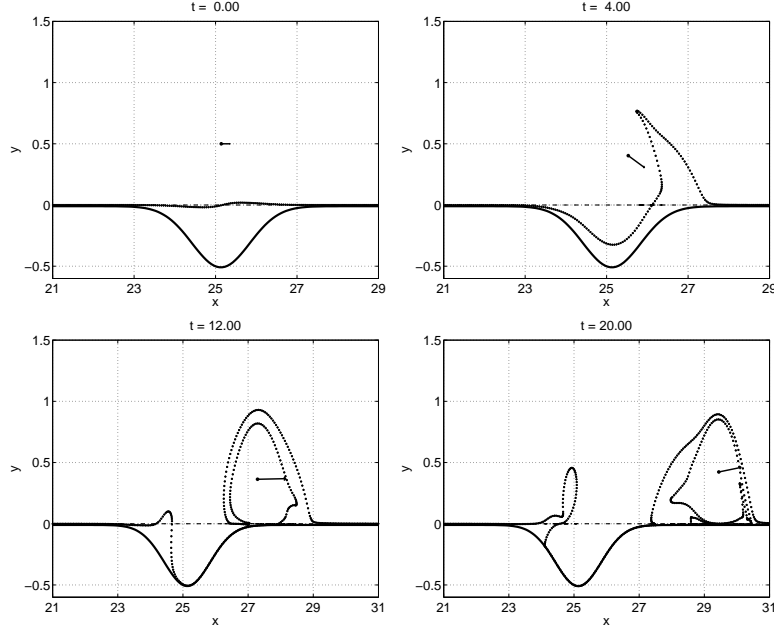
move away from the coast as it does in the standard case as well as the case with $Y_0 = 0.5$. Instead, it stays near the western edge of the bay after formation for quite a long time. It is expected that some of the water within the cyclonic eddy will finally go back to the bay as the two eddies interact with each other.

In the cyclone-induced interaction, the cross-escarpment exchange is apparently weaker as the vortex is further away from the coast (Fig.2.24. The southward growth of the trough by the vortex is slow compared with the eastward propagation of the frontal structure, so when the eastern side of the trough touches the eastern boundary of the bay, the amplitude of the trough is still small and a large amount of bay water is trapped southward of the trough. Other than that, the evolution of the front is very similar to all cyclone-induced cases that have been studied up to now.

Similar to changing the parameter Δq, changing the meridional distance between the vortex and the escarpment also has a strong effect on the time evolution of anticyclone-induced interactions. All shelf water tends to be taken out of the bay as an isolated eddy when the vortex is initially
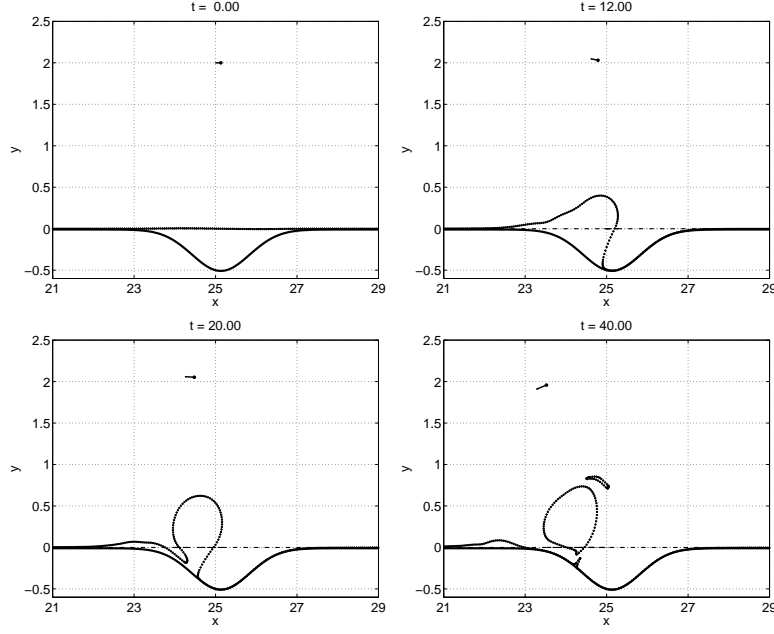
Figure 2.24: The case with $X_0 = 8\pi$, $Y_0 = 2.0$, $\Delta q = 1$ and $\Gamma = -1$. The time evolution of the PV front for the anticyclone-induced interaction. The thick solid line denotes the southern boundary of the domain. The dash-dot line denotes the position of the escarpment. The dotted line denotes the PV front. The velocity vector of the vortex is illustrated by an arrow starting from a dot representing the location of the vortex.

close enough to the shelf. As the vortex is located further away from the shelf, even though a big topographic eddy still forms from the coast during the process, its interaction between the anticyclonic eddy within the bay may dominate the subsequent motions of the cyclonic eddy and some of the bay water may return to the shelf. For the cyclone-induced interactions, the time evolution of the PV front doesn't vary a lot as we change the meridional location of the vortex. For both anticyclone- and cyclone-induced interactions, the cross-escarpment transport is slower when the vortex is further away from the bay.

2.7 Conclusions

Using a contour dynamics model, we have examined barotropic interactions between a point vortex and a small escarpment with the presence of a bay in the shallow area. Two control mechanisms are found important for the time evolution of the PV front generated by the step-like topography.
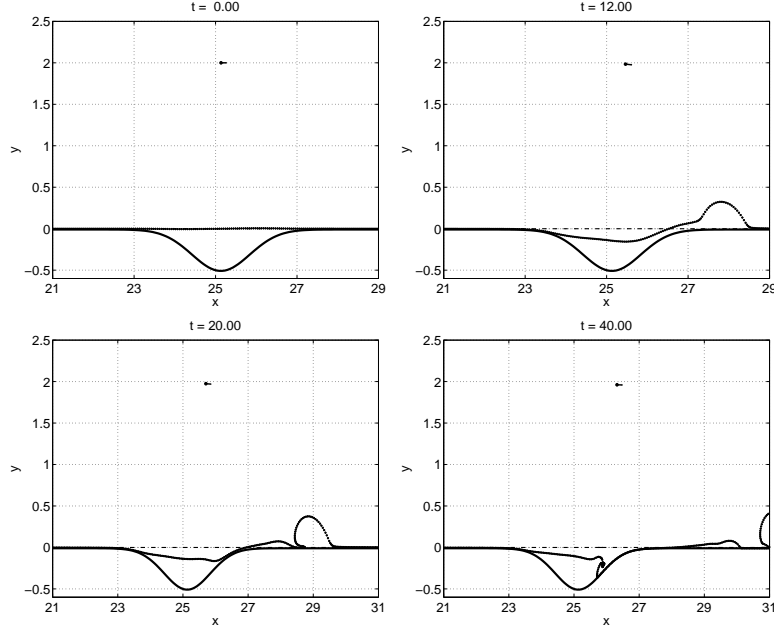
Figure 2.25: The case with $X_0 = 8\pi$, $Y_0 = 2.0$, $\Delta q = 1$ and $\Gamma = 1$. The time evolution of the PV front for the cyclone-induced interaction. The thick solid line denotes the southern boundary of the domain. The dash-dot line denotes the position of the escarpment. The dotted line denotes the PV front. The velocity vector of the vortex is illustrated by an arrow starting from a dot representing the location of the vortex.

In the limit of zero depth difference across the escarpment, the interface is advected by the vortex which at the same time translates along the boundary due to the image effects. Evolutions of the front are anti-symmetric for anticyclone- and cyclone-induced interactions. On the other hand, when the vortex is too far away to have influence on the motions near the shelf, the evolution of the PV front is mostly due to the topography-trapped waves, which as Rossby waves, propagate in a single direction along the escarpment. The variation of the shelf width induces changes of wave properties. As long as the shelf width is not too large compared with the wave length, linear analysis shows that waves become steeper as they approach the eastern boundary of the bay. In the full, nonlinear problem, wave troughs are squeezed against the eastern boundary extending themselves southwestward into the bay while crests move eastward over the eastern edge of the bay and turn into cyclonic eddies. Strong cross-escarpment motions occur near the eastern edge of the bay due to the interaction between the topographic waves and the boundary.

When both the depth difference and the vortex are present, the evolution of the PV front is determined by the relative strengths of the two mechanisms. In anticyclone-induced interactions, the

two mechanisms advect the frontal structure in opposite directions. Therefore, the balance between the two mechanisms can lead to a large amount of bay water being taken off the topography as an isolated cyclonic eddy which moves away with the vortex into the open ocean. In cyclone-induced interactions, the two mechanisms work together to move the frontal structure eastward. The shelf water can only be taken out of the bay through its eastern edge by crests which continue their eastward motion along the coast. Usually, the cross-shelf transport in cyclone-induced interactions is weaker than that in anticyclone-induced interactions.

By changing the depth difference across the topography or the meridional distance between the vortex and the escarpment, we examined different cases which have variable strengths of the two mechanisms. Pulling the vortex away from the topography has similar effects to increasing the parameter Δq in that both of them make the wave advection mechanism stronger. Compared with the cyclone-induced interactions, the anticyclone-induced interactions are more sensitive to parameter changes. One similarity between the anticyclone- and cyclone-induced interactions is that large topography works to prevent cross-escarpment transport.

Vortex-escarpment interactions are very different in cases with and without the curved coastline although the formation of a cyclonic eddy in anticyclone-induced interactions is not affected by the existence of the boundary. When the shallow region is bounded by a curved coastline, topographic waves interact with the boundary resulting in shorter wave lengths, stronger nonlinearity, and more importantly, transport of bay water into the deep ocean by wave crests. Because of the single propagation direction of the topographic waves, the strong wave-boundary interaction happens only near one side of the boundary so is the resultant strong cross-escarpment transport. This mechanism and associated asymmetry between the western and the eastern side of the bay's boundary are crucial for the transport out of a bay that is under the persistent yet episodic forcing of a strong open ocean current in Chapter 4.

For the vortex-escarpment interactions occurring in the Southern Hemisphere, the PV front evolution and the motion of the vortex are the same as those obtained in this chapter except that all results are flipped around about the central longitude of the channel, which means the "west" in the northern hemisphere becomes the "east" in the southern hemisphere.

68

Chapter 3

Baroclinic Interaction between a Surface Anticyclone and a Continental Slope with a Bay-shaped Shelf

3.1 Introduction

Two physical mechanisms important for eddy-topography interactions in the presence of a curved coastline were found through the study of vortex-escarpment interaction in Chapter 2: the vortex advection and propagation of topography-trapped waves. Their relative relation causes fundamental differences in anticyclone- and cyclone-induced interactions. The wave mechanism is found strongly dependent on the shelf width and wave motions become more nonlinear in narrow shelf regions. These results are enlightening, and they deserve further investigation. It is so not only because of their significance but also because the restrictions imposed by the contour dynamics model, such as the constant density and the small step-like topography, are very different from situations in the real ocean. Mechanisms disclosed by the simple model may be strongly affected by these restrictions. For example, in the one-layer model, the velocity field of the point vortex has a large length scale of decay that is on the order of the external deformation radius. In the real ocean the advection by mesoscale eddies declines within a length scale on the order of the first deformation

radius, much smaller than the external one. The boundary's effect is amplified in the barotropic vortex-escarpment interactions. The striking phenomenon that all the bay water can be driven off the escarpment by a single anticyclonic point vortex is therefore questionable.

In this chapter, a primitive equation model will be used to investigate the problem of interactions between a single baroclinic eddy and a continental slope with a bay. Both the restrictions on the stratification and the topography are relaxed. Interactions are examined within a two-layer model and the continental slope is allowed to be high enough to enter the upper layer. The incorporations of the stratification and the smooth topography will certainly increase the model complexity, but they will also reveal new dynamical features that are qualitatively different from those demonstrated in the previous chapter.

In Chapter 2, multiple processes associated with the vortex-escarpment interaction were examined such as the formation of a topographic cyclone, generation of topographic waves and their interaction with the curved coastline, motion of the forcing vortex, and cross-escarpment transport. Most previous theoretical studies concerned only some not all of them.

The problem of eddy motion and evolution over topography has been addressed in many numerical investigations. Smith and O'Brien (1983) examined the propagation of an isolated eddy onto a topographic slope. They used a two-layer primitive equation model and the topographic slope is entirely in the lower layer. With the water depth increasing eastward from a western boundary on β-plane, they found the dispersion induced by both the planetary and the topographic β-effect give the eddy an asymmetric spatial structure. Nonlinear self-advective propagation tendencies are induced by this asymmetry and play an important role in the direction of propagation of the eddy. Using the same model, Smith (1986) studied the motions of Loop Current eddy when it interacts with topography in the western Gulf of Mexico. Depending on the eddy's lower layer rotational strength, the eddy motion is governed by two dynamical regimes. Anticyclones with significant lower layer anticyclonic structure develop offshore directed self-advective tendencies; eddies with weak lower layer flow rapidly evolve to upper layer features through topographic dispersion.

LaCasce (1997) examined the evolution of a geostrophic vortex over a slope on f-plane. The model employed two layers, quasi-geostrophic dynamics, and a linear slope, so the topographic

slopes were weak and contained in the lower layer. He found that topography favors dispersal of deep flows, and surface-trapped vortices over barotropic ones. In addition, topography can stabilize a surface vortex, permitting the existence of baroclinic vortices larger than the deformation radius. The two effects are gauged by two parameters, each obtained by scaling. Given published dimensions for oceanic rings and the principal topographic features they interact with, he made estimates about the two parameters which suggest that those vortices all fall into the category of rapid dispersal of deep flow and baroclinic stability over the slope.

White and McDonald (2004) considered the motions of point vortices in a two-layer fluid near large-amplitude step-like topography. The topography separated regions composed of two layers and one layer. The depth variation over the topography in the upper layer is small compared with the total layer thickness, so quasi-geostrophy applied everywhere. According to their results, vortices in the upper layer readily exhibit nonlinear behavior, and contour dynamics predict that cyclones propagate toward and may cross the step, whereas anticyclones propagate away from the step due to dipole formation.

Some researchers studied motions over shelf/slope in eddy-topography interactions. Using a linearized two-layer β-plane ocean model, Qiu (1990) examined the shelf/slope responses induced by localized forcing sources which may propagate in the along-slope direction or have oscillating amplitudes. The slope he used was also entirely below the interface. He found that when the forcing source propagates in the along-slope direction with the shelf to the right, the shelf/slope responses are dominated by the bottom-trapped waves with intensity dependent on the propagation speed of the forcing.

The work that is most relevant to our study in the present chapter is by Frolov et al.(2004). They examined the interaction of a LCE(Loop Current Eddy)-type anticyclone with a realistic western boundary topography in the western Gulf of Mexico. The model they used was a two-layer, intermediate equations, model which allowed for the intersection of the bathymetry and the layer interface. The key feature of their study is the realistic continental shelf that penetrated into the upper layer. They addressed the formation of surface cyclones as a result of eddy-topography interaction and its effect on motions of the original anticyclone. They also studied the effects of lower

71

layer eddies on LCE motions. These deep eddies were generated due to stretching and compression of the lower layer by the moving LCE. The image effect of the western boundary was found to be bigger when the shelf was narrower.

As reviewed above, few investigations about the eddy-topography interactions have concerned the realistic continental shelf that is high into the upper layer, and no theoretical work has been done on the role of the curved coastline in the eddy-topography interactions. Our study in the present chapter has two important features. First, as Frolov et al. (2004), we will construct a realistic continental shelf which enters the upper layer. Second, the boundary is indented shoreward to form a bay, so effects of the bay's boundary can be examined. All important processes listed above and their dependence on different parameters such as the strength, the size, the initial location of the offshore eddy, and the slope profile are thoroughly explored in this chapter, which makes the study a general one for the eddy-topography interaction problem.

It is found that the two mechanisms that control the vortex-escarpment interaction in Chapter 2 are still crucial for the baroclinic eddy-slope interaction in this chapter with qualitatively new, important features. The most prominent feature is the shoreward decay of the eddy advection mechanism and the increase of the significance of the wave mechanism since the intrinsic scale for the problem, the first internal deformation radius is much smaller than the external one in Chapter 2. The two mechanisms are also found have very different effects on the cross-isobath transport. The cross-isobath transport directly driven by the eddy advection occurs within a small along-slope range corresponding to the location of the offshore eddy; the cross-isobath transport driven by the wave mechanism is spread in the wave propagation direction within a much greater range. Moreover, one side of the bay's boundary that is in the wave propagation direction acts to intensify the cross-isobath transport through interaction with the topographic waves. These results are especially important to understanding the slope/shelf circulation and cross-slope/shelf transport in the presence of a strong open ocean jet in Chapter 4.

The chapter is organized as follows: section 3.2 describes the model formulation; section 3.3 contains the model results; section 3.4 gives a summary of the study.

3.2 Model Formulation

3.2.1 Equations

We consider a rotating, hydrostatic, adiabatic ocean contained within a zonally reentrant channel on the f-plane in the Northern Hemisphere. The modeled ocean has two immiscible layers with uniform densities. The model used is the Hallberg Isopycnal Model (HIM)(Hallberg and Rhines, 1996) in Cartesian coordinates. Equations for the two layers are:

$$\frac{\partial \mathbf{u}_1}{\partial t} + q_1 \mathbf{k} \times (h_1 \mathbf{u}_1) = -\nabla B_1 - \frac{A}{h_1} \left\{ \nabla \cdot h_1 \nabla (\nabla^2 \mathbf{u}_1) \right\}, and \tag{3.1}$$

$$\frac{\partial \mathbf{u}_2}{\partial t} + q_2 \mathbf{k} \times (h_2 \mathbf{u}_2) = -\nabla B_2 - \frac{A}{h_2} \left\{ \nabla \cdot h_2 \nabla (\nabla^2 \mathbf{u}_2) \right\} - \frac{C_{drag}}{h_2} |\mathbf{u_2}| \mathbf{u_2}. \tag{3.2}$$

In the above equations, $\mathbf{u}_i$ is the horizontal velocity, h_i is the layer thickness, ρ_i is the density, A is the coefficient for the momentum-conserving diffusion and C_{drag} is the bottom drag coefficient. The layer potential vorticity, q_i, is equal to

$$q_i = \frac{f + \mathbf{k} \cdot (\nabla \times \mathbf{u}_i)}{h_i} = \frac{f + \zeta_i}{h_i}, \tag{3.3}$$

where f is the Coriolis parameter, ζ_i denotes the vertical component of the vorticity. The Bernoulli function, B, is equal to $\phi_i + \frac{1}{2}|\mathbf{u}_i|^2$. ϕ_i, the pressure in layer i(0 is the top) equals to $\phi_0 - g \sum_{j=0}^{i-1} \frac{\rho_i - \rho_j}{\rho_i} h_j$.

The energy is dissipated either by the bottom friction in form of a quadratic bottom drag or by the lateral friction. Compared with the harmonic(or Laplacian) viscosity, the biharmonic viscosity is more scale-selective putting more viscous damping on small scale motions and leaving the large-scale dynamics less affected. This behavior is consistent with our desire that the resolved flow dominates the sub-grid motions. Therefore, the lateral friction is parameterized as biharmonic viscosity in the momentum equations.

The mass conservation equation for the layer i is

$$\frac{\partial h_i}{\partial t} + \nabla \cdot h_i \mathbf{u}_i = 0 \tag{3.4}$$

with no cross-interface mass flux permitted.

3.2.2   Model Specification

The specification of the model parameters is described in this section. As mentioned before, The Coriolis parameter f is constant, equal to $1.1 \cdot 10^{-4} s^{-1}$. The reduced gravity $g' = g \Delta \rho / \rho$ is set to $0.02 ms^{-2}$. The baroclinic Rossby radius, $R_1 = g' H_1 H_2 / (H_1 + H_2)^{1/2} f_0^{-1}$, is about $35 km$ if the thickness of the resting layers is set as $H_1 = 1000 m$ and $H_2 = 3000 m$. Our grid-size is constant $\Delta x = \Delta y = 7.5 km$, so motions of the deformation radius scale can be resolved using 5 grid points.

The coefficient of the biharmonic horizontal viscosity A is specified as $0.6 \cdot 10^9 m^4 s^{-1}$ and the bottom drag coefficient C_{drag} is 0.001. These two parameters can be interpreted as spin-down times. Assuming the flow is exclusively dissipated by the bottom drag, we have the relation $\frac{du_2}{dt} = -\frac{C_{drag}}{h_2}|u_2|u_2$ and the spin-down time ϵ is $\frac{h_2}{C_{drag} u_2}$, inversely proportional to the flow magnitude. Taking $H_2 = 3000 m$ and $u_2 = 0.1 ms^{-1}$, we get a rough estimate of ϵ of about 350 days, while the spin-down time for motions on the deformation radius scale dissipated by the lateral friction is $A^{-1} R_1^4 = 79$ years. Clearly, the dominant friction in this sense is the bottom drag. The time-step Δt is chosen to be $100 s$. We have performed experiments with smaller Δt or bigger A values and have not found qualitative differences in results.

The model domain is zonally reentrant, extending zonally from $x = 0$ to $x = 1500 km$. Meridionally, the domain is bounded in the north by a zonal wall, B_n, at $y = 750 km$. Depending on the shape of the southern boundary, B_s, there are two types of domains. For the first type, the southern boundary changes its meridional location according to a Gaussian function of x. Half way between the west and the east end of the channel, the southern boundary bends from $y = 155 km$ southward to $y = 0$ as in Fig.3.1. This domain is used in most experiments. For the second type, the southern boundary is zonal and located along $y = 0$, so the whole domain is a channel as demonstrated in
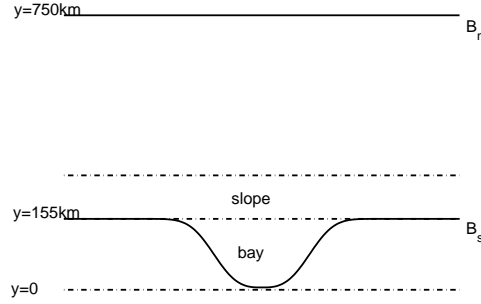
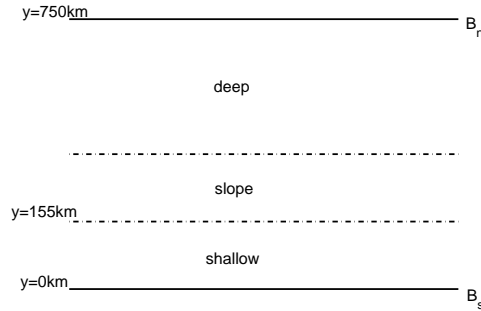y=750km _____ B_n

slope

y=155km _____

bay

y=0

Figure 3.1: A schematic of the first type of the domain. Solid lines denote the solid wall within the domain. The northern boundary of the domain B_n is along $y = 750km$, the southern boundary B_s has its southern most point at $y = 0$ and northern most point at $y = 155km$. From south to north, there are three dash-dot lines. The first one is along the latitude at $y = 0$, the second one at $y = 155km$ is the northern edge of the bay or the southern boundary of the channel, and the third one represents the northern edge of the topography.

y=750km _____ B_n

deep

slope

y=155km

shallow

y=0km _____ B_s

Figure 3.2: A schematic of the second type of the domain. Solid lines denote the solid wall within the domain. The northern boundary of the domain B_n is along $y = 750$, the southern boundary B_s is at $y = 0$. Northward of B_s, the first dash-dot line represents the boundary between the sloping and the flat-bottomed shallow region, and the second dash-dot line represents the northern edge of the topography.

Fig.3.2. The second domain is used in only one experiment which is aimed at understanding the effect of the bay's boundary on the cross-isobath transport. The maximum water depth is $4000m$. The topography is a zonally uniform slope connected with a shelf against the southern boundary. The slope penetrates into the upper layer, so southward of the intersection line between the topography and the layer interface, there is only one layer of water overlying the bottom. In the first type of the domain, the shelf region has the shape of a bay as bounded by the latitude of $y = 155km$ in the north and the curved wall B_s in the south, while in the second type of domain, the shelf region is between the latitude of $y = 155km$ and the latitude of $y = 0$ and zonally unbounded.

As demonstrated in the previous chapter as well as previous numerical investigations, anticy-

clones are more effective in inducing cross-isobath transport, so in this chapter, we only consider the interactions between a prescribed anticyclone and the continental slope/shelf. According to LaCasce (1997) topography favors surface vortices over barotropic ones and strong slopes tend to stabilize surface vortices, so in all experiments, the offshore anticyclones are surface intensified. Initially, the lower layer is motionless and the upper layer potential vorticity (PV hereafter) anomaly is zero everywhere except within a circle of radius r_0,

$$
q_1 = \begin{cases} \dfrac{f(1+\alpha)}{H_1} & \text{if } r <= r_0 \\[2ex] \dfrac{f}{H_1} & \text{otherwise,} \end{cases}
$$

, where q_1 is the upper layer PV, α is the parameter determining the strength of the PV anomaly. For anticyclones, α is always negative independent of the sign of f. r is the distance to the eddy's center. The thermal wind equation in polar coordinates including the centrifugal term for the upper layer is

$$
f v_0 + \frac{v_0{}^2}{r} = g' \frac{\partial h_0}{\partial r} \tag{3.5}
$$

where v_0 is the swirl velocity of the eddy, h_0 is the upper layer thickness and g' is the reduced gravity. Combining these two equations with the definition of PV which is $q_1 = \dfrac{f + \dfrac{1}{r}\frac{\partial(r v_0)}{\partial r}}{h_0}$, we can solve for v_0 and h_0 numerically and use them as the initial conditions for the model.

3.2.3 Model Verification

HIM is a C-grid, isopycnal coordinate, primitive equation ocean model developed by Hallberg (Hallberg, 1997). This model was initially based on the Arakawa and Hsu (1990) isentropic coordinate atmospheric model, but it has been extensively modified for use as an ocean model. The model has been used by many researchers to explore different physical processes that are important for the large-scale ocean circulation or configured as an idealized model for Geophysical Fluid Dynamics Studies.

As a verification of the model in our study in the present chapter, we first use the model to simulate the evolution of a surface anticyclone on the f-plane in a flat-bottomed channel with the

southern and the northern boundary at $y = 0$ and $y = 750km$. Parameters specified are $r_0 = 60km$, $\alpha = -0.4$, $H_1 = 1000m$, $H_2 = 3000m$, and $f = 1.1 \cdot 10^{-4} s^{-1}$. The anticyclone is initially located at the center of the channel, far enough from the zonal boundaries so the walls' effects are negligible. Within 60 days, the anticyclone remains in its initial location. The intensity of the eddy, measured as the interface depression at the eddy center, varies less than one percent through the simulation.

Then, we simulate the evolution of the same anticyclone within the same domain but on the β-plane with $\beta = 2 \cdot 10^{-11} m^{-1} s^{-1}$. The surface anticyclone is seen translating southwestward in the simulation, consistent with previous numerical as well as observational studies. The westward motion of the mesoscale eddy is induced by dispersion of Rossby waves on the β-plane. The meridional component of motion is related to the circular asymmetry of the eddy which is induced by initial dispersion tendencies. During the period of 60 days, the average westward and southward translation rates are $0.03 ms^{-1}$ and $0.038 ms^{-1}$. These rates are quantitatively consistent with previous investigations such as that of Mcwilliams and Flierl (1979).

3.2.4   Tracer Experiment Set-up

A conservative tracer with concentration T is used to explore the cross-isobath transport. It is advected according to the following equation:

$$\frac{\partial hT}{\partial t} + \nabla \cdot (\mathbf{u}hT) = 0, \tag{3.6}$$

where h is the layer thickness. The tracer concentration T in units of $kgkg^{-1}$ represents how much tracer is contained within a water body of unit mass. Subtracting the mass conservation equation multiplied by T from the above equation, we get the conservation equation of T following a water particle:

$$\frac{\partial T}{\partial t} + \mathbf{u} \cdot \nabla T = 0. \tag{3.7}$$

To calculate the mass transport across a specific latitude during the eddy-topography interactions, we will initially specify the tracer concentration to be 1 southward of the latitude and 0 any-

where else. This latitude is called the 1-0 boundary of the tracer. To compare the transport across different latitudes during the same period of time, multiple tracers with different 1-0 boundaries will be applied.

3.3   Anticyclone-slope/shelf Interaction

Several experiments are examined in this section to model the baroclinic interactions between the surface anticyclones and the continental slope/shelf. Cases and parameters are listed in Table3.3. As noted, parameter α represents the amplitude of the initial PV anomaly in the upper layer, parameter r_0 represents the size of the PV anomaly. Parameter "D" represents the meridional distance from the eddy center to the intersection line between the layer interface and the topography. "S" denotes different profiles of the continental slope. "BAY" denotes whether the coastline is in the shape of a bay as in Fig.3.1 or along the latitude of $y = 0$ as in Fig.3.2. The 11 cases are divided into the following 4 categories according to their goals: dependence on the existence of the bay, dependence on the anticyclones properties, dependence on the upper-slope and dependence on the lower-slope. The eddy-topography interaction process will be first described qualitatively in the standard case E1.

List of Experiments

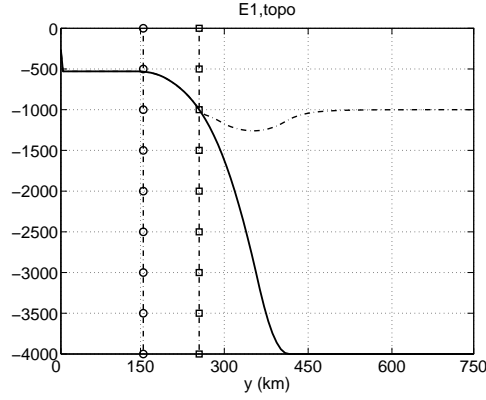| Case	α	$r_0(km)$	$D(km)$	S	BAY
E1	-0.4	60	100	standard(S1)	yes
E2	-0.4	60	70	standard(S1)	yes
E3	-0.4	60	130	standard(S1)	yes
E4	-0.6	60	100	standard(S1)	yes
E5	-0.4	80	100	standard(S1)	yes
E6	-0.4	73	100	standard(S1)	yes
E7	-0.4	60	90	S7(flat upper)	yes
E8	-0.4	60	90	S8(steep upper)	yes
E9	-0.4	60	100	S9(wide lower)	yes
E10	-0.4	60	100	S10(narrow lower)	yes
B1	-0.4	50	70	S11	yes
B2	-0.4	50	70	S11	no

Figure 3.3: Case E1. The thick solid line denotes the depth profile over the topography. The dash-dot line denotes the initial layer interface which is perturbed downward from the resting depth. The dash-dot-diamond line denotes the intersection line between the interface and the slope which is at $y = 255km$. The dash-dot-circle line denotes the northern edge of the bay which is at $y = 155km$. The water depth shoreward of $y = 155km$ is constant.

3.3.1 Standard Case E1

In the standard case E1, the resting layer interface is at depth of $1000m$, intersecting the topography at $y = 255km$ as shown in Fig.3.3. The slope above the interface is about $100km$ wide in the y direction bounded by the line of circles and the line of diamonds in Fig.3.3. The water depth over the slope increases from $500m$ to $1000m$. The surface anticyclone has a PV anomaly of $\alpha = -0.4$ within a round patch of $120km$ in diameter. Its swirl velocity has a profile as shown in Fig.3.4. The velocity amplitude first increases linearly from 0 at the eddy center to about $0.9ms^{-1}$ at the edge of the PV anomaly patch, then declines to about $0.05ms^{-1}$ at the distance of $150km$ from the center. The interface displacement is negative and the maximum depression is about $250m$ at the eddy center. Defining the distance across which the interface displacement drops to e^{-1} of its maximum value as the radius of the eddy, we find it about $70km$, twice of the internal deformation radius. Initially, the anticyclone is located at $(x = 750km, y = 350km)$, $100km$ seaward of the intersection line. The magnitude of the swirl velocity along the intersection line is about $0.24ms^{-1}$.

Displayed in Fig.3.5 is the time evolution of the upper PV contours in case E1 during the first 20 days. After $t = 0$, the clockwise velocity field of the anticyclone advects PV contours seaward. As water columns originally over the slope come down the topography, they are stretched vertically
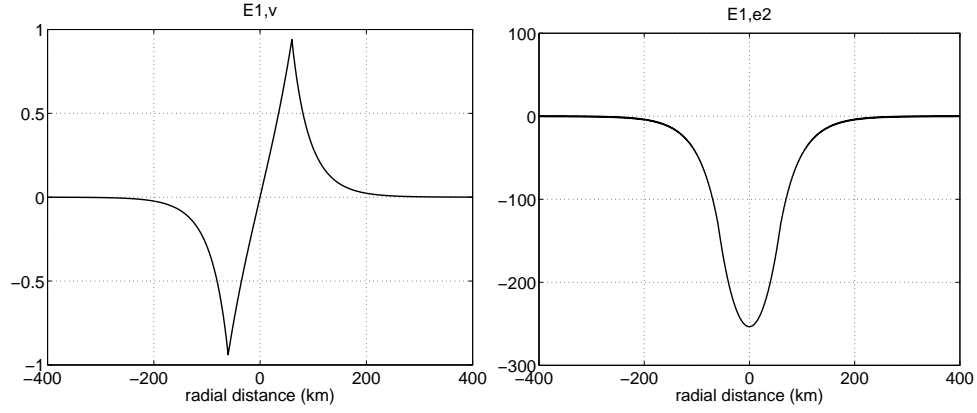
79

Figure 3.4: Case E1. Left panel: swirl velocity of the anticyclone against radial distance in units of ms^{-1}. Right panel: interface displacement of the surface anticyclone against radial distance in units of m.

and so positive relative vorticity is generated. The velocity field induced by the blob of water that has been driven off the slope is anti-clockwise. As a result of its interaction with the original anticyclone, the blob of the slope water and the anticyclone move away from the slope. Their northward displacement is quite small compared with the length of the domain and can hardly be seen in the plot of the PV contours, but can be clearly observed from the plot of the anticyclone's trajectory in Fig.3.8. As advected northward by the anticyclone, the seaward PV deformation evolves into a big head with its connection to the slope narrowing in time as in the panel of day 12 in Fig.3.5. The big head finally detaches from the slope at about day 14 into an isolated cyclonic eddy. The two eddies, the forcing anticyclone and the detached cyclone, form a dipole moving northward into the deep ocean as shown in the panel of day 20.

Although a cyclonic eddy forms from the topography as in the previous chapter, the present case and the barotropic vortex-escarpment interaction exhibit very different behaviors in evolutions of the PV contours. Most obviously, the PV front in the previous chapter deforms so much that it attaches to the boundary everywhere within the bay, whereas in the current case, the deformations of PV contours don't seem to be affected by the coastline at all. This occurs because in the previous chapter, the velocity induced by the PV anomaly of the point vortex declines slowly from the vortex with the decay scale on the order of the external deformation radius. The velocity magnitude is still finite near the boundary, so responses to the coastline are strong and can be easily identified. On the other hand, the velocity field induced by a baroclinic PV anomaly drops more quickly with
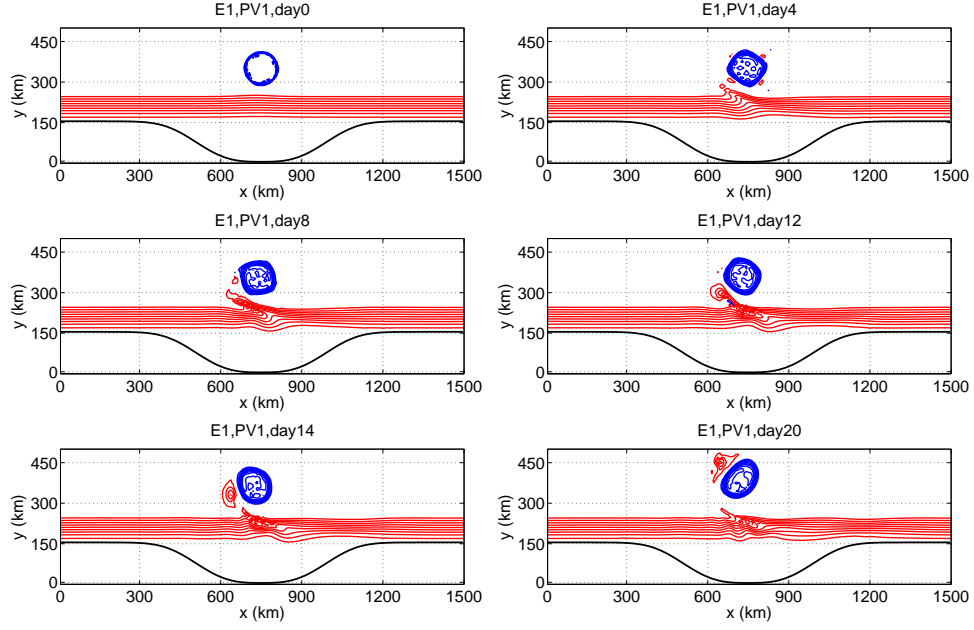
Figure 3.5: Case E1. The time evolution of the upper layer PV contours. Blue contours have PV values between $4 \cdot 10^{-8} m^{-1} s^{-1}$ and $1 \cdot 10^{-7} m^{-1} s^{-1}$ denoting the anticyclone. Intervals are $0.5 \cdot 10^{-8} m^{-1} s^{-1}$. Red contours have PV values between $1.2 \cdot 10^{-7} m^{-1} s^{-1}$ and $3 \cdot 10^{-7} m^{-1} s^{-1}$ denoting waters over the slope. Intervals are $0.1 \cdot 10^{-7} m^{-1} s^{-1}$.

the decay scale on the order of the internal deformation radius. According to our setting of the initial PV anomaly, the barotropic flow field is rather weak and we observe a big decrease of the anticyclone's swirl velocity shoreward from the first-layer slope edge. The velocity is basically zero near the coastline. Consequently, the amplitude of the seaward deformation on the PV contours that is directly induced by the anticyclone decreases southward as shown in the panel of day 4 in Fig.3.5. This initial perturbation of the PV contours further triggers topography-trapped waves which bend the PV contours shoreward to the west of the seaward deformation and tend to advect the frontal structure eastward. On the PV contours near the slope edge, the eastward propagation tendency is countered by the strong, westward advection of the anticyclone so it is hardly seen. On the PV contours further shoreward, the strength of the eddy advection is much weaker and the frontal structure is seen propagating eastward from day 8 to day 12.

Shown in Fig.3.6 are $x - t$ diagrams of PV anomaly along the first-layer slope edge which is at $y = 255 km$ and along the latitude of $y = 190 km$ which is at the middle portion of the slope. Along the slope edge, the eddy advection is so strong that the PV anomaly is large and positive
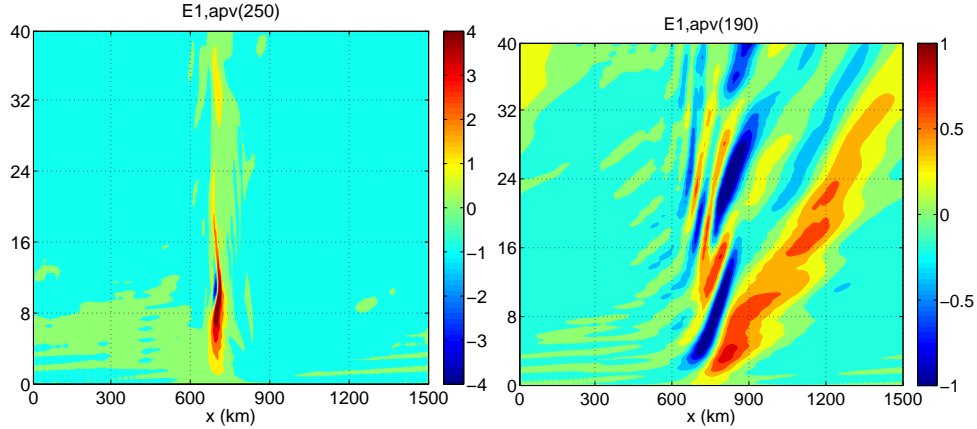
Figure 3.6: Case E1. $x - t$ diagrams of PV anomaly along the slope edge (right panel) and along the latitude of $y = 190km$ in units of $10^{-8}m^{-1}s^{-1}$.

concentrated within about 15 days and a zonal range comparable to that of the eddy's length scale. Along the latitude of $y = 190km$, the $x - t$ diagram is characterized by oscillations to the east of the anticyclone's position. The amplitude of the initial positive anomaly that is directly generated by the anticyclone is even a little bit smaller than the amplitude of the PV anomaly in wave motions. In addition, the PV anomalies along $y = 190km$ take place within a range much greater than that along the slope edge, and also remain for a long time after the eddy-topography interaction finishes. All these features clearly demonstrate the shoreward decline of the eddy advection as well as the increase of the significance of the wave mechanism. To the west of the offshore eddy, the wave motions are very weak because eastward-propagating waves are forced around $x = 750km$ and it takes time for waves to pass the eastern half of the channel and reenter it from the western end.

Defining the strength of an eddy as the total PV anomaly contained within the PV contour along which the PV anomaly drops to e^{-1} of its maximum value, we calculate the time variation of strengths for both the original anticyclone and the newly formed cyclone (Fig.3.7). There is a weak tendency for a decrease in the anticyclone's strength during 40 days indicating the energy loss through processes such as the interaction with the cyclone. The cyclone's strength first increases nearly linearly during the interaction period which lasts for about 15 days and remains around the same level afterwards. This result indicates that after the detachment of the cyclone from the slope, the motions of both eddies are mostly determined by the interactions between each other and no more eddy-slope interactions take place. The original anticyclone is more than 10 times stronger
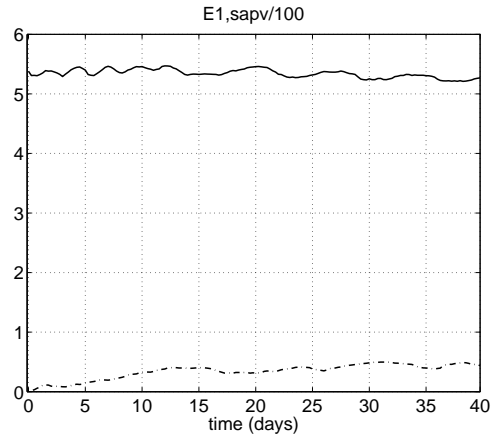
82

Figure 3.7: Case E1. The area integrated PV anomaly (absolute value) of the forcing anticyclone(solid line) and the topography-generated cyclone (dash-dot line). Both are in units of $100ms^{-1}$.
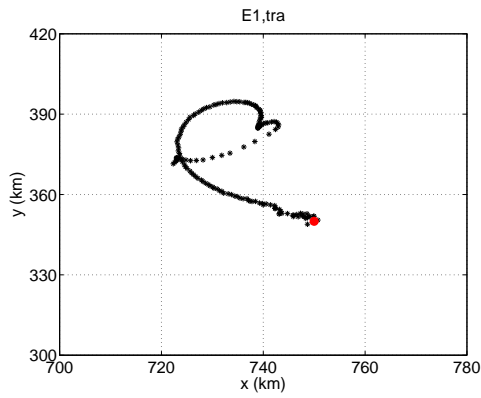

Figure 3.8: Case E1. The trajectory of the anticyclone within 40 days. The red dot denotes the initial position of the anticyclone.
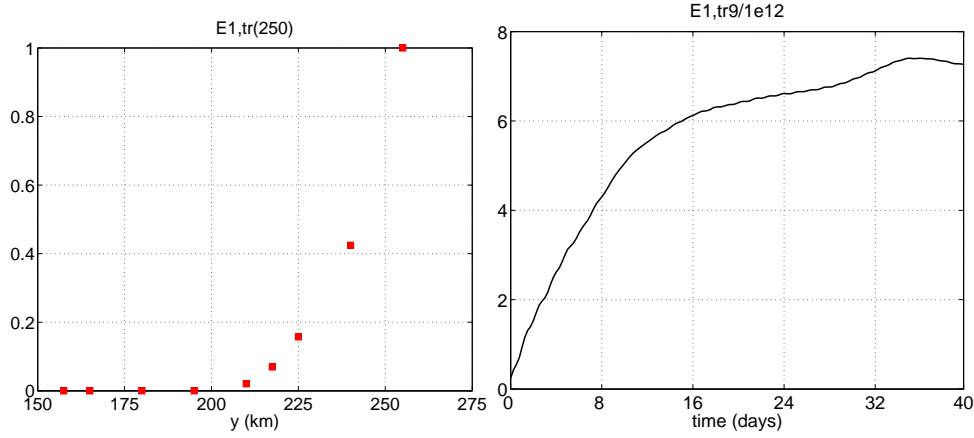
Figure 3.9: Case E1. Left panel: transport of nine tracers (named as 1-9) across $y = 255km$ within 40 days. The x-axis denotes the 1-0 boundary of each tracer, the y-axis is the ratio of transport of each tracer across $y = 255km$ to that of tracer 9 across $y = 255km$. Right panel: the time cumulative volume transport across the slope edge at $y = 255km$ in units of $10^{12}m^3$.

than the cyclone, so the pairing motion of the two is in favor of the anticyclone and along a clockwise path.

The trajectory of the anticyclone, whose center is defined as the position of the maximum interface depression, is displayed in Fig.3.8. Before the cyclone detaches from the slope, the propagation of the anticyclone is directed northwestward. Its northward displacement is about 30km, roughly the same as its westward displacement. After the cyclone leaves the slope, the two eddies rotate around each other and a complete rotation finishes at about day 40 when both eddies return to their locations upon the detachment. Because the cyclone is very weak, the anticyclone moves slowly and the circle that it moves around is very small, only about 20km in diameter.

The shoreward decline of the eddy advection naturally leads to a question of how far shoreward over the slope the eddy's effect can actually reach. One way to answer the question is to explore origins of water masses that finally leave the slope into the open ocean. We use nine tracers (tracer 1-9) with different initial 1-0 boundaries over the slope. As noted, the 1-0 boundary of a tracer refers to the latitude separating areas where the tracer concentration is initially 1 and 0. The 1-0 boundary of tracer 9 is the slope edge, so its volume transported across the line of $y = 255km$ is equal to the total volume driven off the slope. Tracer 5 is initially specified as 1 southward of $y = 207km$. Its volume transported across $y = 255km$ tells us amid waters that is finally driven off the slope,
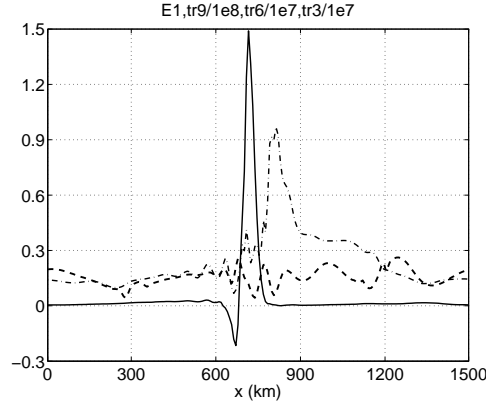
84

Figure 3.10: Case E1. Volume transport across $y = 255km$ in units of $10^8 m^3$ (solid line), volume transport across $y = 214km$ (dash-dot line) in units of $10^7 m^3$, and volume transport across $y = 176km$(thick dash line) in units of $10^7 m^3$ within 40 days.

how much comes from the region south of $y = 207km$. As shown by Fig.3.9, the further shoreward from the slope edge, the less water can be driven off the slope. During 40 days, more than 80% of water transported off the slope originates between $y = 225km$ and $y = 255km$. Southward of the 1-0 boundary of tracer 4 which is at $y = 192km$, no tracer mass is transported across the slope edge, while the number corresponds to tracer 5 is still different from zero. Therefore, the southernmost latitude where the slope water can be finally taken off the slope is estimated to be between $y = 192km$ and $y = 207km$. The range between this latitude and the first-layer slope edge is called the effective range of the forcing anticyclone. The difference of percentage between the two neighboring tracers, i.e., tracer 5 and tracer 6, indicates how much water originiated in the region bounded by the 1-0 boundaries of the two tracers can be driven off the slope.

The right panel of Fig.3.9 displays the time cumulative volume transported across the slope edge at $y = 255km$. Obviously, the flux off the slope has two stages. During the early period which is from the beginning to about day 12 when the topographic cyclone is about to detach from the slope, the flux across the slope edge is strong and the cumulative volume transported into the open ocean increases nearly linearly with time. After the cyclone detaches from the slope and moves away with the forcing anticyclone, the flux quickly slows down and the plot in the figure is much flatter than before.

The evolution of the PV contours during the eddy-topography interaction process has revealed

85

the existence of two mechanisms, the eddy advection and the wave mechanism. These two mechanisms are also control mechanisms we found important for barotropic vortex-escarpment interactions in the previous chapter. Features of the two mechanisms in driving cross-isobath transport are clearly demonstrated through comparison among transports along different latitudes over the slope. As shown in Fig.3.10, the northward transport across the slope edge is highly concentrated within a very narrow region corresponding to the zonal position of the forcing eddy. Having positive relative vorticity, the slope water that has been off the slope advects some of it back onto the slope. This reversing is demonstrated as the small negative peak on the west of the positive one in the plot. Near the shoreward boundary of the eddy's effective range, the zonal distribution of the cross-isobath transport is strikingly different from that along the slope edge: the transport along the slope edge is only nonzero within a narrow region in x, while it is positive everywhere along the latitude of $y = 214km$. A peak corresponding to the seaward PV contour deformation initially generated by the anticyclone can still be identified at $y = 214km$, but its position shifts eastward from its counterpart along the slope edge. Eastward of the peak, the amplitude of the transport is apparently greater than that to the west. Further shoreward, the transport across $y = 176km$ is even more homogeneously distributed along the latitude, and no prominent peaks can be identified from the plot. Therefore, the cross-isobath transport by eddy advection mechanism tends to be concentrated within the region of the eddy, while the wave mechanism tends to spread the transport in the direction of wave propagation which is eastward in the Northern Hemisphere within the current depth configuration.

In the standard case E1, two processes, the eddy advection and the wave mechanism, were found important for interactions between the baroclinic eddies and the continental slope/shelf as for the barotropic vortex-escarpment interactions in the previous chapter. Similar to the barotropic vortex-escarpment interactions, in anticyclone-induced interactions, a cyclonic eddy forms from the slope and moves with the original eddy into the open ocean. However, the magnitude of the velocity field induced by a baroclinic eddy decays much faster with distance compared with that by a barotropic eddy, so the shoreward weakening of the eddy advection mechanism is prominent in baroclinic eddy-topography interactions which makes the wave mechanism increasingly important towards the coast. As a measure of how far shoreward the eddy advection effect can reach over the

slope, the effective range of the anticyclone was defined and estimated by analyzing the origins of different water masses that were driven off the slope within 40 days. In the standard case, that range is about $50km$ in the y direction, and shoreward of the range, no slope water can get off the slope.

The two mechanisms are quite different in inducing the cross-isobath transport. The cross-isobath transport induced by the eddy advection mechanism is concentrated in time as well as in x, while the wave mechanism works to promote the cross-isobath transport in a much wider region as well as a much longer period of time.

Since the strength of the eddy advection mechanism declines quickly onshore, the velocity induced by the offshore anticyclone is basically zero near the bay-shaped coast and the effects of the boundary on the PV contours are hardly seen. This is strikingly different from what we observed in the previous chapter where the PV front is attached to the boundary within the bay.

3.3.2   The Effect of the Shelf Geometry—Cases B1 and B2.

In the standard case E1, we identified the two mechanisms controlling the eddy-topography inter-action process and their characters in driving the cross-isobath transport. The wave mechanism was found to be strongly affected by the eastern boundary of the bay in our study of the barotropic vortex-escarpment interactions in Chapter 2. On the other hand, the time evolution of the PV con-tours in the standard case E1 looks as if there were no boundary in the shallow area at all. This disparity makes it necessary to further explore the boundary's effect in the baroclinic situation. In this section we will compare results of two cases B1 and B2 that have different types of domain: case B1 has the first type of domain as in Fig.3.1 and case B2 has the second type as in Fig.3.2. Other than that, the two cases are exactly the same in all aspects such as the slope profile, the an-ticyclone's strength, size and initial location. In order to make the boundary's effect more easily identified, the slope profile, the anticyclone's properties as well as the layer thickness are chosen to be different from those in the standard case.

In case B1 and B2, the depth of the resting layer interface is set to be $650m$. The intersection line between the interface and the slope as shown in Fig.3.11 is further shoreward from case E1 and
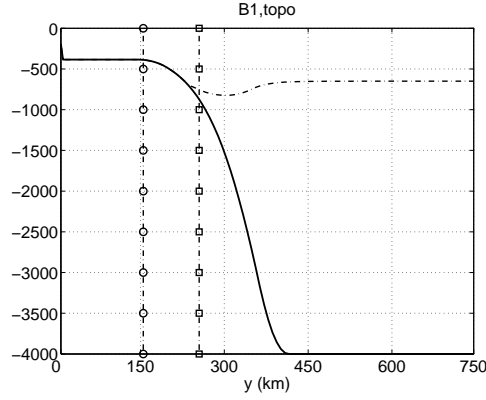
Figure 3.11: Case B1-B2. The thick solid line denotes the depth profile over the topography. The dash-dot line denotes the initial layer interface which is perturbed downward from the resting depth. The dash-dot-diamond line denotes the intersection line between the interface and the slope at $y = 230km$. The dash-dot-circle line denotes the northern edge of the bay at $y = 155km$, southward of which the water depth is constant.

the first-layer sloping region extends from $y = 155km$ to $y = 230km$, narrower than that in the standard case. We still use nine tracers to study the cross-isobath transport. Their 1-0 boundaries are over the first-layer slope, and the boundary for tracer 9 is just the slope edge at $y = 230km$.

The eddy-topography interactions in case B1 and B2 appear very similar to each other in that a cyclonic eddy forms from the slope and pairs with the original anticyclone into the open ocean. The southern boundary of the anticyclone's effective range in both cases is between the 1-0 boundaries of tracer 4 and tracer 3 at about $y = 180km$ as shown in Fig.3.12. Furthermore, in plots of the origins of the water masses that are finally driven off the slope in Fig.3.12, the time variations of the strengths of the anticyclone and the newly formed cyclone in Fig.3.13, and the trajectory of the forcing eddy in Fig.3.14, no discernible differences between the two cases are observed.

The only aspect showing differences between the two cases is the cross-isobath transport. Fig.3.15 displays the volume transport across different latitudes over the slope in both cases. The transport in case B2 is stronger than that in case B1. Especially shoreward of the southern boundary of the anticyclone's effective range around $y = 180km$, the difference of the transport becomes prominent. Therefore, the southern boundary in case B2 tends to suppress the cross-isobath transport by affecting mostly the wave mechanism.

The two side boundaries have different influence on the transport across the bay opening.
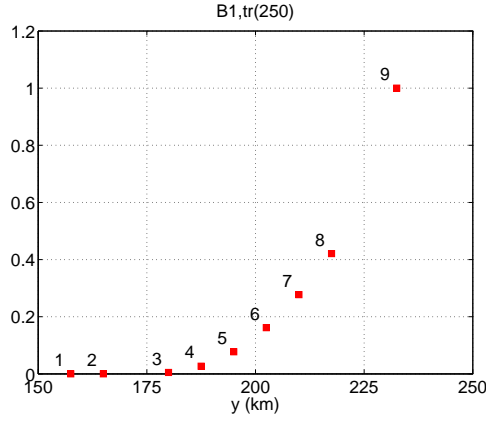
88

Figure 3.12: Case B1. Transport of nine tracers (named as 1-9) across the slope edge at $y = 230km$ within 40 days. The x-axis denotes the 1-0 boundary of each tracer, the y-axis is the ratio of transport of each tracer across $y = 230km$ to that of tracer 9 across $y = 230km$.
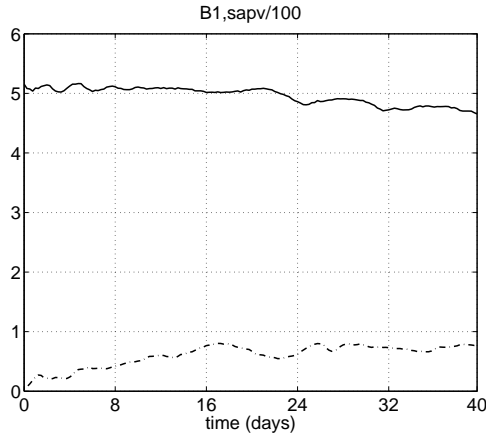

Figure 3.13: Case B1. Area integrated PV anomaly (absolute value) in the original anticyclone (solid line) and the newly formed cyclone (dash-dot line) in units of $100s^{-1}m^2$.
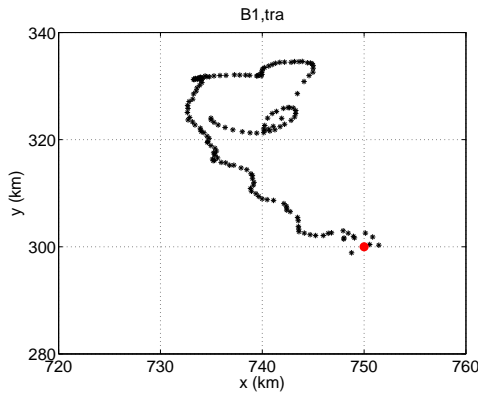

Figure 3.14: Case B1. The trajectory of the offshore anticyclone within 40 days. The red dot denotes the initial location of the anticyclone.
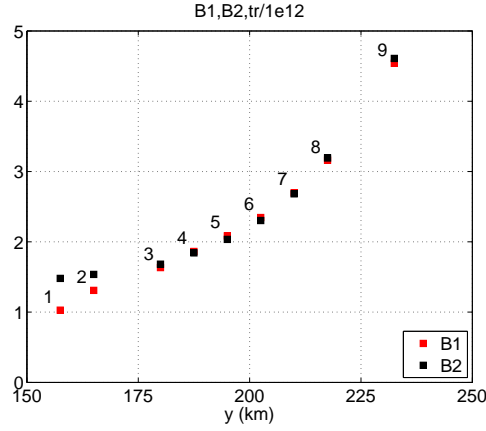
Figure 3.15: Case B1-B2. Cross-isobath volume transport against latitude within 40 days in case B1(red squares), and B2 (black squares). Units are $10^{12}m^3$.
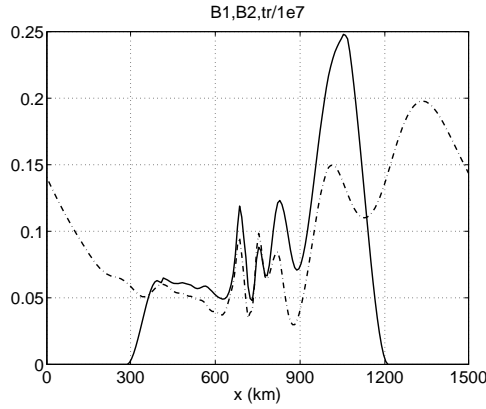

Figure 3.16: Case B1-B2. Volume transport across the latitude of bay opening at $y = 155km$ within 40 days in units of 10^7m^3 in case B1(solid line), and B2(dash-dot line).

Fig.3.16 shows the zonal distribution of the volume transport across the latitude of $y = 155km$ in the two cases. In case B1, along this latitude, the shelf is partially enclosed and the cross-isobath transport is non zero only within the bay opening, while in case B2, the shelf region is zonally unblocked and the meridional transport is allowed everywhere. Within the zonal range of the bay opening which extends approximately from $x = 300km$ to $x = 1200km$, the volume transport in case B1 is greater than that in case B2 and the difference increases eastward. Near the eastern boundary, the transport is greatly amplified in case B1 indicating the strengthening effect of the eastern boundary on the cross-isobath transport.

Using two experiments B1 and B2 which have the same slope profile and the same anticyclone located at the same position but different types of the southern boundary, we examined the effects of the partially enclosed shelf versus the zonally unblocked shelf. With a surface anticyclone located about $70km$ away from the first-layer slope edge and its shoreward boundary of the effective range about $30km$ seaward of the latitude of the bay opening, whether the shelf region, the region shoreward of $y = 155km$, is zonally unblocked or semi-enclosed as a bay makes no difference to the formation of the cyclonic eddy from the slope, its strength and its pairing motion with the original anticyclone. The geometry of the shelf does influence the cross-isobath transport. First, the cross-isobath volume transport over the slope tends to be smaller with a bay-shape shelf than that with a zonally unbounded shelf. Second, along the latitude of the bay opening and within the zonal range of the bay, the cross-isobath transport out of a bay-shape shelf is bigger than that out of a zonally unbounded shelf; the cross-isobath transport is strengthened near the eastern boundary of the bay. This result is consistent with one of our conclusions from Chapter 2 that the cross-escarpment volume transport is stronger near the bay's eastern boundary as the topographic waves strongly interact with the boundary.

3.3.3 Dependence on Anticyclone's Offshore Distance "D"—Cases E2 and E3

In previous sections, we have studied the important processes of the eddy-topography interactions including the formation of a cyclonic eddy and the cross-isobath transport. In following sections, we will explore their dependence on variable parameters such as the anticyclone's strength, size, location and the slope profile. We begin with the effect of changing the offshore distance using cases E2 and E3. The configurations of cases E2 and E3 are almost the same as those in case E1 except that compared with case E1, the forcing anticyclone is initially $30km$ closer to the slope in case E2 and $30km$ further away in case E3. Consequently, the anticyclone's swirl velocity magnitude over the slope varies greatly among the three cases and so are responses over the topography.

The formation of a topographic cyclone by the anticyclone in case E2 (Fig.3.17 is much faster than that in case E1 (Fig.3.5): the cyclonic eddy is about to detach from the slope at about day 8 in case E2 while at about day 12 in case E1. Furthermore, due to the small distance between
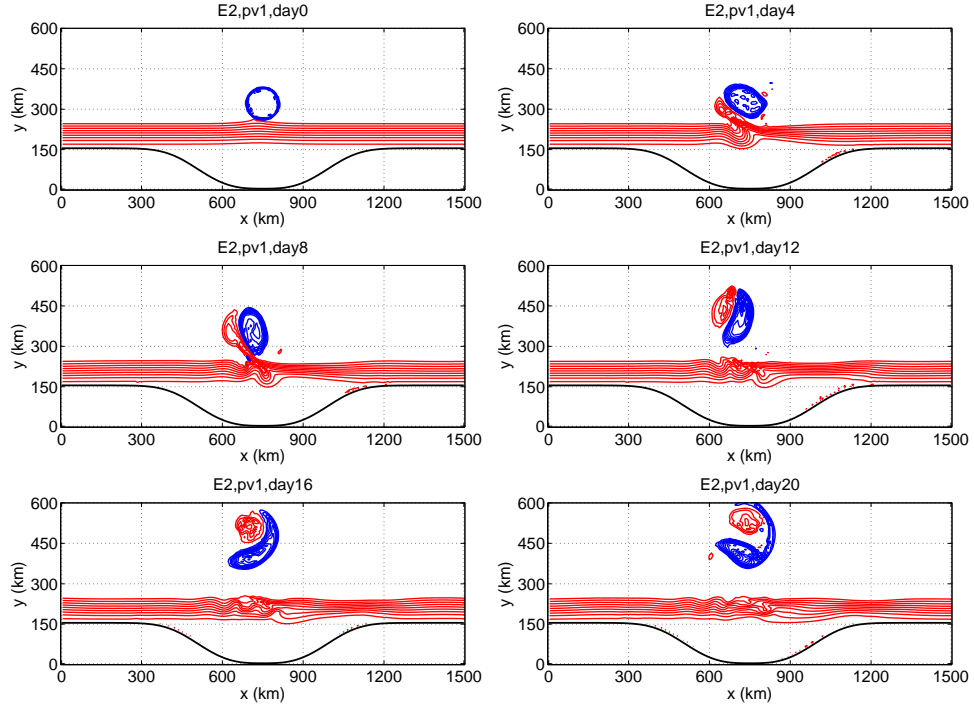
Figure 3.17: Case E2. The time evolution of the upper layer PV contours. Blue contours have PV values between $4 \cdot 10^{-8} m^{-1} s^{-1}$ and $1 \cdot 10^{-7} m^{-1} s^{-1}$ denoting the anticyclone. Intervals are $0.5 \cdot 10^{-8} m^{-1} s^{-1}$. Red contours have PV values between $1.2 \cdot 10^{-7} m^{-1} s^{-1}$ and $3 \cdot 10^{-7} m^{-1} s^{-1}$ denoting waters over the slope. Intervals are $0.1 \cdot 10^{-7} m^{-1} s^{-1}$.
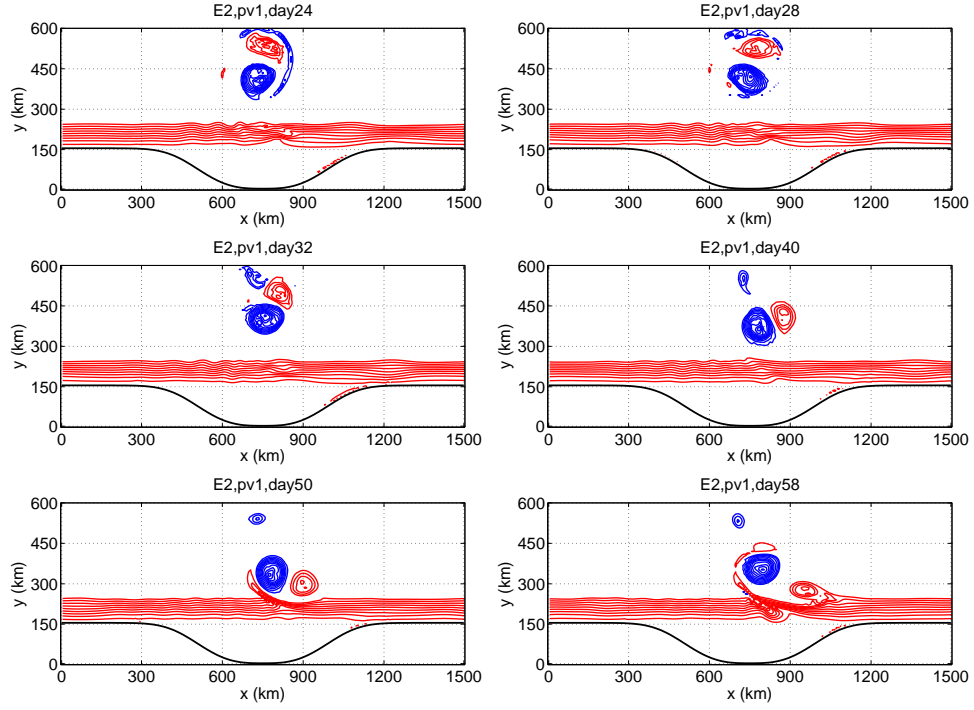
Figure 3.18: Case E2. The time evolution of the upper layer PV contours. Blue contours have PV values between $4 \cdot 10^{-8} m^{-1} s^{-1}$ and $1 \cdot 10^{-7} m^{-1} s^{-1}$ denoting the anticyclone. Intervals are $0.5 \cdot 10^{-8} m^{-1} s^{-1}$. Red contours have PV values between $1.2 \cdot 10^{-7} m^{-1} s^{-1}$ and $3 \cdot 10^{-7} m^{-1} s^{-1}$ denoting waters over the slope. Intervals are $0.1 \cdot 10^{-7} m^{-1} s^{-1}$.
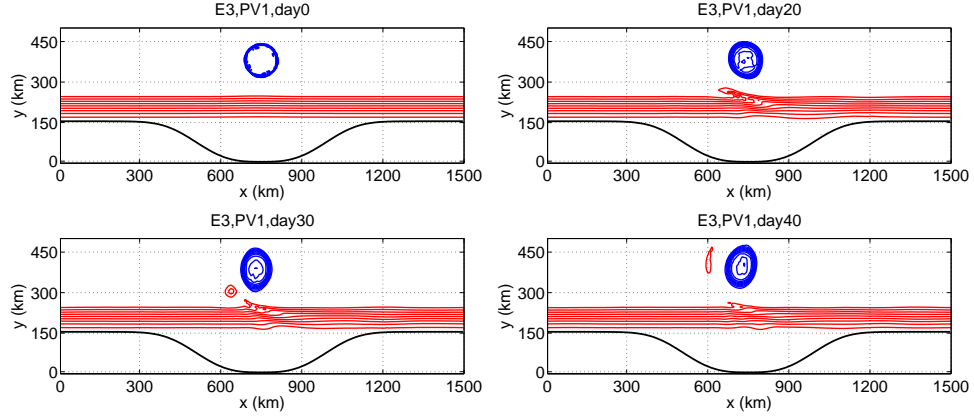
Figure 3.19: Case E3. The time evolution of the upper layer PV contours. Blue contours have PV values between $4 \cdot 10^{-8} m^{-1} s^{-1}$ and $1 \cdot 10^{-7} m^{-1} s^{-1}$ denoting the anticyclone. Intervals are $0.5 \cdot 10^{-8} m^{-1} s^{-1}$. Red contours have PV values between $1.2 \cdot 10^{-7} m^{-1} s^{-1}$ and $3 \cdot 10^{-7} m^{-1} s^{-1}$ denoting waters over the slope. Intervals are $0.1 \cdot 10^{-7} m^{-1} s^{-1}$.

the original anticyclone and the slope in case E2, the seaward PV deformation and the subsequent cyclonic eddy are very close to the forcing eddy as in the panel of day 4 in Fig.3.17. As a result of the strong interaction between the deformed PV contours and the anticyclone, the anticyclone is stretched more in the northwest-southeast direction and becomes asymmetric. This asymmetry gets stronger after the detachment of the cyclone. In the pairing motion of the two eddies, the northern end of the forcing anticyclone evolves into an elongated tail and is advected counter-clockwise around the nearby cyclone as shown in the panel of day 20 in Fig.3.17. The tail detaches from the main body of the forcing anticyclone at about day 24 and becomes an isolated smaller anticyclone afterwards. Compared with this newly formed smaller anticyclone, the cyclone is more effective in influencing the motion of the reminder of the original anticyclone. Therefore, the cyclone and the remaining, bigger, anticyclone begin to move together along a clockwise path towards the slope at about day 40. At about day 50, they get very close to the slope and the anticyclone is driving the slope water off the slope for the second time. The cyclone, on the other hand, generates a shoreward PV deformation over the slope which in turn pulls the cyclone towards the slope and at the same time advects it eastward as shown in the panel of day 58 in Fig.3.18. Slowly, this cyclone will return to the slope with its PV anomaly dispersed as the topography-trapped waves. Also shown in this panel, the original anticyclone has generated a new cyclone from the slope and moves together with it.
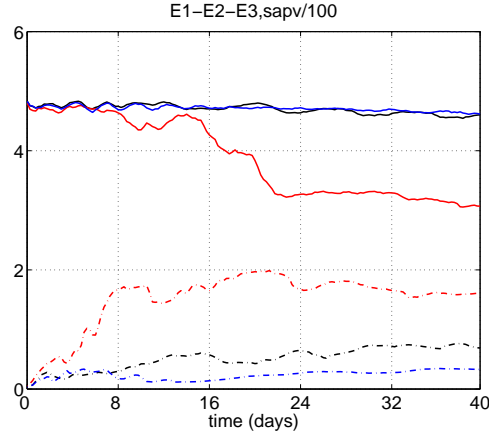
Figure 3.20: Case E1-E2-E3. The area integrated PV anomaly (absolute value) of the forcing anticyclone (solid line) and the topography-generated cyclone (dash-dot line) in case E1(black lines), E2(red lines), and E3(blue lines). Units are $100ms^{-1}$.

Fig.3.19 shows the time evolution of the PV contours in case E3, in which the anticyclone is initially furthest away from the slope. As a result of the weak advection of the anticyclone, it takes about 30 days for a small cyclonic eddy to form and detach from the topography. During the formation and the following pairing motions, the forcing anticyclone is very symmetric about its center.

Differences among cases E1, E2, and E3 are also clearly demonstrated in the time variations of strengths of the two eddies, the forcing anticyclone and the newly formed cyclone as in Fig.3.20. The strength of the topographic cyclone is inversely proportional to the initial distance between the forcing anticyclone and the slope. With a shorter distance, it takes a shorter period of time for the cyclone to form. The strength of the forcing anticyclone remains nearly constant in cases E1 and E3, but drops quickly within about 10 days shortly after the cyclone forms in case E2. This weakening of the forcing anticyclone corresponds to the splitting of the original eddy into two eddies as described in Fig.3.18.

In all three cases, the forcing anticyclone moves along a clockwise path since it is always stronger than the newly formed cyclone. The translation rate of the anticyclone depends on the strength of the cyclone. In case E2 which has the strongest cyclone generated, the anticyclone has the largest net drift which is more than $60km$ in x and about $100km$ in y. In case E3 which has the
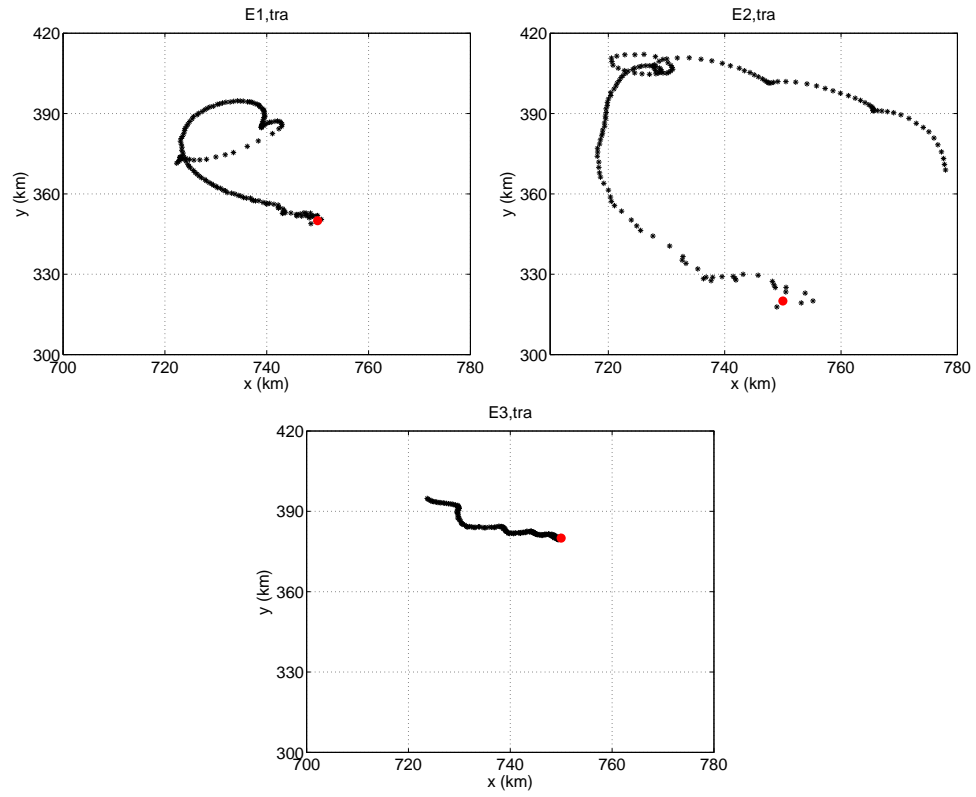
95

Figure 3.21: Case E1-E2-E3. The trajectory of the anticyclone in case E1(first panel), E2(second panel), and E3(third panel) within 40 days. Red dots denote initial locations of anticyclones.
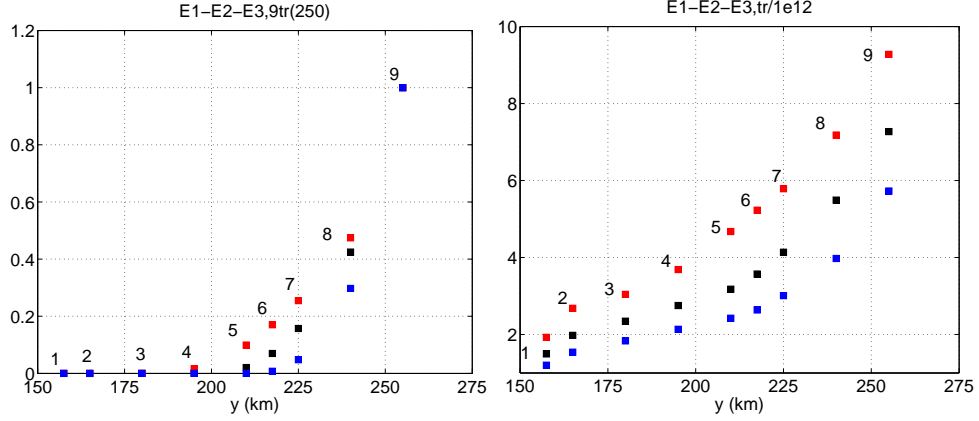
Figure 3.22: Case E1-E2-E3. Left panel: transport of nine tracers (named as 1-9) across $y = 255km$ within 40 days in case E1(black squares), E2(red squares), and E3(blue squares). The x-axis denotes the 1-0 boundary of each tracer, the y-axis is the ratio of transport of each tracer across $y = 255km$ to that of tracer 9 across $y = 255km$. Right panel: cross-isobath volume transport against latitude within 40 days in case E1(black squares), E2(red squares), and E3(blue squares). Units are $10^{12}m^3$.

weakest cyclone, the anticyclone's net displacement is less than $20km$ in both directions.

Using the same method as in case E1, we find out the origins of water masses that are driven off the slope during 40 days which give a general idea of the effective range of the forcing anticyclone over the slope (first panel in Fig.3.22). The southern boundary of the anticyclone's effective range in case E2 is between the 1-0 boundaries of tracer 3 and tracer 4, while that in case E3 is between the 1-0 boundaries of tracer 6 and tracer 7. So the anticyclone's effect reaches furthest shoreward in case E2 and nearest in case E3. The cross-isobath volume transport over the slope also declines in a row in cases E2, E1, and E3 as shown in the right panel of Fig.3.22.

The distance from the surface anticyclone to the intersection line between the layer interface and the slope is varied in cases E1, E2 and E3. The anticyclone's swirl velocity magnitude over the slope is strongest in case E2 but weakest in case E3. As a result, the strength of the topographic cyclone generated during the eddy-topography interactions is biggest in case E2 and smallest in case E3. The forcing anticyclone has a larger effective range over the slope when it is closer to the slope. The cross-isobath transport is also proportional to the anticyclone's offshore distance. Furthermore, the anticyclone has a larger net drift through the simulation when it is initially closer to the shelf.
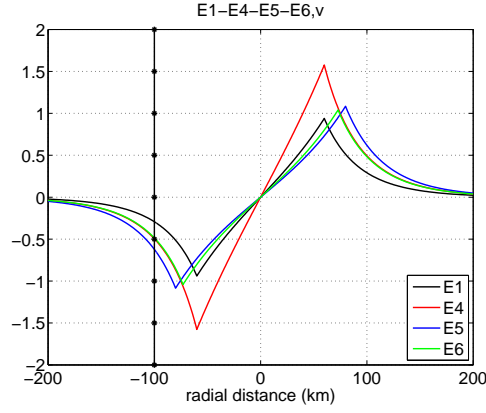
Figure 3.23: Case E1-E4-E5-E6. Left panel: swirl velocity of the anticyclone against radial distance in units of ms^{-1} in case E1(black line), E4(red line), E5(blue line) and E6(green line). The dash-dot-star line in both panels denote the y position of the first-layer slope edge relative to the offshore anticyclone.

3.3.4   Dependence on Anticyclone's PV Anomaly and Size—E4, E5 and E6.

In this section, we will explore the dependence of the eddy-topography interaction on the anticyclone's initial PV anomaly α and its size r_0. Three cases, E4, E5, and E6 are performed and compared with previous cases. Compared with the standard case E1 which has $\alpha = -0.4$ and $r_0 = 60km$, case E4 has greater PV anomaly $\alpha = -0.6$; case E5 and case E6 have larger sizes which are $80km$ and $73km$. The parameter settings other than those mentioned above are the same as those in the standard case.

As shown in Fig.3.23, the magnitude of the swirl velocity over the slope declines sequentially in cases E5, E4 and E1 and that in case E6 is almost the same as that in case E4. As to the maximum swirl velocity of the anticyclone, it is largest in case E4 due to the biggest PV anomaly while smallest in case E5 in which the eddy size is largest.

The time evolution of the PV contours in case E4(Fig3.24) in which the anticyclone has bigger PV anomaly but standard size, looks quite similar to that in the standard case E1. The time evolutions of the PV contours in case E5 and E6(Fig.3.25 and 3.26) which have larger anticyclones are very similar to that described in case E2 in which the anticyclone is very close to the slope. In cases E5 and E6, the forcing anticyclone becomes asymmetric during the formation of the topographic cyclone. While moving together with the cyclone, the outer area of the anticyclone is peeled off
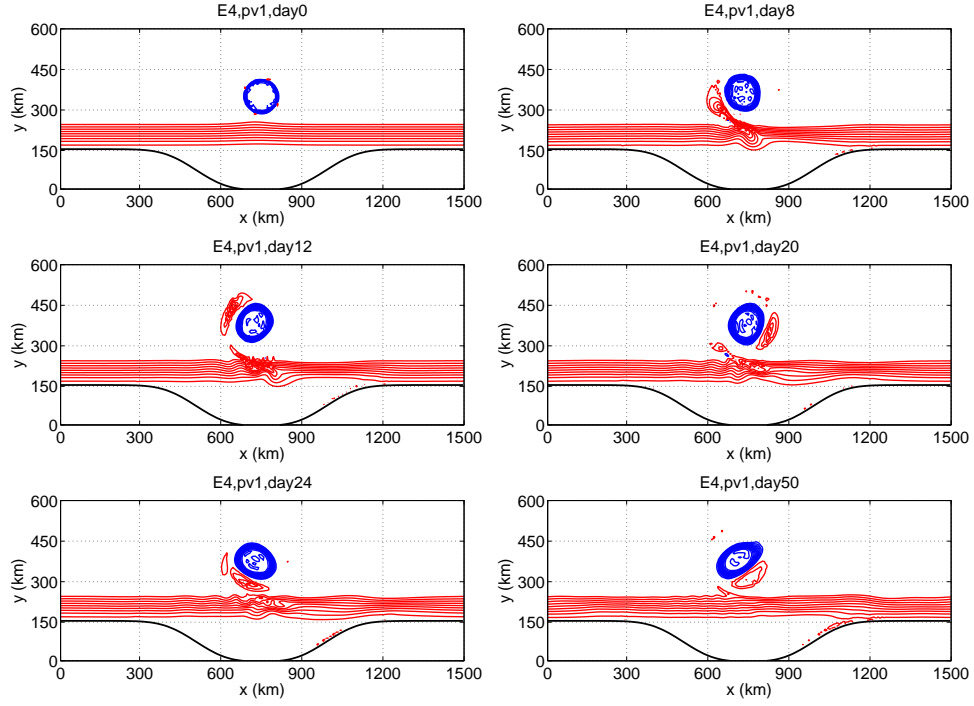
98

Figure 3.24: Case E4. The time evolution of the upper layer PV contours. Blue contours have PV values between $4 \cdot 10^{-8} m^{-1} s^{-1}$ and $1 \cdot 10^{-7} m^{-1} s^{-1}$ denoting the anticyclone. Intervals are $0.5 \cdot 10^{-8} m^{-1} s^{-1}$. Red contours have PV values between $1.2 \cdot 10^{-7} m^{-1} s^{-1}$ and $3 \cdot 10^{-7} m^{-1} s^{-1}$ denoting waters over the slope. Intervals are $0.1 \cdot 10^{-7} m^{-1} s^{-1}$.

Figure 3.25: Case E5. The time evolution of the upper layer PV contours. Blue contours have PV values between $4 \cdot 10^{-8} m^{-1} s^{-1}$ and $1 \cdot 10^{-7} m^{-1} s^{-1}$ denoting the anticyclone. Intervals are $0.5 \cdot 10^{-8} m^{-1} s^{-1}$. Red contours have PV values between $1.2 \cdot 10^{-7} m^{-1} s^{-1}$ and $3 \cdot 10^{-7} m^{-1} s^{-1}$ denoting waters over the slope. Intervals are $0.1 \cdot 10^{-7} m^{-1} s^{-1}$.
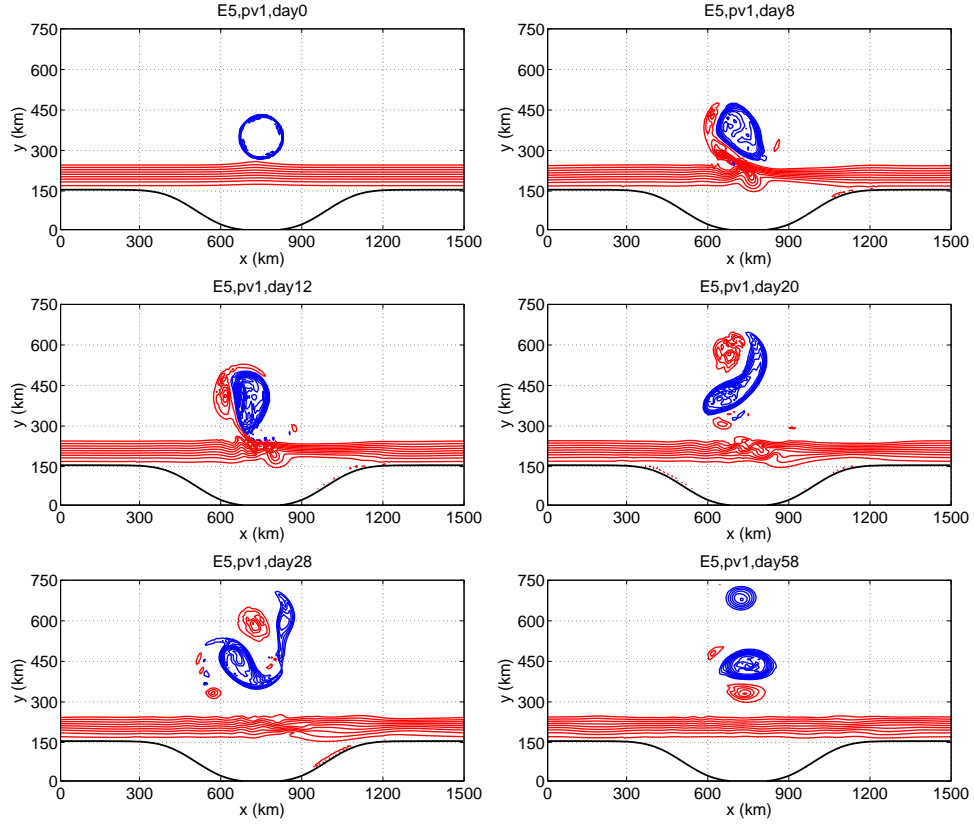
Figure 3.26: Case E6. The time evolution of the upper layer PV contours. Blue contours have PV values between $4 \cdot 10^{-8} m^{-1} s^{-1}$ and $1 \cdot 10^{-7} m^{-1} s^{-1}$ denoting the anticyclone. Intervals are $0.5 \cdot 10^{-8} m^{-1} s^{-1}$. Red contours have PV values between $1.2 \cdot 10^{-7} m^{-1} s^{-1}$ and $3 \cdot 10^{-7} m^{-1} s^{-1}$ denoting waters over the slope. Intervals are $0.1 \cdot 10^{-7} m^{-1} s^{-1}$.
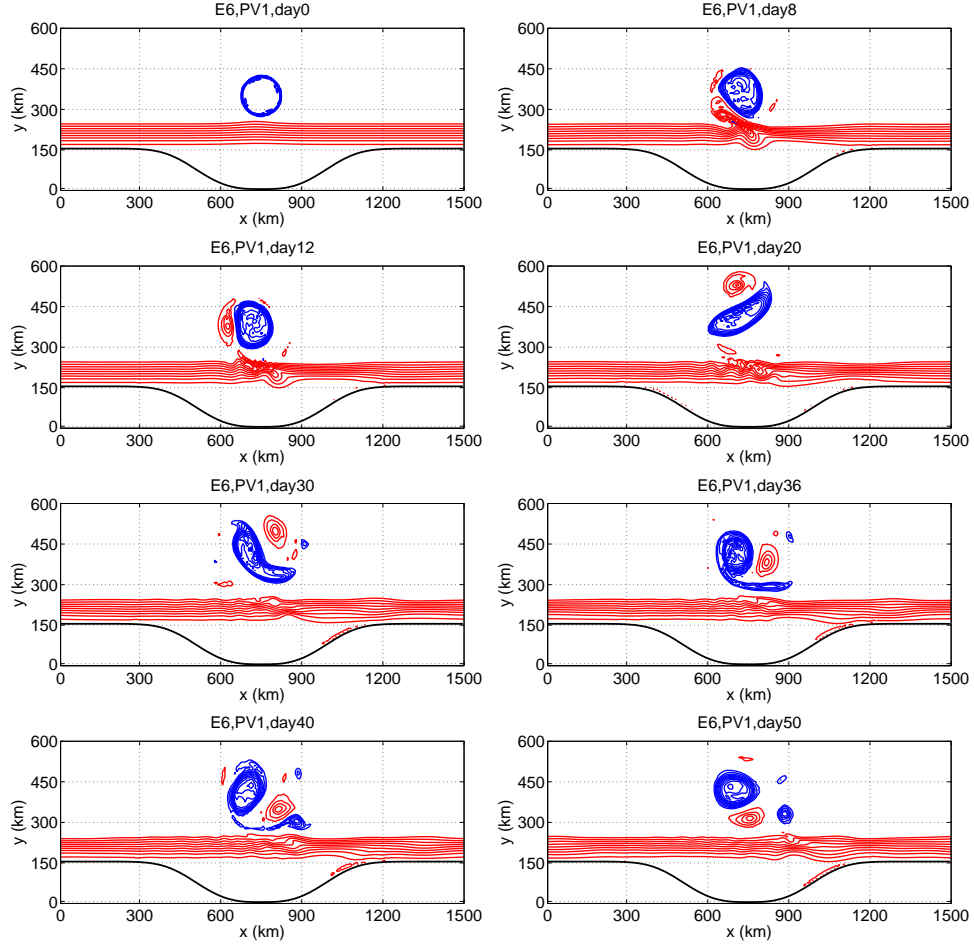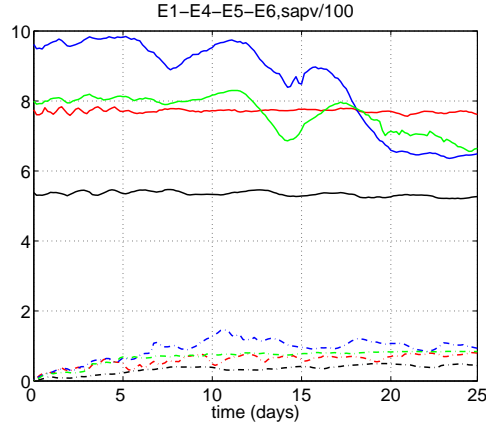
Figure 3.27: Case E1-E4-E5-E6. The area integrated PV anomaly (absolute value) of the forcing anticy-clone(solid line) and the topography-generated cyclone(dash-dot line) in case E1(black lines), E4(red lines), E5(blue lines) and E6(green lines). Units are $100ms^{-1}$.

from the core and evolves into one or more anticyclones much smaller than the reminder. After that, the cyclone continues to move with the big anticyclone along a clockwise path. Although the anticyclone in case E4 has bigger PV anomaly, the larger size of the anticyclone in case E6 makes the two eddies equal in strength as shown in Fig.3.27. On the other hand, the cyclones generated from the topography in the two cases have almost the same strengths. Since the anticyclone in case E6 evolves differently from that in case E4 after the detachment of the topographic cyclone, the size of the anticyclone is a decisive factor for the peeling-off phenomenon compared with the amplitude of the PV anomaly. The amplitude of the strength of the topographic cyclone is largest in case E5, smallest in the standard case E1 and the two cyclones in case E4 and E6 are almost equal. This re-lation corresponds well with the relation of the swirl velocity magnitude over the slope in Fig.3.23, So local amplitude of the swirl velocity is dominant in determining the strength of the cyclone that forms from the topography.

As to the motion of the anticyclone, the anticyclone in case E5 moves furthest northward as well as westward among the four cases as in Fig.3.28. The net drift of the anticyclone in case E6 is the second largest and that in the standard case E1 is smallest. So the total PV anomaly contained by the anticyclone is important in determining the anticyclone's net drift. For two anticyclones with the same initial strength as those in case E4 and E6 which also generate cyclones with the same strength, the larger one has bigger net drift.
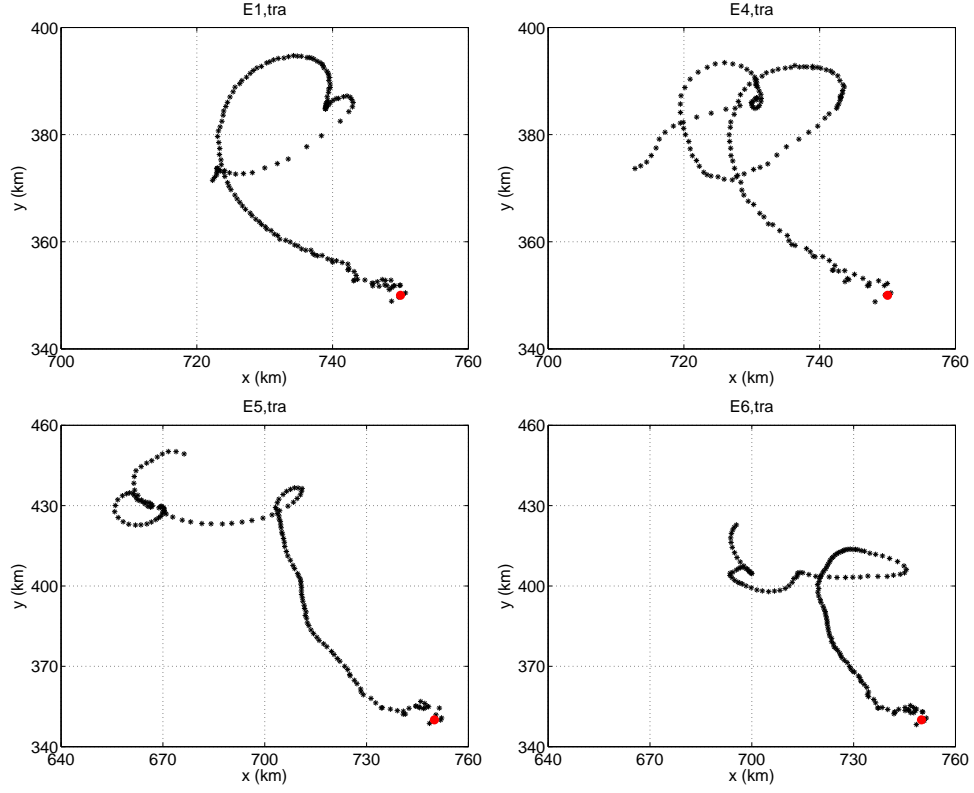
Figure 3.28: Case E1-E4-E5-E6. The trajectory of the anticyclone in case E1(first panel), E4(second panel), E5(third panel), and E6(fourth panel) within 40 days. Red dots denote initial locations of anticyclones.
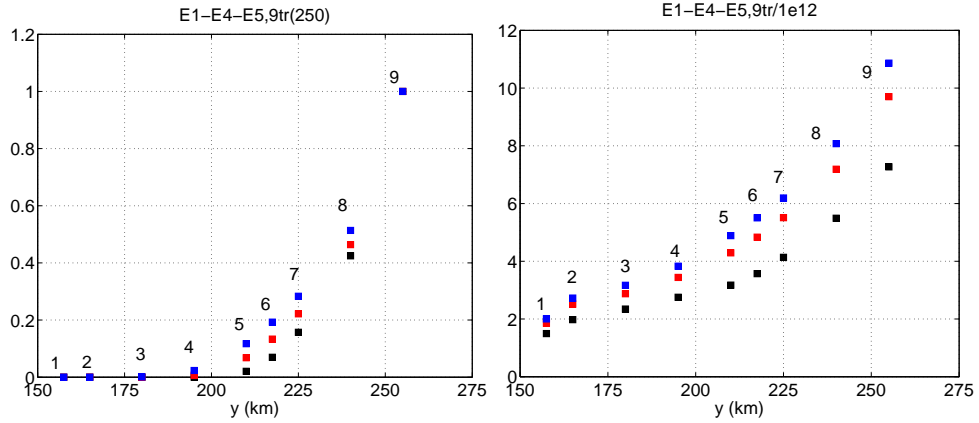
Figure 3.29: Case E1-E4-E5. Left panel: transport of nine tracers (named as 1-9) across $y = 255km$ within 40 days in case E1 (black squares), case E4 (red squares) and case E5 (blue squares). The x-axis denotes the 1-0 boundary of each tracer, the y-axis is the ratio of transport of each tracer across $y = 255km$ to that of tracer 9 across $y = 255km$. Right panel: cross-isobath volume transport against latitude within 40 days in case E1(black squares), case E4 (red squares), and case E5 (blue squares). Units are $10^{12}m^3$.

103

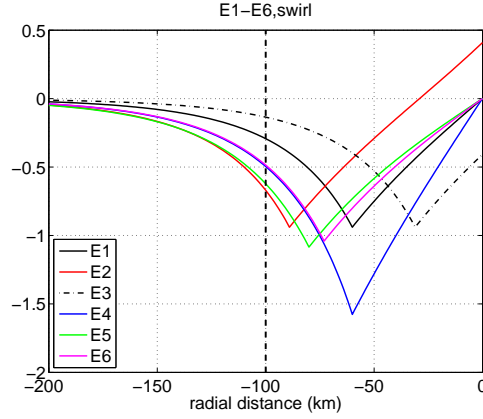**Figure 3.30:** Case E1-E2-E3-E4-E5-E6. The anticyclone's initial swirl velocity over the slope against the radial distance to the eddy center in units of ms^{-1}. The thick dash line denotes the position of the slope edge relative to the offshore anticyclone.

The shoreward boundary of the anticyclone's effective range in case E5 is between the 1-0 boundaries of tracer 3 and tracer 4 and is furthest shoreward among the cases as shown in Fig.3.29. The cross-isobath volume transport as shown in the right panel of Fig.3.29 is also strongest in case E5. The case E4 is intermediate among case E1, E4 and E5 in both aspects. Results of the case E6 have no discernible difference from those of case E4 and are not displayed in Fig.3.29. Therefore, the amplitude of the swirl velocity over the slope determines the anticyclone's effective range as well as the cross-isobath transport.

By comparing cases E4, E5, E6, and the standard case E1, we examined the effects of the anticyclone's PV anomaly and size on the eddy-topography interactions. Both the variations of the two parameters, α and r_0, induce changes in the strength of the anticyclone and also different swirl velocity profiles over the slope. The magnitude of the swirl velocity over the slope is an important factor determining the strength of the topographic cyclone, the anticyclone's effective range as well as the cross-isobath transport. The strength of the forcing anticyclone is important in influencing its pairing motions with the cyclone. In addition, the larger anticyclone tends to have the peel-off process in the eddy-topography interactions.

In this and the previous section, we have explored the responses of different aspects in the eddy-topography interactions to changing parameters of the forcing anticyclone including its offshore distance, PV anomaly and size. The eddy-topography interactions in cases E1 to E6 are qualitatively
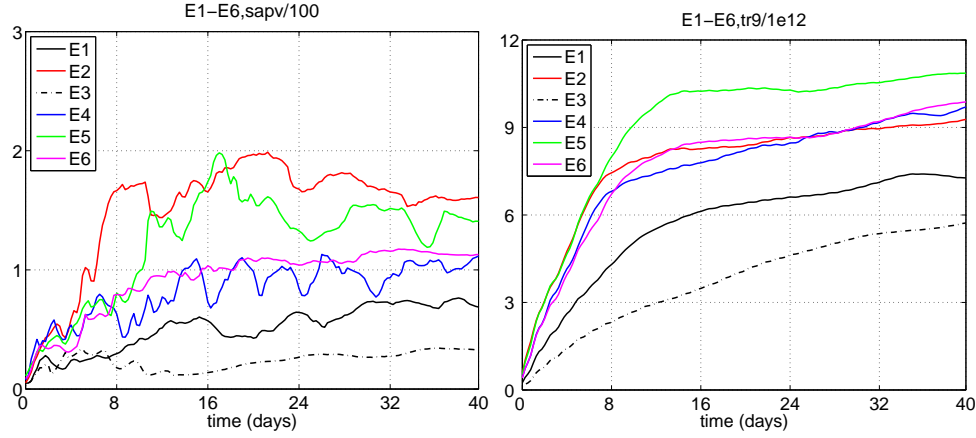
104

Figure 3.31: Case E1-E2-E3-E4-E5-E6. Left panel: the strength of the topographic cyclone in units of $100ms^{-1}$. Right panel: the time cumulative volume transported across the slope edge at $y = 255km$ in units of $10^{12}m^3$.

similar to each other in that a topographic cyclone forms from the slope and pairs with the forcing anticyclone along a clockwise path into the open ocean. Nevertheless, quantities such as the strength of the topographic cyclone do depend on the parameters.

It is found that the amplitude of the anticyclone's initial swirl velocity plays an very important role in determining the strength of the topographic cyclone and the cross-isobath transport. As shown in Fig.3.30, initially the amplitudes of the anticyclone's swirl velocity shoreward of the slope edge (left of the thick dash line in the figure) in case E2 and case E5 are strongest and nearly equal to each other; those in case E4 and E6 are smaller but also equal to each other; the swirl velocity in case E3 is the smallest because of its largest distance to the slope. The strength of the newly formed cyclone in each case as shown in the left panel of Fig.3.31 is proportional to the amplitude of the anticyclone's swirl velocity and so is the level of the cumulative volume transported across the slope edge as shown in the right panel of Fig.3.31. As noted in our discussion about the standard case E1, during the formation of the topographic cyclone, the cumulative volume of the slope water off the slope increases nearly linearly with time. From the beginning to about day 8, their amplitudes in different cases correspond very well to the amplitudes of the anticyclone's swirl velocity over the slope: the volumes are largest and almost equal in cases E2 and E5, smaller but also equal in cases E4 and E6, and smallest in case E3. Meanwhile, how long the formation process lasts is also important since it determines the length of this "fast-growing phase". Although initially cases

105

E5 and E2 have similar swirl velocities over the slope, case E5 has a much longer period of eddy formation than case E2 in which the dipole starts to move away from the slope at about day 8. Consequently, after day 8, the volume in case E5 becomes greater than that in case E2. However, this factor is of secondary importance compared with the swirl velocity amplitude which clearly determines the rough level of the volume transport within 40 days.

3.3.5 Dependence on Upper-layer Slope—case E7 and E8

Until now, the parameter study has been focused on the eddy advection mechanism by varying the PV anomaly, size and initial location of the forcing anticyclone. It was demonstrated using contour dynamics model that the slope/shelf responses to variable anticyclones also strongly depend on the depth difference across the step topography. Therefore, we are going to examine the effect of different slope profiles on baroclinic eddy-topography interactions. Since the anticyclones are surface intensified, we will study the upper-layer and lower-layer slope profiles separately in this and the next section.

Two cases, case E7 and E8, are examined in this section. Compared with the standard case E1, they have the same anticyclone initially located at the same position. The slope profiles in the three cases are the same in the lower layer but are different above the interface. As shown in Fig.3.32, case E7 has a flat slope and case E8 has a steep one. The initial layer interface intersects with both profiles at the latitude of $y = 260km$.

The eddy-slope interactions in both cases look very similar to that in the standard case E1. A topographic cyclone forms around the same time in each case and then pairs with the original anticyclone along a clockwise path (Fig.3.33). Upon detachment from the topography, the cyclone formed from the steep slope has greater strength than that generated from the flat slope as shown in Fig.3.34. The stronger cyclone is more powerful in advecting the forcing anticyclone, so the anticyclone as shown in Fig.3.35 has a larger net drift in the west and north direction. Due to the smaller difference of strength between the pairing eddies, the circle the anticyclone moves along with the stronger cyclone is apparently larger than that with the weaker cyclone.
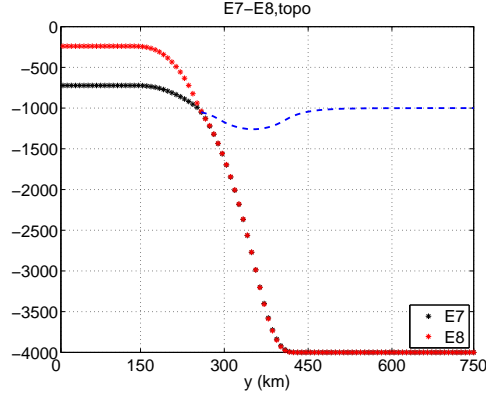
106

Figure 3.32: Case E7-E8. The depth profile against y in E7(black stars) and E8(red stars). The blue dash line denotes the initial depth of the layer interface.
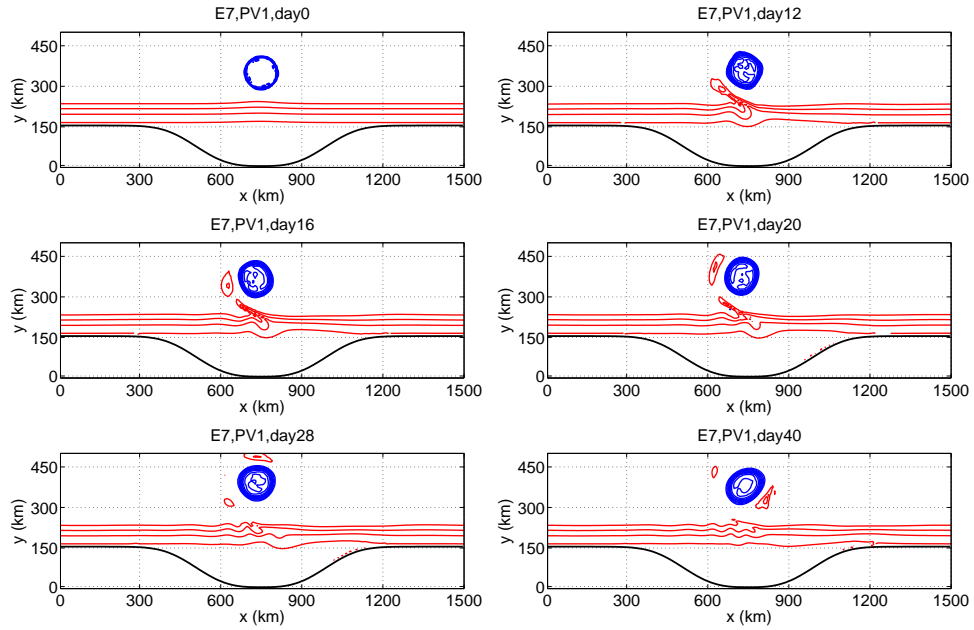
Figure 3.33: Case E7. The time evolution of the upper layer PV contours. Blue contours have PV values between $4 \cdot 10^{-8} m^{-1} s^{-1}$ and $1 \cdot 10^{-7} m^{-1} s^{-1}$ denoting the anticyclone. Intervals are $0.5 \cdot 10^{-8} m^{-1} s^{-1}$. Red contours have PV values between $1.2 \cdot 10^{-7} m^{-1} s^{-1}$ and $3 \cdot 10^{-7} m^{-1} s^{-1}$ denoting waters over the slope. Intervals are $0.1 \cdot 10^{-7} m^{-1} s^{-1}$.

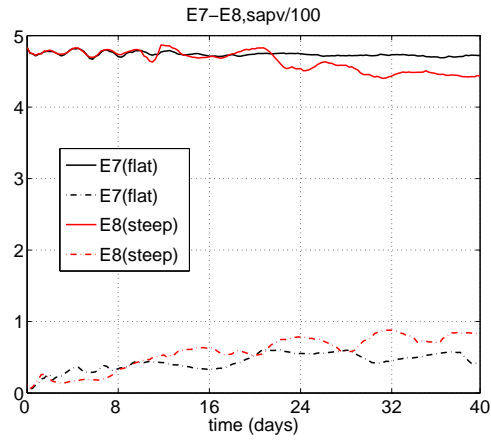**Figure 3.34:** Case E7-E8. The area integrated PV anomaly (absolute value) of the forcing anticyclone(solid line) and the topography-generated cyclone(dash-dot line) in case E7(black lines) and E8(red lines). Units are $100ms^{-1}$.
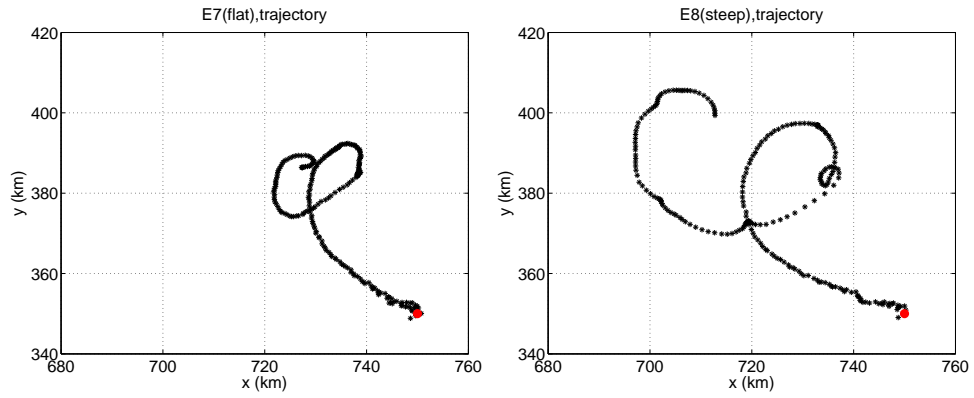

Figure 3.35: Case E7-E8. The trajectory of the anticyclone in case E7 (left panel) and E8 (right panel) within 40 days. Red dots denote initial locations of anticyclones.
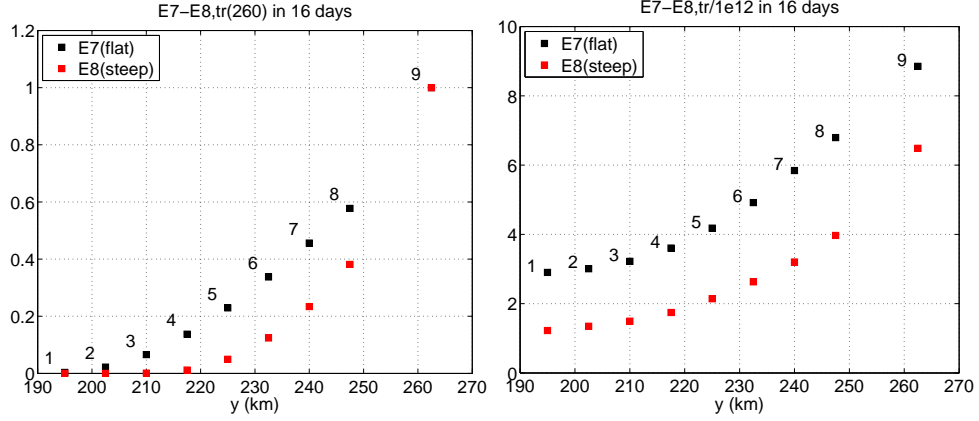
Figure 3.36: Case E7-E8. Left panel: transport of nine tracers (named as 1-9) across $y = 260km$ within 16 days in case E7(black squares) and E8 (red squares). The x-axis denotes the 1-0 boundary of each tracer, the y-axis is the ratio of transport of each tracer across $y = 260km$ to that of tracer 9 across $y = 260km$. Right panel: the volume transport of nine tracers across their 1-0 boundaries within 16 days in case E7(black squares) E8(red squares). Units are $10^{12}m^3$.

As shown in Fig.3.36, the anticyclone's effect in driving water off the slope within 16 days(the time cyclones detach from the slope) in case E8 which has the steep slope diminishes at about $y = 225km$(40km shoreward of the slope edge), while that in case E7 which has the flat slope remains finite even beyond the line of $y = 200km$ resulting in an effective range of 60km. Clearly, the steep slope works as a barrier blocking the anticyclone's effect reaching further shoreward. As described in the standard case E1, when interacting with the slope, the anticyclone first generates a seaward PV deformation extending northwest-southeast over the slope. Along with this deformation, water columns cross isobath into deeper region generating positive relative vorticity to conserve PV. Therefore, the seaward deformation can be regarded as a big cyclonic eddy over the slope and right to the south of the forcing anticyclone. Shoreward of this cyclonic patch, the velocity field produced by this patch is counterclockwise, opposite to that by the forcing anticyclone. So the seaward PV deformation acts against the anticyclone in driving water off-slope in regions southward of it. When the slope is steep, the strength of the vorticity contained by this patch would be larger, so its opposing effect would be greater and the effective range is smaller. It needs to be noticed that the effective range is a result of competition between the two: the anticyclone's advection and the advection by local PV deformations. The latter is dependent on the slope steepness while the former declines shoreward. We can think of this competition between the two mechanisms as the
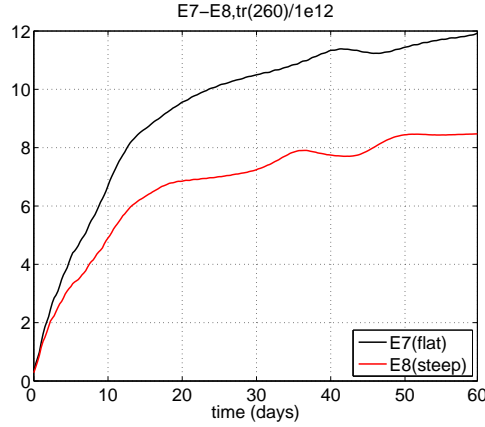
109

Figure 3.37: Case E7-E8. Time cumulative volume transport across the latitude of $260km$ in case E7(black line) and E8(red line) in units of $10^{12}m^3$.

competition between two relative voticities: one is the relative vorticity gained by a water column by moving from its original latitude to the slope edge and the other is the relative vorticity of the anticyclone within the same range L, the range bounded by the water column's original latitude to the slope edge. The relative vorticity induced by crossing isobath is $\beta_T L$ where β_T is the PV gradient due to the topography and is proportional to the slope steepness. If the range L is not much bigger than the deformation radius, the relative vorticity of the anticyclone across L can be estimated as $\dfrac{\Delta U}{L}$. The ratio of the two relative voticities is therefore $\dfrac{\Delta U}{\beta_T L^2}$. For a water column to be driven off the slope, this parameter needs to be bigger than 1, so $L \leq \sqrt{\dfrac{\Delta U}{\beta_T}}$ which means the range is inversely proportional to the slope steepness. This is consistent with one of our solutions that the anticyclone's effective range is small when the slope is very steep and big when the slope is flat. However, when L is much bigger than the deformation radius within which $\dfrac{\Delta U}{L}$ is not a proper estimate for the anticyclone's relative vorticity any more, the size of the effective range will be limited by the local velocity amplitude of the anticyclone no matter how flat the slope is.

As to the exchange process, the flat slope is more favorable for the cross-isobath transport. The second panel of Fig.3.36 shows the total transport within 16 days across different latitudes over the slope in the two cases. The transport in the flat-slope case is greater than that in the steep-slope case everywhere over topography even outside the anticyclones' effective ranges. Fig.3.37 shows time cumulative transports across the slope edge in both cases during 60 days. The two plots have similar
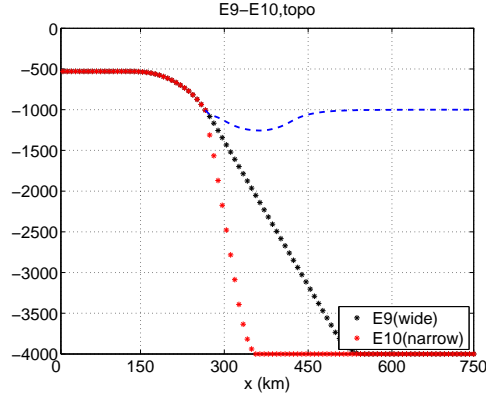
110

Figure 3.38: Case E9-E10. The depth profile against y in case E9(black stars), and E10(red stars). The blue dash line denotes the initial depth of the layer interface.

structures: the transport is strong during cyclone formation process and weak after the anticyclone and the cyclone move away from the slope. The transport across the slope edge in case E7 is more than 50% of that in case E8 at the end of the process.

3.3.6 Dependence on Lower-layer Slope—Case E9 and E10

The effect of the lower-layer slope is studied in this section using cases E9 and E10 which have identical slope profiles above the layer interface at $1000m$. In the lower layer, the slope in case E9 extends from about $y = 270km$ to $y = 350km$, while in case E10 the slope is much wider extending northward till $y = 460km$. The anticyclones interacting with topography in the two cases have the same PV anomaly $\alpha = -0.4$, the same radius $r_0 = 60km$ and are located at the same position $x = 750km, y = 360km$. The lower-layer slope in case E10 is narrower than that in all cases carried out so far. The surface anticyclone therefore has a better chance to move beyond the sloping region in case E10 inducing lower layer eddy motions which will be described in detail in the following.

Eddy-topography interactions in the two cases are qualitatively similar to each other and also similar to previous cases (Fig.3.39). Actually, the time variations of the strengths of the forcing anticyclone and the newly formed cyclone are almost the same till after cyclones detach from the slope as in Fig.3.40. During pairing motions of the forcing anticyclone and the topographic cyclone,
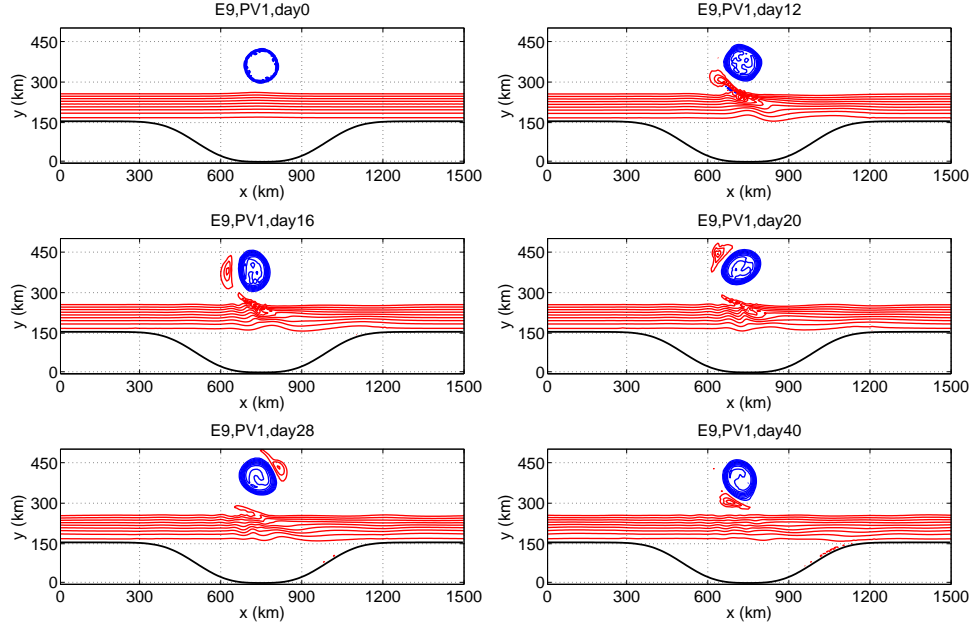
111

Figure 3.39: Case E9. The time evolution of the upper layer PV contours. Blue contours have PV values between $4 \cdot 10^{-8} m^{-1} s^{-1}$ and $1 \cdot 10^{-7} m^{-1} s^{-1}$ denoting the anticyclone. Intervals are $0.5 \cdot 10^{-8} m^{-1} s^{-1}$. Red contours have PV values between $1.2 \cdot 10^{-7} m^{-1} s^{-1}$ and $3 \cdot 10^{-7} m^{-1} s^{-1}$ denoting waters over the slope. Intervals are $0.1 \cdot 10^{-7} m^{-1} s^{-1}$.

the anticyclone's strength in the narrow-slope case becomes smaller than that in the wide-slope case, while the cyclone's strength in the narrow-slope case becomes larger than its counterpart in the wide-slope case. The cumulative volume transported across the slope edge at about $y = 270 km$ in the two cases are nearly the same till the pairing motion starts as shown in Fig.3.41. After that, the cross-slope transport becomes stronger in the wide-slope case.

The above results indicate that processes related to responses over the first-layer slope show very little difference because of the same upper-layer slope profile in the two cases. Differences between the two cases become sensible after about day 20 when the dipole has left the first-layer slope and move around into the open ocean. To understand the effect of the lower-layer slope, we need to examine the motions below the interface.

The mechanism of upper eddies inducing motions in the lower layer can be explained as follows. Consider a situation where a first-layer anticyclone moves westward within a flat-bottomed two-layer ocean, the interface to the west of the anticyclone center is depressed and the interface to the

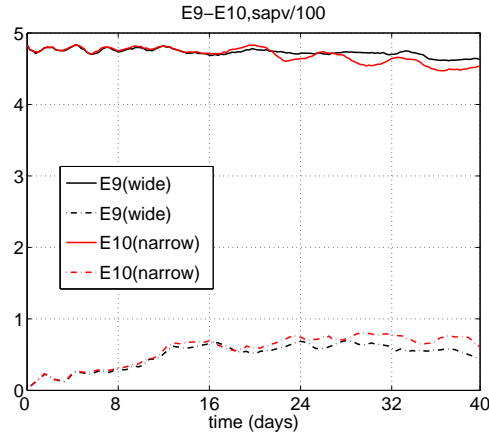**Figure 3.40:** Case E9-E10. The area integrated PV anomaly (absolute value) of the forcing anticyclone(solid line) and the topography-generated cyclone(dash-dot line) in case E9(black lines) and E10(red lines). Units are $100ms^{-1}$.
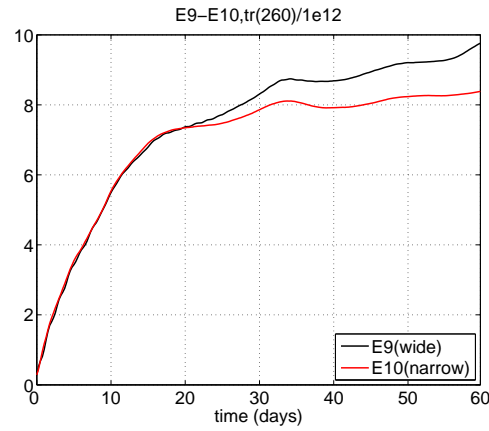

Figure 3.41: Case E9-E10. Time cumulative volume transport across the latitude of $260km$ in case E9(black line) and E10(red line) in units of $10^{12}m^3$.
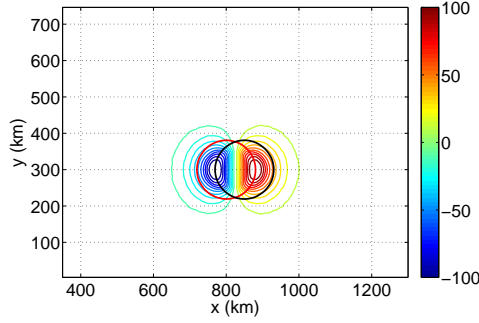
Figure 3.42: Case E10. The schematic view of the generation of lower dipole structure by the motion of the upper-layer anticyclone which has $\alpha = -0.4$ and $r_0 = 60km$. The location of the anticyclone's center is $(850km, 300km)$ at t_1 and $(800km, 300km)$ at t_2. The black and the red circles represent the location of the $-70m$ interface displacement at t_1 and t_2 respectively. Colored contours indicate the interface variation from t_1 to t_2. Contours of negative values indicate the interface is depressed while contours of positive values indicate the interface is enhanced. From the figure, it is obvious that along the track of the anticyclone, a lower-layer anticyclone appears in the front and a lower-layer cyclone at the back.

east of the eddy center is raised. Squeezed water columns have negative vorticities and stretched ones have positive voticities. Therefore, along the track of the first-layer anticyclone, a lower-layer anticyclone appears at the front to the west and a lower-layer cyclone at the back east as shown in Fig.3.42. The lower layer eddy structure induced by interface displacement associated with motions of the upper eddies can only be easily identified in the flat-bottom region because perturbations in the sloping region quickly disperse into topographic waves that propagate away as shown in Figure 3.43. Since the lower layer slope is very wide in case E9, motions in the lower layer are dominated by the topography-trapped waves and we can only observe the lower layer eddy motions in case E10(Fig.3.44).

The motion of the forcing anticyclone during the earlier period is northwestward as advected by the seaward PV deformation over the slope, so in the lower layer and along the slope edge, an anticyclone appears to the northwest of the upper anticyclone's center and a cyclone to its east as shown in the panel of day 10 in Fig.3.44. When a topographic cyclone forms from the slope and enters the flat-bottom region, a lower layer cyclone forms to its north as shown in the panel of day 16 in Fig.3.44. Around day 20, most part of the upper layer anticyclone has left the sloping region, the lower layer eddy structure becomes more complicated as the upper eddies change their translation directions. In the panel of day 24 in Fig.3.44, two dipoles can be recognized in the lower layer

114

Figure 3.43: Case E10. The time evolution of the lower layer relative vorticity contours. Contours have values between $-0.6 \cdot 10^{-5} s^{-1}$ and $0.6 \cdot 10^{-5} s^{-1}$ with intervals of $0.04 \cdot 10^{-5} s^{-1}$. The two dash lines denote the latitudes of the first- and second-layer slope edges.
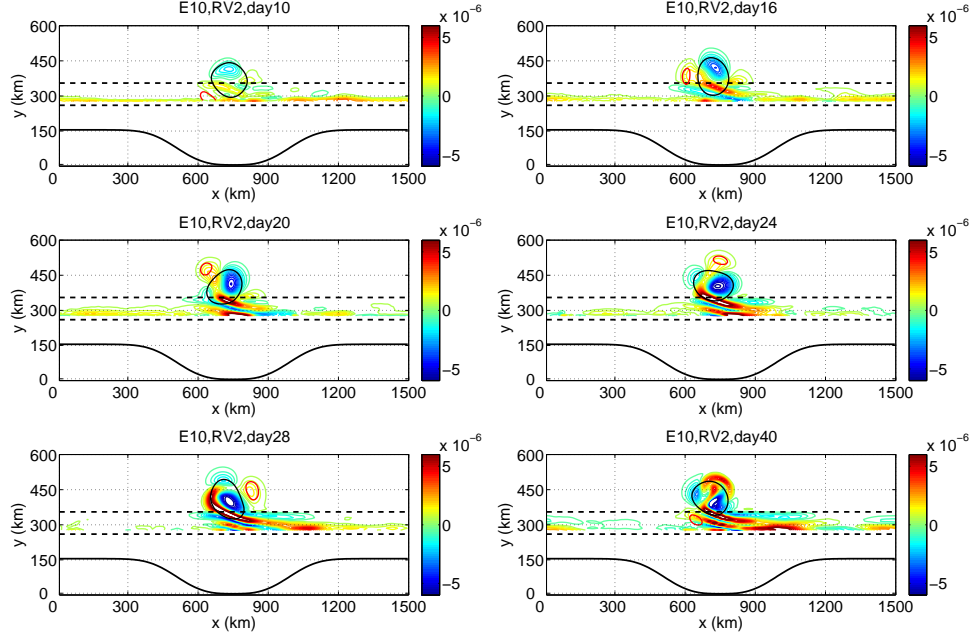

Figure 3.44: Case E10. The time evolution of the lower layer relative vorticity contours. Contours have values between $-0.6 \cdot 10^{-5} s^{-1}$ and $0.6 \cdot 10^{-5} s^{-1}$ with intervals of $0.04 \cdot 10^{-5} s^{-1}$. The two dash lines denote the latitudes of the first- and second-layer slope edges.
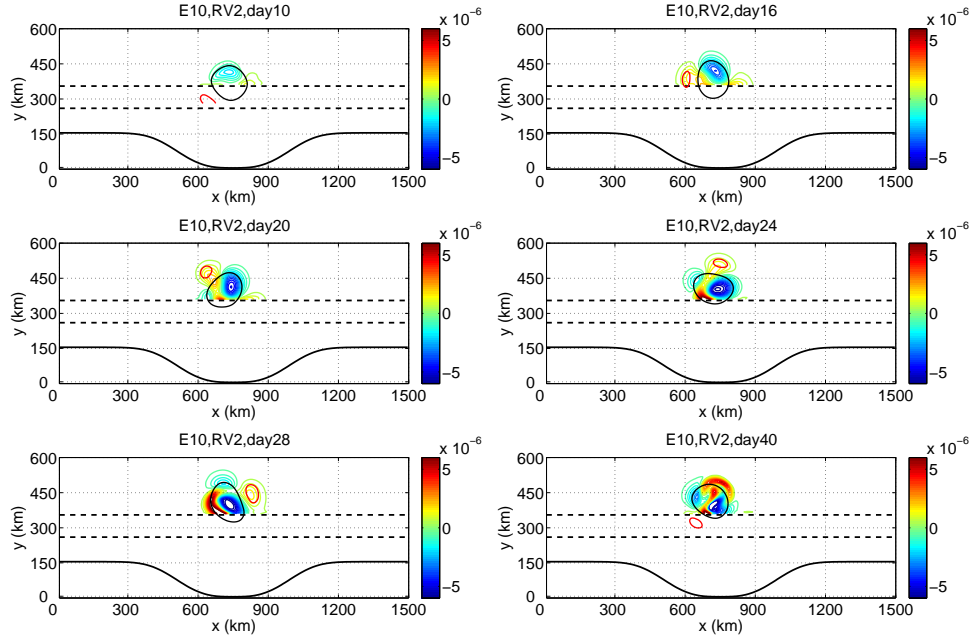
115
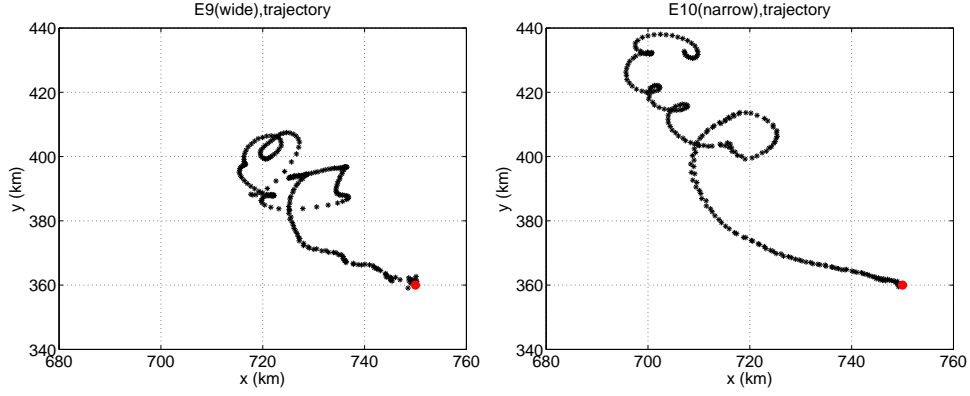
Figure 3.45: Case E9-E10. The trajectory of the anticyclone in case E9(left panel) and E10(right panel) within 60 days. Red dots denote initial locations of anticyclones.

and the upper dipole is entirely over the flat-bottom. This is about the time when the two cases starts to show differences in cross-slope volume transport. According to the generation mechanism of the lower-layer eddies that has been described in the previous paragraph, the maximum second-layer stretching or squeezing from the motion of the upper-layer eddy is less than or equal to the maximum interface displacement associated with the upper-layer eddy, so the relative vorticity of the generated lower-layer anticyclone or cyclone is less than $\frac{\Delta h f}{H_2}$, where Δh is the maximum interface displacement, $f = 1.1 \times 10^{-4} s^{-1}$ is the Coriolis parameter and $H_2 = 3000m$ is the second-layer thickness in the flat-bottomed region. Looking more carefully at Fig.3.44, we find the strength of these lower-layer eddies confirms this estimate.

In summary, motions in the lower layer in the wide-slope case, E9, are mostly topography-trapped waves propagating eastward along isobath, while eddies are induced in the lower layer northward of the slope in the narrow-slope case, E10. Due to this major difference in lower layer motions, we observe quantitative differences, though small, in the upper layer between the two cases. In addition, compared with the anticyclone in the wide-slope case, the anticyclone in the narrow-slope case has stronger net drift both northward and westward as shown in Fig.3.45. In other words, the anticyclone tends to be limited to the slope when the lower-layer slope is wide. This is why the volume transport across the slope edge in the later period is stronger in the wide-slope case as displayed in Fig.3.41.

116

3.4　Conclusions

Interactions between a surface anticyclone and a continental slope/shelf in the presence of a bay are examined in this chapter. Both mechanisms found important for barotropic vortex-escarpment interactions in the previous chapter are also identified in the baroclinic eddy-topography interactions. The baroclinic eddy-slope interactions are found to be similar to the barotropic vortex-escarpment interactions in that a topographic cyclone forms during the interaction between an anticyclone and the slope and pairs away with the anticyclone into the open ocean. However, the anticyclone's advection declines more quickly in the baroclinic case with a decay length scale on the order of the internal deformation radius. Responses over the slope are very weak near the coastline, so the boundary's effect on the evolution of PV contours can hardly be seen. Nevertheless, the boundary's effect can still be found in cross-isobath transport. In spreading cross-isobath transport eastward in propagation direction of topography-trapped waves, wave motions are affected by the eastern side boundary of the bay. As a result, the cross-isobath transport is intensified near the eastern boundary, although in the zonally integrated sense, the cross-isobath transport is smaller in the type 1 domain compared with that in the type 2 domain.

The dependence of the baroclinic eddy-topography interaction on variable parameters including anticyclone's PV anomaly, its size, its initial location, the upper-, and lower-layer slope profiles is also studied in this chapter. For a fixed slope profile, the magnitude of the anticyclone's initial swirl velocity over the slope, which is not only dependent on the anticyclone's PV anomaly and its size but also on its initial location, determines the level of the strength of the topographic cyclone as well as the level of the volume transported across the first-layer slope edge. The time length of the formation process for the topographic cyclone is of secondary importance in influencing the volume transport since after the dipole moves away from the slope, the volume transport quickly slows down. As demonstrated by our results, a large anticyclone tends to stay close to the slope for a longer period of time when it interacts with the topography, therefore, a large anticyclone with big swirl velocity over the slope is most effective in pulling water off the topography.

Both properties of the forcing anticyclone and the newly formed cyclone affect their paring motions after the detachment of the cyclone from the slope. As they rotate around each other, the

circle the anticyclone moves around tends to be larger when the cyclone is stronger. The outer area of a large or a strong anticyclone tends to peel off from the eddy's core as a result of the interaction with the nearby cyclone. In this situation, the remaining, larger, anticyclone tends to have a bigger net drift.

The formation process of the topographic cyclone only depends on the slope profile in the upper layer. When the same anticyclone interacts with slopes that have different upper-layer profiles, stronger topographic cyclones are generated from steep slopes. Flat slopes favor cross-isobath volume transport and induce larger effective range of the anticyclone. The slope profile in the lower layer only affects evolutions of the dipole structure as well as cross-isobath transport after the detachment of the cyclone. With a wider lower-layer slope, the dipole travels shorter distance away from the slope edge, so the cross-isobath transport is greater than that in the narrow-slope case.

All experiments performed in this chapter are assumed to be in the Northern Hemisphere. If we consider the Southern Hemisphere($f < 0$) and the same model domain with the shelf near its southern boundary, we can find similar interaction processes between the anticyclones(whose swirl velocity is anticlockwise) and the topography. Actually, the interaction is exactly the same in the opposite hemisphere if we flip the east and the west.

Chapter 4

Slope/shelf Circulation and Cross-slope/shelf Transport out of a Bay driven by Eddies from a Strong Open Ocean Current

4.1 Introduction

The interaction between topography and a single eddy in the presence of a bay-shaped shelf has been thoroughly examined in a one-layer contour dynamics model and a two-layer isopycnal model. The two basic mechanisms, eddy advection and wave propagation, and their dependence on the bay's boundary were discussed and compared between the two models. In this chapter, the eddy-topography interaction is studied in the presence of an ACC-like turbulent flow which can spontaneously generate eddies or meanders to force the slope and the bay-shaped shelf. The goal of this chapter is to understand the slope/shelf circulation and the cross-slope/shelf transport under the persistent yet episodic forcing from the strong open ocean current through the mechanism of eddy-topography interaction.

In the world's oceans, ACC is the only current that flows around the globe without continental barriers. It serves as a conduit of all oceanic tracers between different ocean basins. Some tracers such as heat and salt can influence the ocean stratification and circulation, so the ACC is important

for the global heat budget and Earth's climate. Due to the absence of the meridional boundaries at the latitudes of Drake Passage, the eastward momentum imparted by the wind stress can not be balanced by the pressure force as usually seen in other ocean basins. The momentum balance of the ACC was therefore considered a mystery for a long time. The most generally accepted theory was put forward by Munk and Palmen (1951), in which the eastward momentum is transferred downward to the depth and balanced by the bottom form drag, a force associated with the pressure difference between the upstream and downstream sides of submarine ridges or sea mounts. Aside from the wind forcing and the bottom form drag, the diabatic forcing, such as the atmospheric heating and cooling at the surface and the diapycnal fluxes in interior, is important for the ACC dynamics as it helps maintain the density contrast across the current which is vital for the vertical shears of velocity through the thermal wind relation, and hence influences the transport in the current. Although the diabatic processes are important, the turbulent feature of the ACC, which is thought most relevant to driving the slope/shelf circulation and cross-slope/shelf transport, can still be plausibly represented in models where the diabatic processes are absent such as quasi-geostrophic (QG) models of adiabatic wind-driven channel flow (McWilliams et al., 1978; Treguier and McWilliams, 1990; Wolff et al., 1991; Treguier and Panetta, 1994; Sinha and Richards, 1999).

Using a two-layer eddy-resolving QG model, McWilliams et al. (1978) studied the wind-driven adiabatic flow in a zonally periodic channel extending $1000km$ in the meridional direction with the model deformation radius about $36km$. The wind stress is constant in the zonal direction and varies as a *sine* function with its maximum at the central latitude. The bottom is either flat or is occupied by a Gaussian-shaped mountain submerged in the lower layer in the center of the channel. Their model results illustrated that the eastward momentum input in the first layer is transferred downward by the eddy interfacial form drag which serves as a driving force for the second layer and is balanced by the form drag over the seamount and the bottom friction over the flat bottom. In the upper layer, the horizontal Reynolds' stress divergence works to accelerate the flow in the center of the jet while decelerate it in both flanks. Baroclinic instability is found responsible for the growth of eddies that transfer mean potential energy to eddy energy and then supply kinetic energy to the mean that is dissipated by the bottom friction. In the flat-bottomed case, the mean jets in both layers have their maxima at the central latitude and are symmetric about that latitude. The surface wind

stress is completely balanced by the bottom friction resulting in a transport greatly exceeding the observed value. With an isolated seamount in the lower layer, the model zonal transport becomes much smaller than in the flat-bottomed case.

Subsequently, also using the two-layer QG models and the channel geometry, Wolff et al., (1991) and Treguier and McWilliams (1990) examined the wind-driven turbulent flow over different topographies. Their model results demonstrated similar dynamical balance consisting of the wind stress, the interfacial form drag, and the bottom form drag to that of McWilliams et al. (1978). Wolff et al. (1991) studied the response of the system to different values of bottom friction and different locations of the topographic obstacles which are either isolated mountains or meridionally orientated ridges. They found that the resulting flow magnitude as well as the zonal transport depends heavily on the location and the shape of the topography. Treguier and McWilliams (1990) studied the influence of isolated mountains and ridges with different horizontal as well as vertical scales. They found that the bottom form drag provided by the topography increases with its length scale and its height, and the topographies with length scales comparable with the forcing scale make the largest contribution in balancing the wind.

Using QG models with the channel geometry, Treguier and Panetta (1994) and Sinha and Richards (1999) examined the multi-jet feature of the ACC. Treguier and Panetta (1994) studied the jet structure with variable wind profiles in a channel with the meridional extent of $2000km$, 100 times of the model deformation radius. Their model results showed that more than one jet can appear and persist in the quasi-steady state when the meridional scale of the wind stress is large enough. When the wind stress has little meridional variation in the center of the channel, two jets are present, but they can merge into one when the wind profile approaches the $sine$-shape profile. Sinha and Richards (1999) studied the influence of changing the topographic β_t on the number and spacing of the jets by changing the flat bottom into a linear slope and varying its steepness. Their model results showed that the number of jets increases with the positive topographic β_t.

The model used in the present chapter is still the Hallberg Isopycnal Model (HIM), which, since its development, has been used in studies of a number of different ocean circulation problems and Geophysical Fluid Dynamics problems. For example, it was used to examine the buoyancy-

121

driven circulation within a closed basin with sloping bottom intersecting the interface (Hallberg and Rhines, 1996), the response of the North Pacific Ocean to decadal variability in atmospheric forcing (Thompson and Ladd, 2004), and the internal wave generation in a global domain (Simmons et al., 2004). The model has also been used to study dynamics of the ACC. Hallberg and Gnanadesikan (2001) studied the effects of transient eddies on the transport of a wind- and buoyancy-driven current using a two-layer HIM with a zonally reentrant channel. More recently, they examined the role of eddies in the overturning circulation of the Southern Ocean using the hemispheric HIM with realistic geometry and resolution as high as 1/6 degree (Hallberg and Gnanadesikan, 2006). The model allows the intersection between the topography and the layer interface which is an important feature of the eddy interaction with a , so it is adequate for the present study. Furthermore, the wide and successful application of HIM makes it sensible to use the model in this chapter.

In HIM, the ACC is simulated as a wind-driven adiabatic flow in a two-layer zonally reentrant channel on a β plane as in the aforementioned QG models. Three cases are examined in this chapter. The model domain of the first two experiments is simply a zonal channel. The channel in the first case, case FB, is flat bottomed and the model set-up is almost the same as that in the flat-bottomed case of McWilliams et al. (1978). This case is aimed at understanding the dynamical balance of the wind-driven channel flow in the primitive equation (PE) channel model and learning about differences between the PE model and the QG model. On the basis of that, a zonally uniform slope is constructed in the second layer next to the southern boundary in the second experiment, case SB (Fig.4.1). The effects of this topography on the turbulent flow are studied by comparing with the flat-bottomed case. A striking feature of the results is the formation of a potential vorticity (PV) front a little bit shoreward of the sloping bottom in the first layer. To distinguish this PV front from the PV gradient maximum at the jet axis, we call this new front the second PV front. Although less prominent, the mean zonal flow in the upper layer also has a second local maximum around the same location. The generation of this second jet is related to the local dynamics near the bottom slope and is different from the zonation addressed by Treguier and Panetta (1994) and Sinha and Richards (1999). In the third case, case BAY1, the model domain is modified to have a channel where the wind stress with the same *sine* function profile is applied to the ocean and a bay with constant depth in the south (Fig.4.2). The bottom slope is extended into the upper layer and is connected with the

shelf that is enclosed by the curved southern boundary. By the same formation mechanism of the second jet found in the second case, a second PV front appears in the first layer near the base of the bottom slope. It continuously interacts with both the jet in the center of the channel as well as the slope/shelf region. Three questions are to be answered in this case: what is the circulation on the slope and within the bay that is due to the presence of the strong current as well as the topography; how the water over the slope or within the bay is exchanged during the process; what are the effects of the bay's boundary on the shelf circulation and cross-shelf exchange.

It should be noted that a topographic obstacle producing zonal depth variations is indispensable for the bottom form drag which can balance the eastward wind stress and at the same time help restrain the volume transport becoming too large. In the three cases to be examined, the bottom is either flat or has a zonally uniform slope, so the wind stress is completely balanced by the bottom friction which, with a reasonable friction parameter, results in an exceedingly large volume transport.

4.2 Model Set-up

The model equations are the same as those in Chapter 3 except that an extra term $\dfrac{\tau}{\rho h_1}$ appears on the right hand side of the first layer momentum equation representing the wind stress applied to the first layer as a body force:

$$\frac{\partial \mathbf{u}_1}{\partial t} + q_1 \mathbf{k} \times (h_1 \mathbf{u}_1) = -\nabla B_1 - \frac{A}{h_1} \left\{ \nabla \cdot h_1 \nabla (\nabla^2 \mathbf{u}_1) \right\} + \frac{\tau}{\rho h_1}, \tag{4.1}$$

$$\frac{\partial \mathbf{u}_2}{\partial t} + q_2 \mathbf{k} \times (h_2 \mathbf{u}_2) = -\nabla B_2 - \frac{A}{h_2} \left\{ \nabla \cdot h_2 \nabla (\nabla^2 \mathbf{u}_2) \right\} - \frac{C_{drag}}{h_2} |\mathbf{u_2}| \mathbf{u_2}. \tag{4.2}$$

In addition, the model ocean is on a β plane in the Southern Hemisphere with $f < 0$. The cross-interface mass flux is inhibited, so only the adiabatic dynamics of the ACC is simulated in the model.

$$\frac{\partial h_i}{\partial t} + \nabla \cdot h_i \mathbf{u}_i = 0 \tag{4.3}$$
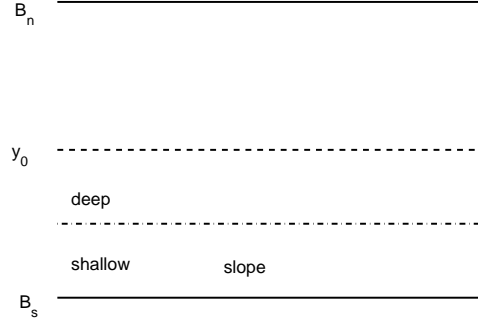
123

Figure 4.1: A schematic view of the domain in case FB and case SB. Solid lines denote solid walls within the domain. The dash line indicates the latitude of the maximum wind stress as denoted by y_0. The dash-dot line indicates the boundary between the sloping and the flat-bottomed regions. The northern boundary of the domain is denoted as B_n, the southern boundary is denoted as B_s.

The model domain is zonally reentrant, extending from $x = 0$ to $x = 2000km$. Meridionally, the domain is bounded in the north by a zonal wall, B_n, at $y = 1200km$. In the flat-bottomed case FB and the slope-bottomed case SB, the domain's southern boundary, B_s is zonal, aligned with $y = 0$ (Fig.4.1). In both cases, the resting layer interface is at the depth of $1000m$ and the total depth is $4000m$. In case SB, a zonally uniform slope occupies the region between $y = 0$ and $y = 200km$ across which the water depth increases linearly from $2000m$ to $4000m$. In case BAY1, the domain's northern boundary is also at $y = 1200km$, but its southern boundary is curved (Fig.4.2). Begin with 0 at $x = 1000km$, its y location smoothly approaches $155km$ east- and westward and remains constant afterwards. The bay area that is enclosed by the southern boundary and the latitude of $y = 155km$ is about $800km$ long and has the constant depth about $500m$, connected with a zonally-orientated slope extending meridionally from $y = 155km$ to about $y = 400km$. The total water depth is the same as in the first two cases, but the first layer is initially $1200m$ deep.

The current in all cases is driven by a steady, zonally invariant, eastward wind, which changes meridionally as a *sine* function within the channel in the first two cases and out of the bay in case BAY1:

$$\tau = \begin{cases} \tau_0 sin\left(\dfrac{\pi(y - Y_s)}{L_c}\right) & \text{if } y >= Y_s \\ 0 & \text{otherwise,} \end{cases}$$

where Y_s is the meridional location of the southern boundary of the channel which is zero in case FB and case SB, and $155km$ in case BAY1. L_c is the meridional range of the wind forcing which is
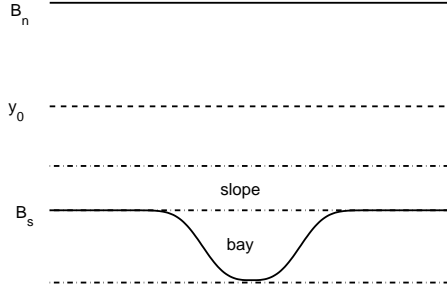
124

Figure 4.2: A schematic view of the domain for case BAY1. Solid lines denote the solid wall within the domain. The dash line indicates the latitude of the maximum wind stress, y_0. From south to north, there are three dash-dot lines. The first one is the latitude at $y = 0$, the second one indicates the northern edge of the bay or the southern boundary of the channel, and the third one represents the northern edge of the topography.

$1200km$ in the first two cases and $1045km$ in case BAY1. The maximum wind stress amplitude, τ_0 is at the central latitude of the channel as indicated by the dash lines in Fig.4.1 and Fig.4.2 and set to be $0.15kgm^{-1}s^{-2}$ in case FB and case SB and $0.12kgm^{-1}s^{-2}$ in case BAY1.

The sinusoidal shape of the wind stress has been commonly used in the previous studies of the QG channel flows (McWilliams et al. 1978; Wolff et al., 1991; Olbers et al. 2000) and our winds' magnitudes are also comparable with their values, thus comparisons between our model and previous studies are possible.

The absence of the wind stress within the bay enables us to study the bay circulation that is driven exclusively by the open ocean current, although winds may be very important for the circulation in the Marguerite Bay and west Antarctic Peninsula (WAP) shelf region.

The reduced gravity $g' = g\Delta\rho/\rho$ is $0.02ms^{-2}$ resulting in a baroclinic Rossby radius of $R_1 = g'H_1H_2/(H_1 + H_2)^{1/2}f_0^{-1}$ of about $35km$, similar to those in the studies of McWilliams et al. (1978) and Wolff et al. (1991). The model resolution is uniformly $10km$, higher than the previous QG models. It needs to be noticed that due to the computation limits, our model deformation radius is larger than the observed value in Marguerite Bay and West Antarctic Peninsula shelf region ($10\sim15km$ in austral summer and fall). As a result, important length scales from our model results that are related to the deformation radius, such as the characteristic length scale of the variability associated with the second PV front offshore, would be smaller in the actual system.

The coefficient of biharmonic horizontal viscosity A is specified as $1.5 \cdot 10^9 m^4 s^{-1}$ and the bottom drag coefficient C_{drag} is 0.0011. The spin-down time by the bottom friction is about 110 days, and it takes about 30 years for motions on the scale of the deformation radius to be dissipated by the horizontal friction. The free-slip boundary condition is applied on both walls preventing the momentum flux through the boundary out of the domain. The time-step Δt is chosen to be $400s$. We have performed experiments with smaller Δt or bigger A values and have not found qualitative differences in results.

4.3 Model Spin-up

All experiments are started from rest and the integration in each experiment reveals three distinct phases as demonstrated by the time series of layer integrated energies in case FB (Fig.4.3). Features of each phase are very similar to those of the wind-driven channel flow in the QG models which were described in detail by Wolff et al. (1991). In the first phase, a zonal flow appears and strengthens in both layers without any meridional variations. The layer interface is continuously raised up in the south and pressed down in the north. Its time tendency supplies eastward momentum to the second layer. When the bottom friction which increases with the velocity amplitude balances the time tendency of the interface displacement, the lower layer flow stops accelerating and its kinetic energy remains constant afterwards as shown in Fig 4.3 while meantime, both the available potential energy and the first layer kinetic energy keep growing linearly with time. By linearizing the governing equations for a two-layer adiabatic wind-driven flow, Wolff (1991) solved the analytic solution for this linear-growth stage, in which the constant value of the lower layer zonal velocity during the later period was $\dfrac{\tau_0}{\epsilon H_2}$ where τ_0 was the wind's maximum amplitude, ϵ was the linear bottom drag parameter and H_2 was the second layer resting thickness. This relation basically states that during this linear-growth period, the second layer flow becomes steady when the bottom friction balances the wind stress. Using this relation, we can estimate the value for our model and the difference between the estimated value and the model results is less than 10% of the value itself. Given the fact that our model uses the quadratic bottom drag law while Wolff adopted the linear drag law, the difference between his solution and our model is really small, which means the model is reliable at
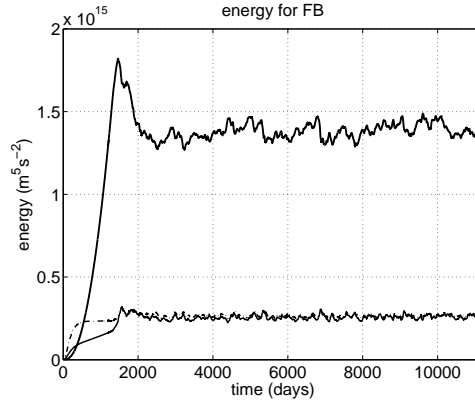
Figure 4.3: Case FB. Time series of layer integrated kinetic energy in the upper layer (solid line) and the second layer(dash-dot line) and the potential energy for the interface (thick solid line). Units are $m^5 s^{-2}$.

least within this growth period. After the flow becomes baroclinically unstable, a small perturbation that breaks the zonal symmetry will lead to the development of energetic eddies and also a transient stage to the quasi-steady state which takes about 3000 days. The quasi-steady state is roughly identified as the state where there are no apparent trends in the total layer energies.

All our analysis uses model results from the final phase, the quasi-steady state. The time averaged quantities are usually values averaged over a period of 4000 days, which requires the entire integration to be longer than 10000 days.
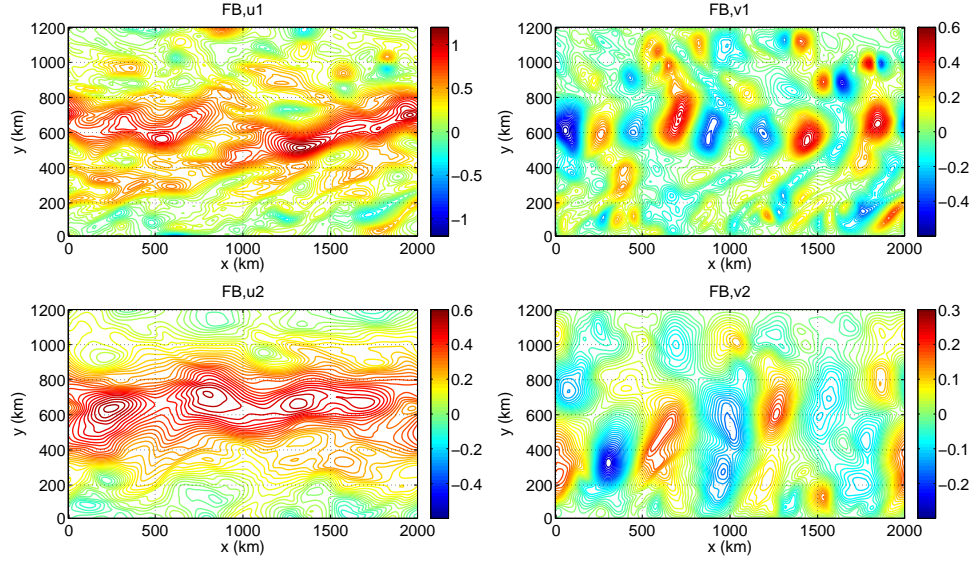
Figure 4.4: Case FB. Contours of zonal and meridional velocity in the first layer (upper panels) and in the lower layer(lower panels). The contour interval is $0.04ms^{-1}$ for the first-layer zonal velocity, $0.02ms^{-1}$ for the second-layer zonal velocity and the first-layer meridional velocity, and $0.01ms^{-1}$ for the second-layer meridional velocity.

4.4 Results and Discussions

4.4.1 Case FB

In the simplest case, case FB, the model domain is a zonally periodic, flat-bottomed channel. The zonal wind stress varies only in the meridional direction as a *sine* function with the maximum amplitude at the central latitude of $y = 600km$. The total water depth is $4000m$ and the interface is initially at $z = -1000m$. Although simple, case FB is fundamental to understanding the dynamics of the wind-driven channel flows. It also offers an opportunity to examine the possible differences between our PE model and the QG models. In the following discussions, we will first present a qualitative description of the turbulent flow, both instantaneous and with time and zonal averages, and then examine the dynamical balance of the system by analyzing the time and zonally averaged momentum budget.
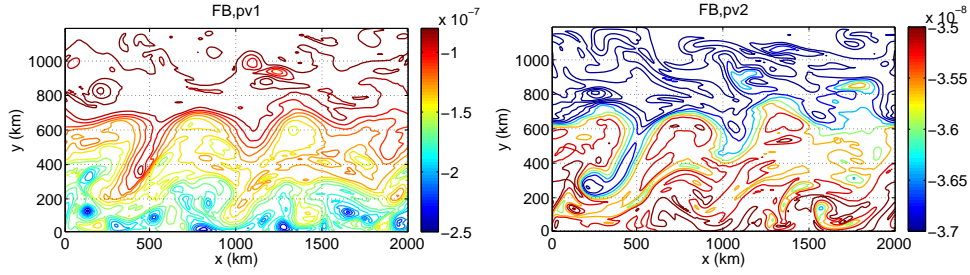
Figure 4.5: Case FB. PV contours in the upper layer (left panel) and lower layer (right panel) with contour intervals of $0.1 \cdot 10^{-7} m^{-1} s^{-1}$ and $0.04 \cdot 10^{-8} m^{-1} s^{-1}$ respectively.

Flow Description

Instantaneous patterns of the zonal and meridional velocity as well as PV during the quasi-steady state (Fig.4.4 and Fig.4.5) clearly show a zonal jet in the channel characterized by meanders and eddies. The meridional scale of meanders is as large as $400km$. The eddies have length scales roughly about the deformation radius. Compared with the jet in the first layer, the lower-layer jet is weaker and slightly broader.

This feature is also displayed by the plot of time and zonally averaged zonal velocity against y as in Fig.4.6. In addition, there are two features in the plot that make the results distinguishable from those in the QG models. First, the maximum amplitude of the zonal flow is not at but to the north of the latitude of the strongest wind stress. Second, a "plateau" appears on the first-layer velocity profile between $y = 250km$ and $y = 450km$ indicating a region of very low meridional shear, but to the north of the jet center, the zonal velocity varies smoothly. Compared with the profile in the first layer, the zonal flow in the lower layer is more symmetric about the jet axis.

Shown in Fig.4.7 is the mean eddy kinetic energy profiles, in which the weakening of the jet from the first layer to the lower layer is even more prominent than the zonal velocity profiles display. In terms of the amplitude, the modeled eddy kinetic energies are roughly on the same order as observations, but greater. Using direct current measurements, Phillips and Rintoul (2000) found the upper layer eddy kinetic energy level to be around $400cm^2 s^{-2}$ in the energetic Subantarctic Front south of Australia, similar to those observed in Drake Passage and southeast of New Zealand, but is far less than the values in the jet in our model. Our model results of zonal velocities and eddy
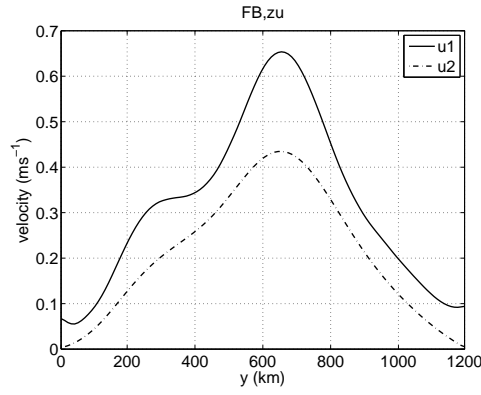
Figure 4.6: Case FB. The time and zonally averaged zonal velocity in the first layer(solid line) and second layer(dash-dot line) in units of ms^{-1}.
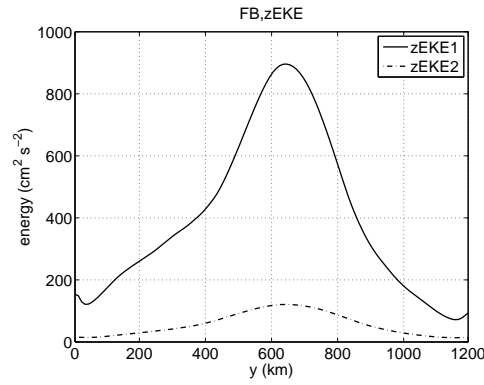

Figure 4.7: Case FB. The time and zonally averaged eddy kinetic energy $\frac{1}{2}\overline{u_i'^2 + v_i'^2}$ in the upper layer (solid line) and the lower layer (dash-dot line) in units of $cm^2 s^{-2}$.
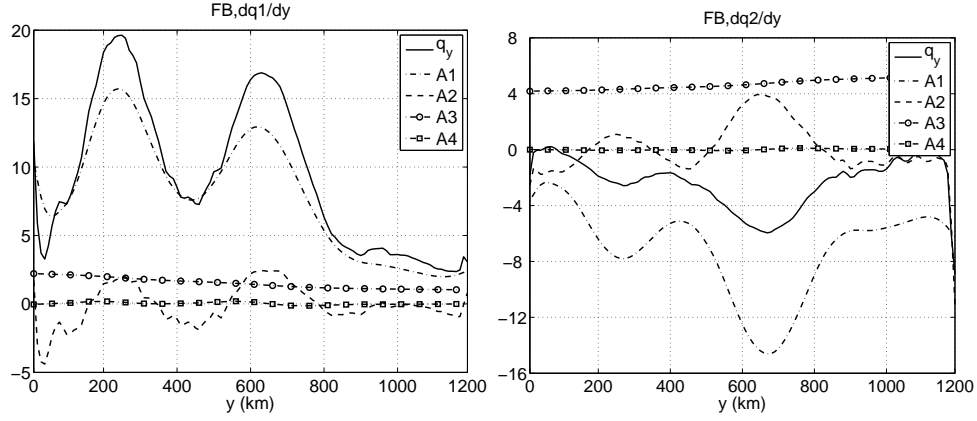
Figure 4.8: Case FB. Time and zonally averaged meridional gradient of PV and its four components. Solid line: $q_y = \dfrac{\partial q_i}{\partial y}$, dash-dot line: $A_1 = -\dfrac{f}{h_i^2}\dfrac{\partial h_i}{\partial y}$; dash line: $A_2 = \dfrac{1}{h_i}\dfrac{\partial \zeta_i}{\partial y}$; dash-dot-circle line: $A_3 = \dfrac{\beta}{h_i}$; dash-dot-square line: $A_4 = -\dfrac{\zeta_i}{h_i^2}\dfrac{\partial h_i}{\partial y}$. The left panel is for the upper layer ($i = 1$), the unite is $10^{-14}m^{-1}s^{-1}$; the right panel is for the lower layer($i = 2$), the unit is $10^{-15}m^{-1}s^{-1}$.

energies are very similar, both qualitatively and quantitatively, to those of the flat-bottomed experiment examined by McWilliams et al. (1978). The eddy energy levels and the volume transport in their study were greatly reduced from the flat-bottomed case to the case with an isolated topography over the bottom in which the wind stress input can be largely balanced by the bottom form drag. Therefore, it is thought that the absence of the bottom form drag is one possible reason for the large volume transport and the high eddy kinetic energies in both our model and the QG models, although factors that are ignored in both models, such as the thermodynamics of the system, may also be critical. Therefore, the effect of eddies on the slope/shelf circulation and the cross-slope/shelf transport would probably be overestimated in the model.

The time and zonally averaged meridional PV gradients have differing signs in the two layers as shown in Fig.4.8, so the necessary condition for baroclinic instability is satisfied, we expect the flow to be baroclinically unstable and this presumption is verified through analysis of the Reynolds' stress divergence.

We decompose the PV gradient into four parts $\dfrac{\partial q_i}{\partial y} = -\dfrac{f}{h_i^2}\dfrac{\partial h_i}{\partial y} + \dfrac{1}{h_i}\dfrac{\partial \zeta_i}{\partial y} + \dfrac{\beta}{h_i} - \dfrac{\zeta_i}{h_i^2}\dfrac{\partial h_i}{\partial y} =$ $A1+A2+A3+A4$ representing contributions from the stretching, the relative vorticity, the planetary vorticity and the stretching in the presence of the relative vorticity. In both layers, the stretching part,

131

A1, has the biggest amplitude. Its ratio to the relative vorticity part, A2, according to the geostrophic relation, is $\dfrac{L^2}{R^2}$, where L is the length scale of the motion and R is the deformation radius. For large scale motions, this ratio should be much greater than one, generally consistent with our model results.

Similar to the mean zonal velocity, the PV gradient in Fig.4.8 also shows meridional asymmetries especially in the first layer. Besides the one at the jet axis, there is a second PV maximum around the same region of the velocity "plateau" in Fig.4.6 and its magnitude is even a little bigger than the central one.

Zonal Momentum Balance

One way to understand the dynamics of the wind-driven channel flow is through its zonal momentum budget. The zonally averaged equations for the zonal momentum and mass are as follows:

$$\frac{\partial}{\partial t}\overline{u_i} + \overline{q_i \cdot v_i h_i} = \overline{D_i} + \overline{F_i} \tag{4.4}$$

$$\frac{\partial}{\partial t}\overline{h_i} + \frac{\partial}{\partial y}\overline{h_i v_i} = 0, \tag{4.5}$$

where the zonal mean variables are denoted by overbars. D_i represents the lateral friction, F_1 represents the surface stress $\dfrac{\tau}{\rho \overline{h_1}}$ and F_2 represents the bottom drag $-\dfrac{C_{drag}}{h_2}|u_2|u_2$. The effect of eddies on the large-scale motions appears in both the momentum equation as $q_i'(v_i h_i)'$ and the mass equation as $v_i' h_i'$, where eddy perturbations are denoted as primes. To have a clearer picture of the eddy effects on the large-scale mean flow, we transform the above equations in a similar way to the transformed Eulerian mean approach (Andrews and McIntyre 1976, 1978).

Defining the volume averaged thickness of layer i as H_i, we can write the mass conservation equation in a simpler form:

$$\frac{\partial h_i}{\partial t} + H_i \nabla \cdot \mathbf{u}_i^\dagger = 0, \tag{4.6}$$

where $\mathbf{u}_i^{\dagger}$ is the "residual circulation" and its relation with the actual mass flux is:

$$\frac{\mathbf{u}_i h_i}{H_i} = -\nabla \times (\psi_i \hat{\mathbf{k}}) + \mathbf{u}_i^{\dagger} = \hat{\mathbf{k}} \times \nabla \psi_i + \mathbf{u}_i^{\dagger}. \tag{4.7}$$

We split the PV into a part corresponding to the constant thickness H_i and a part representing the departure from it, then the momentum equation without external forcing terms are:

$$\frac{\partial \mathbf{u}_i}{\partial t} + f_0 \hat{\mathbf{k}} \times \frac{h_i}{H_i} \mathbf{u}_i + Q_i \hat{\mathbf{k}} \times \frac{h_i}{H_i} \mathbf{u}_i = -\nabla B_i, \tag{4.8}$$

where $Q_i = H_i(\frac{\zeta_i + f}{h_i} - \frac{f_0}{H_i})$ and the transformed Bernoulli function $B_i^{\dagger} = \phi_i + \frac{1}{2}|\mathbf{u}_i|^2 - f_0 \psi_i$. Applying the zonal mean operator to the transformed zonal momentum equation yields:

$$\frac{\partial}{\partial t}\overline{u_i} + f_0\overline{v_i^{\dagger}} = \frac{1}{H_i}\overline{Q_i v_i h_i} + \overline{D_i} + \overline{F_i}, and \tag{4.9}$$

$$\frac{\partial}{\partial t}\overline{h_i} + H_i\frac{\partial}{\partial y}\overline{v_i^{\dagger}} = 0. \tag{4.10}$$

Within these equations $v_i^{\dagger}$ depends only on the time tendency of the zonal mean layer thickness and boundary conditions. If the flow is statistically steady, both $\frac{\partial}{\partial t}$ terms can be dropped in Eq.4.9 and 4.10. The meridional mass flux has to vanish at the zonal boundaries of the channel, so from Eq.4.10 we know that it vanishes everywhere and $\overline{v_i^{\dagger}} = \frac{1}{H_i}(\overline{v_i}\overline{h_i} + \overline{v_i' h_i'}) = 0$. Therefore, both terms on the left hand side of Eq.4.9 are negligible and the zonal momentum is expected to be balanced among the newly defined PV flux $\frac{1}{H_i}\overline{Q_i v_i h_i}$, the forcing F_i and the lateral friction D_i.

This expectation is confirmed by Fig.4.9 except that the lateral friction term is found much smaller than the other two terms in both layers, so the momentum is primarily balanced between the PV flux and the forcing F_i. The dynamics of the flow can be summarized as follows. In the upper layer, the zonal wind stress provides a source of eastward momentum balanced by the meridional PV flux; in the lower layer, the PV flux yields eastward momentum dissipated by the bottom drag. The PV flux has opposite signs in the two layers just contrary to those of the meridional gradient of the mean PV. The PV flux is therefore down the PV gradient in the system.

To have a better understanding of the momentum balance, we can also examine the dynamics of
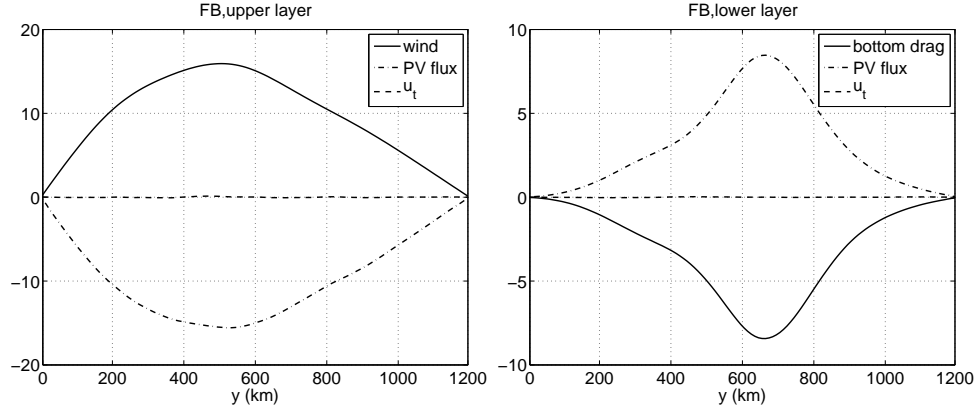
133

Figure 4.9: Case FB. Terms in time and zonally averaged zonal momentum equations. Left panel is for the upper layer and right panel is for the lower panel. The unit is $10^{-8}ms^{-2}$

the depth-integrated momentum $u_i h_i$. Integrating the zonal momentum and the mass equations for the first layer vertically and adding them together lead to:

$$\frac{\partial}{\partial t}h_1 u_1 - f v_1 h_1 + \frac{\partial}{\partial x}u_1 \cdot (h_1 u_1) + \frac{\partial}{\partial y}v_1 \cdot (h_1 u_1) = -h_1 \frac{\partial p_1}{\partial x} + D_1 h_1 + F_1 h_1. \tag{4.11}$$

Taking the zonal average of the above equation gives:

$$\frac{\partial}{\partial t}\overline{h_1 u_1} - f\overline{v_1 h_1} + \frac{\partial}{\partial y}\overline{v_1 \cdot (h_1 u_1)} = -\overline{h_1 \frac{\partial p_1}{\partial x}} + \overline{D_1 h_1} + \overline{F_1 h_1}. \tag{4.12}$$

Similarly, the momentum equation for the second layer is

$$\frac{\partial}{\partial t}\overline{h_2 u_2} - f\overline{v_2 h_2} + \frac{\partial}{\partial y}\overline{v_2 \cdot (h_2 u_2)} = -\overline{h_2 \frac{\partial p_2}{\partial x}} + \overline{D_2 h_2} - \overline{F_2 h_2}. \tag{4.13}$$

For the quasi-steady state, the first two terms in Eq.4.12 and 4.13 vanish and the term of the lateral friction $D_i h_i$ can be neglected according to our previous results, therefore the depth-integrated zonal momentum is balanced among the momentum flux divergence term $\frac{\partial}{\partial y}\overline{v_i \cdot (h_i u_i)}$, the pressure term $-\overline{h_i \frac{\partial p_i}{\partial x}}$ and the forcing $F_i h_i$ which represents the wind stress in the first layer and the bottom drag in the lower layer:

$$0 = -\frac{\partial}{\partial y}\overline{v_1 \cdot (h_1 u_1)} - \overline{h_1 \frac{\partial p_1}{\partial x}} + \overline{F_1 h_1}. \tag{4.14}$$

134

$$0 = -\frac{\partial}{\partial y}\overline{v_2 \cdot (h_2 u_2)} - \overline{h_2 \frac{\partial p_2}{\partial x}} + \overline{F_2 h_2}. \tag{4.15}$$

Since there is no meridional flux of momentum through zonal boundaries, the meridional integration of the term $\frac{\partial}{\partial y}\overline{v_i \cdot (h_i u_i)}$ across the channel is zero, which means the momentum flux divergence works to distribute the momentum horizontally within the layer but has no influence on the total momentum of the whole layer. The pressure term on the other hand represents the transfer of momentum from one layer to the other. To see this, we use the hydrostatic relation to write the pressure force in terms of positions of the surface $\eta_0(x, y)$ and the interface $\eta_1(x, y)$ (Vallis, 2006):

$$\frac{\partial p_1}{\partial x} = g\frac{\partial \eta_0}{\partial x}, and \tag{4.16}$$

$$\frac{\partial p_2}{\partial x} = g\frac{\partial \eta_0}{\partial x} + g'\frac{\partial \eta_1}{\partial x}. \tag{4.17}$$

The first layer reaches from the surface at $z = \eta_0$ to the interface at $z = \eta_1$ and the lower layer extends from η_1 to the bottom at $z = -H = constant$, so the pressure terms in Eqs.4.14 and 4.15 are

$$-\overline{h_1 \frac{\partial p_1}{\partial x}} = -\overline{g(\eta_0 - \eta_1)\frac{\partial \eta_0}{\partial x}} = \overline{g\eta_1 \frac{\partial \eta_0}{\partial x}}, and \tag{4.18}$$

$$-\overline{h_2 \frac{\partial p_2}{\partial x}} = -\overline{(\eta_1 + H)\frac{\partial(g\eta_0 + g'\eta_1)}{\partial x}} = -\overline{g\eta_1 \frac{\partial \eta_0}{\partial x}}, \tag{4.19}$$

which are equal and opposite to each other suggesting that the layers exert a pressure force on each other. This force is called the form drag, a force existing only when the layer boundaries vary with positions. Integrating Eqs.4.14 and 4.15 meridionally and adding them together, we obtain the momentum balance for the whole ocean: the momentum is transferred into the ocean by the wind stress and extracted out of the lower layer by the bottom form drag when the bottom varies in x.

We further decompose the PV flux into three terms $Q_i\frac{v_i h_i}{H_i} = fv_i + \zeta_i v_i - \frac{f_0}{H_i}v_i h_i$, which are advection of the planetary vorticity, advection of the relative vorticity and a term related to the meridional mass flux.

In the quasi-geostrophic regime, variations of layer thickness are small compared with the layer thickness itself. If motions' length scales are much smaller than the external deformation radius, the mass conservation equation can be simplified as $\nabla \cdot \mathbf{u}_i = 0$. Using this relation, the meridional

advection of the relative vorticity can be written as

$$v_i \zeta_i = -\frac{\partial}{\partial y}(u_i v_i) + \frac{1}{2}\frac{\partial(v_i^2 - u_i^2)}{\partial x},\tag{4.20}$$

and is thus related to the momentum flux. Taking the zonal average of this equation and noting that $\overline{v_i}$, the ageostrophic velocity component, is on the order of Rossby number, same as $\overline{\zeta_i}$, we obtain the relation

$$\overline{v_i' \zeta_i'} = -\frac{\partial}{\partial y}\overline{u_i' v_i'},\tag{4.21}$$

the right hand side of which is the horizontal Reynolds' stress divergence. In the remainder of the thesis, we will use this name to refer to the advection of the relative vorticity.

Decomposing variables in Q into the zonal mean and perturbations leads to $\overline{Q_i\frac{v_i h_i}{H_i}} = \overline{\zeta_i' v_i'} - \frac{f_0}{H_i}\overline{v_i' h_i'} + (f\bar{v}_i - \frac{f_0}{H_i}\bar{v}_i\bar{h}_i) + \bar{\zeta}_i\bar{v}_i = B1 + B2 + B3 + B4$. Terms $B1$ and $B4$ are horizontal Reynolds' stress divergence from the eddies and the mean flow. Though seemingly different from the definition of the form drag in Eqs.4.18 and 4.19, the term B_2 also represents the transfer of momentum between the layers. In addition, in the quasi-geostrophic regime, v_i' is the geostrophic component of the velocity. Using the geostrophic relation $v_i' = \frac{1}{f_0}\frac{\partial \eta_0}{\partial x}$, we can easily show that $\overline{v_i' h_i'}$ is proportional to the form drag, and so it is called the interfacial form drag through the chapter.

As shown in Fig.4.10, during the quasi-steady state, in both layers, term $B4$ is negligible compared with $B1$. In the upper layer, the horizontal Reynolds' stress divergence and the interfacial form drag have similar amplitudes. The former redistributes the horizontal momentum obtained from the wind stress by concentrating the jet in middle latitude and decelerating the flow in the jet flanks. This is the evidence that the current is baroclinically unstable, releasing the available potential energy into the eddy field which in turn feeds kinetic energy into the jet. The interfacial form drag is negative at every latitude transferring eastward momentum downward to the lower layer. In the lower layer, the horizontal Reynolds' stress divergence has similar meridional structure as that in the upper layer but is much smaller than the interfacial form drag which adds eastward momentum to the layer. These results are very similar to those obtained from the QG models (McWilliams
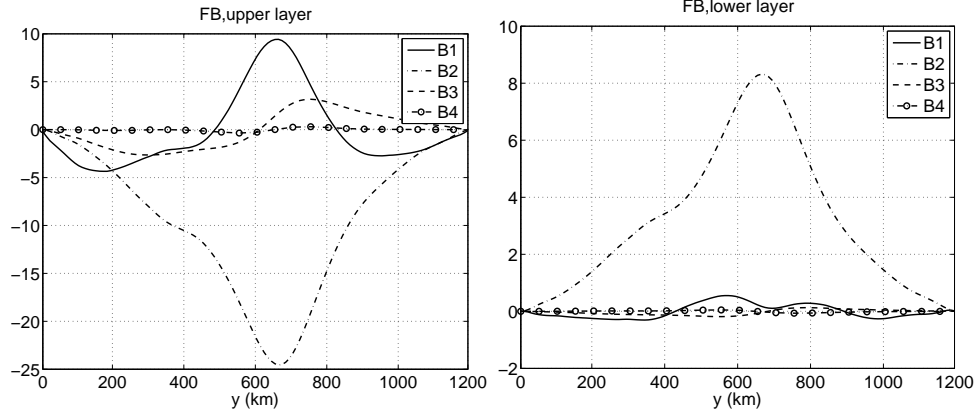
Figure 4.10: Case FB. Components of time and zonally averaged $\overline{Q_i v_i h_i}$. Left panel is for the upper layer and right panel is for the lower panel. Solid lines denote term $B1 = \overline{\zeta_i' v_i'}$; dash-dot lines denote term $B2 = -\dfrac{f_0}{H_i} \overline{v_i' h_i'}$; dot lines represent term $B3 = (f \bar{v}_i - \dfrac{f_0}{H_i} \bar{v}_i \bar{h}_i)$; dash-dot-circle lines represent term $B4 = \bar{\zeta}_i \bar{v}_i$. The unit is $10^{-8} m s^{-2}$

et al., 1978). The amplitude of term $B3$ is very small in the lower layer, but is of the same order as the horizontal Reynolds' stress divergence in the upper layer. Furthermore, the way it works to influence the mean flow is different from the Reynolds' stress term and the interfacial form drag term which are roughly symmetric about the jet axis. Term $B3$ is antisymmetric about the channel center: it tends to accelerate the mean flow in the northern half with stronger strength while it decelerates the flow in the southern half with weaker strength. Under its influence, the mean flow tends to be strengthened to the north of the central latitude. Clearly, it is the big meridional variation of $\overline{h_1}$ that produces the finite amplitude of the term $B3$ compared with other two terms in the PV flux. On the other hand, in a QG regime, this term is basically zero due to the basic assumption of quasi-geostrophy: layer thickness variation is on the order of Rossby number compared with the layer thickness itself. Therefore, the term $B3$ is responsible for the asymmetric features described at the beginning of this section including the northward displacement of the jet's center and the "plateau" on the meridional profile of the mean flow in the first layer.

Conclusions

Through case FB, we obtained some basic understanding of the dynamics of the wind-driven channel flows. The dynamics revealed by the model results, for example, the zonal momentum budget,

is in good agreement with results of the QG models. Meanwhile our model results also show notice-able asymmetries about the central latitude, and this difference between the PE and the QG models is considered due to the big displacement of the layer interface that is dynamically neglected in the QG regime. Similarities of results between our model and the QG models as well as differences that can be well explained by differences of the two types of models suggest that our model is reliable in studying the problem.

Some conclusions from case FB are important for subsequent experiments. First, the eddy-induced PV flux is down the the mean PV gradient in both layers working to homogenize the PV fields. Second, the zonal momentum of the second layer is balanced between the interfacial form drag and the bottom friction, while in the upper layer, both Reynolds' stress divergence and the interfacial form drag contribute to the momentum balance though work differently. Compared with the interfacial form drag whose sign as well as the layer integrated value are "constrained" by the surface wind stress, the horizontal Reynolds' stress divergence is more free. It reacts indirectly to the wind stress to help accomplish the zonal momentum balance.

As mentioned in introduction, the absence of any bottom obstacles in the zonal direction makes the bottom form drag impossible, so the eastward momentum supplied by the wind stress to the system has to be entirely balanced by the bottom friction, causing a large volume transport and also high eddy kinetic energy levels. Both of these two aspects are thought to be improved by adding the isolated seamounts or ridges on the bottom, which is beyond the scope of this thesis.

4.4.2   Case SB

With the purpose of understanding the effect of the bottom slope on the channel flow, a zonally uniform slope(Fig.4.11) is constructed within the second layer in case SB. The total water depth increases linearly from $2000m$ at the southern boundary to $4000m$ at about $y = 200km$. The steepness of the slope is 0.01. Other than the inclusion of the slope, the model set-up is the same as that in case FB.

A comparison with case FB is made and then the reason for difference is explored. Finally,

the significance of the new feature revealed in case SB to the shelf/slope circulation and the cross-slope/shelf exchange is discussed.

Comparison between case SB and case FB

The inclusion of the bottom slope doesn't change one fundamental fact of the channel flow: the jet in the center of the channel works as a generator of eddies maintaining the momentum balance by transferring momentum downward to the lower layer, but the flow character near and above the slope is changed locally, not only in the lower layer but also in the upper ocean.
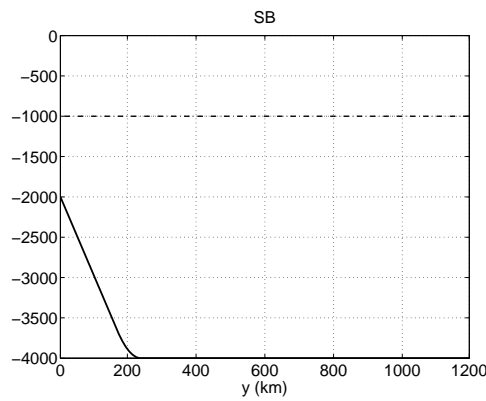

Figure 4.11: Case SB. The meridional profile of the water depth over the slope in units of m.

As shown by Fig.4.12, differences of the mean zonal velocities between the two cases are distinct. The amplitude of the eastward zonal flow in the second layer decreases more rapidly southward towards the slope from its maximum value near the center of the channel to zero at the slope edge. Southward of the slope edge, the flow direction is reversed and the flow amplitude first increases and then decreases. As to the mean flow in the first layer, a second maximum appears on the edge of the slope. Within the sloping region, the velocity magnitude as well as its meridional shear is much greater than that in the flat-bottomed case. In addition, the jet in case SB is moved southward back to the central latitude from its location in case FB.

The second jet near the slope edge observed from the velocity plot is more prominent as a strong PV front, denoted as '2' in the right panel of Fig.4.13 with peak amplitude far exceeding the value in the flat-bottomed region where the two cases look quite similar to each other. The great increase
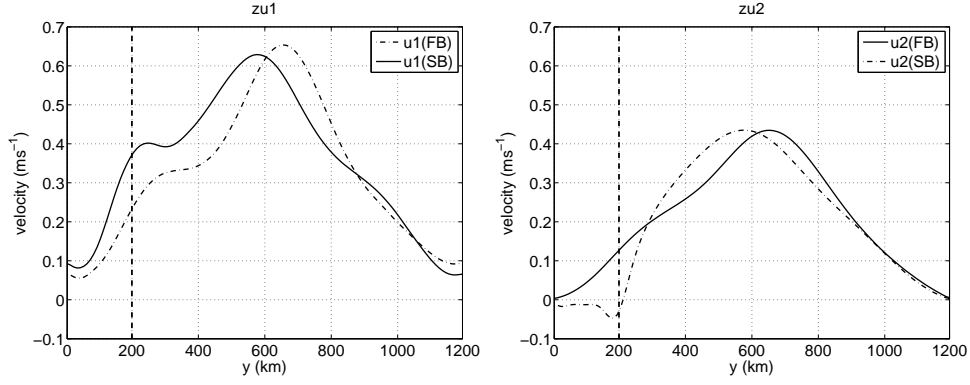
139

Figure 4.12: Case FB—SB. Meridional profile of the time and zonally averaged zonal velocity in the two layers (left panel is for the first layer, right panel is for the second layer) and in the two cases (solid lines are for case SB and dash-dot lines are for case FB). The unit is ms^{-1}.

of the PV gradient from interior towards the slope is mostly caused by the increase of the stretching component which is $-\dfrac{f}{h_1^2}\dfrac{\partial h_1}{\partial y}$. The component of the relative vorticity, $\dfrac{1}{h_1}\dfrac{\partial \zeta_1}{\partial y}$, though has similar meridional structure as the stretching component, is much less significant due to its much smaller amplitude. The reason for the small amplitude of $\dfrac{1}{h_1}\dfrac{\partial \zeta_1}{\partial y}$ compared with the stretching component has been explained in case FB. The second-layer PV gradient over the slope is positive due to the northward decrease of the topographic height, opposite to its value off the slope but the same as the PV gradient over the slope in the first layer. Thus, the necessary condition for baroclinic instability is not satisfied locally in the sloping region any more and in this sense, the bottom slope works to stabilize the flow.

It has been found by previous studies about the mechanism of meandering and eddy detachment in a baroclinic unstable jet like the Gulf Stream, that the existence of a positive slope(same sense as isopycnal tilt as in the current case) at the bottom suppresses the growth of meanders and eddy pinch-off in the upper ocean (Sutyrin et al. 2001; Wang and Ikeda 1997; Kontoyannis 1997). In flat-bottomed ocean, deep eddies are found play an important role in the final stage of growth or eddy pinch-off process of the meander above it through phase-locking between the two, but with a positive bottom slope, the growth of upper-layer meanders and ring formation are limited as the deep eddy structure is modified by the slope.

Differences between the two cases can be explained through eddy-topography interactions in
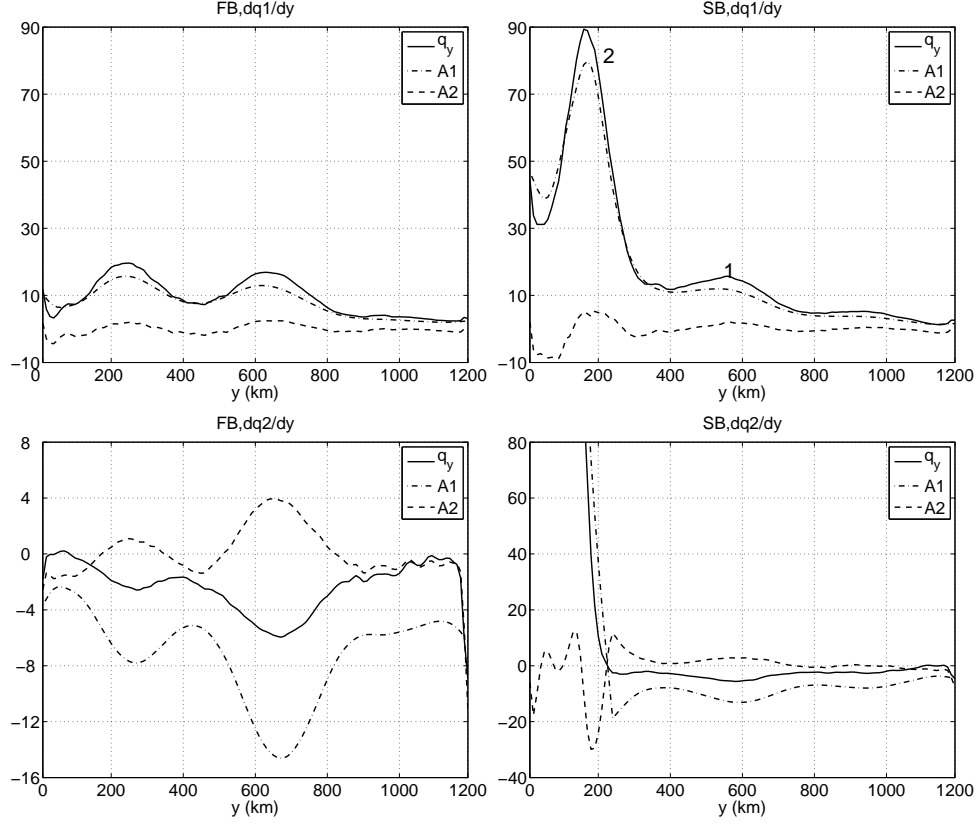
140

Figure 4.13: Case FB—SB. Time and zonally averaged meridional gradient of the PV in two cases (left panels are for case FB and right panels are for case SB) and two layers(upper panels are for the first layer and lower panels are for the second layer). Solid lines denote the total meridional gradient of PV, dash-dot lines denote the stretching component $A1 = -\dfrac{f}{h_i^2}\dfrac{\partial h_i}{\partial y}$ and dash lines denote relative vorticity component $A2 = \dfrac{1}{h_1}\dfrac{\partial \zeta_1}{\partial y}$. The unit for the upper layer PV gradient is $10^{-14}m^{-1}s^{-1}$ and the unit for the lower-layer PV gradient is $10^{-15}m^{-1}s^{-1}$. In the upper right panel, the number "1" denotes the PV front associated with the main jet near the central latitude and the number "2" denotes the PV front caused by the inclusion of the bottom slope.

the second layer. In the flat-bottomed case, the meridional gradient of PV is negative throughout the second layer and at least one order smaller than that in the upper layer. Including the topography brings a big, positive PV gradient to the lower layer, opposite to and much greater than the interior value. Consider an eddy generated from the center of the jet getting close to the topography. Based on results of the interaction between a single eddy and the slope examined in Chapter 3, we know that water columns that originally lie over the slope, which have large, negative PV, will be replaced by water columns from the interior which have small, negative PV. Slope water columns are stretched when they go down the slope and to conserve PV, negative relative vorticity is generated. On the other hand, interior water columns are squeezed when they climb up the slope and at the same time, positive relative vorticity is produced. Therefore, through the interaction between the eddy and the slope, negative PV is transported off the slope and the net change of relative vorticity is negative off the slope while positive on the slope.

If the eddy-topography interaction occurs commonly along the slope and frequently in time, the relative vorticity field near the slope will be determined predominantly by this mechanism and we expect to see the time averaged relative vorticity is negative off the slope and positive on the slope. This hypothesis is verified by the plot of time averaged second-layer relative vorticity in the two cases in Fig.4.14. In case FB, the time averaged relative vorticity is negative and weak throughout the southern half of the channel. In case SB, however, the negative relative vorticity is strengthened from interior towards the slope till very close to the slope edge followed by a very rapid decrease in amplitude within a narrow meridional region. Southward across the slope edge, the relative vorticity becomes positive with the amplitude greatly declining towards the south. Through less than $105km$, the amplitude of this positive relative vorticity over the slope as in the third panel in Fig.4.14 has dropped to almost zero. The small meridional length scale of the zonal band of positive relative vorticity compared with the meridional length scale of the slope is reminiscent of the "effective range" of the anticyclone discussed in Chapter 3. The anticyclone's velocity field weakens shoreward over the slope. Also, the seaward deformation of the PV contours over the slope directly generated by the off-slope anticyclone counteracts the effects of the original anticyclone because its velocity field is opposite to that of the anticyclone over the slope. Due to these two reasons, the anticyclone's effects decline quickly shoreward over the slope. Consequently, water
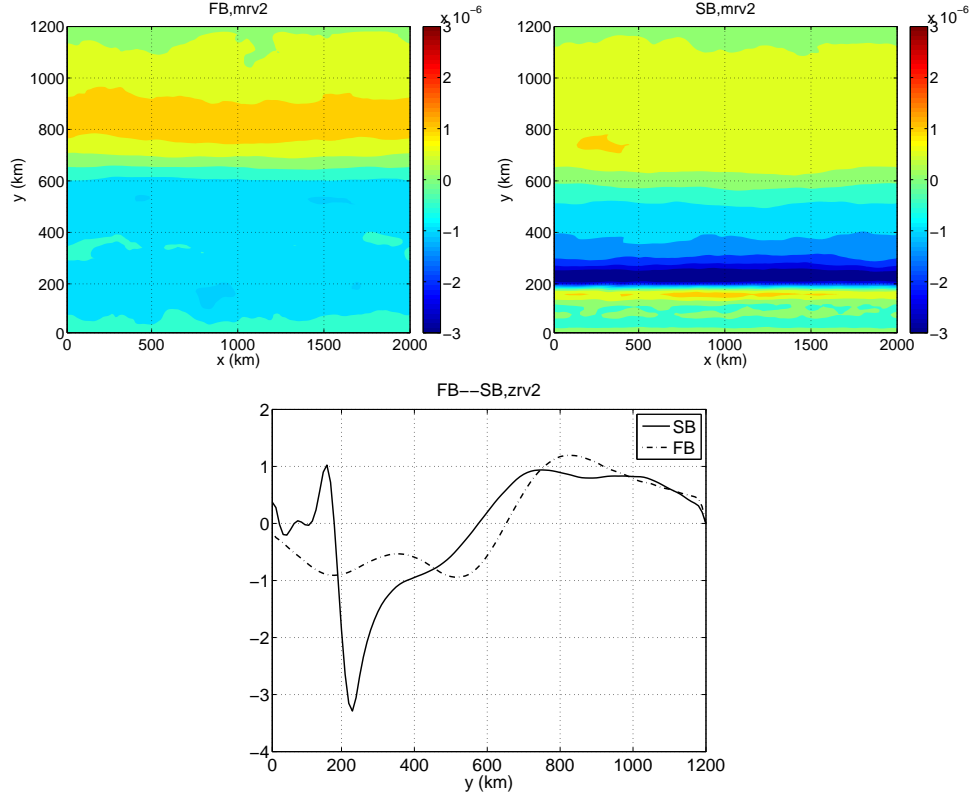
Figure 4.14: Case FB—SB. First two panels: contours of time averaged relative vorticity in the second layer in the two cases. The third panel is the time and zonally averaged relative vorticity in the second layer in the two cases (solid:SB, dash-dot:FB). The unit is s^{-1}.

columns that originated from the interior can not get very far onto the slope except when the off-slope anticyclone is very strong.

Another demonstration of the common occurrence of eddy-topography interactions along the slope is obtained from the time and zonally averaged interface depth in both cases in Fig.4.15. Water columns from interior are squeezed when they are pushed onto the slope by the off-slope eddies. Positive relative vorticity generated by the squeezing of the water columns further pushes the interface upward. Therefore, compared with the flat-bottomed case, the interface over the slope is raised further upward towards the south in the same way as the ocean bottom. Because the bottom and the layer interface tilt in the same way, the lower layer is stretched more over the slope compared with the flat-bottomed case. Equivalently, the first layer experiences more squeezing due to the bottom slope, so the PV gradient is greatly enhanced locally.
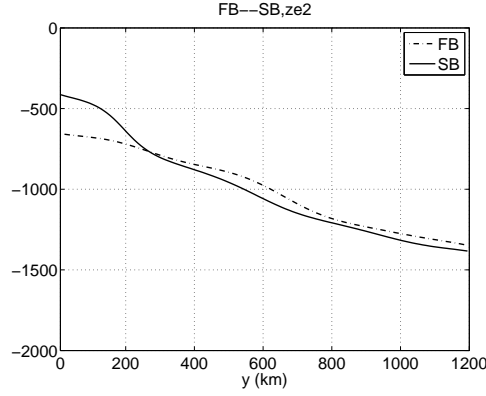
Figure 4.15: Case SB—FB. Time and zonally averaged interface depth in unit of m.
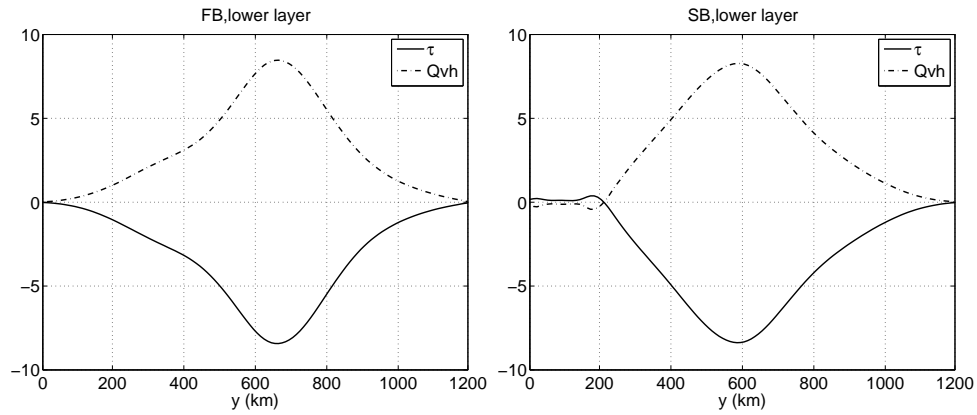

Figure 4.16: Case FB—SB. Terms in time and zonally averaged zonal momentum equations. Solid lines denote the meridional flux of PV and dash-dot lines denote the bottom drag. The unit is $10^{-8} ms^{-2}$.

As a result of the water exchange in the eddy-topography interaction, the mean PV flux is negative near and over the slope, opposite to its value in the interior, but still down the mean PV gradient. Instead of producing eastward momentum to the layer as within most of the domain, the PV flux over the slope works as a source of westward momentum as in Fig.4.16. We have seen from the discussion of case FB that at all latitudes in the second layer, the zonal momentum is balanced between the PV flux and the bottom drag; negative PV flux requires positive bottom drag. The time and zonally averaged zonal flow over the slope in the second layer is therefore westward.

In both cases, the meridional PV flux declines southward from its maximum amplitude set by the maximum wind stress, but the decrease is more rapid in case SB to make the PV flux less than zero over the slope. The PV flux mostly consists of two parts: the horizontal Reynolds' stress divergence
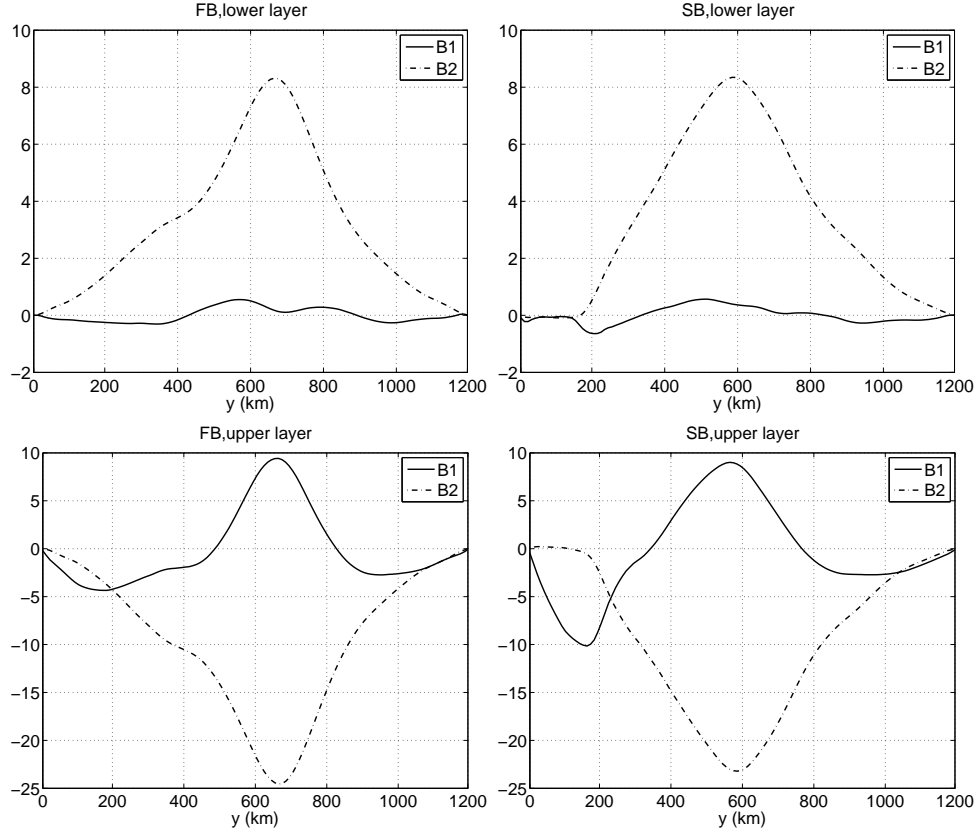
Figure 4.17: Case FB—SB. Terms in time and zonally averaged zonal momentum equations. Solid lines denote the eddy-induced horizontal Reynolds' stress divergence($B1$) and dash-dot lines denote the eddy-induced interfacial form drag ($B2$). The upper panels are for the lower layer and lower panels are for the upper layer. The unit is $10^{-8} ms^{-2}$.

and the interfacial form drag. In case FB, the interfacial form drag is positive at all latitudes with the amplitude much greater than that of the horizontal Reynolds' stress divergence. Although there are different ways to modify the interfacial form drag as well as the horizontal Reynolds' stress divergence to make the sum of them below zero over the slope, the most plausible way is to make the intefacial form drag decrease greatly southward towards the slope. As shown in Fig.4.17, the interfacial form drag has declined to almost zero upon getting on the slope and remains very small over the slope; the horizontal Reynolds' stress divergence which is already below zero in flanks of the jet in case FB, is also decreased over the slope in case SB.

As described previously, one important character of the interfacial form drag is that the forces imparted on the two layers by each other are opposite and equal, so the interfacial form drag over

the slope in the first layer also becomes very small which makes the horizontal Reynolds' stress divergence greatly amplified from its value in case FB in order to balance the wind stress that remains unchanged. Notice that the layer integrated horizontal Reynolds' stress divergence has to be zero; its change over the slope further causes an adjustment of horizontal Reynolds' stress throughout other areas. The result of this adjustment is that the mean flow is strengthened within a bigger area between the jet axis and the slope, and is weakened greatly within the sloping region, which explains the changes observed from the zonal velocity profile in Fig.4.12.

In summary, the eddy-topography interaction in the lower layer changes the local structure of the meridional flux of PV. Through the interfacial form drag, the first layer "feels" the existence of the topography and makes an adjustment of the horizontal momentum flux which further changes the character of the mean flow in the upper ocean. Compared with case FB, the time and zonally averaged zonal velocity in the first layer is strengthened near the edge of the slope and declines more quickly southward towards the southern boundary. On the other hand, the first layer thickness is smaller within the sloping region in case SB than in case FB due to the eddy-topography interactions in the lower layer. Both changes contribute to the formation of a strong PV front over the slope in the first layer.

Given the second bump of the PV gradient as well as the weak meridional shear in the first layer north of $y = 200km$ in case FB, it may be wondered whether this front-like feature observed in case FB is a precursor and also imperative for the second PV front developed in case SB. The answer is no. The two fronts have different formation mechanisms: the one in case FB is related to the big layer thickness variations while the one in case SB is the consequence of the bottom slope. Therefore, the location and the strength of the second front in case SB would be strongly dependent on the meridional extent of the slope. Furthermore, it may even more strongly rely upon whether the slope is against the southern boundary or the northern boundary. If the same bottom slope is constructed against the northern boundary with the water depth increasing southward, the topographic β_t is negative, opposite to the planetary β but the same as the PV gradient in the flat-bottomed case. If the magnitude of β_t is greater than β which is usually true for continental slopes, the PV gradient in the lower layer will become large and negative over the slope. According to the study of Wang and Ikeda (1997) about baroclinic unstable waves and meanders over a sloping

146

bottom, a steep negative slope("negative" means the tilts of the interface and the slope are opposite, which is probably true for the problem in question) will reduce the maximum growth rate of unstable waves. However, it is not clear what the PV flux will look like in our channel flow and whether there will be a second PV front formed over the slope in the first layer. For the situation in case SB, in particular, the relative relation between the slope and the interface is similar to the physical setting of the Gulf Stream along the eastern continental slope, while the negative slope just mentioned resembles the situation of Labrador Current. Both are interesting problems of jet-slope interactions and the latter one would be a good topic for the future work.

Flow Character in Case SB

In this section, we are going to examine the character of variability near the southern boundary which is decisive to the eddy-topography interactions if there were a slope/shelf region further southward in the first layer.

Meridional structures of velocity variances, $\sqrt{\overline{u_i'^2}}$ and $\sqrt{\overline{v_i'^2}}$ ($i = 1, 2$), in case SB and FB are shown in Fig.4.18. In case FB, the eddy variability is concentrated at the location of the mean jet and is roughly symmetric about the center of the jet. Compared with case FB, the location of intense eddy variability is displaced southward towards the slope from the central latitude. Except $\sqrt{\overline{v_2'^2}}$, all other three r.m.s. quantities, $\sqrt{\overline{u_1'^2}}$, $\sqrt{\overline{v_1'^2}}$, and $\sqrt{\overline{v_2'^2}}$, are bigger than in case FB near and over the slope. $\sqrt{\overline{v_2'^2}}$, however, is greatly reduced near and over the slope suggestive of the weak meridional perturbations due to the strong PV gradient.

Fig.4.19 and Fig.4.20 show instantaneous patterns of PV in the two cases. Compared with case FB, the most striking feature in Fig.4.19 is the heterogeneity of the variability within the domain. Eddy fields on the two sides of the PV front denoted as "A" in the first panel in Fig.4.19 have different features. Eddies to the north are generated from the main jet in the center of the channel. They have length scales on the order of the deformation radius. The variability to the south of the front is related to the front itself either as meridional deformations, meanders or detached eddies. Limited by the closeness of the front to the southern boundary, the variability near the southern boundary has length scales smaller than that in the interior. Furthermore, due to the existence of the strong
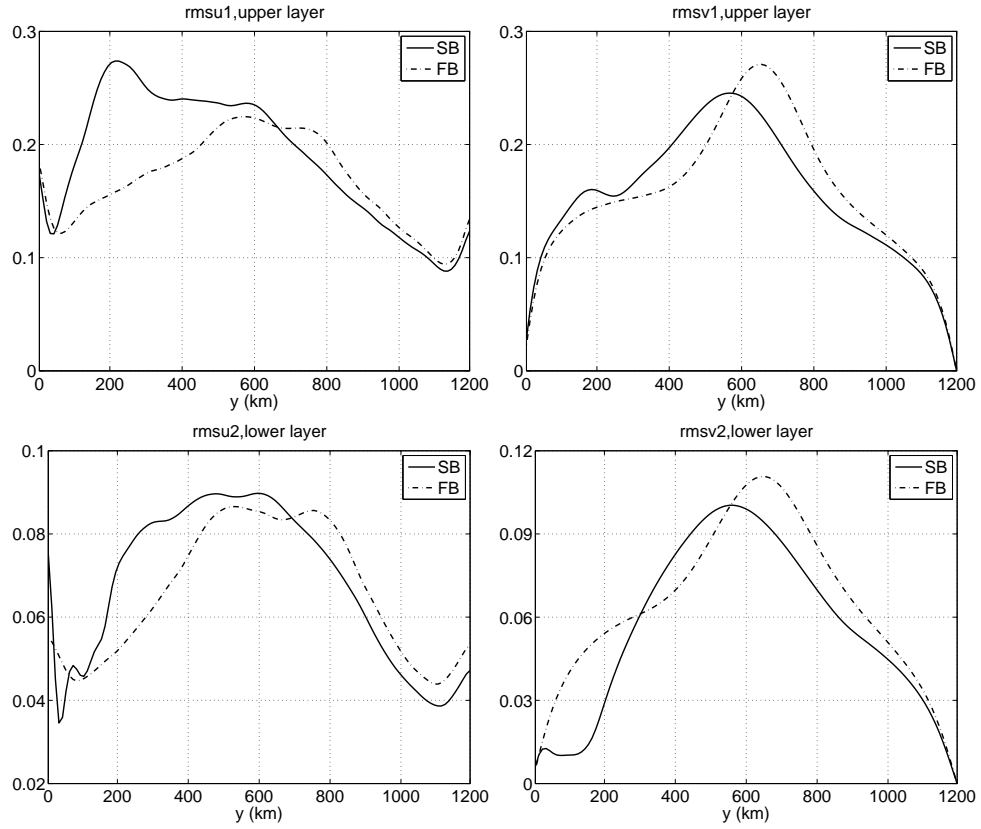
147

Figure 4.18: Case FB—SB. Root mean square quantities in the two cases. The upper left panel is $\sqrt{\overline{u_1'^2}}$, the upper right panel is $\sqrt{\overline{v_1'^2}}$, the lower left panel is $\sqrt{\overline{u_2'^2}}$, and the lower right panel is $\sqrt{\overline{v_2'^2}}$. Solid lines are for case SB and dash-dot lines are for case FB. The unit is ms^{-1}
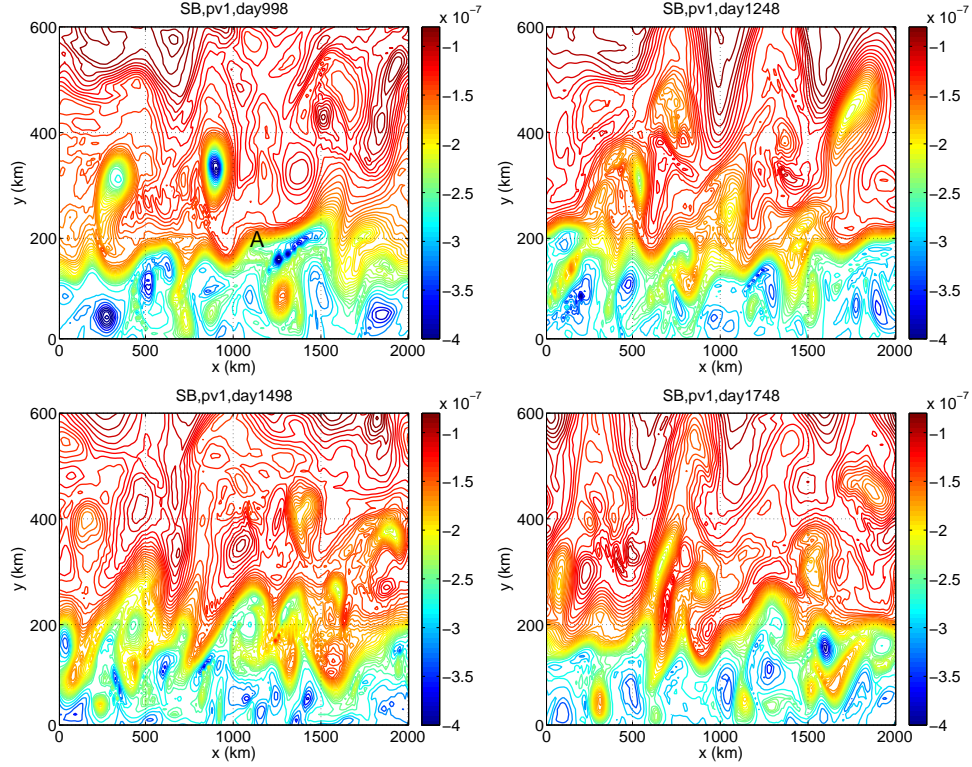
Figure 4.19: Case SB. Instantaneous patterns of PV in the first layer with intervals of $0.2 \cdot 10^{-7} m^{-1} s^{-1}$ for contour values below $-2.5 \cdot 10^{-7} m^{-1} s^{-1}$ and $0.05 \cdot 10^{-7} m^{-1} s^{-1}$ for contour values above $-2.5 \cdot 10^{-7} m^{-1} s^{-1}$.

PV front over the slope, large eddies generated from the main jet can hardly approach the southern boundary as they often do in case FB.

Conclusions

Case SB is an intermediate case between case FB, a wind-driven flow within a flat-bottomed channel and case BAY1 describing a full system of a jet, a slope and a bay that are dynamically linked together through interactions. The significance of this case is the demonstration of the formation of a strong PV front due to the inclusion of a slope in the lower layer. As revealed by instantaneous PV patterns, this front plays an dominant role in generating variability further south and thus very important for driving slope/shelf circulation and cross-slope/shelf exchange in case BAY1.

The bottom slope that is entirely submerged in the second layer is found have two contrary effects on nearby variability. On one hand, as investigated by previous studies, a positive slope at
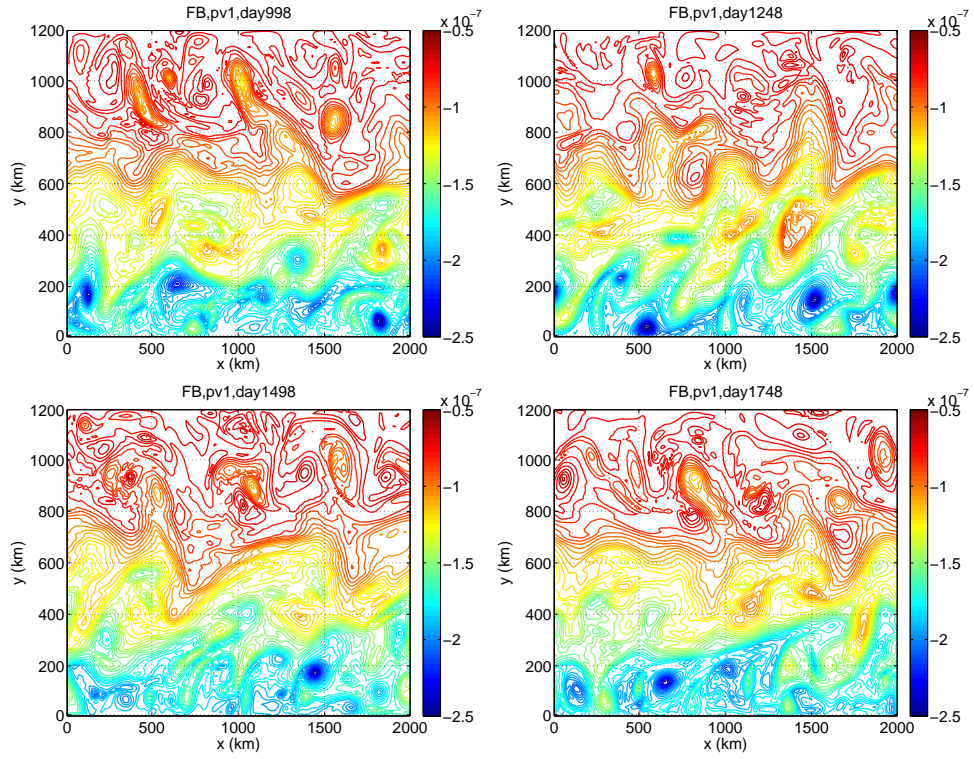
Figure 4.20: Case FB. Instantaneous patterns of PV in the first layer with intervals of $0.05 \cdot 10^{-7} m^{-1} s^{-1}$.

bottom works to stabilize the baroclinic jet by limiting growth of meanders and eddy pinch-off in the upper layer (Sutyrin et al. 2001). This is consistent with our result from case SB that the necessary condition for the baroclinic instability is not satisfied within the sloping region. But on the other hand, the bottom slope in the current case induces the formation of a strong PV front in the upper layer greatly enhancing local eddy variance.

The eddy-topography interaction is found important for changes from case FB to case SB. Local changes of dynamics in the second layer influence the dynamics of the upper layer in a bigger range. The near vanishing of the interfacial form drag over the slope is a key factor. Through analysis of the zonal momentum budget, we know that it results from the reversing of the PV flux on and off the slope but it is not clear why dynamically it has to be so.

4.4.3 Case BAY1

In case BAY1, the model domain has two sub-regions: a zonally periodic channel in the north and a bay in the south bounded by the curved southern boundary whose meridional location varies in x (Fig.4.21). The bay extends meridionally from $y = 0$ to $y = 155km$, the water depth within the bay is constant about $400m$ and much shallower than the first-layer thickness. A zonally uniform slope starts from the northern edge of the bay extending northward till $y = 400km$ with the steepness first increasing to about 0.03 at about $y = 350km$ and then dropping to 0.

The flow within the channel (north of $y = 155km$) is forced by the wind stress with the maximum amplitude of $\tau_0 = 0.12kgm^{-1}s^{-2}$ at the latitude of $y = 677km$. The isopycnal is initially at the depth of $1200m$ intersecting the sloping topography at about $y = 250km$. After the model is started, the intersection line continues to move upward along the slope till the quasi-steady state is achieved. The initial interface depth is chosen in such a way that during the quasi-steady state, the interface depth off the first-layer slope is similar to the depth of the Circumpolar Deep Water (CDW) found off the west Antarctic Peninsula (WAP) shelf.

The following discussion is divided into two parts. In the first part, we will describe qualitatively the flow character in the quasi-steady state including the flow directly driven by the wind and the
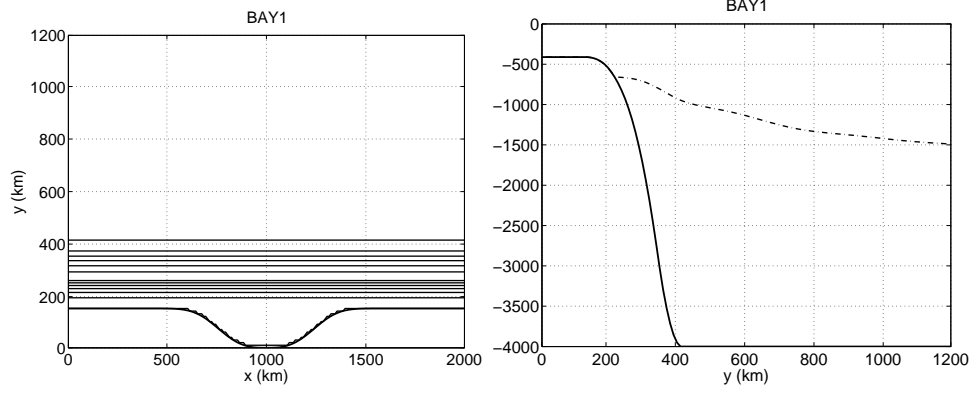
151

Figure 4.21: Case BAY1. Left panel: model domain and bathymetry. Thin solid lines are isobaths of water depth with intervals of $500m$ for water depths of $1000m$ above and $50m$ for $1000m$ below. The thick solid line denotes the southern boundary. Right panel: meridional profile of water depth in units of m.
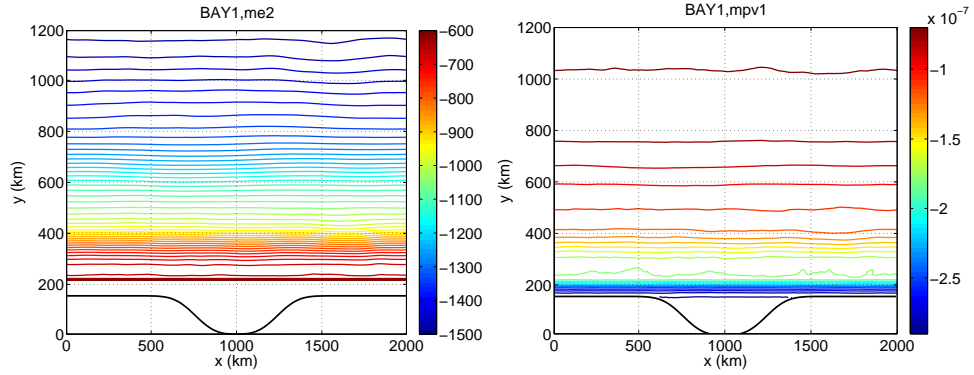
Figure 4.22: Case BAY1. Left panel: the time averaged interface depth with intervals of $20m$. Right panel: the time averaged PV in the first layer with intervals of $0.1 \cdot 10^{-7}m^{-1}s^{-1}$.

circulation within the bay. In the second part, we will focus on the cross-shelf/slope exchange driven by the open ocean variability. Tracer experiments are performed to examine quantitatively the cross-slope/shelf transport and the associated features.

Mean Flow within the Channel

The time averaged isopycnal depth and the first-layer PV in Fig.4.22 show little variation in the zonal direction northward of the bay opening, so it is reasonable, as in case FB and case SB, to study the character of the time and zonally averaged flow within the channel.

152

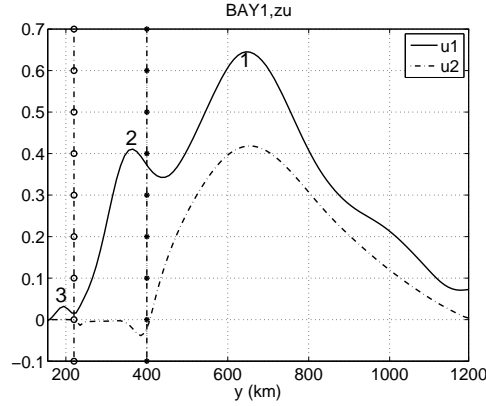**Figure 4.23:** Case BAY1. The time and zonally averaged zonal velocity in the first layer (solid line) and the second layer (dash-dot line) in units of ms^{-1}. The dash-dot-circle line denotes the y location of the intersection of isopycnal and the slope. The dash-dot-star line denotes the location of the northern edge of the bottom slope.

The intersection line depicted in Fig.4.21 separates the domain into two regions. Southward of the line, there is only one layer of water overlying the slope as well as the shelf and being influenced by the bottom drag. Northward of the intersection line, the flow dynamics is expected to be similar to that in case SB, although the bottom topography has "grown" into the first layer.

First, the time and zonally averaged zonal velocities of both layers have similar meridional structures to those in case SB. The peak amplitudes of the zonal velocities are around the location of the maximum wind stress. Besides the strong jet near the central latitude, there is a secondary jet with differing signs in the two layers near the base of the bottom slope denoted as "2" in Fig.4.23. Second, corresponding to the secondary jet, a second PV front denoted as "2" in the left panel of Fig.4.24 is at about the same latitude in the upper layer. Third, the pattern of the time averaged second-layer relative vorticity (Fig.4.25) also reveals the feature similar to that in case SB: there are two zonal bands of differing signs right along the northern edge of the slope at about $y = 400km$ with the positive one to the south and the negative one to the north. As the evidence for the common occurrence of eddy-topography interaction in the lower layer, this feature suggests that our argument used to explain effects of the second-layer slope on the flow in both layers works well in the current case.

Besides the major and the second PV front denoted as "1" and "2" in Fig.4.24, there is another
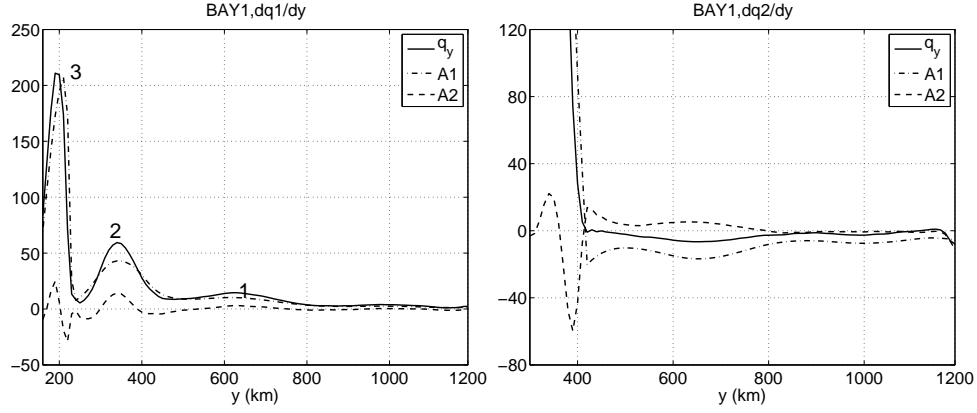
Figure 4.24: Case BAY1. The time and zonally averaged meridional gradient of the PV and its two components A_1 and A_2. Solid line: $q_y = \dfrac{\partial q_i}{\partial y}$; dash-dot line: $A_1 = -\dfrac{f}{h_i^2}\dfrac{\partial h_i}{\partial y}$; dash line: $A_2 = \dfrac{1}{h_i}\dfrac{\partial \zeta_i}{\partial y}$. The left panel is for the upper layer ($i = 1$), the unit is $10^{-14}m^{-2}s^{-1}$; the right panel is for the lower layer($i = 2$), the unit is $10^{-15}m^{-2}s^{-1}$.
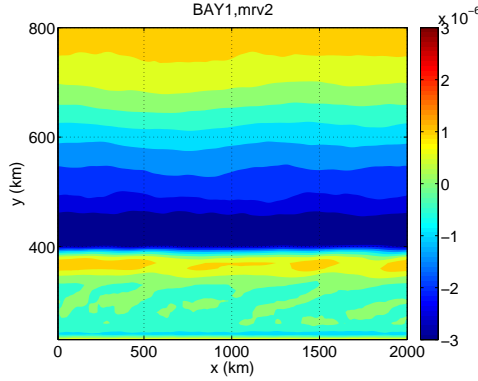
Figure 4.25: Case BAY1. The time averaged relative vorticity in the second layer in units of s^{-1}.

one, "3", somewhere between the northern edge of the bay and the intersection latitude with the maximum amplitude among the three. The formation of this PV front is mostly due to the variation of the topography whose contribution to the PV gradient is $-\dfrac{f}{D^2}\dfrac{\partial D}{\partial y}$ where D represents the depth of the topography. Although the meridional variation of D, $\dfrac{\partial D}{\partial y}$, decreases southward within this region, the component of $-\dfrac{f}{D^2}$ increases southward because of the shallowing of the topography. The opposite changing tendencies of the two components induce the local maximum of the PV gradient.

The two-band structure of the time averaged relative vorticity is also observed in the first
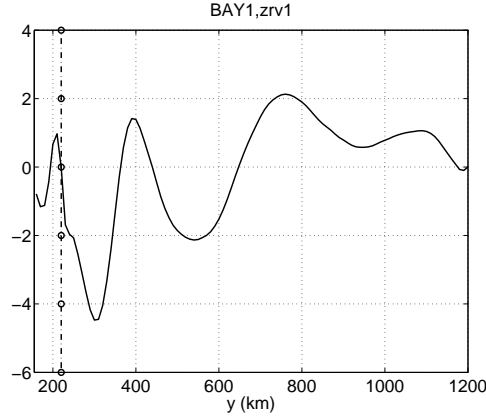
Figure 4.26: Case BAY1. The time and zonally average relative vorticity in the first layer in units of $10^{-6}s^{-1}$. The dash-dot-circle line denotes the location of the first-layer slope edge.

layer along the intersection line of the isopycnal with the bottom (Fig.4.26) indicating the eddy-topography interactions. But the time averaged relative vorticity remains positive only within a very narrow region right next to the slope edge and then declines southward to below zero. To explain the formation of the band of negative relative vorticity along the southern boundary of the channel, we will examine the momentum balance for this one-layer sloping region.

The flow between the southern boundary of the channel and the intersection line is driven by the eastward wind stress, dissipated by the bottom drag as well as the lateral friction:

$$\frac{\partial}{\partial t}\overline{u_1} + f_0\overline{v_1^\dagger} = \frac{1}{H_1}\overline{Q_1v_1h_1} - C_{drag}\overline{h_1|u_1|u_1} + \overline{\frac{\tau}{\rho h_1}} + \overline{lateral friction}. \qquad (4.22)$$

As shown in Fig.4.27, the zonal momentum balance for the time and zonally averaged flow is basically among the first three terms on the right hand side of Eq.4.22: the wind stress, the bottom drag and the PV flux which consists of only horizontal Reynolds' stress divergence since the interfacial form drag vanishes without the lower layer. Northward of the intersection line and over the second-layer slope, the amplitude of horizontal Reynolds' stress divergence is less than that of the wind stress since it has the same sign as the interfacial form drag and the two together balance the wind stress. Without any mechanism that could locally enhance the horizontal Reynolds' stress divergence, it remains weaker than the wind within the one-layer sloping region and works in the same way as the bottom drag. The bottom drag is important for the momentum balance within the
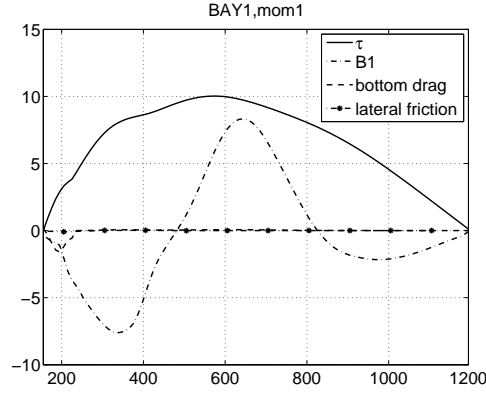
155

Figure 4.27: Case BAY1.Terms in the time and zonally averaged zonal momentum equation for the first layer. The solid line denotes the wind stress; the dash-dot line denotes the eddy-induced horizontal Reynolds' stress divergence($B1$); the dash line denotes the bottom drag; the dash-dot-star line denotes the lateral friction. The unit is $10^{-8} ms^{-2}$. The bottom drag is the force exerted on the fluid by the solid earth. Northward of the intersection line, it is the lower layer that is affected by the bottom drag while southward of the intersection line, the bottom drag is exerted directly on the upper layer.

region but negligible outside. Since it is proportional to the velocity amplitude, the time averaged zonal velocity is expected to first increase northward and then decrease towards the intersection line. The time averaged relative vorticity is therefore negative in the south and positive in the north.

Eddy-driven Flow within the Bay

The goal of this section is to answer two questions about the flow within the bay. First, without the wind stress, what drives the flow within the bay? The bay's boundary can be roughly divided into three parts: a western side boundary, an eastern side boundary and a southern boundary that is further to the bay opening. The flow within the bay must be influenced by those boundaries. Our second objective is to examine effects of boundaries on the flow.

The PV equation for the flow within the flat-bottomed bay area reads:

$$\frac{d}{dt}\left(\frac{f+\zeta}{h}\right) = F, \tag{4.23}$$

where ζ and h are relative vorticity and layer thickness of the flow, and F denotes the sink and source of PV. Without the wind stress, F represents effects of the lateral friction and bottom drag.

Motions within the bay have length scales much less than the external deformation radius which is over $1500km$ in the current case, so Eq.4.23 and the mass conservation can be simplified as:

$$\frac{\partial \zeta}{\partial t} + \mathbf{u} \cdot \nabla(f + \zeta) = F H_0, \, and \tag{4.24}$$

$$\nabla \cdot \mathbf{u} = 0, \tag{4.25}$$

where H_0 is the water depth within the bay. Multiplying Eq.4.25 by $(f + \zeta)$ and combining it with Eq.4.24 lead to:

$$\frac{\partial \zeta}{\partial t} + \nabla \cdot \mathbf{u}(f + \zeta) = F. \tag{4.26}$$

Integrating Eq.4.26 around the bay area S (Fig.4.28) with the boundary ∂S and using the Divergence Theorem, we have

$$\frac{\partial}{\partial t} \iint_S \zeta dA + \oint_{\partial S} (f + \zeta)\mathbf{u} \cdot \mathbf{n} ds = \iint_S F dA, \tag{4.27}$$

where $\mathbf{n}$ is the outward pointing vector normal to the boundary. Since the flow on the solid boundary has no normal component, $\mathbf{u} \cdot \mathbf{n}$ is zero everywhere except along the opening b as shown in Fig.4.28, and $\oint_{\partial S} (f + \zeta)\mathbf{u} \cdot \mathbf{n} ds = \int_b (f + \zeta)v dx$. Averaging Eq.4.27 over the period of 4000 days yields:

$$\int_b \langle (f + \zeta)v \rangle dx = \iint_S \langle F \rangle dA, \tag{4.28}$$

where $<>$ denotes the time average and the tendency term has been neglected. The mass within the bay is conserved, the total transport across the opening is zero $\int_b \langle f v_1 \rangle dx = 0$, and the above balance can be further written as

$$\int_b \langle v\zeta \rangle dx = \iint_S \langle F \rangle dA. \tag{4.29}$$

As revealed by the model results, the eddy-induced PV flux, $\langle v'\zeta' \rangle$, is at least 10 times bigger than that caused by the mean flow $\langle \zeta \rangle \langle v \rangle$ within the bay and near its northern edge over the slope.

Having shown that the motions within the bay are forced by time-dependent motions at its northern edge, we now look at the character of the eddy-driven mean flow illustrated by the three
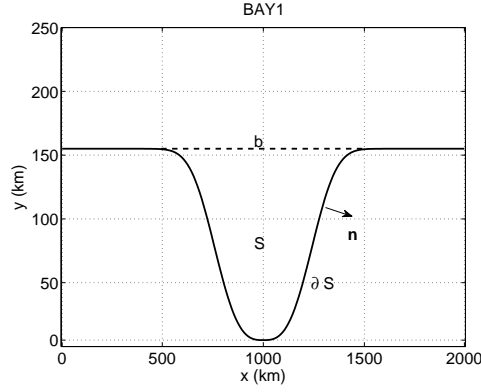
Figure 4.28: Case BAY1

panels in Fig.4.29. First of all, the mean flow around the bay is rather weak with amplitude on the order of $10^{-3}ms^{-1}$, from which the Rossby number is estimated much less than one. In addition, the bay is flat-bottomed, so contours of the surface elevation can be viewed as streamlines of the mean flow. Clearly demonstrated in the first panel of Fig.4.29, streamlines originating inside the bay are closed and most of them cross the bay opening. Circulations along those cross-opening streamlines are clockwise, directing westward within the bay, leaving the bay from the west, moving eastward over the slope and finally returning to the bay from the east. The time averaged westward zonal velocity weakens southward inside the bay indicating the southward decay of effects of the forcing at the northern edge. Compared with the mean zonal velocity, the mean meridional velocity has even smaller amplitude but more complicated spatial structures. The northward mean flow across the opening concentrates within a fairly narrow region near the western edge of the bay while the southward returning flow is more widely distributed within the region to the east. So the former has much greater amplitude than the latter to conserve mass within the bay. Within a very narrow region near the western boundary, there are streamlines closed without crossing the bay's northern edge, the associated circulation is counterclockwise, opposite to the bay-scale circulations.

For circulations along streamlines crossing the bay opening, variation of the layer thickness due to the slope needs to be considered in the PV equation. The depth variation is small compared with the depth itself within the region enclosed by those streamlines, so we can use the quasi-geostrophic
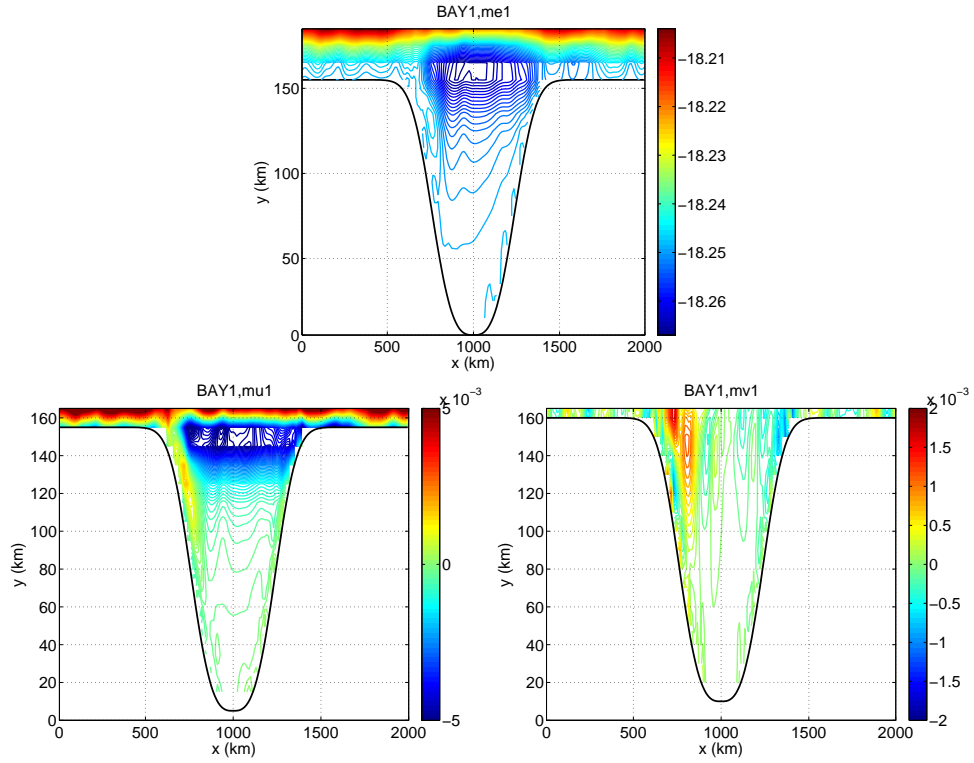
158

Figure 4.29: Case BAY1. First panel: contours of the time averaged surface elevation with intervals of $10^{-3}m$. Second panel: contours of the time averaged zonal velocity with intervals of $0.1 \cdot 10^{-3}ms^{-1}$. Third panel: contours of the time averaged meridional velocity with intervals of $0.1 \cdot 10^{-3}ms^{-1}$

PV equation to study the bay-scale circulations:

$$\frac{d}{dt}\left(\frac{f + \zeta}{H_0} - \frac{f_0 h_0}{H_0^2}\right) = F, \tag{4.30}$$

where the total layer depth D is equal to H_0 within the bay and $H_0 + h_0(y)$ over the slope. h_0 increases northward from zero at the bay's opening. Time averaging Eq.4.30 over 4000 days during the quasi-steady state and neglecting the time tendency term yield:

$$(\beta + \gamma)\langle v \rangle + \langle \mathbf{u} \cdot \nabla \zeta \rangle = F H_0, \tag{4.31}$$

where β is the meridional gradient of the planetary vorticity, $\dfrac{\partial f}{\partial y}$, and γ represents the meridional gradient of the PV induced by the depth variations, $-\dfrac{f_0}{H_0}\dfrac{dh_0}{dy}$. In the Southern Hemisphere, f is negative, so γ is positive, the same as β. In terms of amplitude, $\beta = 1.4 \cdot 10^{-11} m^{-1} s^{-1}$, but γ is on the order of $10^{-10} m^{-1} s^{-1}$ near the opening of the bay and at least 10 times bigger than β. The term $\langle \mathbf{u} \cdot \nabla \zeta \rangle$ is equal to the horizontal divergence of advection of the relative vorticity $\nabla \cdot \langle \mathbf{u}\zeta \rangle$ in the quasi-geostrophic regime and its magnitude is on the order of $10^{-13} s^{-2}$ near the bay opening. Therefore, the term $\gamma \langle v \rangle$ could balance the eddy forcing near the bay opening, and the strong meridional mean flow near the western edge of the bay can be explained as a western boundary current due to the topographic β effect.

Compared with the mean flow, the eddy variability is much stronger within the bay as suggested by the Root Mean Square value of the zonal and meridional velocity as in Fig.4.30. Similar to the mean flow, the time-dependent motion weakens southward from the bay opening, so the southern boundary of the bay has little influence on the flow within the bay. Contours of variances in Fig.4.30 are roughly along latitudes within the bay, but are southward orientated near the two side boundaries indicating the strengthening effects of both side boundaries. Strengthening of the flow near side boundaries results from the requirement that there is no flow through the solid wall. Whenever the interior flow approaches the boundary with component normal to the wall, the boundary's effects can be regarded as that of one or multiple vortices outside the boundary with proper signs and magnitudes generating a flow with normal component cancelling the normal component of the interior flow. One important side effect of this steering is that the along-boundary component of
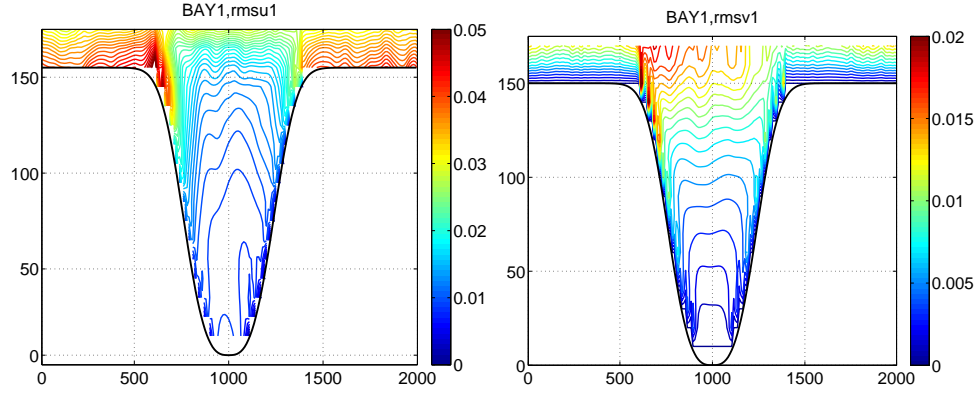
160

Figure 4.30: Case BAY1. First panel: contours of the r.m.s. value of the zonal velocity $\sqrt{\overline{u_1'^2}}$ with intervals of $10^{-3}ms^{-1}$. Second panel: contours of the r.m.s. value of the meridional velocity $\overline{v_1'^2}$ with intervals of $10^{-3}ms^{-1}$.

the virtual vortices is in the same direction as that of the interior flow, so the flow is enhanced on boundaries.

Differences of $\sqrt{\langle u_1'^2\rangle}$ and $\sqrt{\langle v_1'^2\rangle}$ between the western and the eastern boundaries are related to the single propagation direction of topographic Rossy waves which is westward in the current case. The mechanism was studied in Chapter 2 and will be reviewed here in detail since it turns out to be very important for the exchange process across the bay opening.

Consider a one-layer ocean in the Southern Hemisphere. The zonally uniform slope is simplified as a step-like topography at $y = 0$ across which the water depth increases abruptly northward. A bay exists in the shallow area partially closed by the boundary with meridional location Y_b varying in x. The northern boundary is assumed to be far enough from the topography so has no influence on the motions near the topography.

Suppose the PV interface, aligned with $y = 0$ when the ocean is at rest, is perturbed with some deformations at $t = 0$ in Fig.4.31, and we are going to look at the subsequent evolutions of this interface using the contour dynamic model as in Chapter 2. Due to the PV difference across the topography, water columns contained within the seaward interface deformations generate negative relative vorticity while those contained within the shoreward deformations generate positive relative vorticity. Assuming the amplitudes of these initial perturbations are much smaller than their zonal length scales, the nonlinear effect is weak and water particles around the topography oscil-

161

late meridionally across $y = 0$ to transport the initial deformation westward as topography-trapped waves and at the same time generate new wave patterns following the initial deformations. However, the southward motion of water particles near the western edge of the bay is blocked by the western boundary, so the initial trough is pushed against the wall by the following westward-propagating initial crest as shown in the panel of $t = 4$ in Fig.4.31. The zonal length scales of deformations are shortened towards the western edge of the bay resulting in enhancement of the effect of advections. For example, at $t = 14.0$, the western side of the trough following the initial crest has been aligned with the boundary. The velocity field generated by the trough itself works to deepen the trough along the wall while the velocity field generated by the following crest amplifies the crest northward. The nonlinear effects are weak when the length scales of the waves are large compared with waves' amplitudes, but are enhanced as the waves' length scales are decreased. In other words, as the nonlinear effect gets stronger, wave amplitudes are amplified towards the western edge. The initial crest is advected by the following trough as well as itself westward over the western edge of the bay into the deep ocean, and the following trough is continuously squeezed against the wall by the second crest which will also be pushed over the western edge in later time. The phenomenon of crests being pushed over the bay's western edge is episodic but persistent as long as the PV interface has deformations propagating westward. The squeezing and deepening of troughs along the western boundary make it possible for water columns well inside of the bay but near the western boundary to be advected northward. In contrast to the neighbourhood of the western edge, the region near the eastern boundary is more quiescent, characterized by small-amplitude perturbations and a big distance between the PV interface and the solid wall.

Overall, two conditions are required to have the asymmetry between the western and the eastern side boundaries. First, there are topographic waves propagating only in one direction which is westward in our experiment. Second, the western side boundary is close enough to the southern edge of the slope(shelf-break) to influence the time evolution of PV deformations by preventing the southward amplification of the PV contours. The first condition is the basis for differences between the two side boundaries and the second one determines the strength of the boundary's effects and also the contrast between the two side boundaries. When both conditions are met, deformations of PV contours have greater amplitudes near the western boundary. The anticlockwise velocity field of
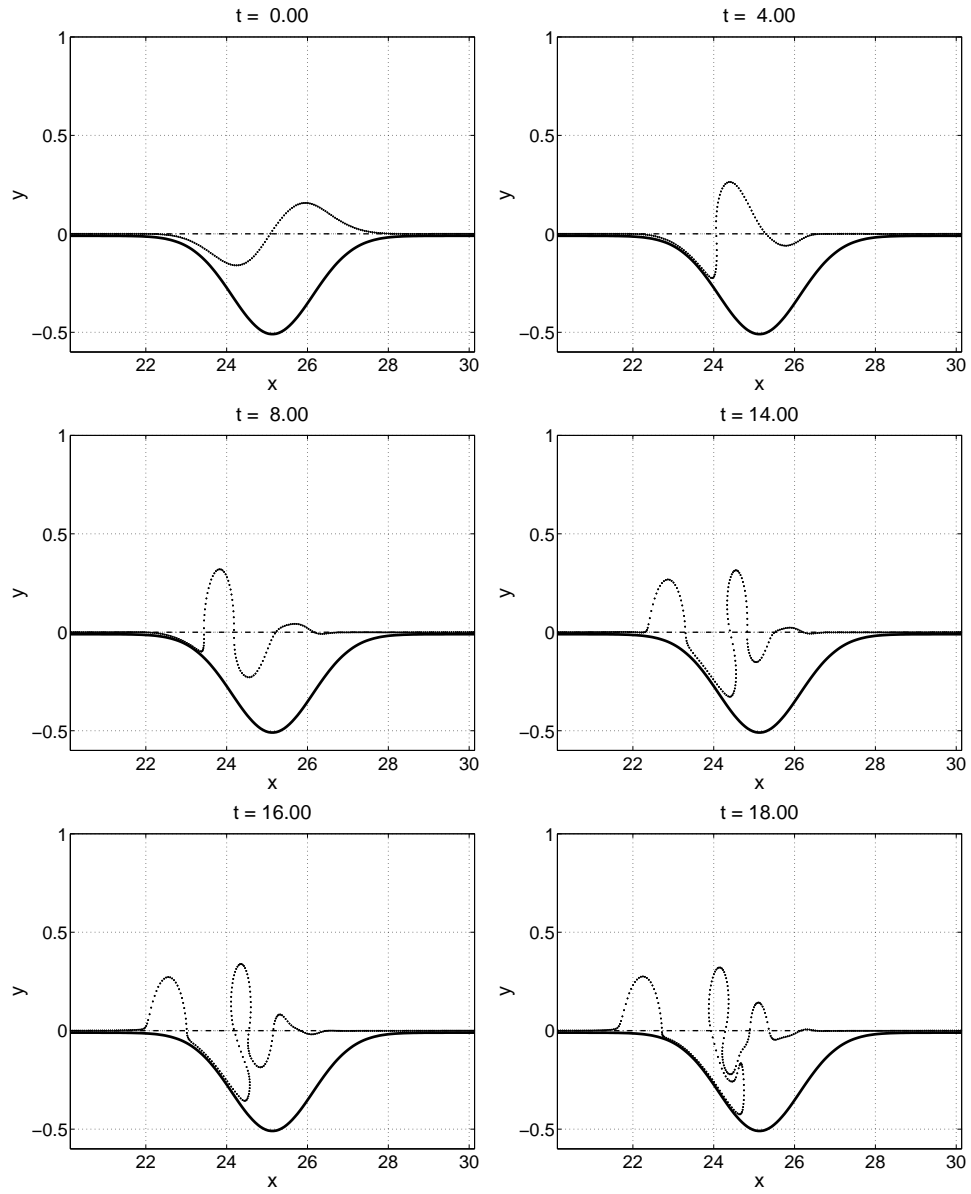
162

Figure 4.31: Case BAY1. The time evolution of PV interface(dot line). The dash-dot line represents the position of the step-like topography. The thick solid line denotes the southern boundary. The area between the southern boundary and the topography is shallower than the area northward of the topography.

163

the big trough along the western boundary advects water columns lying in the far south of the bay northward towards the bay opening. Meanwhile, big crests in front of the squeezed troughs move westward into the deep ocean along with which water is taken away from the bay.

Looking carefully at panels after $t = 14.0$ in Fig.4.31, we find some similarities between the simple contour dynamic experiment and the mean meridional velocity in BAY1 in Fig.4.29. The strong northward flow near the western edge of the bay in Fig.4.29 corresponds to the second crest in Fig.4.31 which is amplified by the nonlinear effect; the strong but narrow southward flow right along the western boundary in Fig.4.29 corresponds to the southward branch of the velocity field of the trough in Fig.4.31 which is elongated into a very narrow strip along the wall. Therefore, this mechanism could explain not only differences of eddy variance between the two side boundaries but also the structure of the mean meridional velocity. One thing needs to be noticed is that the lateral friction may also play a role in the formation of the near-boundary features observed in BAY1 but is ignored here.

Eddy-topography Interactions

Our study in following sections will be focused on the interactions between the open-ocean variability and the slope as well as the bay in the first layer. It has been illustrated in case SB that due to the existence of eddy-topography interactions in the lower layer, a second PV front, denoted as "2" in Fig.4.24, forms over the second-layer slope in the first layer with amplitude much greater than the one in the middle of the channel. It works as a wall separating the domain into two regions whose eddy fields have different features. Northward of it, eddies and meanders are generated from the main jet through baroclinic instability while southward of it, the variability is mostly related to deformations of the second PV front. Therefore, for eddy-topography interactions occurring in the first layer, the second PV front is of great importance. Our first objective in this section is to describe qualitatively the features of the off-slope variability. As the front interacts with the slope and the bay, the front may also be influenced by the slope or bay water that has been driven off the slope and how this happens is the second question that is going to be answered.

To answer those questions, three types of processes are described using time evolution patterns

164

of PV in the first layer over a period of 20 days during the quasi-steady state.

1. Eddy-topography interactions.

There are two types of variability that induce strong interactions and cross-slope exchanges: one is the isolated, pinched-off anticyclones and the other one is the shoreward deformation or meander of the front marked by "A" in the panel of day 236 in Fig.4.32. One formation process of the first type of variability will be described in the following section and the second type of variability forms whenever the front is perturbed. The length scale of the first type variability is at most on the order of the deformation radius. Interactions between a single eddy with length scales of the deformation radius and a slope have been examined thoroughly in Chapter 3. During interactions, a cyclonic eddy forms beside the original anticyclone and then leaves the slope with the anticyclone as a dipole.

The second type has length scales on the order of hundreds of kilometers and behaves more like waves with amplitudes oscillating in time. The meander approaches the slope during its southward growth and leaves as a result of the amplitude decrease. How long the meander stays close to the slope interacting with the topography is mostly determined by the dynamics of the mean flow itself rather than the topographic cyclone generated from interactions. When a shoreward deformation of the front marked by "B" in the panel of day 236 in Fig.4.32, interacts with the slope, due to both the large length scale of the deformation and the eastward mean flow, the slope water leaves the slope in form of a long and thin streamer continuously advected northeastward along the edge of the front. When the streamer gets into the northward crest on the east of the deformation, the anti-clockwise velocity field of the crest works to combine the water columns within the streamer together into a round-shaped cyclone.

2. Interactions between slope cyclones and the shoreward deformations of the front.

Many slope-originated cyclones can be recognized within the region between the front and the slope by their low, strongly negative PV values. After formation, they are usually swept clockwise along the edge of the PV front. Mergings of several small slope cyclones or slope streamers generated from different eddy-topography interaction events into a big, strong cyclone are frequently observed as the one to the west of the shoreward deformation denoted as "B" in Fig.4.32. The
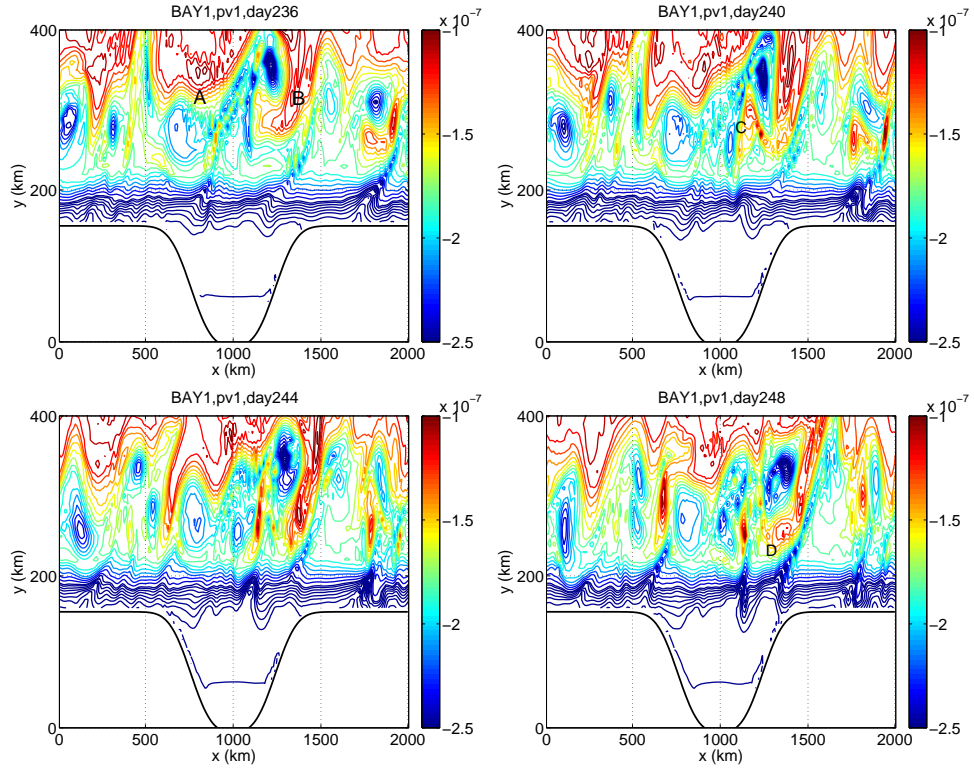
165

Figure 4.32: Case BAY1. Time evolutions of PV contours in the first layer with intervals of $0.1 \cdot 10^{-7} m^{-1} s^{-1}$. The letter "A" denotes the PV front generated by the eddy-topography interactions in the second layer; the letter "B" denotes the shoreward meander of the PV front that interacts with the first-layer slope.
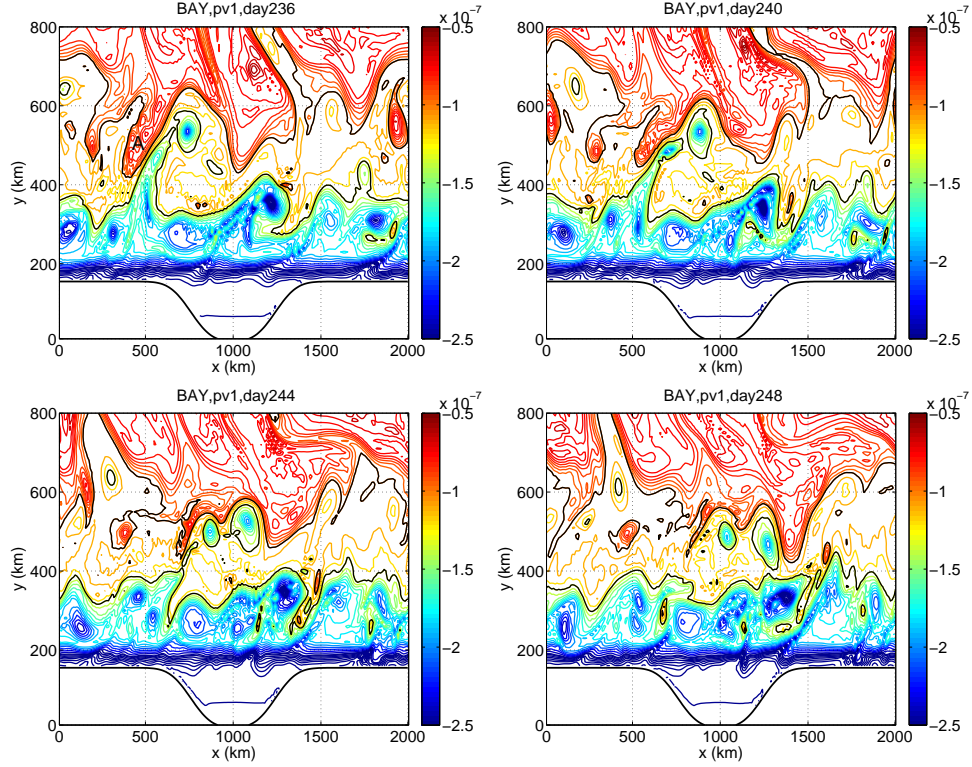
Figure 4.33: Case BAY1. The time evolution of PV contours in the first layer with intervals of $0.1 \cdot 10^{-7}m^{-1}s^{-1}$ for contours with values below $-1.0 \cdot 10^{-7}m^{-1}s^{-1}$ and $0.04 \cdot 10^{-7}m^{-1}s^{-1}$ for contours with values above $-1.0 \cdot 10^{-7}m^{-1}s^{-1}$. The two black contours denote the centers of the two PV fronts. The northern one has the value of $-1.0 \cdot 10^{-7}m^{-1}s^{-1}$ representing the center of the main jet; the southern one has the value of $-1.3 \cdot 10^{-7}m^{-1}s^{-1}$ representing the center of the second PV front. The letter "A" denotes the shoreward meander of the main jet.

slope cyclone advects the shoreward deformation clockwise and at the same time is advected anticlockwise. The result of the interaction between the two is the growth of the deformation into a large meander and finally into an isolated anticyclone, marked by "C" in the panel of day 240 in Fig.4.32. Afterwards, the slope cyclone interacts with the remainder of the meander and another isolated anticyclone, denoted as "D", is about to break off the front at day 248 which may also induce eddy-topography interactions in later time. Generally, due to the interaction with the slope cyclone, the shoreward meander stays for a longer period of time near the slope which may induce more cross-isobath transport.

3. Interactions between the second PV front and the main front.

The second PV front can also generate cyclones when forced by the main jet in the middle of the channel. As shown in Fig.4.33, at day 236, a large shoreward meander of the main front gets very close to the western side of a seaward deformation of the second PV front, denoted as "A" in the first panel of Fig.4.33. As continuously forced by the anti-clockwise velocity field of the big shoreward meander, the seaward deformation grows northeastward and by day 244, a cyclone has been pinched off. The growth of the shoreward deformation of the main jet is, however, prevented by the clockwise velocity field of the seaward deformation of the second front. Actually, the shoreward deformation of the main jet starts to retreat once it gets close to the seaward deformation of the second front.

In summary, the second PV front interacts with the slope generating slope cyclones. Interactions between the front and the slope cyclones enhance the growth of shoreward meanders and lead to generations of anticyclones both of which strengthen interactions with the slope. It is hard to have eddies originated from the main jet cross the second front into the shallow region. But water from the south of the second front can get across the front into the interior in form of cyclones from the seaward deformation of the second front as it is forced by a shoreward meander of the main jet to its west.

Cross-slope/shelf Exchange

As demonstrated in the previous section, during interactions between the second PV front and the first-layer slope, slope-originated water is driven off the slope in form of streamers or isolated cyclones. Using a simple contour dynamic experiment, we showed that the bay-originated water can also be replaced by water from the outside due to the increase of the nonlinearity of the topography-trapped waves. Mechanisms associated with these two processes are fundamentally different, so we name the exchange of water between the first-layer slope and the interior as the cross-slope exchange and the exchange of water between the bay and the outside as the cross-shelf exchange.

The cross-slope/shelf exchanges are examined by simulations of conservative passive tracers. We first describe the set-up of the tracer simulation and then examine the mechanisms important for the cross-slope/shelf exchanges in the interactions between a single anticyclone and the slope as
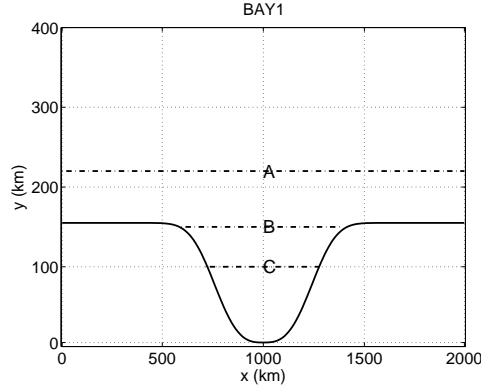
168

Figure 4.34: Tracer initial specification, denoting northern boundaries of regions where tracer A(line denoted as 'A'), B and C are specified as 1 at the starting time.

those in Chapter 3 as well as the effect of the side boundary of the bay on the cross-shelf exchange. Characters of the two mechanisms are also found in cross-slope/shelf exchanges in case BAY1 where there is an energetic mean flow off the slope.

1. Tracer experiment set up.

To study the exchange process, we use the conservative tracer, T, which is advected and diffused according to the following equation:

$$\frac{\partial hT}{\partial t} + \nabla \cdot (\mathbf{u}hT) = 0, \tag{4.32}$$

where h is the layer thickness. T, in units of $kgkg^{-1}$, is the concentration of tracer representing how much tracer is contained within a water body of unit mass. Subtracting the mass conservation equation multiplied by T from the above equation, we get an equation which states that T is conserved following a water column:

$$\frac{\partial T}{\partial t} + \mathbf{u} \cdot \nabla T = 0. \tag{4.33}$$

The conservative-tracer model is used throughout the period from day 12000 to day 26000 when the quasi-steady state has been well achieved. Initially, the tracer concentration is specified as 1 in the area of interest and 0 throughout the rest of the domain. In order to examine exchanges between
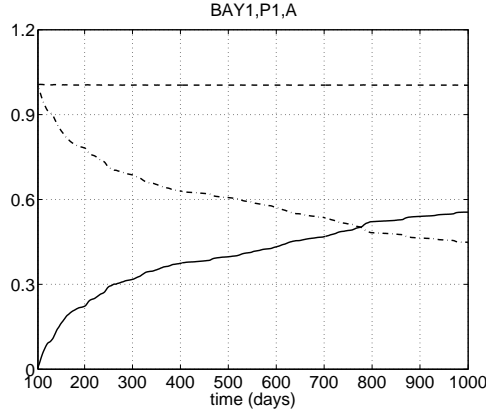
169

Figure 4.35: Tracer conservation test, showing modelled times series of the cumulative mass across the line of $y = 220km$ denoted as dash-dot line, mass of tracer remaining within the region south of the line(solid line), and the sum(dot line). Masses are presented as percentages of initial mass at the starting time.

different regions, three tracers with different initial distributions are simulated as shown in Fig.4.34. Tracer A is specified as 1 within the bay and over the slope in the first layer. It is used to examine the cross-slope exchange. Tracer B is specified as 1 within the bay and tracer C is nonzero only within the southern part of the bay; both of them are used to study the cross-shelf exchange. Throughout the 14000-day simulation, tracer concentrations are re-initialized every 1000 days. In each 1000-day sub-period, tracer concentrations are fixed during the first 100 days and are allowed to evolve according to Eq.4.32 within the remaining 900 days. We choose 900-day as the length of each run because of two reasons. First, it is long enough that features of cross-slope/shelf exchange are well demonstrated. Second, limited by computation ability, we can not afford to have many model runs with lengths much longer than 1000 days.

The conservation of tracer by the model is tested by examining the mass of tracer A remaining within the region south of the first-layer slope edge, $y = 220km$, and the cumulative mass of tracer A transported across that line. The sum of the two should be equal to the initial mass of the tracer. Time series of these three variables as shown in Fig.4.35 are taken from the first sub-period from day 12100 to day 13000. The difference between the total mass and the mass at the starting time remains smaller than 0.3% during the whole simulation.

There are altogether 12 periods recorded within the simulation. We take the first period, P1, between day 12100 and day 13000 as a standard case to study in detail the exchange process, and

170

then examine similarities as well as differences among all periods.

2. A review of results from Chapter 3: Interactions between a single eddy and the slope without the jet in the open-ocean.

Before we start to examine cross-slope/shelf exchange in BAY1, we first review some results of Chapter 3 about important mechanisms of the cross-isobath exchange in interactions between a single anticyclone and a slope.

Two eddy-topography interaction experiments are performed on a f plane in the Southern Hemisphere. In both of them, the cross-isobath transport is induced by the same off-slope anticyclone located at the same position of $x = 1000km$, $y = 300km$. There is no mean flow in the channel. Initially, the PV in the first layer is perturbed within a circle with radius of $50km$ as

$$
q_1 = \begin{cases} \dfrac{f(1+\alpha)}{H_1} & \text{if } r <= r_0 \\ \dfrac{f}{H_1} & \text{otherwise,} \end{cases}
$$

where $\alpha = -0.3$, $r_0 = 50km$ and H_1, the resting layer thickness, is $650m$, intersecting the slope at about $y = 220km$. The model domain as well as the bottom topography in the first case(case S1) is the same as that in BAY1; in the second case(case S2), the same bottom topography is applied, but instead of a curved coastline, a zonal wall is located along $y = 0$ as the southern boundary. The concentration evolution of tracer A and B are also simulated in the two cases. The 0-1 interface is the latitude of $y = 220km$ for the concentration of tracer A and the latitude of the bay opening for tracer B.

Shown in Fig.4.36 is the time evolution of PV contours in case S1. After the model is started, PV contours over the slope and to the south of the anticyclone are forced seaward and this seaward deformation pushes contours to its east southward into a shoreward deformation. The anticyclone's swirl velocity declines away from the eddy center and the zonal length scale of the seaward deformation is on the order of the deformation radius, much smaller than the zonal length of the slope. As the forcing continues, the northern part of the seaward deformation extends beyond the slope in form of a streamer advecting the off-slope anticyclone northward. Its southern part remains on the
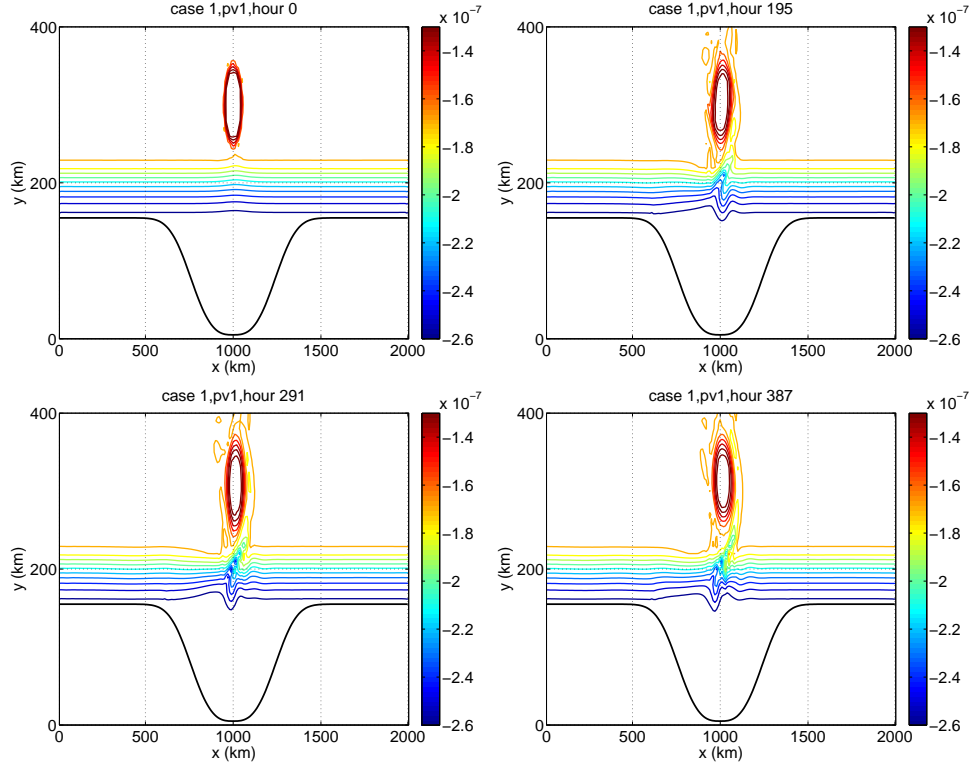
Figure 4.36: Case S1. The time evolution of PV contours during the interaction between an anticyclone and the slope with intervals of $0.1 \cdot 10^{-7}s^{-1}$.

slope and orientates southwest-northeast as influenced by the westward-propagating topography-trapped waves. During the interactions, the seaward deformation persists around $x = 1000km$ since the zonal drift of the anticyclone is negligible compared with the length of the channel. There are also shoreward perturbations generated by the seaward deformation on its east and away from the slope edge.

In case S1, the northward flux of tracer A across the slope edge is concentrated within the region of the seaward deformation of PV contours and within about 15 days as shown in the first panel of Fig.4.37. On the longitude-time diagram of the flux of tracer B across the bay opening, besides the bright patch centered around $x = 1000km$ representing the transport directly driven by the anticyclone, a crest and a trough propagating westward from around $x = 1000km$ can also be recognized. For a fixed location along the bay opening westward of $x = 1000km$, water particles are advected northward across the opening with the arriving of the crest of PV contours and then
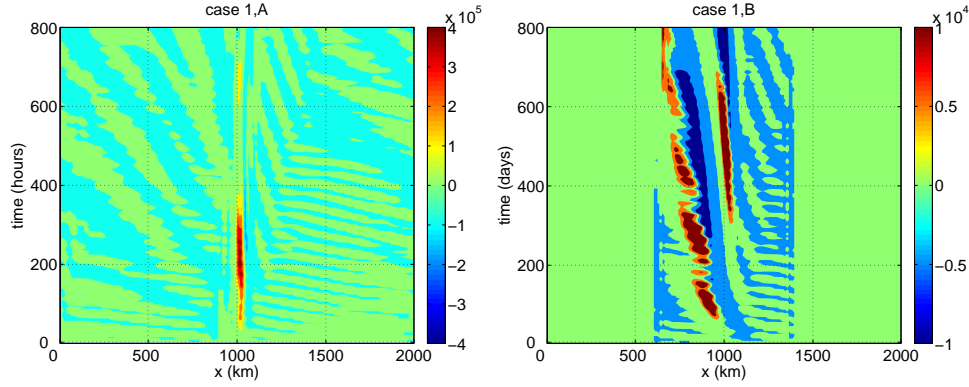
Figure 4.37: Case S1. Left panel: the longitude-time diagram of tracer A flux across the slope edge. Right panel: the longitude-time diagram of tracer B flux across the bay opening.

moved back as the trough approaches.

On the plot of the transport of tracer A across the slope edge against x in Fig.4.38, there are two pulses of differing signs right next to each other around $x = 1000km$. The positive pulse has much greater amplitude representing the formation of the streamer from the slope; the negative pulse to the east has much smaller amplitude representing the reversing of some tracer advected back onto the slope by the streamer's clockwise velocity field. The zonal range covered by the two pulses is less than $200km$ and no contributions come from regions outside.

On the plot of the transport of tracer B across the bay opening, besides the pulse around $x = 1000km$, there are also contributions from other regions within the bay opening, and the amplitude of the cross-shelf transport westward of $x = 1000km$ is as big as that corresponding to the anticyclone. Differences of the two mechanisms are thus clearly demonstrated: the cross-isobath transport mostly driven by the off-slope anticyclone is localized within a region with length scales on the order of the deformation radius, while the cross-isobath transport induced by the wave mechanism takes place within a much wider region especially in the direction of the wave propagation. Along the slope edge, the advection by the off-slope anticyclone is apparently much stronger than that by the waves, so the cross-slope transport is highly concentrated in x. Along the bay opening, the anticyclone's effect declines to become comparable with that of the waves, so the cross-shelf transport shows not only the pulse-like character of the eddy effect but also the westward-spreading character of the wave effect. In other words, along the slope edge, the wave mechanism may act to
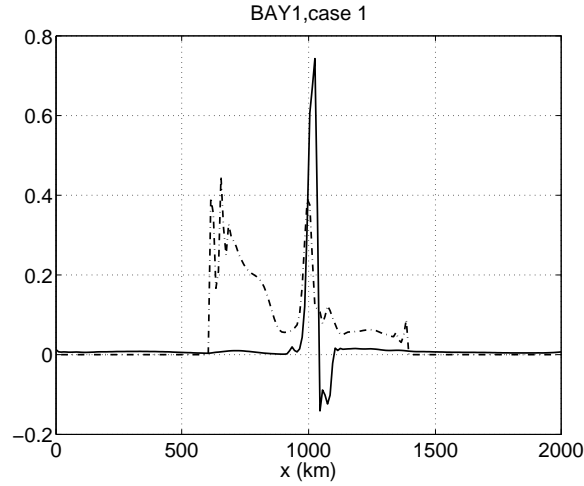
Figure 4.38: Case S1. The total transport within 40days against x. The solid line is the transport of tracer A across the slope edge in units of $10^8 kgkg^{-1}m^3$; the dash-dot line is the transport of tracer B across the bay opening in units of $10^7 kgkg^{-1}m^3$. The southern boundary of the model domain in this case is the same as that in BAY1.

prevent the cross-isobath transport, but along the bay opening and away from the anticyclone, the wave mechanism enables water particles to move quickly in y and be more likely to escape from their original isobaths. In this sense, the wave mechanism enhances the cross-isobath transport.

As revealed by Fig.4.38, the transport of tracer B across the bay opening tends to be enhanced near the western edge of the bay with the amplitude similar to that right to the south of the off-slope anticyclone. This feature suggests the possible effect of the side boundary, so it is necessary to study the second case. In case S2, we use the same anticyclone, the same slope profile but change the southern boundary of the model domain into a zonal wall along the latitude of $y = 0$ to remove the effects of the western side boundary. Without the blocking effect of the side boundaries, the topographic waves propagate freely westward, along with which tracers are transported across the isobath through oscillatory motions. Differences of the tracer B flux between case 1 and 2 not only exist without the zonal range of the bay opening but also near the longitude of the western side boundary of the bay, where the tracer flux is intensified (Fig.4.39). Meanwhile, the cross-slope transport of tracer A show little difference between the two cases which means the bay's boundary in case 1 is too far away from the slope edge to have any noticeable effect on the cross-slope exchange.
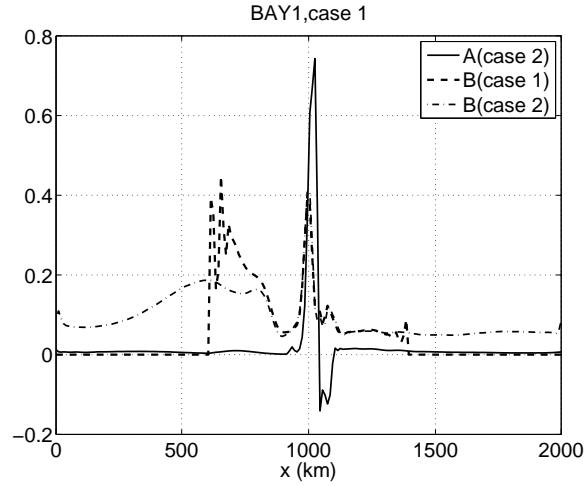
Figure 4.39: Case S2. The total transport within 40days against x. The solid line is the transport of tracer A across the slope edge in units of $10^8 kgkg^{-1}m^3$; the dash-dot line is the transport of tracer B across the latitude of bay opening in units of $10^7 kgkg^{-1}m^3$. The southern boundary of the model domain in case S2 is along $y = 0$. The thick dash line is the transport of tracer B across the bay opening in units of $10^7 kgkg^{-1}m^3$ in case S1.

The enhancement of the cross-shelf exchange near the western side boundary in case S1 is due to the same mechanism explained through the contour dynamics experiment in Fig.4.31. Blocked by the western side boundary, topographic waves' length scales are shortened towards the western edge resulting in the increase of waves' amplitudes and strengthening of particles' cross-isobath motions.

In summary, in the two cases of interactions between a single off-slope anticyclone and the topography without the presence of the mean flow, two mechanisms important for the cross-isobath transport are identified. The first mechanism is the advection by the off-slope anticyclone. It is characterized by the concentration of strong cross-isobath transport within the region of the seaward deformation of PV contours that is directly generated by the anticyclone. The second mechanism is the meridional oscillation due to the topography-trapped waves. It is characterized by the westward expansion of the region of cross-isobath transport. Shoreward of the slope edge, the effect of the second mechanism becomes more prominent but the effect of the first mechanism weakens. Provided that the zonally integrated cross-isobath transport declines quickly shoreward, the first mechanism dominates the cross-isobath exchange. Along a specific isobath, the amplitude of the cross-isobath transport induced by waves is usually much weaker than that induced by the anticyclone except
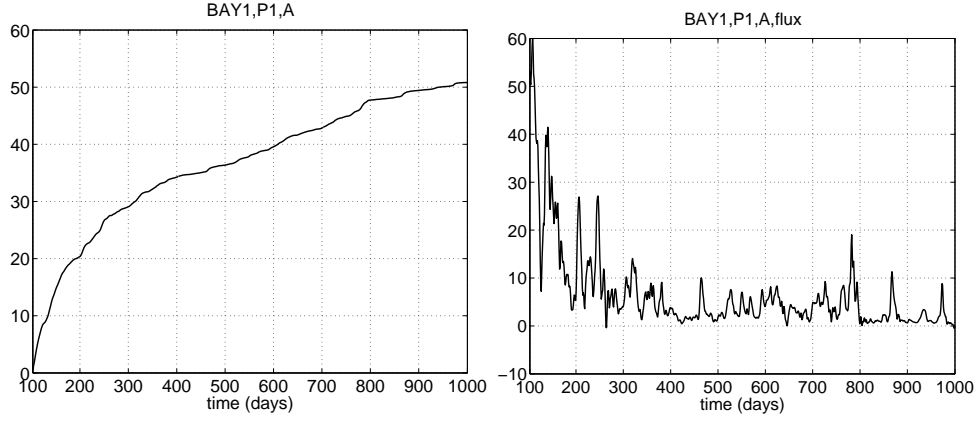
175

Figure 4.40: Case BAY1, P1. Left panel: time series of the cumulative mass of tracer A transported across the latitude of $y = 220km$ in units of $10^{12} kg kg^{-1}$. Right panel: time series of the mass flux of tracer A across the latitude of $y = 220km$ in units of $10^5 kg kg^{-1} s^{-1}$.

near the western side boundary which can block the propagation of the topographic waves. In other words, the effect of the second mechanism can be greatly amplified when the propagation of waves is disrupted by a side boundary.

In case BAY1, anticyclones or anticyclonic meanders are spontaneously generated from the mean flow continuously interacting with the slope, so the eddy-topography interaction in BAY1 is at least seemingly much more complicated than that in case S1. Whether the mechanisms found important for the cross-isobath exchange in case S1 or S2 are also important for the case BAY1 and if so, are there any new features in BAY1 compared with that in case S1? These two questions are going to be answered in the following three parts.

3. Cross-slope exchange in P1, the period from day 12100 to day 13000.

As shown by the first panel of Fig.4.40, the cumulative mass of tracer A transported across the latitude of $y = 220km$ increases smoothly and within 900 days more than 50% of the tracer mass was lost from the first-layer slope.

Fig.4.41 shows the time evolution of tracer A concentration within the domain in P1. As the tracer is transported into the interior by off-slope variability, the tracer concentration over the slope declines resulting in the slow-down of tracer transport at later times as demonstrated by both panels in Fig.4.40. In addition, the main and the second jets can also be clearly observed from tracer

176

distributions as two fronts of closely-located concentration contours: one is around $y = 600km$ and the other is around $y = 400km$. A cyclone, denoted as "A" in the panel of day 800 in Fig.4.41, is seen detaching from the main jet.

The mechanism that is most important for the cross-slope transport of tracer A in P1 is the generation of slope streamers or cyclones during eddy-topography interactions and is also the first mechanism found in case S1 and S2. For a fixed location along the slope edge, the approaching of anticyclonic eddies or meanders is intermittent. Consequently, the time series of the meridional tracer flux shown in Fig.4.42 consists of a few large-amplitude pulse-like events separated by big intervals of quieter periods. Accompanying each exchange event, large and negative PV anomalies above the time average occur along the latitude of $y = 220km$ as shown in the right panel of Fig.4.42 suggestive of strong fluxes of the slope water being advected off the slope by offshore variability.

In the longitude-time diagram of the tracer flux across the slope edge between day 100 and day 200 (days are counted from the beginning of P1) in Fig.4.43, strong eddy-topography interaction events are recognized as bright patches. Due to the eastward drift of off-slope eddies or meanders with the mean flow, the zonal position of the maximum flux during one single event moves eastward with time and the bright patches in the longitude-time diagram of the cross-slope flux orientate southwest-northeast, different from that in case S1 as shown in the first panel of Fig.4.37. The strongest exchange event starts from day 130 around $x = 1250km$ lasts for about 30 days and covers more than $250km$ along the slope edge. Other events usually last for about 10 days and cover shorter zonal ranges even when their peak amplitudes of the flux are as big as the aforementioned one.

Defining an exchange event as an area surrounding the local maximum in the time-space diagram of the tracer flux across the slope edge and bounded by the $x - t$ contour along which the tracer flux drops to e^{-1} of the maximum value in the center, we can locate all events occurred during P1 and calculate transports accomplished by each of them. Sorted by the maximum flux during an event, 20 strongest events are identified from P1 carrying 35.0% of the total transport across the latitude. Because the tracer concentration to the south of $y = 220km$ declines with time, more strong events are found during the early intervals of P1: 16 of 20 are between day100 and day400 with
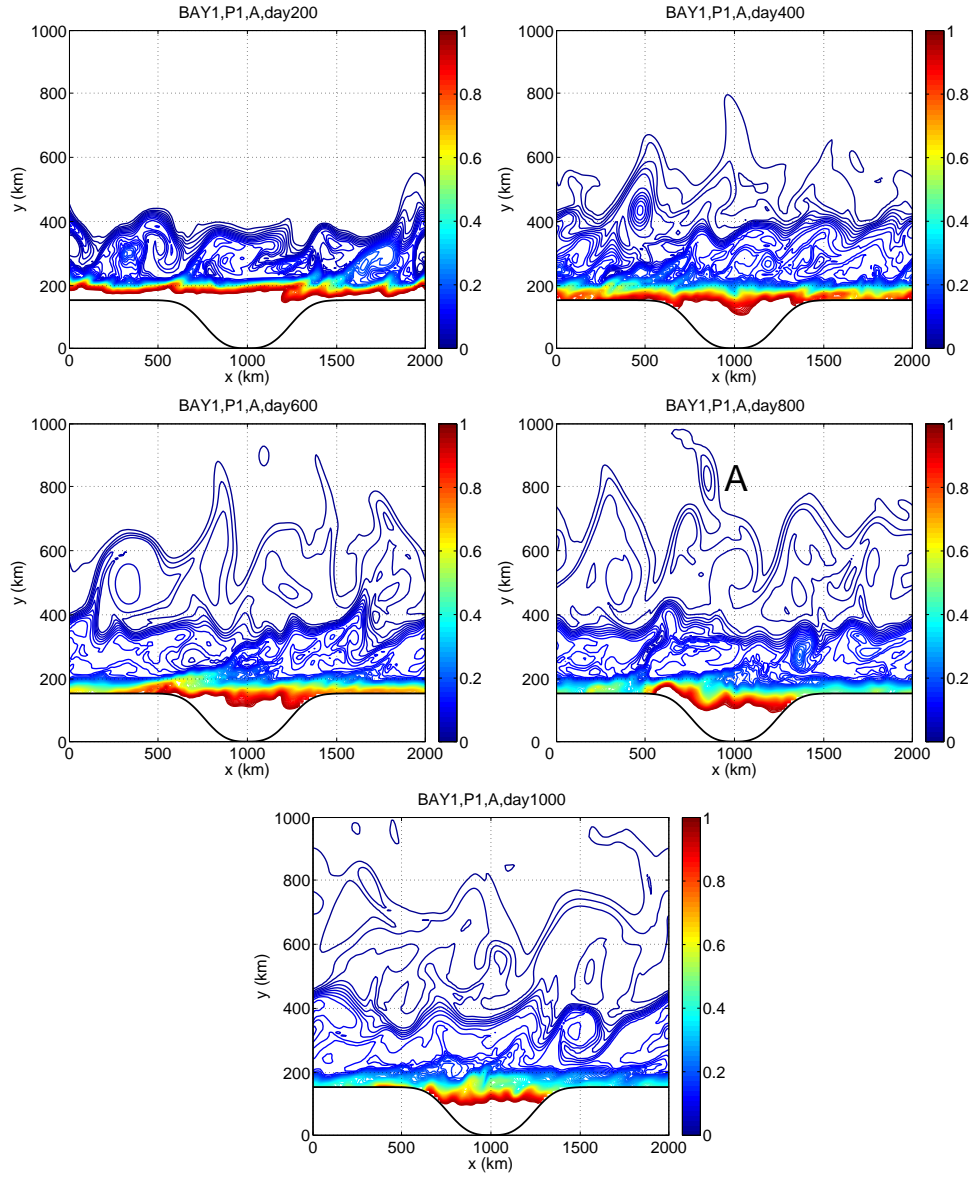
Figure 4.41: Case BAY1, P1. The time evolution of contours of tracer A concentration with intervals of $0.01 kg kg^{-1}$. The range of concentration plotted is between $0.01 kg kg^{-1}$ and $0.95 kg kg^{-1}$. The region to the south of the contour with highest value is filled with tracers with concentration higher than $0.95 kg kg^{-1}$.
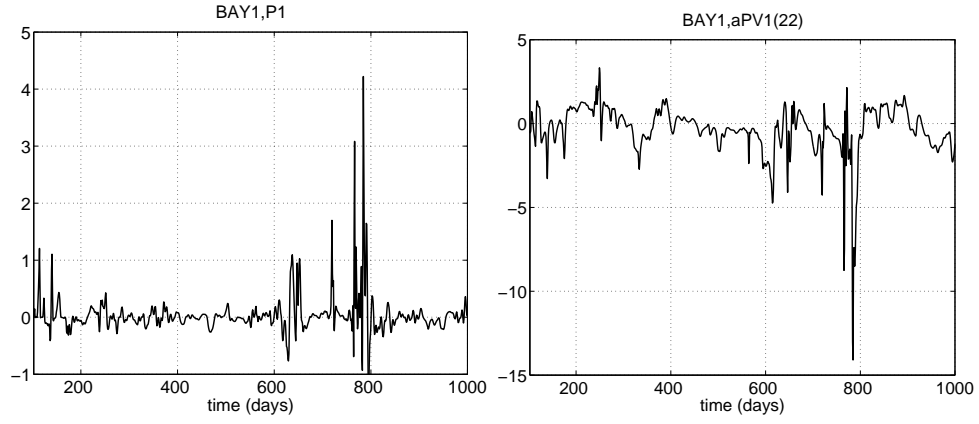
Figure 4.42: Case BAY1, P1. Left: time series of tracer A flux across the slope edge at $x = 1000km$ in units of $10^5 kgkg^{-1}m^3s^{-1}$. Right: time series of the first layer PV anomaly along the slope edge in units of $10^{-8}m^{-1}s^{-1}$.

Figure 4.43: Case BAY1, P1. Longitude-time diagram of tracer A flux across the slope edge at $x = 1000km$ during between day100 to day 200 in P1. The unit is $10^5 kgkg^{-1}m^3s^{-1}$.

Figure 4.44: Case BAY1, P1. Left panel: occurring time and zonal location of 17 strongest exchange events. Right panel: transport of each event in units of $10^{12}kgkg^{-1}m^3$.
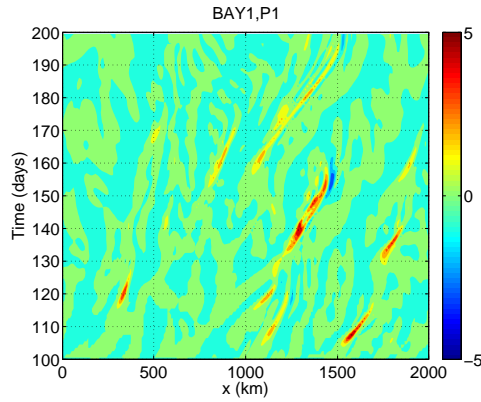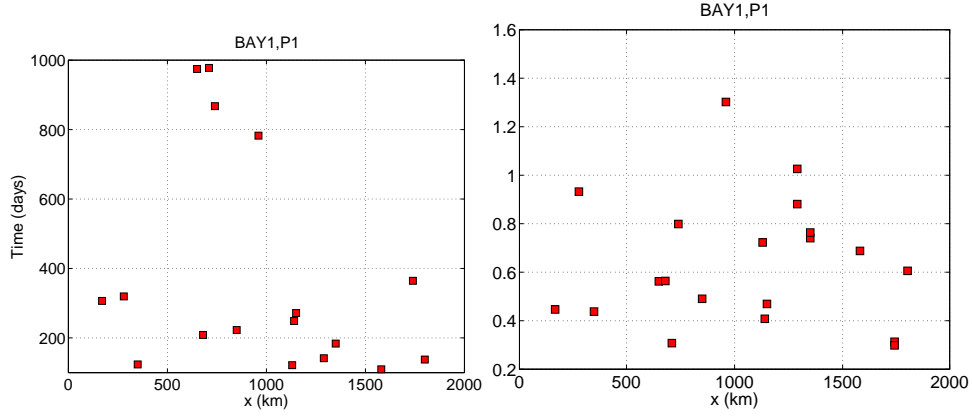
28% of the total transport. No zonal position discrimination for these events are observed. Since the tracer concentration has little zonal variation as shown in Fig.4.41, there is no space discrimination for occurence of ancyclonic eddies or meanders near the slope if the zonal location is defined as the location for the maximum flux during an event as in Fig.4.44. This feature means that the eddy-topography interaction is generally homogeneous along the slope edge within time scales on the order of 100 days. The time durations of these events are on the order of 10 days and most of them are between 10-20 days. The magnitude of the strongest event is on the order of $10^{12}kgkg^{-1}m^3$, similar to that in case S1 and S2. Therefore, on average, the advection by the offshore variabilities over the slope is much weaker than that of the anticyclone simulated in case S1.

Since the tracer concentration quickly declines over the slope while it increases off the slope as the eddy-slope interaction goes on, the tracer mass flux across the slope edge during the later period of the 900 days may underestimate the volume of the water driven off the slope. An estimate is made using the tracer mass flux during the first 100 days of the experiment and the resulting zonal mean volume flux is about $1.19m^3s^{-1}$, comparable with the Ekman transport which is about $1.36m^3s^{-1}$ at the center of the channel.

4. Cross-shelf exchange in P1

Differences between the cross-slope and cross-shelf exchanges in P1 are demonstrated by time series of the cumulative mass of tracer B and C transported across the opening of the bay in Fig.4.45.

180

First, the cross-shelf exchange process is much less efficient. The zonal mean transport of tracer A across the slope edge within 900days is about $2.54 \cdot 10^7 kgkg^{-1}$ while the zonal mean transport of tracer B across the bay opening during the same period is only about $1.08 \cdot 10^7 kgkg^{-1}$, less than 50% of the former. Second, the cumulative mass of tracer B transported across the bay opening is not increasing monotonically with time as that of A across the slope edge. There are some periods of reversing fluxes of B, when the return of the mass that has been driven out of the bay exceeds the northward flux, so the cumulative mass declines temporally. The reversing flux is more prominent in the time series of the tracer flux at a fixed location along the bay opening as shown by the plot in Fig.4.46. The right panel in Fig.4.46 shows the PV anomalies above the time mean PV value along the latitude of $y = 180km$, half way between the slope edge and the bay opening. Different from those along the slope edge which are composed of strong, negative spikes (Fig.4.41), the PV anomalies along $y = 180km$ oscillate with similar negative and positive amplitudes, and only strong exchange events can be identified like the one taking place around day 800. Both the time series of PV anomalies and tracer fluxes show that shoreward from the slope edge, the physical process changes dramatically from being dominated by eddy advection to significantly influenced by wave motions. The zonal mean volume flux across the bay opening is about $0.4m^3s^{-1}$, estimated as the mean mass transport of tracer B during the first 100 days of P1. If the wind stress within the bay is not zero, but grows, by the same sinusoidal profile used in the model, from the southern tip of the bay, the Ekman transport along the bay opening would be about $0.4m^3s^{-1}$, comparable with that by the offshore current. Therefore, the mechanism studied in the thesis is at least not negligible compared with the surface wind in driving the water offshore, and more likely, it is as important as the wind mechanism could be.

Up to now, we have shown that both mechanisms found important for the cross-isobath exchange in interactions between a single anticyclone and the slope are also important for the cross-slope/shelf exchanges in BAY1. Since the transport driven by the first mechanism is highly concentrated in space, the cross-slope exchange in BAY1 can be regarded as the sum of the cross-slope exchange from many independent interaction events occurring at different time and different zonal locations and between different anticyclones and the slope. As to the second mechanism, waves excited during different eddy-topography interaction events unavoidably interact with each other, so the net
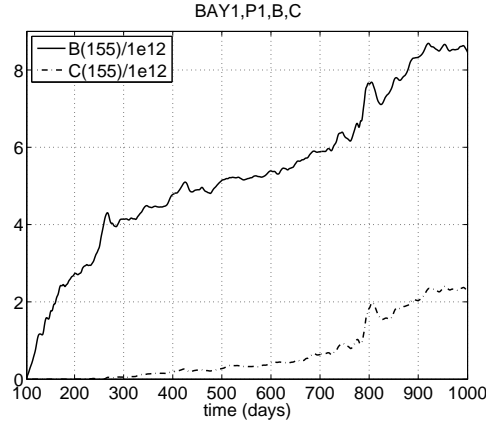
Figure 4.45: Case BAY1, P1. Times series of the cumulative mass across the opening of the bay in units of $10^{12}kgkg^{-1}m^3$. The solid line denotes the mass of tracer B and the dash-dot line denotes the mass of tracer C.
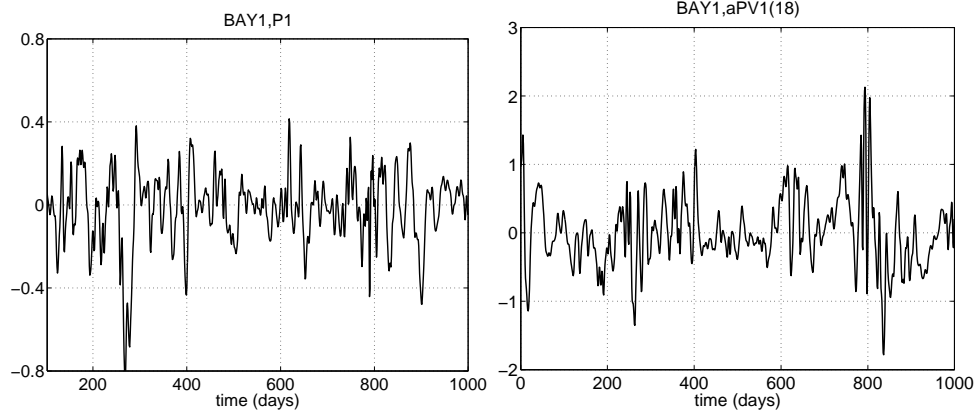
Figure 4.46: Case BAY1, P1. Left: time series of tracer B flux across the bay opening at $x = 1000km$ in units of $10^5kgkg^{-1}m^3s^{-1}$. Right: time series of the first layer PV anomaly along the slope edge in units of $10^{-8}m^{-1}s^{-1}$.
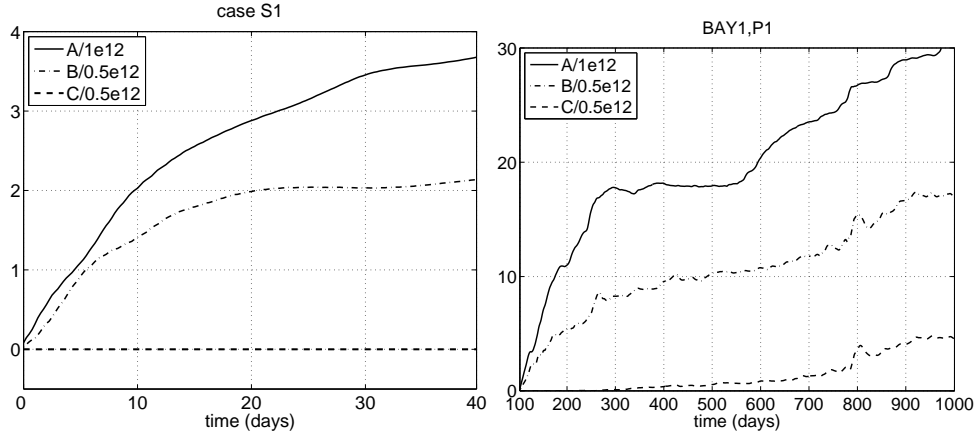
Figure 4.47: Case BAY1, S1—P1. The solid lines denote the time cumulative mass of tracer A transported across the slope edge in units of $10^{12}kgkg^{-1}m^3$; the dash-dot lines denote the time cumulative mass of tracer B transported across the bay opening in units of $0.5 \cdot 10^{12}kgkg^{-1}m^3$, and the thick dash lines denote the time cumulative mass of tracer C across the bay opening in units are $0.5 \cdot 10^{12}kgkg^{-1}m^3$. The left panel is for case S1. The right panel is for P1 and only fluxes of tracer A within the zonal range of the bay opening are used to produce the time series.

effect may not be equal to the sum of the effects from different events. A comparison of the cross-isobath transport between the single-eddy-slope interaction case and BAY1 is made as follows.

The plots in the left panel of Fig.4.47 give us a sense of how the cross-isobath transport varies shoreward in the single-anticyclone-slope interactions. In case S1, the total transport of tracer A across the slope-edge is about 3 times greater than the total transport of tracer B across the bay opening, and during the same period of time, the transport of tracer C, which is originally distributed southward of the latitude of $y = 105km$, across the bay opening is basically 0, which means all the water that could get out of the bay is originally distributed northward of the latitude of $y = 105km$. Furthermore, all the water that gets off the slope during the 40 days comes from the sloping region northward of the bay suggesting that the anticyclone's effect in driving water off the slope stops somewhere over the slope and can not reach into the bay.

The right panel in Fig.4.47 is made in the same way as the left one except that in calculating the cross-slope transport of tracer A, only the fluxes within the zonal range corresponding to the bay opening are considered. The ratio between the transport of tracer A across the slope edge and the transport of tracer B across the bay opening is a little smaller than that in the single-eddy-

183

slope interaction case. As mentioned before, the average offshore variability is weaker than the anticyclone in case S1 in driving the water off the slope, so it is not surprising that the ratio between the tracer A and B is smaller in P1. However, in P1, among the mass transported out of the bay, which is about $8.4 \cdot 10^{12} kgkg^{-1}m^3$, around $2.23 \cdot 10^{12} kgkg^{-1}m^3$ comes from the region southward of $y = 105km$. This result suggests that as the offshore variability continuously forces the shelf and generates the topography-trapped waves, particles further inside the bay can move across the shelf and get out of the bay. The drifts of tracers towards the bay opening must be slow since it is sometime after day 300 that the transport of tracer C out of the bay becomes distinguishable from zero. The northward drift speed can be roughly estimated by taking the distance between the latitude of $y = 105km$ and the bay opening as the net drift during 200 days, and the result is $0.0029ms^{-1}$. This is probably an overestimate of the actual drift speed for tracers since they may not move along a straight path. How the tracers are transported out of the bay can be seen from the time evolution of tracer distributions.

As in case S1 and S2, the effect of the wave mechanism is most significant near the western boundary of the bay. Since the bay is flat-bottomed, amplitudes of the topography-trapped waves decay southward inside the bay. Water columns that are well inside the bay are therefore less influenced by both mechanisms and the tracer concentration increases southward within the bay in Fig.4.48 as well as over the slope in Fig.4.41. But different from those patterns in Fig.4.41which show little zonal variation of tracer concentration except near the southern boundary of the channel, the concentration of tracer B near the western boundary becomes appreciably higher than other regions along the same latitude after about day 600. In the pattern of day 1000 in Fig.4.49, concentration contours are aligned with the western boundary but almost perpendicular to the eastern boundary. The pattern of day 800 shows strong similarity to the PV interface pattern at $t = 14.0$ in Fig.4.31, so the high tracer concentration along the western boundary is also related to the strengthening of the nonlinear effects towards the western boundary as in case S1 and also in Fig.4.31. When a shoreward deformation of PV interface comes near the western boundary, it is blocked by the solid wall and at the same time squeezed by the following seaward deformation. The strengthened nonlinear effect amplifies the northward velocity along the western boundary, so the nearby concentration contours are more meridionally orientated and a large amount of tracer mass is ad-

184

Figure 4.48: Case BAY1, P1: The time evolution of contours of tracer B concentration with interval of $0.01kgkg^{-1}$. The range of concentration plotted is between $0.01kgkg^{-1}$ and $0.95kgkg^{-1}$. The region to the south of the contour with highest value is filled with tracers with concentration higher than $0.95kgkg^{-1}$.

vected westward with the seaward deformation of the PV interface over the western edge of the bay. After moving into the channel from the bay, the blob of tracer mass is more influenced by the mean flow as well as variability off the slope, so with the presence of strong eddies or meanders nearby off the slope, its westward motion along the boundary is reversed with some of the mass driven northward off the slope and some advected back into the bay. The strong interaction between the topography-trapped waves and the western boundary occurs intermittently as represented by the events of the strong flux along the boundary in the longitude-time diagram of tracer B in Fig.4.49. Events of strong westward flux near the western end of the bay are prominent and some of them are followed by strong reversing fluxes. For example, during the event occurred around day 800, a big blob of tracer mass is advected out of the bay through its western edge, but due to a large meander that arrived at the western edge at about the same time, part of the blob is advected back into the bay and a large amount of tracer is driven off the slope by the meander. Due to the large size of tracer mass contained within the blob, its escape from the bay and its return to the bay strongly influenced the total tracer flux across the opening. Therefore, we can clearly see a steep increase followed by a quick decline on the plot of tracer B in Fig.4.48. In the longitude-time diagram of the eastern side boundary in Fig.4.49, amplitudes of fluxes are much weaker and no such events are observed.

Fig.4.49 also shows the longitude-time diagram of the flux of tracer C along the boundary, in which the strong westward flux events are observed around the western edge of the bay at about the same time as those events of tracer B. This indicates that the strong interaction between the topography-trapped waves and the western boundary acts to drive the water that lies further inside the bay onto the slope. Much more tracer C is observed to be transported out of the bay near its western boundary as shown in Fig.4.50.

Aside from tracer A, B, and C, the other six tracers BW, BE, CW, CE, DW, and DE are simulated during the period P1 with different initial distributions as illustrated in Fig.4.51. The time evolutions of tracer concentration in Fig.4.52, 4.53, and 4.54 reveal motions of tracer particles within different regions of the bay.

Near the bay opening, i.e., northward of $y = 105km$, tracer particles move northward onto the slope by the wave motions (Fig.4.52). Since the wave motions tend to be stronger near the western

186
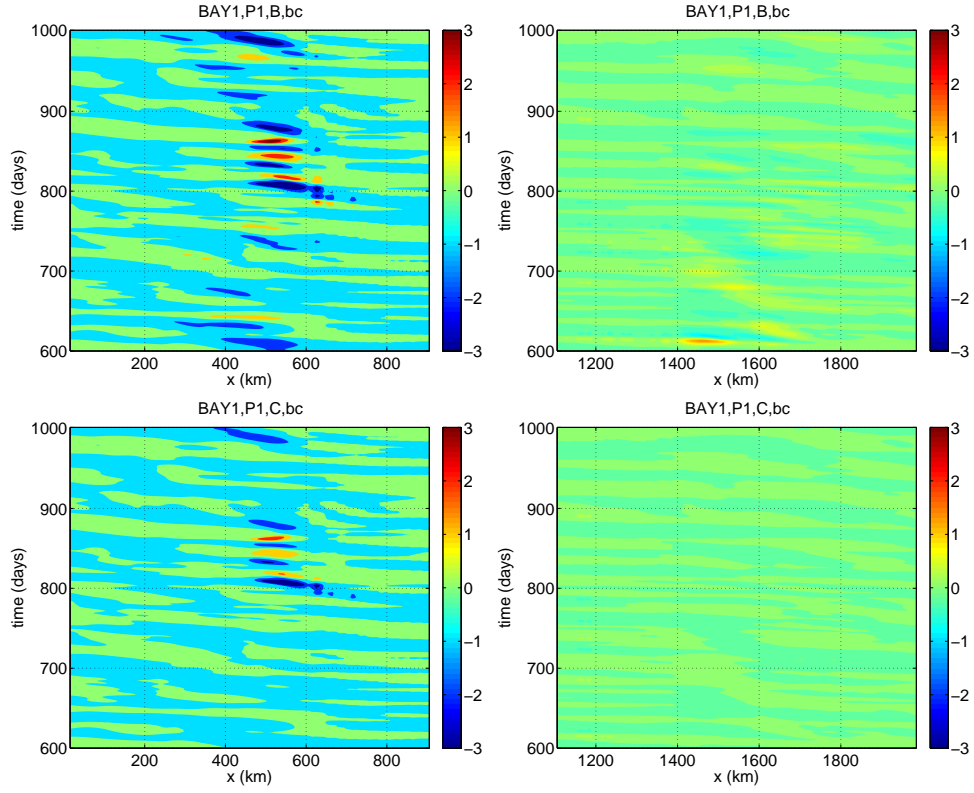
Figure 4.49: Case BAY1,P1. Fluxes along the boundary of the bay of tracer B (upper) and tracer C (lower) in units of $10^5 kgkg^{-1}m^3s^{-1}$.
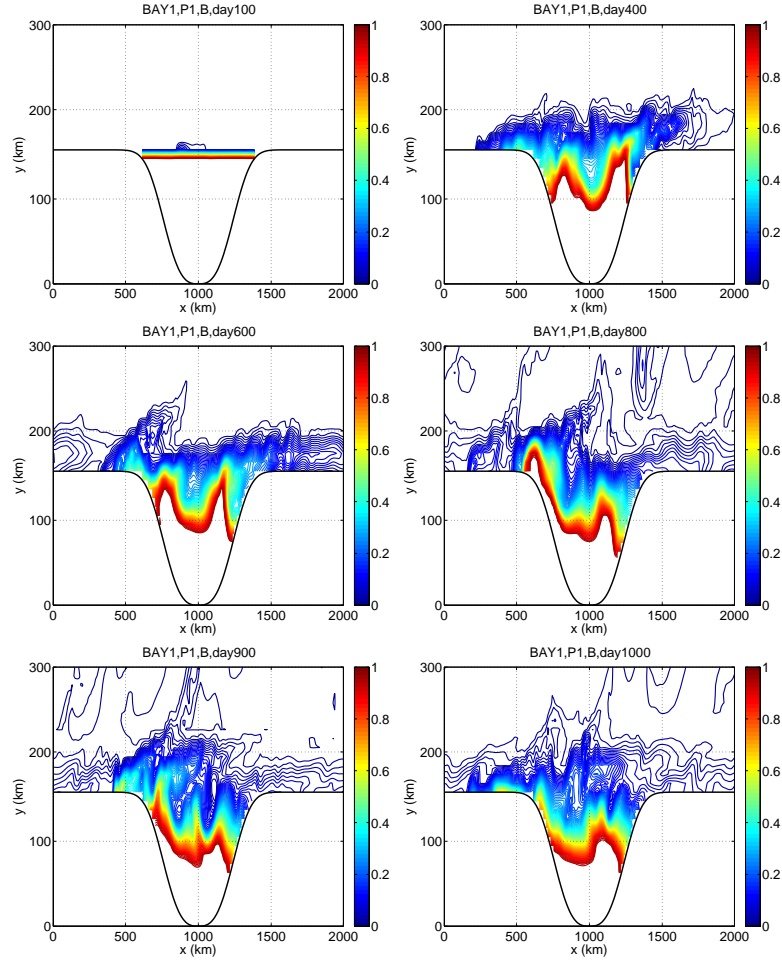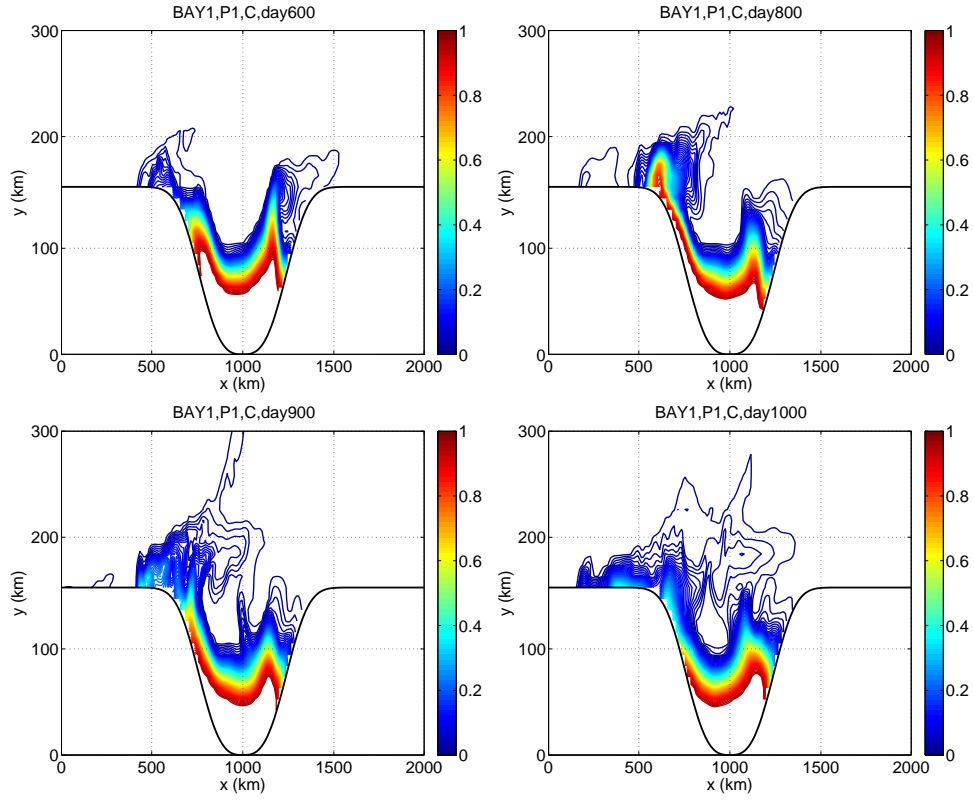
Figure 4.50: Case BAY1, P1. The time evolution of contours of tracer C concentration with interval of $0.01kgkg^{-1}$. The range of concentration plotted is between $0.01kgkg^{-1}$ and $0.95kgkg^{-1}$. The region to the south of the contour with highest value is filled with tracers with concentration higher than $0.95kgkg^{-1}$.
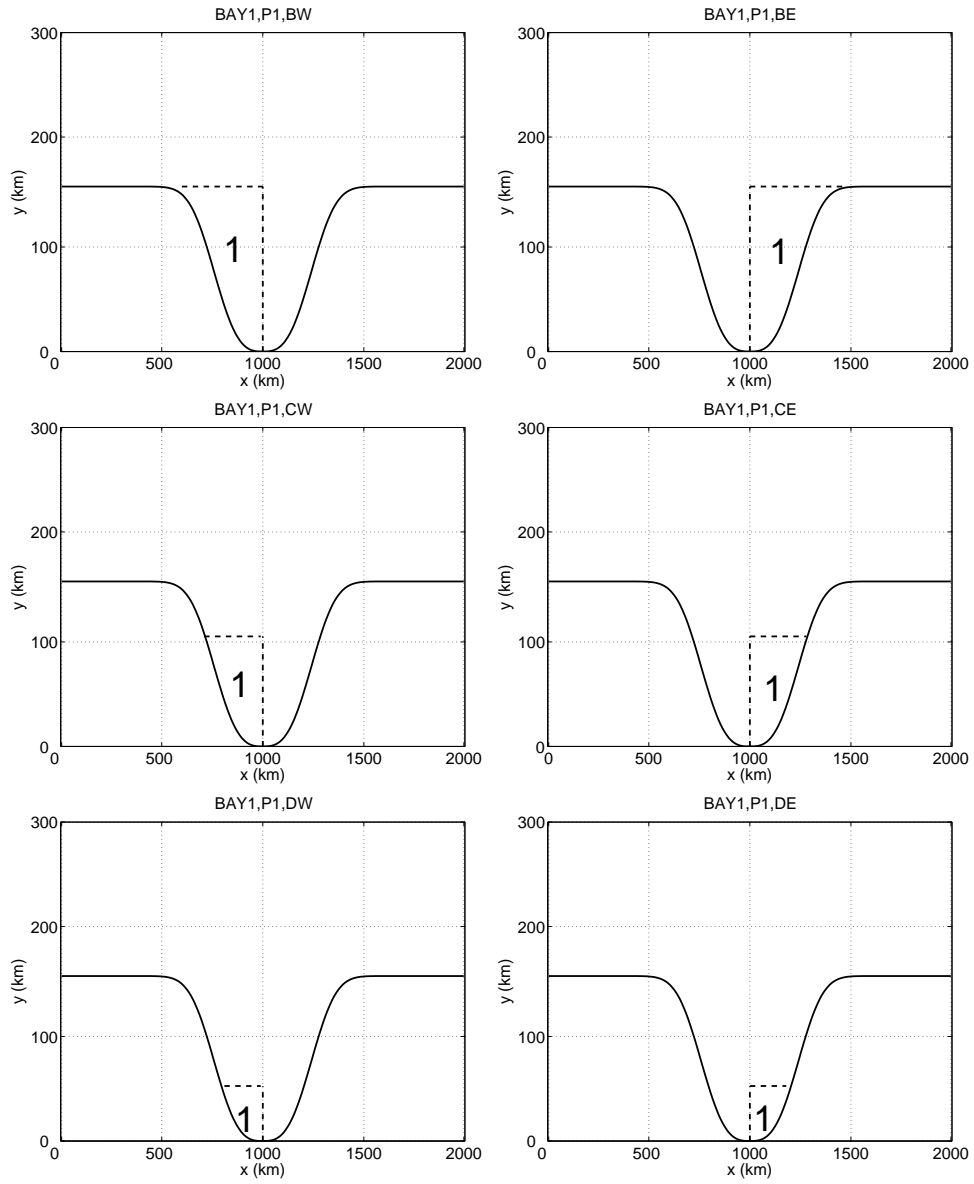
Figure 4.51: Case BAY1, P1. The initial distribution of trace BW (upper left), tracer BE (upper right), tracer CW (middle left), tracer CE (middle right), DW (lower left), and tracer DE (lower left). In the area that is enclosed by the bay's boundary and the thick dash line, the tracer concentration is initially 1, and 0 otherwise.

189

boundary due to the interaction with the boundary, more tracer particles move out of the bay from the west. During 900 days, the total mass of tracer B transported out of the bay from west of the central longitude is about $6.10 \cdot 10^{12} kg kg^{-1} m^3$, about 3 times the total mass transported from the east. After tracer particles get onto the slope, they generally move eastward with the mean flow, but sometimes near the western edge of the bay, they can move westward a little bit by strong wave motions before being caught by the mean eastward jet. Inside the bay and away from the boundaries, tracer particles tend to move westward towards the western boundary.

Further shoreward, the difference of the tracer particle motions between the western and the eastern part of the bay becomes more prominent (Fig.4.53). Tracer particles tend to move westward to the west of the central longitude while eastward to the east. Near the western boundary, particles move northward along the boundary out of the bay with strong wave motions and may continue their westward drift along the coast. On the other hand, tracer particles to the east of the central longitude may also move northward towards the bay opening, but the motion is much weaker compared with those in the west.

As displayed in Fig.4.54, tracer particles that originate near the western boundary and close to the southern tip of the bay may move all the way out of the bay along the boundary, while tracer particles near the eastern boundary move very little during the same period of time. Therefore, the southeastern part is probably the most isolated area compared with other regions of the bay.

In the Lagrangian point of view, we focus on 8 particles with different initial positions and follow their motions by integrating the Eulerian velocity field with necessary interpolations. The motions of these particles as reflected by their trajectories in Fig.4.55 are generally consistent with what we concluded from the evolutions of tracer concentration in that all particles tend to move westward within the bay and particles near the western boundary move northward along the boundary. Aside from that, the trajectories also suggest that particles originating near and to the east of the central longitude move southwestward. This result is consistent with the tracer evolution in Fig.4.50, from which the intrusion of the slope water is in the middle and east of the bay.

The cross-slope/shelf exchange has been studied in detail for the period P1. Similar to the cross-isobath exchange in interactions between a single anticyclone and the slope without the presence of
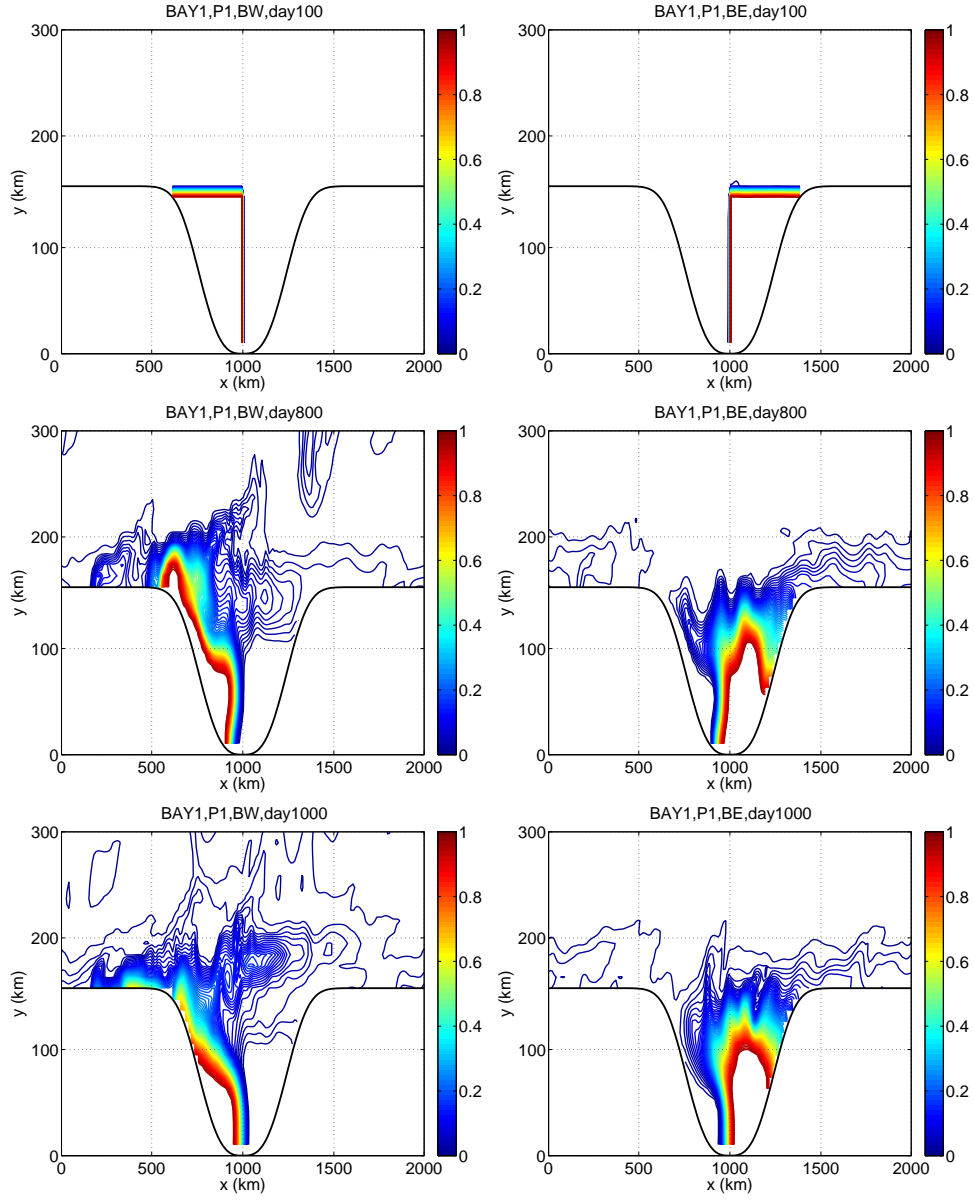
Figure 4.52: Case BAY1, P1. Contours of concentrations of tracer BW (left) and BE (right) with interval of $0.01 kg kg^{-1}$. The range of concentration plotted is between $0.01 kg kg^{-1}$ and $0.95 kg kg^{-1}$. The region to the south of the contour with highest value is filled with tracers with concentration higher than $0.95 kg kg^{-1}$.
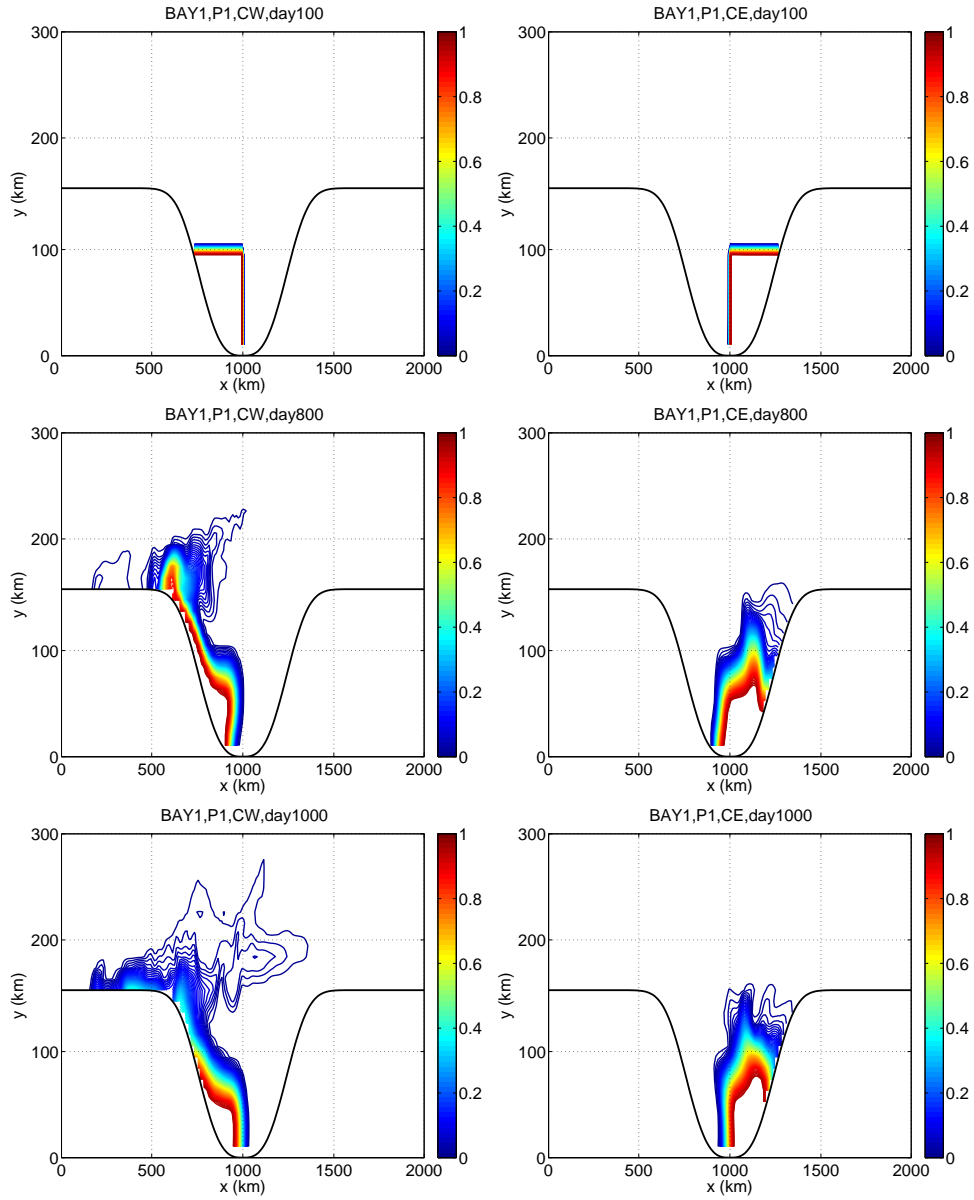
Figure 4.53: Case BAY1, P1. Contours of concentrations of tracer CW (left) and CE (right) with interval of $0.01kgkg^{-1}$. The range of concentration plotted is between $0.01kgkg^{-1}$ and $0.95kgkg^{-1}$. The region to the south of the contour with highest value is filled with tracers with concentration higher than $0.95kgkg^{-1}$.
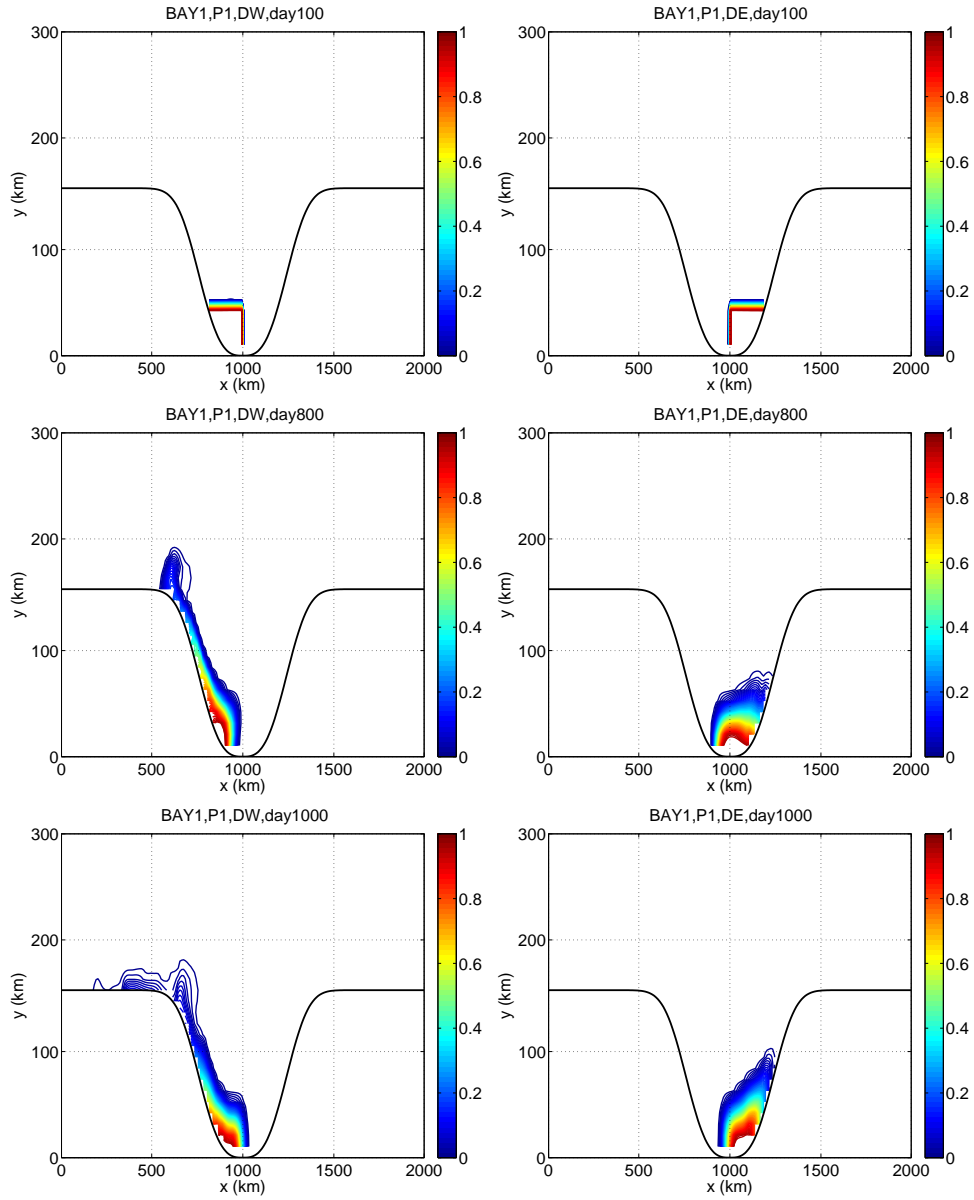
Figure 4.54: Case BAY1, P1. Contours of concentrations of tracer DW (left) and DE (right) with interval of $0.01 kgkg^{-1}$. The range of concentration plotted is between $0.01 kgkg^{-1}$ and $0.95 kgkg^{-1}$. The region to the south of the contour with highest value is filled with tracers with concentration higher than $0.95 kgkg^{-1}$.
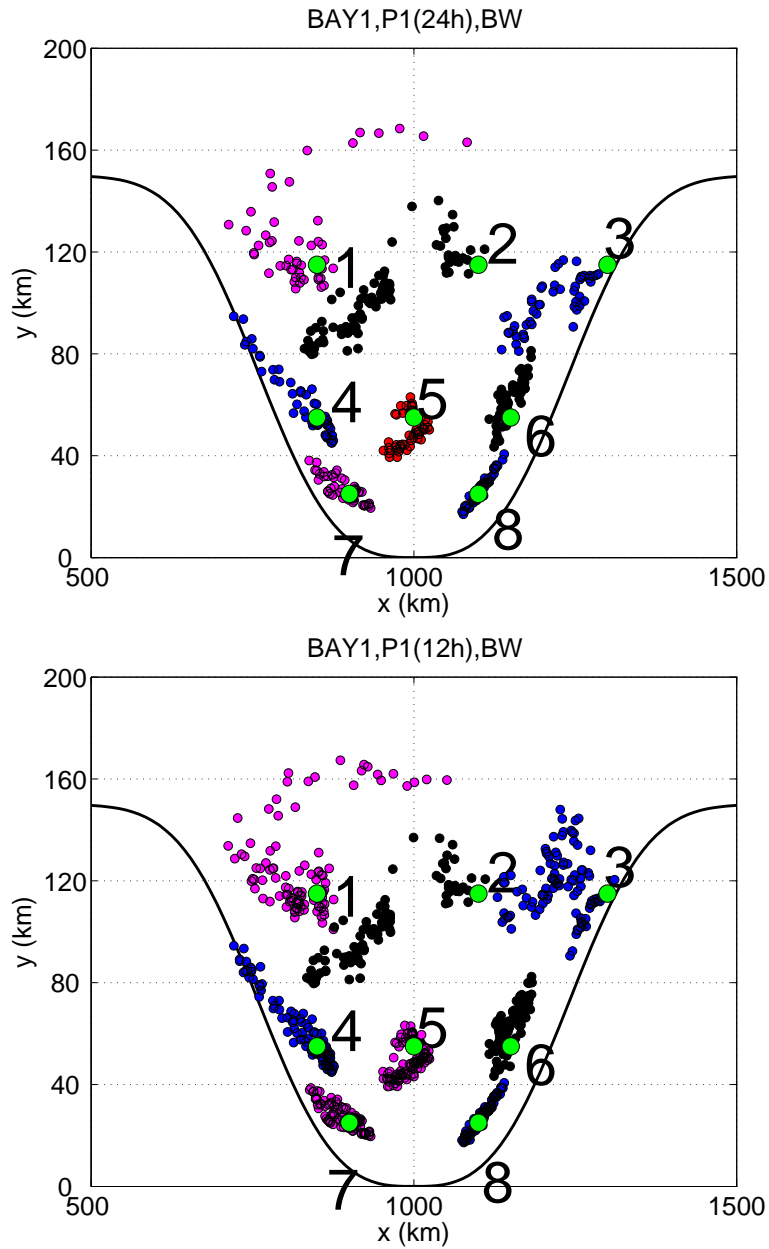
Figure 4.55: Case BAY1, P1. Trajectories of nine particles whose initial locations are denoted as big green dots. The trajectory of particle 1 is denoted as magenta dots, the trajectory of particle 2 is denoted as black dots, the trajectory of particle 3 is denoted as blue dots, the trajectory of particle 4 is denoted as blue dots, the trajectory of particle 5 is denoted as red dots, the trajectory of particle 6 is denoted as black dots, the trajectory of particle 7 is denoted as magenta dots, the trajectory of particle 8 is denoted as blue dots. The integration time-step is 24 hours in the upper panel and 12 hours in the lower panel. The two panels are very close to each other, so the integration is not affected by the length of the time-step.

194

the mean flow, two basic mechanisms are important for the exchange: the advection of the forcing eddy and the mechanism associated with the topography-trapped waves.

Along the slope edge, the northward advection by the anticyclonic eddies or meanders is much stronger than the oscillating tendency due to the westward propagation of the topography-trapped waves. The cross-slope transport is therefore accomplished by a few pulse-like events corresponding well with eddy-topography interactions. The offshore variability on average is weaker in driving the water offshore than the anticyclone applied in case S1, the case in which the interaction between a single surface anticyclone and the slope is simulated.

The effect of eddies or meanders interacting with the slope declines shoreward, so the wave mechanism becomes important along the opening of the bay. Compared with case S1, the effect of this mechanism is more prominent in BAY1 because of the continuous generation of waves. Due to the interaction between the topography-trapped waves and the western boundary, the cross-shelf exchange shows strong asymmetries between the two side boundaries. Big blobs of tracer mass are taken northward along the western boundary onto the slope by crests of topography-trapped waves. This is the most important way for tracers originally distributed well inside the bay to be transported off the slope, which is hardly seen in the interaction between a single anticyclone and a slope.

The rough estimates for the cross-slope and the cross-shelf volume fluxes are $1.19 m^3 s^{-1}$ and $0.4 m^3 s^{-1}$ and are both on the same order as the model Ekman transport. This suggests that the mechanism of the eddy-slope interaction can be as efficient as the wind in driving the cross-isobath transport. Based on the rate of the volume flux out of the bay, it takes about 2.8 years for the water within the bay to be completely replaced with the slope water.

Tracer particles tend to move westward within the bay and turn northward near the western boundary, where they are taken out of the bay by topography-trapped waves. Tracer particles in the southeast of the bay move very little compared with those in the west. The Lagrangian flow is examined by following the motions of some specific particles. Their trajectories show patterns consistent with the evolutions of tracers. All particles that are tracked move westward within the bay. Particles near and to the west of the central longitude move northward, while particles in the east move southward. Near the western boundary, particles tend to move northward along the wall.

195
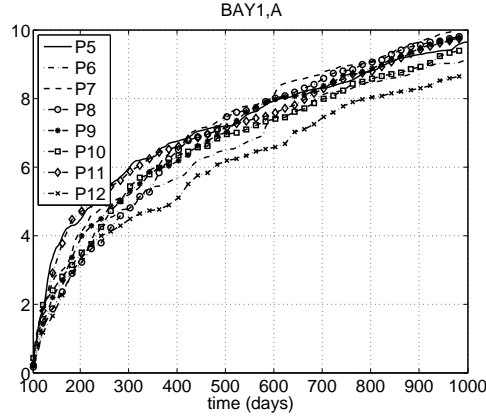
Figure 4.56: Case BAY1, P5–P12: Time series of the cumulative mass of tracer A transported across the first-layer slope edge at $y = 220km$ in units of $5 \cdot 10^{12}kgkg^{-1}m^3$.

Furthermore, the net drifts of particles decay shoreward from the bay opening.

5. Exchanges in periods P5—P12.

Tracer simulations in periods P5—P12 are started with the same initial distributions as those in the period P1, but as the model circulation is only statistically steady and the eddy-slope interaction happens intermittently, starting from different time, the eight periods are different in particular eddy events. In this part, we will examine similarities as well as differences of the cross-slope/shelf exchange among different periods.

As described in the previous part, the cross-slope flux is mostly driven by the off-slope eddies or meanders, so the flux of tracer A across the slope edge can be regarded as an indicator of the offshore forcing. As displayed by Fig.4.56, the time series of the cumulative mass of tracer A transported across the entire slope edge are not only qualitatively similar but also quantitatively close to one the other during 900 days, but this is not true for the transports within smaller zonal ranges. Fig.4.57 shows the cross-slope transports of tracer A within the zonal sections of $600km \leq x \leq 1000km$ and $1000km \leq x \leq 1400km$ which correspond to the western and the eastern half of the bay opening. Differences of the cumulative transports across both sections are as big as or even bigger than the transports themselves. Meanwhile, for a specific period, the transports out of the two sections tend to compensate with each other. These features suggest that the characteristic length scale of the advection by the offshore variability is a few hundred kilometers, greater than the model

196
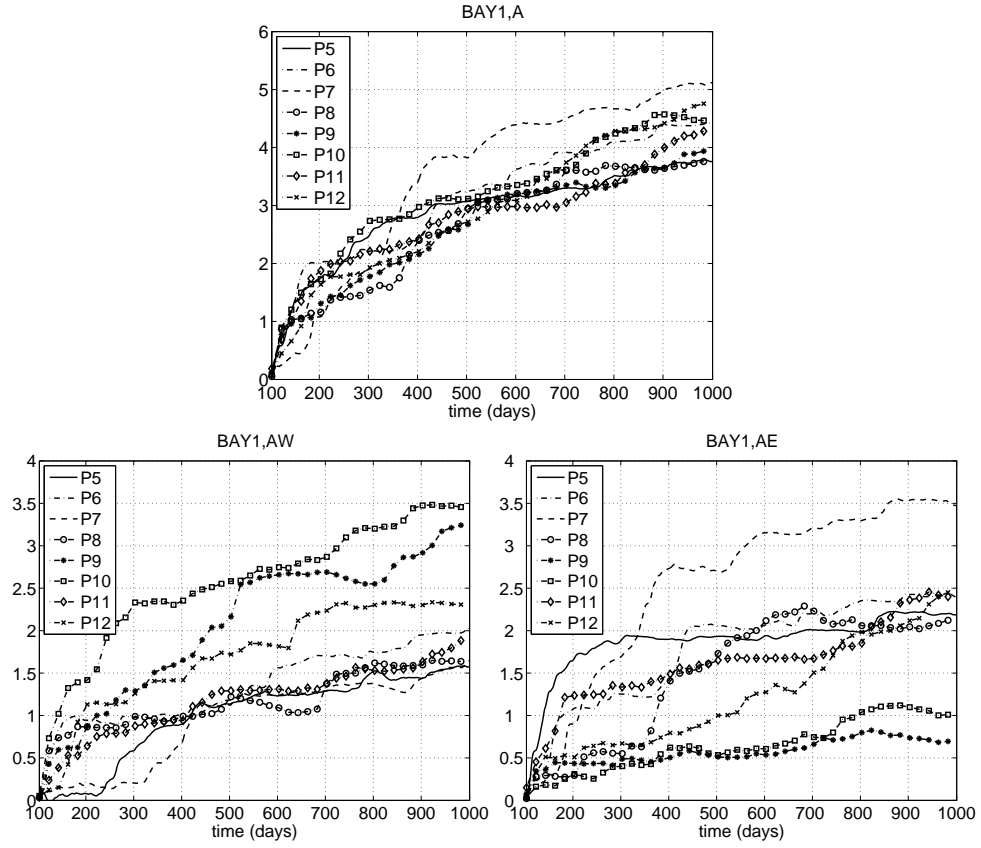
Figure 4.57: Case BAY1, P5–P12. Time series of the cumulative mass of tracer A transported across the slope edge of the bay opening (upper), between $x = 600km$ and $x = 1400km$ (lower left) and between $x = 1000km$ and $x = 1400km$ (lower right) in units of $5 \cdot 10^{12} kg kg^{-1} m^3$.

Figure 4.58: Case BAY1, P5–P12. Time series of the cumulative mass of tracer B (upper), tracer BW (lower left), and tracer BE (lower right) transported across the opening of the bay in units of $10^{12} kg kg^{-1} m^3$.

deformation radius but smaller than the length of the channel. Within zonal ranges of a few hundred kilometers, the occurrence of the offshore eddies or meanders is intermittent, while for the entire slope edge or for the range of the bay opening as in the first panel in Fig.4.57, the intermittency is less significant. In this sense, the width of the bay opening is important for the cross-isobath transport.

The cross-shelf transports of tracer B out of the bay opening in the 8 periods as shown in the first panel of Fig.4.58are somewhat similar to that of the cross-slope transports of tracer A within the same zonal range, but among the mass of tracer B transported out of the bay, much more originates from the western part of the bay. This is true for all periods. Tracers that initially distributed within the eastern part of the bay are transported out of the bay only within the earlier period of the 900 days.

198

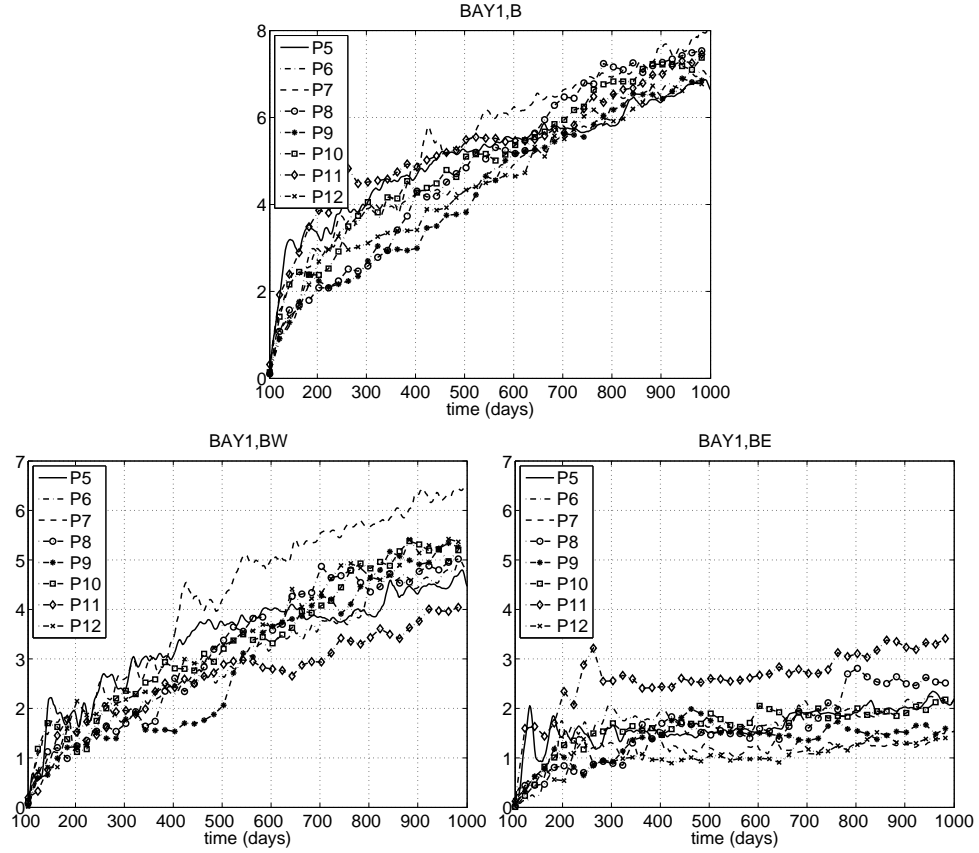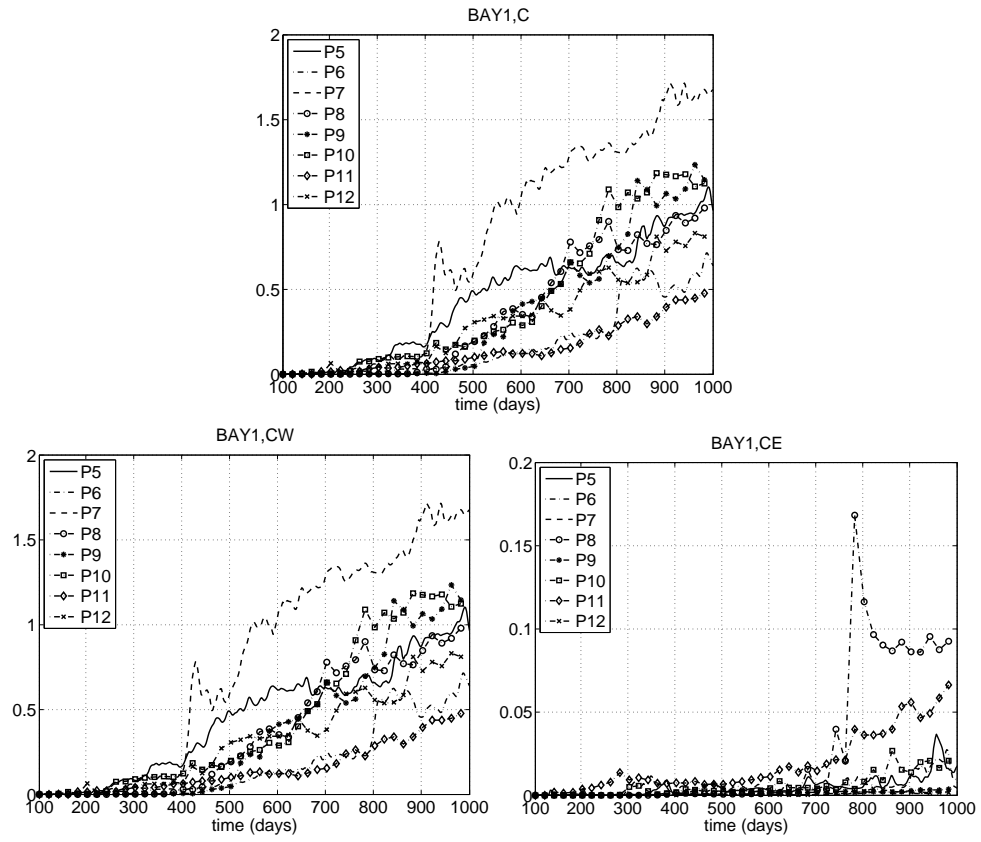**Figure 4.59:** Case BAY1, P5–P12. Time series of the cumulative mass of tracer C (upper), tracer CW (lower left), and tracer CE (lower right) transported across the opening of the bay in units of $10^{12}kgkg^{-1}m^3$.

For tracers that are initially distributed well inside the bay as tracer C, tracer CW, and tracer CE, the differences of their transports out of the bay are much more prominent than those of tracer A and B as in Fig.4.59. More interestingly, the transport of tracer CE out of the bay is negligible compared with that of tracer CW, which means for tracers distributed southward of $105km$, only those to the west of the central longitude can be transported out of the bay within 900 days while those to the east remains within the bay.

From the above description of the cross-shelf transports in periods P5—P12 and P1, we can get a general idea of how particles of tracer B move within the bay. At the beginning of each period, the transport of tracer B out of the bay is somewhat homogeneous along the bay opening. However, due to the effect of topography-trapped waves, the interface between the high and low tracer values, which is initially along the bay opening, becomes asymmetric about the central longitude: it tends to be advected more to the north in the west but more to the south in the east. Along with it, tracer B particles in the east of the bay tend to move southward, further away from the offshore forcing. The cross-shelf transport in the east is therefore slowed down and more tracers to the west are advected out of the bay. In other words, the combining effect of the offshore variability and the topography-trapped waves "squeeze" tracers out of the bay from the west and "pushes" the slope-water into the bay from the east. As a result, tracers that are originally within the eastern half of the bay and further away from the bay opening move very slowly southwestward within the bay. As shown in Fig.4.57, the offshore variability within the zonal range of the eastern half of the bay opening is strongest in P7 among the 8 periods. For the cross-shelf transport, i.e., the transport out of the bay, it is the transport within the western half not the eastern half of the bay that is strongest. This feature is consistent with our hypothesis that the correspondence between the cross-slope and the cross-shelf transports is non-local: the strong offshore variability within the zonal range of the eastern half of the bay produces the strong cross-shelf transport in the western half of the bay. This is because the tracer interface tends to be further north in the west but further south in the east away from the offshore forcing. After the earlier period, i.e., 300-400 days, the effect of the offshore variability is mostly demonstrated by the transport in the west of the bay through the westward propagation of the topography-trapped waves. The strength of this asymmetry is not same in different periods, and in periods when the west-east asymmetry of the tracer interface is insignificant, the cross-slope

transport of tracer C is weak. For example, in P9 and P10, the transports of tracer C out of the bay are large, so are the asymmetries of their interfaces about the central longitude; in P11, the transport of tracer C is weakest among the 8 periods, and its interface does not look very different near the western and the eastern boundary as in Fig.4.60.

In summary, the cross-slope transport of tracer A and the cross-shelf transport of tracer B are largely independent of the starting time as long as the zonal range in question is bigger than or comparable with the width of the bay opening. The cross-shelf transport of tracer C is highly variable among different periods, and its magnitude is related to the asymmetry of the tracer interface. The water that is in the western part of the bay is more easily transported out of the bay than that in the east; the water that in the southeast moves very little within the bay. The rough estimates of the cross-slope and the cross-shelf volume transport made for the period P1 are plausible since the differences of the transport of tracer A and B are small during the earlier periods.

The northward tilt of the tracer interface in the west is an interesting feature and is important for the transport out of the bay. It is closely related to the topography-trapped waves. Because waves excited by different offshore eddies may interact with each other, the evolution of the tracer interface is dependent not only on the factors of the offshore eddies such as the strength, the size and the offshore distance, but also the occurrence time and location of these different eddies. This is more complicated than the transport across the slope edge. Because the wave mechanism is far less significant than the eddy advection along the slope edge, the transport across the slope edge can be regarded as the sum of the transports from different eddies and is therefore determined only by the magnitudes of the swirl velocities of different eddies but not the occurrence time of each eddy.

Generally speaking, under the continuous offshore forcing, the water tends to get out of the bay from the west while moves into the bay from the east. On the other hand, along the slope edge and under the effect of an anticyclonic offshore eddy or meander in the Southern Hemisphere with $f < 0$, the water gets off the slope from the east and gets onto the slope from the west. The cross-slope and cross-shelf exchanges seem to be opposite to each other, and this is another interesting feature of the model results.
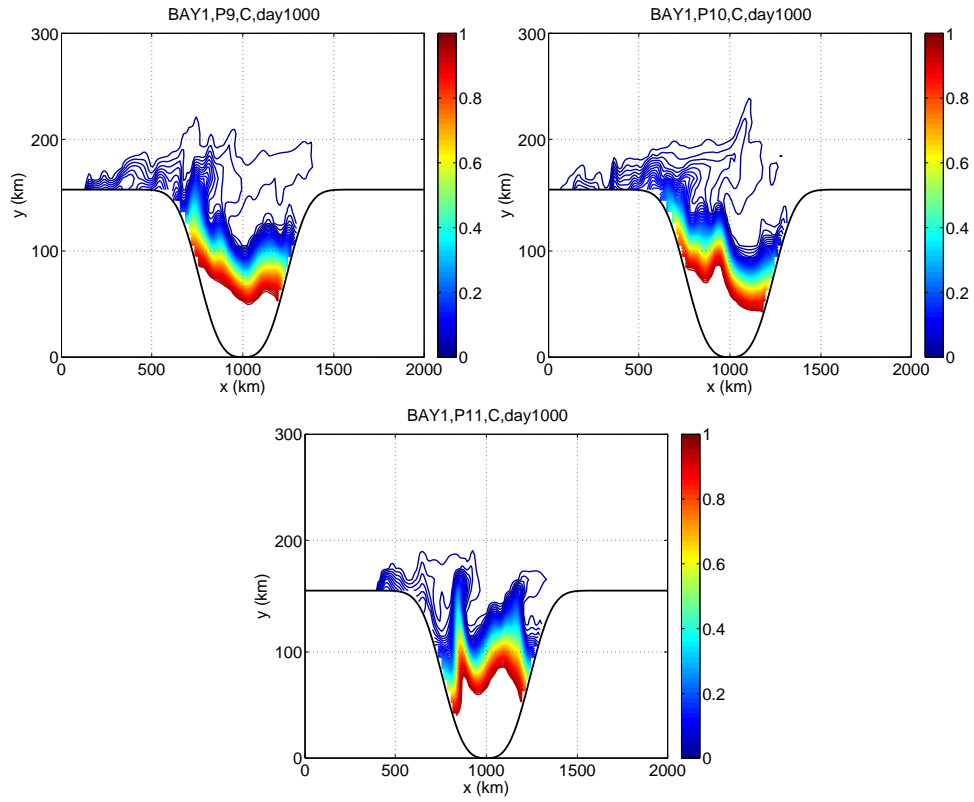
Figure 4.60: Case BAY1, P9, P10, and P11. Contours of tracer C concentration at the final day in the periods P9, P10, and P11 with intervals of $0.01kgkg^{-1}$. The range of concentration plotted is between $0.01kgkg^{-1}$ and $0.95kgkg^{-1}$. The region to the south of the contour with highest value is filled with tracers with concentration higher than $0.95kgkg^{-1}$.

4.5   Conclusions

The interaction between a continental slope/shelf with an offshore baroclinic jet has been examined in this chapter with a two-layer isopycnal model. The jet that is driven by the wind stress is baroclinically unstable generating eddies or meanders which are advected further north or south from the center of the jet. At the jet axis, the PV gradient also has a local maximum. During its quasi-steady state, the zonal momentum is balanced in both layers between the frictional force, i.e., the wind stress on the surface and the friction at the bottom, and the meridional PV flux. The interfacial form drag is crucial for the dynamics as it transfers the zonal momentum downward to the second layer. With a zonally uniform slope against the southern boundary and southward of the main jet, the eddies or meanders from the main jet interact with the slope in the lower layer inducing the formation of a second PV front as well as the local intensification of the flow variability in the first layer near the base of the topography. The formation of this second PV front and the associated jet suggest a possible explanation for the formation of those circumpolar fronts in the ACC such as the Southern ACC Front. The second PV front is continuously perturbed by the main, meandering jet in the center of the channel and forms its own meanders or eddies. Meanwhile, it acts as a barrier preventing fluctuations, i.e., eddies or meanders, of the main jet from crossing itself into the region to the south. And this feature is independent of the height of the topography. When the slope penetrates into the upper layer and is connected with a bay-shaped shelf region to the south, a second PV front forms in the first layer a little bit shoreward from the northern edge of the bottom slope. Both the bay and the first-layer slope are directly forced by this second PV front.

There are several processes associated with the second PV front such as its interaction with the slope/shelf, with the topographic eddies that have been generated during previous eddy-slope interactions, and with the main jet in the center of the channel. The process that is most interesting and is also the primary motive of the thesis is the interaction between the front and the slope/shelf as well as the cross-slope/shelf exchange.

Without the wind stress in the bay, the variability at the bay opening is responsible for driving a clockwise mean circulation around the bay, where amplitude decays away from the bay opening and intensifies near the western boundary. This intensification is attributed to the interaction between

the topography-trapped waves and the boundary, quite in the similar way as the formation of the western boundary current in those ocean basins due to the planetary β effect.

Compared with the mean circulation which is only on the order of $10^{-3}ms^{-1}$, the variability within the bay is at least one order stronger, but its spatial structure is similar to that of the mean flow.

The volume exchanges across the first-layer slope edge and the bay opening, which we have called cross-slope and cross-shelf exchange, are examined during the quasi-steady state. The two mechanisms important for the interaction between a single eddy and the slope are also present and play important roles in the system. The cross-slope exchange is dominated by the first mechanism, i.e., the advection by eddies or meanders from the second PV front. This mechanism is characterized by time and spatial concentration of the strong volume transport. As a result, the cross-slope transport can be regarded as the sum of the transports associated with different single-eddy-slope interaction events. As demonstrated in chapter 3, the effect of the eddy advection declines quickly onshore due to both the decay of the eddy's velocity field and the response to the offshore eddy over the slope. Therefore, along the bay opening, the effect of the wave mechanism becomes prominent. Due to the interaction between the topography-trapped waves and the western boundary of the bay, more shelf water is transported out of the bay along a path near the western boundary. And this feature is more striking for the transport of tracers that are originally distributed well inside the bay. Within the bay, water particles tend to move southwestward in the northeast while northwestward in the northwest. The water in the southeast of the bay is the least likely to be transported across the bay opening.

On time scales of 100 days or longer, the transport of the slope water across the entire slope edge and the transport of the bay water out of the bay can be regarded as steady processes. On the other hand, the transport of tracers that are distributed well inside the bay varies greatly among different periods. The magnitude of this transport is consistent with the west-east asymmetry of the tracer interface: when the interface is more to the north in the west and more to the south in the east, more tracers are transported out of the bay. We think the occurrence time as well as location of the strong offshore variability is important for this asymmetric structure.

Both the volume transported across the slope edge and across the bay opening are comparable with the Ekman transport in the center of the channel, suggesting that the mechanism examined in the thesis is important in driving the cross-slope/shelf transport. The total volume of the water within the bay divided by the mean volume flux out of the bay opening is around 3 years, but the time for the bay to be completely emptied of the shelf water may be much longer given the fact that in some areas, such as the southeastern region of the bay, the water moves very little.

The model set-up is intended to reflect some important features of the interaction between the ACC and the Marguerite Bay/WAP shelf region, but some results of this chapter may also be applied to other continental shelf areas where a strong ocean current passes by and interacts with the topography. If the current is baroclinically unstable and the isopycnal tilts in the same way as the continental slope as the shelf region near the Gulf Stream, the current-slope interaction in the lower layer would induce a similar variation of the eddy-driven cross-jet PV flux in the model which will further change the interaction between the layers and the Reynolds' stress divergence in the upper layer. As both the isopycnal and the Reynolds' stress divergence are modified, the flow characteristics such as the mean velocity, variability, and PV gradient will be changed accordingly. Although the exact response of the current to the presence of the slope depends on the basic dynamical balance of the current as well as the relative location of the topography to the current, how the lower-layer topography influences the upper ocean-current dynamics would be similar to what have been studied in this thesis. In shelf regions where the isopycnals' tilts are opposite to that of the continental slope, the topography will also somehow influence the dynamics of the current, but the basic mechanism is expected to be very different from our model results and would require a thorough investigation in the future.

Chapter 5

Conclusions

The thesis is motivated by the hypothesis that the persistent yet episodic forcing from the ACC is important in driving the cross-shelf transport and the mean circulation over the Marguerite Bay and the west Antarctic Peninsula (WAP) shelf region. The interactions between a continental slope with a bay-shaped shelf and a strong current are examined with three, simple to more complicated models.

The problem of eddy-slope interaction is studied as the interaction between a single point vortex and a step-like topography in a one-layer contour dynamics model in Chapter 2. Two control mechanisms are identified, which are eddy advection and topographic wave propagation. The former is the advection by the swirl velocity field of the point vortices, and the latter is the motion of the topography-trapped waves that propagate along the topography in a single direction with high PV on the right, westward if in the Southern Hemisphere with shallow water to the south. Both mechanisms are influenced by the boundary of the bay which is not parallel with the escarpment. The bay's boundary influences the first mechanism by advecting the vortex along the wall according to image theory and thus affects the evolution of the PV front; the boundary influences the second mechanism by modifying the wave properties. When the topography-trapped waves approach the western boundary of the bay (Southern Hemisphere, shallow water to the south), troughs tend to be blocked and squeezed against the wall. As a result, the nonlinearity is strengthened and the waves' amplitudes as well as cross-escarpment motions are amplified. In addition, the crests move past the

western edge of the bay into the deep ocean as efficient agents of cross-escarpment transport. The relative relation between the two mechanisms is different in the anticyclone- and cyclone-induced interactions, and the difference is responsible for the fundamental differences between the two kinds of interactions. The two mechanisms tend to move the frontal structure in opposite directions in the anticyclone-induced interactions. Within a certain parameter range, a balance between the two mechanisms is achieved and a cyclonic eddy forms from the topography, which could enclose all the water within the bay due to the effect of the boundary. In the cyclone-induced interactions, however, such balance can never be obtained since the two mechanisms act to push the frontal perturbations in the same direction. The cross-escarpment transport is weaker in the cyclone-induced interactions than in the interactions induced by an anticyclonic vortex of the same strength. Most of the water that can be taken off the topography in the cyclone-induced interactions is contained by a crest that is directly forced by the original cyclone and is advected along the coastline out of the bay. The two kinds of interactions are also different in their dependence on parameters such as the strength of the vortex and the depth difference across the escarpment. Generally speaking, the anticyclone-induced interactions are more sensitive to parameter changes than the cyclone-induced interactions.

One severe restriction imposed in the first model is the assumption of constant density. Due to this assumption, the velocity field induced by a PV anomaly decays with a length scale on the order of the external deformation radius, while the length scale important for the eddies observed in the real oceans is usually the first internal deformation radius, at least an order smaller than the external one. In Chapter 3, this restriction is relaxed with a two-layer isopycnal model. The interaction problem is examined between a zonally uniform slope with a bay to its south and a single surface anticyclone. The slope is allowed to penetrate into the first layer, intersecting the slope at a latitude that is more than twice the deformation radius north of the bay opening. The interaction between the surface anticyclone and the first-layer slope is similar to that in the contour dynamics model in the sense that the two mechanisms found in the previous chapter are also present and important and a topographic cyclone forms and leaves the slope with the original anticyclone. However, the baroclinic interactions also show qualitatively different features compared with the barotropic interactions. With so "wide" a slope compared with the deformation radius, the shoreward decrease of the eddy advection is obvious and so is the effect of the seaward PV deformation directly gener-

ated by the anticyclone. The anticyclone and the seaward PV deformation act against each other in driving the slope water, that is further south, offshore. Defined by the southernmost latitude of the slope water that can be driven off the slope, the anticyclone's effective range is usually limited to the middle slope and can barely get into the bay, in striking contrast to the barotropic interactions which usually have the bay completely emptied of the shelf water. Among variable parameters such as the size, the strength, and the initial location of the offshore anticyclone, the initial swirl velocity over the slope is most important for the strength of the topographic cyclone as well as the cross-slope volume transport. Since the cross-slope exchange quickly slows down after the topographic cyclone forms and leaves the slope, the length of the formation time for the topographic cyclone is of secondary importance. Model results show that a large anticyclone with big swirl velocity initially over the slope is the most effective in driving the slope water off the slope. The interaction process also depends on the profile of the slope. When the first-layer slope is flat, the anticyclone's effective range is larger and the cross-slope transport is stronger. When the first-layer slope is steep, the cyclonic eddy generated by the same anticyclone is stronger. One effect of the wave motions in the lower layer is to trap the surface dipole near the topography, so with a wider lower-layer slope, the surface dipole does not move very far away from the coast, and the cross-isobath transport is consequently larger than in the case with a narrower lower-layer slope.

It is in Chapter 4 that a strong jet resembling the ACC is incorporated into the two-layer isopycnal model and is let evolve upon its own dynamics. The jet is wind-driven with the maximum zonal velocity at the center of the channel where the PV gradient also has a local maximum. The interaction between the jet and the slope in the lower layer induces the formation of a second PV front, which is near and a little bit shoreward from the base of the bottom topography and is associated with a local maximum of the first-layer zonal flow. This second PV front is much stronger than the central one and isolates the southern area from the direct forcing of the main jet. However, when perturbed continuously by the main jet, the second PV front itself interacts with the first-layer slope and the shelf with eddies and meanders inducing a mean circulation as well as the cross-slope/shelf exchange. The mechanism of the formation of this second PV front may play a role in the formation of those persistent and circumpolar fronts in the ACC, such as the Southern ACC Front along the outer shelf in the WAP shelf region.

The flow within the bay is entirely driven by the variability at its opening and simultaneously dissipated by the bottom friction. The mean circulation is clockwise. Its amplitude decreases away from the opening but is intensified near the western boundary. This is a result of the interaction between the boundary and the topography-trapped waves that propagate westward in the Southern Hemisphere with shallow water to the south. The variability within the bay is much stronger than the mean and similar in spatial structure.

The volume transport across the slope edge is mostly directly driven by the eddies or meanders from the second PV front. As the eddy advection declines shoreward, the motions due to waves become as strong as those by the eddy advection, so transport across the bay opening is more influenced by topographic waves. Both the volumes transported across the bay opening and across the slope edge are comparable with the model Ekman transport in the center of the channel, therefore the mechanism examined in the thesis is as important as wind in driving the cross-slope/shelf transport.

Strong wave-boundary interactions occur only near the western not the eastern boundary of the bay due to the single propagation direction of the topographic waves. In interacting with boundaries, wave troughs are blocked by the wall while the crests frequently pass over the western edge of the bay taking some bay water with them. This mechanism is essential for the out-of-bay transport of tracers, especially those that are initially distributed further inside the bay. There is a dramatic difference of cross-shelf transport within the bay: much more tracer tends to be transported out of the bay along or near the western boundary, while less is transported from the east. Strong cross-shelf exchange events occur near the bay opening and the western boundary; regions in the southeast of the bay are most isolated in the sense that tracers or water particles there move around without having big net displacements.

The intermittency of the cross-slope/shelf transport in the presence of the strong, open ocean current is also examined in Chapter 4. It is found that most variabilities driving the cross-slope transport are shoreward meanders of the newly formed PV front over the slope and the characteristic length scale of those meanders is on the order of half of the bay opening. Therefore, for the entire slope edge or part of the slope with length comparable with the characteristic length scale of the

forcing meander, the cross-slope transport is fairly steady and the intermittency is low. On the other hand, for a small section of the slope edge, the occurrence of the forcing meander is highly intermittent and the transport process greatly depends on the particular period. The intermittency is also high for the out-of-bay transport of tracers that are initially distributed well inside the bay and are transported across the bay opening mostly along the western boundary.

Compared with the previous theoretical studies, the thesis is the first to systematically examine the eddy-topography interactions as well as the cross-isobath exchange from the simplest barotropic vortex-escarpment interaction to the baroclinic eddy-slope interaction, and finally to the persistent and episodic interaction between a slope and a strong offshore current. The understanding of the more complicated current-slope interaction is built upon the understanding of the basic mechanisms obtained from the simpler models. Meanwhile, important new features are found from complicated models compared with those of the simpler ones. For example, the shoreward decline of the effect of the eddy advection and the increase of that of the topography-trapped waves are found from the two-layer, single-eddy model against the vortex model. Furthermore, an offshore PV front generated by the continuous interaction between eddies and the lower-layer slope near the southern boundary is found after an energetic jet is incorporated in Chapter 4. The model set-up in the first two stages is more general, so their results can be applied to many shelf regions where the coastline is indented as a bay and affects the propagation of the topography-trapped waves.

Results of Chapter 4 are potentially very important for understanding the actual ACC-WAP system and designing future observations in that area. First, the strong, upper PV front formed over the continental slope and the associated upper ocean jet are found induced by the eddy-slope interaction in the deep ocean. Its formation process offers a possible explanation for the formation of those fronts in the ACC. Second, the model transport out of the bay is entirely driven by offshore variability and is comparable with the model Ekman transport. This feature strongly suggests that the proposed mechanism is important in actual system in driving the cross-shelf exchange. Third, in the WAP shelf region, the onshore intrusion of the CDW is thought to occur at specific locations associated with rough bottom topography such as the Marguerite Trough. In the thesis, the shelf is assumed constant, but the model result nevertheless shows a strongly inhomogeneous pattern of cross-shelf transport within the bay. The periods of strong out-of-bay tracer transport are character-

211

ized by further northward position of the tracer interface in the west and further southward position in the east. This west-east asymmetry suggests that the western boundary is favorable to strong out-of-bay transport. Moreover, more deep-ocean water that intruded onto the shelf are present in the northeast of the bay, shielding water further south from the offshore influence. Thus, the southeastern area of the Marguerite Bay may be a retention region for Antarctic krill where high population of krill is thus more likely to be found; the northwestern part of the Marguerite Bay is probably the region where strong out-of-bay transport are observed; the oceanic CDW water is probably more easily to be observed in the northeast of the bay.

Although the set-up of the third model is intended to resemble that of the ACC and the Marguerite Bay/WAP shelf region, results such as the role that eddies play in the dynamics of the baroclinically unstable current, effects of the lower-layer slope on the jet, and the mechanisms as well as paths of the cross-shelf transport within a bay, can probably find applications in other shelf regions with careful considerations of the local dynamical balance.

The most important condition for the strong wave interaction with the boundary and the associated strong cross-shelf transport near the western boundary is that the shelf width decreases towards the west or in other words, the bay's boundary tends to intersect the isobath as it extends westward. In the thesis, only one limiting situation where the shelf width becomes zero out of the bay is considered, so the westward propagation of the topographic waves is blocked by the western boundary, resulting in strong wave-boundary interactions there. If the shelf extends beyond the bay and the zonally uniform slope starts some distance northward of the bay opening, the wave-boundary interaction as well as the contrast of the cross-shelf transport between the western and the eastern boundary is expected to be weaker than in the thesis. On the other hand, if the continental slope extends into the bay with isobaths intersecting the bay's boundary, the wave-boundary interaction will become stronger. Under circumstances where isobaths exist within the bay but $\frac{f}{H}$ contours close upon themselves, topographic waves are expected to propagate along those closed contours without getting interacting with the bay's boundary. If the region enclosed by those contours is also far from the offshore variability, the water within the region may be trapped there with little chance to get out of the bay.

Simplifications made about the system, such as the steady wind stress, and the zonally uniform continental slope, have been very helpful in demonstrating the basic mechanisms, but they also put constraints on the interaction between the model ACC and the shelf region. For example, without any bottom topography along the path of the current, the bottom form drag is absent from the dynamical balance, which results in a greater volume transport by the model ACC, higher eddy kinetic energy compared with observations, and finally may cause overestimate of the transport driven by the offshore variability. Since the wind stress in the Marguerite Bay/WAP region is highly variable, it is also important to know what the time mean response over the shelf looks like if the wind varies in time with zero mean value. The simplifications, as regarded as limitations of the thesis, also provide interesting topics and await further examinations using more complicated models.

Appendix

The length of the channel is relevant to the problem because the channel is periodic. The zonally periodic channel is used to approximate an annulus like the domain where Antarctic Circumpolar Current flows around the globe. For a vortex somewhere in a reentrant channel with length a, the resolved periodic motion is from not the single vortex lying between $x = 0$ and $x = a$, but an infinite array of equal-strength vortices, spaced along the x-axis from $-\infty$ to $+\infty$ and a distance a apart. Close to the string of vortex, the velocity field, determined mostly by the vortex within the same range, is blind to other vortices. Further away from the string, vortices would appear more and more closely spaced and finally the distance between each pair is indiscernible. So the string of vortex would look like a vortex sheet with finite vortex filament thickness. We know for an infinitely thin vortex sheet, the velocity normal to the sheet is zero, but the tangential velocity is a constant and reverses sign across the vortex sheet. Therefore, when the vortex is far enough from the southern boundary of the periodic channel, the velocity field near the shelf-break is independent of space. And how far is far enough to make the vortex velocity field uniform depends on the spacing of vortices, or the period of the zonal channel. The longer the channel, the further the vortex needs to be. So the period of the channel matters for the problem. This raises the question of how long the channel should be to make sure that the results we get is close to the results of the initial problem we tried to answer. We can answer the question by finding the solution of a single vortex in an annulus and comparing it against the solution in a channel without bay in any boundaries.

Fig.1 shows an annulus lying between two concentric circles which denote the solid boundaries where no-normal flow condition is satisfied. The radii of the two circles are r_1 and r_2 ($r_1 < r_2$). A vortex with strength Γ is located at (x_0, y_0). Instead of solving the problem using circular coordi-
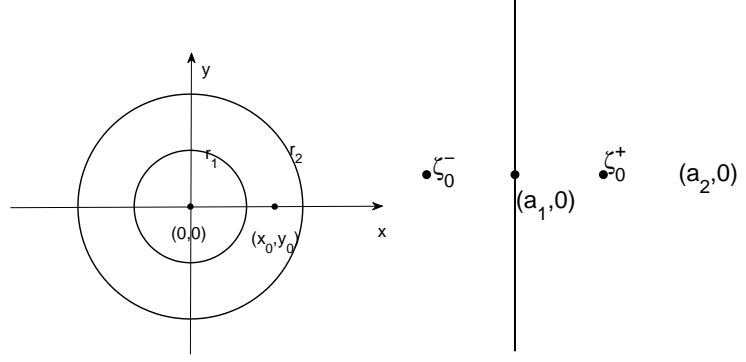
Figure 1: Left panel: a schematic view of an annulus in z space. Right panel: a channel in ζ space.

nate, we can think of a transformation $z = e^{\zeta}$, where $z = x + iy$ is the complex variable in the original space and $\zeta = \kappa + i\eta$ is the complex variable in a new space. Apply the transform to any straight line extending parallel with η-axis from $-\infty$ to $+\infty$ in ζ space, the straight line turns into a circle in the original z space. So, if we can solve the Greens function within a channel bounded by two such straight lines in the new space, getting the solution in the original space would be straightforward. Fortunately, it is pretty easy to find the analytic solution in the new space. Suppose the two straight lines cross κ-axis at $(a, 0)$ and $(b, 0)$ $(b > a)$, and the vortex is located at (κ_0, η_0), then the complex velocity generated in the ζ plane is $\tilde{W} = \tilde{u} - i\tilde{v} = -\dfrac{i\Gamma}{4\pi h} \cot\dfrac{\pi}{2h}(\zeta - \zeta_0^+) - \cot\dfrac{\pi}{2h}(\zeta - \zeta_0^-)$, where $h = b - a$ is the width of the channel, $\zeta_0^+ = \kappa_0 + i\eta_0$, the position of the vortex, and $\zeta_0^- = (2a - \kappa_0) + i\eta_0$, the symmetric point of ζ_0^+ about the left boundary. The complex velocity W within the channel in the z plane is, according to the rules of conformal mapping, $W = \dfrac{\tilde{W}}{\dfrac{dz}{d\zeta}}$, and $a = \ln(r_1)$, $b = \ln(r_2)$, $\zeta_0 = \ln(z_0)$. Shown in the first panel of Fig.2 is the magnitude of velocity at each point on the inner circle of the annulus. The x-axis of the figure indicates the angle of the point on the inner circle which is defined as follows. In polar coordinates, a point on a circle that centered on the origin can be represented by $z = re^{i\theta}$. When the point is right on the positive real axis, $\theta = 0$; when the point is on the positive imaginary axis, $\theta = \dfrac{\pi}{2}$; when it is on the negative imaginary axis, $\theta = -\dfrac{\pi}{2}$. The radii of the two circles in the figure are $r_1 = 10$ and $r_2 = 100$; the vortex which has strength $\Gamma = -1$ is at (11.0), lying on the real axis with distance 1 from the inner cycle. Shown in the second panel is the angle of the velocity vector at each point. Clearly, the vector is tangential to the circle and the flow goes anticlockwise around the circle. Its magnitude, as shown

216

in the first panel, is symmetric about the real axis, declining towards the negative real axis with the maximum value at the point under the vortex. On the right half of the circle facing the vortex, the flow is strong and decreases greatly as the distance to the vortex increases; on the other half of the circle, the flow is very weak and vanishes in a section around the point $(-11, 0)$. If we move the vortex much further away from the inner circle, e.g. $(30, 0)$ as shown in Fig.3, the flow is still anticlockwise along the boundary, but the distribution of flows magnitude has changed. First the maximum value under the vortex is largely reduced, so the variation of the flows magnitude is much smaller. Second, the flows magnitude is nonzero everywhere including the furthest point $(-30, 0)$. From these two figures, we can get the following conclusions: when the distance between the vortex and the inner boundary is small compared with the radius of the circle, as we go along the boundary away from the point under the vortex, the flow magnitude decays to zero; when the former is of the same order as or bigger than the latter, as we move away from the vortex, we do not see much decrease in the flow magnitude and the flow is not zero even for the furthest point. This is similar to the results for the periodic channel: with the distance between the southern boundary and the vortex is big compared with the length of the channel, flow at the southern boundary tends to become uniform. In fact, for a periodic channel with length 2π, flow on the southern boundary becomes uniform as long as the distance between the vortex and the boundary is bigger than 4, but for the annulus, uniform flow along the inner circle is not obtainable until the ratio of the two lengths, the distance between the vortex and the inner circle and the radius of the circle, goes to infinity, which is impossible for any annulus that is realistic for the ACC. Therefore, to solve the original problem using a zonally periodic channel we have to make sure the largest distance between the vortex and the boundary that is interested in the study is small compared with, if not much smaller than, the periodic length of the domain. Hoping to explore cases in which the distance between the vortex and the southern boundary can be as large as 4 or 5, around ten times bigger than the depth of the bay, we apparently have to choose a much longer channel at the cost of much longer computational time.

Figure 2: Left panel: magnitude of velocity along the inner circle of the annulus. Right panel: angle of the velocity along the inner circle in units of π. The vortex is located at $(11, 0)$ in z space.
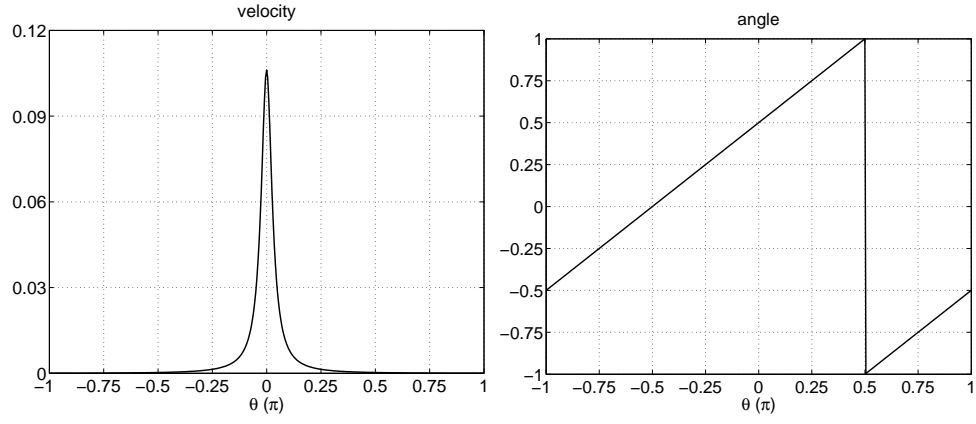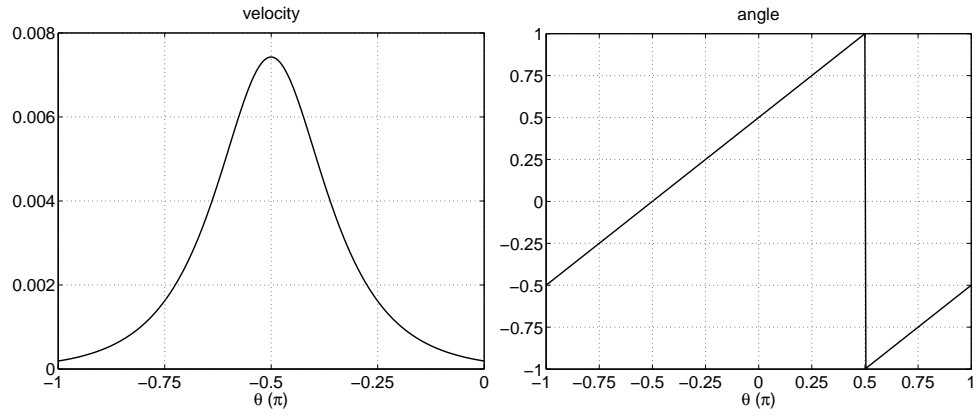

Figure 3: Left panel: magnitude of velocity along the inner circle of the annulus. Right panel: angle of the velocity along the inner circle in units of π. The vortex is located at $(30, 0)$ in z space.

Bibliography

Andrews, D. G., and McIntyre, M. E., 1976. Planetary waves in horizontal and vertical shear: The generalized Eliassen-Palm relation and the mean zonal acceleration. Journal of Atmospheric Sciences, 33, 2031-2048.

Andrews, D. G., and McIntyre, M. E., 1978. Generalized Eliassen-Palm and Charney-Drazin theorems for waves on axisymmetric mean flows in compressible atmosphere. Journal of Atmospheric Sciences, 35, 175-185.

Arakawa, A., and Hsu, Y. J. G., 1990. Energy conserving and potential dissipating schemes for the shallow water equations. Monthly Weather Review, 118, 1960-1969.

Beardsley, R. C., Limeburner, R., and Owens, W. B., 2004. Drifter measurements of surface currents near Marguerite Bay on the western Antarctic Peninsula shelf during austral summer and fall, 2001 and 2002. Deep-Sea Research II 51, 1947-1964.

Bell, G. I., 1990. Interaction between vortices and waves in a model of geophysical flow, Physics of Fluids, A, 2, 575-586.

Bell, G. I., and Pratt, L. J., 1992. The interaction of an eddy with an unstable jet. Journal of Physical Oceanography, 22, 1229-1244.

Chapman, D. C., and Brink, K. H., 1987. Shelf and slope circulation induced by fluctuating offshore forcing. Journal of Geophysical Research, 92, 1174111759.

Cheney, R. E., and Richardson, P. L., 1976. Observed decay of a cyclonic Gulf Stream ring. Deep-Sea Research, 23, 143-155.

Churchill, J. H., Cornillon, P. C., and Milkowski, G.W., 1986. A cyclonic eddy and shelf-slope water exchange associated with a Gulf Stream warm-core ring. Journal of Geophysical Research, 91, 9615-9623.

Dritschel, D. G., 1988. Contour surgery: A topological reconnection scheme for extended integrations using contour dynamics. Journal of Computational Physics, 77, 240-266.

Duncombe Rae, C. M., 1991. Agulhas retroflection rings in the South Atlantic Ocean: An overview. South African Journal of Marine Science, 11, 327344.

Evans, R.H., Baker, K. S., Brown, O. B., and Smith, R. C. 1985. Chronology of warm core ring 82B. Journal of Geophysical Research, 90, 8803-8811.

Frolov, S. A., Sutyrin, G. G., Rowe, G. D., and Rothstein, L. M., 2004. Loop Current interaction with the western boundary in the Gulf of Mexico. Journal of Physical Oceanography, 34, 2223-2237.

Garfield, N., and Evans, D. L., 1987. Shelf water entrainment by Gulf Stream warm-core rings. Journal of Geophysical Research, 92, 13003-13012.

Grimshaw, R. and Yi, Z. X., 1991. Evolution of a potential vorticity front over a topographic slope. Journal of Physical Oceanography, 21, 1240-1255.

Hallberg, R., and Gnanadesikan, A., 2006. The role of eddies in determining the structure and response of the wind-driven Southern Hemisphere overturning: results from the modeling eddies in the Southern Ocean (MESO) project. Journal of Physical Oceanography, 36, 2232-2252.

Hallberg, R., and Gnanadesikan, A., 2001. An exploration of the role of transient eddies in determining the transport of a zonally reentrant current. Journal of Physical Oceanography, 31, 33123330.

Hallberg, R., and Rhines, P., 1996, Buoyancy-driven circulation in an ocean basin with isopycnals intersecting the sloping boundary. Journal of Physical Oceanography, 26, 913-940.

Hofmann, E. E., and Klinck, J. M., 1998. Thermohaline variability of the waters overlying the West Antarctic Peninsula continental shelf. Ocean, Ice and Atmosphere, Interactions at the Continental Margin. Antarctic Research Series, vol. 75. pp. 67-81.

Hofmann, E. E., Klinck, J. M., Costa, D. P., Daly, K. L., Torres, J. J., and Fraser, W. R., 2002, U.S. Southern Ocean Global Ocean Ecosystems Dynamics Program. Oceanography, 15, 64-74.

Hofmann, E. E., and Murphy, E. J., 2004. Advection, krill, and Antarctic marine ecosystems. Antarctic Science, 16 (4), 487-499.

Joyce, T. M., Bishop, J. K. B, and Brown,O. B., 1992. Observations of offshore shelf-water transport induced by a warm-core ring. Deep-Sea Research, 39, Suppl. S97-S113.

Kennelly, M. A., Evans, R. H., and Joyce, T. M., 1985. Small-scale cyclones on the periphery of a Gulf Stream warm-core ring. Journal of Geophysical Research, 90, 8845-8857.

Kontoyiannis, H., 1997: Quasi-geostrophic modeling of mixed instabilities in the Gulf Stream neat $73°W$. Dynamics of Atmospheres and Oceans, 26, 133158.

LaCasce, J. H., 1997. A geostrophic vortex over a slope. Journal of Physical Oceanography, 28, 2362-2381.

Lawson, G. L., Wiebe, P. H., Ashjian, C. J., and Stanton, T. K., 2008. Euphausiid distribution along the Western Antarctic Peninsula—Part B: Distribution of euphausiid aggregations and biomass, and associations with environmental features. Deep-Sea Research II, 55, 432-454.

Louis, J. P., and Smith, P. C., 1982. The development of the barotropic radiation field of an eddy on a slope. Journal of Physical Oceanography, 12, 5673.

Marr, J. W. S., 1962. The natural history and geography of the Antarctic Krill (*Euphausia superba* Dana). Discovery Report, 32, 37-465.

McWilliams, J. C., Holland, W. R., and Chow, J. H. S., 1978. A description of numerical Antarctic Circumpolar Currents. Dynamics of Atmospheres and Oceans, 2, 213-291.

McWilliams, J. C., and Flierl, G. R., 1979. On the evolution of isolated non-linear vortices. Journal of Physical Oceanography. 9, 1155-1182.

Moffat Varas, C. F., 2007. Ocean Circulation and Dynamics on the West Antarctic Peninsula Continental Shelf. Ph. D. Thesis. 186pp.

Moffat Varas, C. F., Owens, B., and Beardsley, R.C., 2009. On the characteristics of Circumpolar Deep Water Intrusions to the west Antarctic Peninsula Continental shelf. Journal of Geophysical Research, 14, C05017.

Munk, W. H., and Palmen, E., 1951. Note on dynamics of the Antarctic Circumpolar Current. Tellus, 3, 53-55.

Nof, D., 1983. On the migration of isolated eddies with application to Gulf Stream rings. Journal of Marine Research, 41, 413425.

Okkonen, S. R., Weingartner, T. J., Danielson, S. L., Musgrave, D. L., Schmidt, G. M., 2003. Satellite and hydrographic observations of eddy-induced shelf-slope exchange in the northwestern Gulf of Alaska. Journal of Geophysical Research, 108(C2), 3033.

Olbers, D., Borowski, D., Volker, C., and Wolff, J. O., 2004. The dynamical balance, transport and circulation of the Antarctic Circumpolar Current. Antarctic Science, 16, 439-470.

Olson, D. B., 1991. Rings in the ocean. Annual Review of Earth and Planetary Sciences, 19, 283311.

Orsi, A. H., Whitworth III, T. W., and Nowlin JR, W. D., 1995. On the meridional extent and fronts of the Antarctic Circumpolar Current. Deep-Sea Research, 42, 641-673.

Phillips, H. E., and Rintoul, S. R., 2000. Eddy variability and energetics from direct current measurements in the Antarctic Circumpolar Current south of Australia. Journal of Physical Oceanography, 30, 3050-3076.

Potter, J. R., and Paren, J. G., 1985, Interaction between ice shelf and ocean in George VI Sound, Antarctic, *in* Jacobs, S., ed., Oceanography of the Antarctic continental shelves: American Geophysical Union Antarctic Research Series, 43, 35-58.

Qiu, B., 1990. Low-frequency shelf/slope responses induced by localized offshore forcings. Journal of Geophysical Research, 95, 9447-9459.

Ross, R. M., Hofmann, E. E., and Quetin, L. B., (Eds.), 1996. Foundation for Ecological Research West of the Antarctic Peninsula. Antarctic Research Series, vol. 70.

Shaw, P. T., and Divakar, S., 1991. Generation of topographic waves over the continental margin, Journal of Physical Oceanography, 21, 1032-1042.

Simmons, H. L., Hallberg, R. W., and Arbic, B. K., 2004. Internal wave generation in a global baroclinic tide model. Deep-Sea Research II, 51, 3043-3068.

Sinha, B., and Richards, K. J., 1999. Jet structure and scaling in Southern Ocean models. Journal of Physical Oceanography, 29, 1143-1155.

Smith, D. A., Hofmann, E. E., Klinck, J. M., and Lascara, C. M., 1999. Hydrography and circulation of the West Antarctic Peninsula Continental Shelf. Deep-Sea Research I, 46, 925-949.

Smith IV, D. C., 1986. A numerical study of Loop Current eddy interaction with topography in the western Gulf of Mexico. Journal of Physical Oceanography, 16, 1260-1272.

Smith, D. C., and O'Brien, J. J., 1983. The interaction of a two-layer isolated mesoscale eddy with bottom topography. Journal of Physical Oceanography, 13, 16811697.

Stammerjohn, S., Martinson, D.G., Smith, R.C., and Lannuzzi, R.A., 2008. Sea ice in the western Antarctic Peninsula region: Spatio-temporal variability from ecological and climate change perspectives. Deep-Sea Research II, 55, 2041-2058.

Stammerjohn, S., and Smith, R.C., 1996, Spatial and temporal variability in west Antarctic Peninsula sea ice coverage. In: Ross, R. M., Hofmann, E. E., Quetin, L. B. (Eds.), Foundations for Ecological Research west of the Antarctic Peninsula, Antarctic Research Series, vol. 70.

Stern, M. E., 1991, Entrainment of an eddy at the edge of a jet. Journal of Fluid Mechanics, 228, 343-360.

Sutyrin, G. G., Ginis, I., and Frolov, S. A., 2001. Equilibration of baroclinic meanders and deep eddies in a Gulf Streamtype jet over a sloping bottom. Journal of Physical Oceanography, 31, 2049-2065.

Swaters, G. E., and Flierl, G. R., 1991. Dynamics of ventilated coherent cold eddies on a sloping bottom. Journal of Fluid Mechanics, 223, 565587.

Treguier, A. M., and McWilliams, J. C., 1990. Topographic influence on wind-driven, stratified flow in a β-plane channel: an idealized model for the Antarctic Circumpolar Current. Journal of Physical Oceanography, 20, 321-343.

Treguier, A.M., and Panetta, R. L., 1994. Multiple zonal jets in a quasigeostrophic model of the Antarctic Circumpolar Current. Journal of Physical Oceanography, 24, 2263-2264.

Thompson, L., and Ladd, C., 2004. The response of North Pacific Ocean to decadal variability in atmospheric forcing: wind versus buoyancy forcing. Journal of Physical Oceanography, 34, 1373-1386.

Thompson, L., 1991: Flow over finite isolated topography, Ph.D. Thesis, MIT/WHOI, WHOI-91-05. 222pp.

Vallis, G. K., 2006. Atmospheric and Oceanic Fluid Dynamics. 745pp.

Wang, X. M., 1992. Interaction of an eddy with a continental slope. Ph.D. Thesis, MIT/WHOI, WHOI-92-08. 216pp.

Wang, J., and Ikeda, M., 1997. Diagnosing ocean unstable baroclinic waves and meanders using the quasigeostrophic equations and Q-vector method. Journal of Physical Oceanography, 27, 11581172.

White, A. J., and McDonald, N. R., 2004. The motion of a point vortex near large-amplitude topography in a two-layer fluid. Journal of Physical Oceanography, 34, 2808-2824.

Wolff, J. O., Maier-Reimer, E., and Olbers, D. J., 1991. Wind-driven flow over topography in a zonal β-plane channel: a quasi-geostrophic model of the Antarctic Circumpolar Current. Journal of physical oceanography, 21, 236-264.

50272-101

REPORT DOCUMENTATION PAGE	1. REPORT NO. **MIT/WHOI 2009-18**	2.	3. Recipient's Accession No.
4. Title and Subtitle Slope/shelf Circulation and Cross-slope/shelf Transport Out of a Bay Driven by Eddies from the Open Ocean			**5. Report Date** September 2009
			6.
7. Author(s) Yu Zhang			**8. Performing Organization Rept. No.**
9. Performing Organization Name and Address MIT/WHOI Joint Program in Oceanography/Applied Ocean Science & Engineering			**10. Project/Task/Work Unit No.** MIT/WHOI 2009-18
			11. Contract(C) or Grant(G) No. (C) OCE-9901654 OCE-0451086 (G)
12. Sponsoring Organization Name and Address National Science Foundaton WHOI Academic Programs Office			**13. Type of Report & Period Covered** Ph.D. Thesis
			14.

15. Supplementary Notes
This thesis should be cited as: Yu Zhang, 2009. Slope/shelf Circulation and Cross-slope/shelf Transport
Out of a Bay Driven by Eddies from the Open Ocean. Ph.D. Thesis. MIT/WHOI, 2009-18.

16. Abstract (Limit: 200 words)
Interaction between the Antarctic Circumpolar Current and the continental slope/shelf in the Marguerite Bay and west Antarctic Peninsula is examined as interaction between a wind-driven channel flow and a zonally uniform slope with a bay-shaped shelf to the south.

Two control mechanisms, eddy advection and propagation of topographic waves, are found important for eddy-topography interactions. The topographic waves become more nonlinear near the western (eastern if in the Northern Hemisphere) boundary of the bay, inducing strong cross-escarpment motions.

A two-layer wind-driven channel flow spontaneously generates eddies through baroclinic instability. A PV front forms in the first layer shoreward of the base of the topography due to the lower-layer eddy-slope interactions. Both the cross-slope-edge transport and the out-of-bay transport are comparable with the model Ekman transport, suggesting the significance of the examined mechanism. The wave-boundary interaction is essential for the out-of-bay transport. Much more water is transported out of the bay from the west, and the southeastern area is the most isolated region. These results suggest that the southeastern region of the Marguerite Bay is a retention area for Antarctic krill

17. Document Analysis   a. Descriptors
bay
transport
jet

b. Identifiers/Open-Ended Terms

c. COSATI Field/Group

18. Availability Statement Approved for publication; distribution unlimited.	19. Security Class (This Report) **UNCLASSIFIED**	21. No. of Pages 222
	20. Security Class (This Page)	22. Price

(See ANSI-Z39.18)   *See Instructions on Reverse*   OPTIONAL FORM 272 (4-77)
(Formerly NTIS-35)
Department of Commerce